Sondre Drevdal Borge

B2B Converter-Based Voltage Control for Isolated Induction Generator supplying Local Variable Loads

Master's thesis in Energy and Environmental Engineering
Supervisor: Trond Leiv Toftevaag
June 2019

Master's thesis

NTNU

Norwegian University of
Science and Technology

Sondre Drevdal Borge

B2B Converter-Based Voltage Control for Isolated Induction Generator supplying Local Variable Loads

NTNU
Kunnskap for en bedre verden

Abstract

The modern world has grown a custom of utilizing electric power to operate a vast range of technologies and utilities. Though todays grids are generally stable and interconnected, an isolated power system could be useful for certain applications. Some examples are remote locations without existing grid infrastructure, applications that requires a stable and high-quality supply and utilization of small-scale renewable energy sources.

The objective of this thesis is to study the use of a filtered back-to-back system topology to control an isolated power system composed of an induction generator (short-circuit rotor, 3-10kW) and local variable AC-loads. Emphasis is placed upon designing a system that can operate the generator within rated conditions, whilst ensuring a stable and high-quality load voltage. The system should additionally be easy to setup for different configurations of loads and generators. The task is approached by building a complete model of the system in MATLAB-Simulink, evaluated by corresponding simulation-tests. Following this is a lab-setup of the proposed system with corresponding experiments, and a controller-implementation test on the Arduino Uno electronics board.

An extensive literature study is conducted to gain insight into the characteristics of the different components, methods of controlling induction machines and methods to generate gate-signals to the converter. The corresponding implementations of the different models and control-systems into MATLAB-Simulink are presented in detail. The level of detail in the models are mainly limited to the electrical properties with ideal characteristics. Some of the core assumptions are balanced operation, instantaneous changes (ideal switching/load-changes), no thermal/temperature-dependence and no processing delays.

The variable load model is built from scratch, based on the fundamental equations describing resistors, capacitors and inductors. For the induction generator, a steady-state and dynamic model is presented. 2L-3ph VSCs are chosen as converters of the B2B topology due to their commonness and four-quadrant operation. A simplified current-input model for the VSC is presented. For the filter, the passive LCL-topology is chosen, including a design procedure found in the literature. A battery is included in the system to enable magnetisation of the isolated induction machine and corresponding voltage build-up of the DC-link in the B2B-topology. A simple hydro-prime mover model is also presented, based on a linear relation of speed and torque. The control-theory covers methods such as V/f (scalar control), FOC (Field oriented control) and DTC (Direct torque control). The signal generation includes methods such as S-PWM, SV-PWM and hysteresis-based switching.

The outcome of the research is used as a basis to design two generator control-systems with the purpose of maintain the DC-link voltage of the converter. They are based on the principles of V/f and FOC, requiring measurements of mechanical speed and stator-currents. One voltage controller is also designed for the loads, with inputs of load-voltage measurements. Some new contributions are the design of a custom increase/decrease flux-controller in the FOC control-system and an RMS/DC-voltage approach to predict the output RMS-voltage of the converter. A step-by-step procedure to dimension the components of the system and tune the controller-parameters is also made and used to create four different configurations based on machines in the range of 4-16kW. The load-grid is defined as 230V (rms) 50Hz. Several simulation-tests are then performed to evaluate the performance, investigating aspects such as the influence of the battery-voltage, the magnetisation and DC-link voltage build-up, operation during load-changes and different speeds.

From analysis of the simulation-tests, the dimensioning and tuning from the proposed design-procedure seems to overall function well. The load-voltage is well maintained, keeping the magnitude within ± 2% RMS and THD <3%. High levels of lagging reactive loads negatively affects the LCL-filter performance, and an increase of reference DC-link voltage is suggested for better margins. The FOC-method is the best performing control-system, handling all test-cases whilst hardly exceeding the rated levels of currents and showing low DC-link voltage overshoots (<3%). It does however exhibit a high torque-ripple, it utilizes a high switching-frequency (50kHz) and its flux-controller results in high currents during light/no-loaded conditions. The V/f-method shows a more oscillating response, with overshoots of current up to 160% and overshoots of DC-link voltage up to 14%. A redesign of the tuning/structure is suggested to improve the performance. In comparison to the FOC-method, it does however display lower torque-ripples and it operates at a lower switching-frequency

(10kHz). In terms of the battery, the amount of work delivered is generally low compared to the machine-ratings. Lower speeds and higher battery-voltages gives higher peaks of battery current.

The lab-experiment is conducted on a 55kW induction machine connected to a 60kVA 2L-3ph VSC and another speed-controlled machine. The built-in control system of the lab-VSC is used as provided. A DC-source in series with a diode is connected to the DC-link. Experiments are performed for various conditions of initial DC-link voltage and speeds. The results verify that a low-voltage source is sufficient in order to magnetize the IM and build up voltage. It managed to successfully magnetize and build up voltage to a 400V reference with initial voltages as low as 10V at rated speed (1000 rpm). Lower speeds did however require a higher initial voltage, up to 40V. No clear pattern is seen in terms of DC-source peak-current, but it seems to generally be low, suggesting that a battery could be a viable DC-source.

A simplified version of the proposed V/f-control system is implemented on the Arduino Uno using MATLAB-Simulink. By comparing the measured output signals to what is theoretically expected, the performance is best for references signals with frequencies below 100Hz. Though the code could be optimized, the Arduino Uno is probably best suited for simple applications that does not need precision down in the milli-seconds range.

Sammendrag

Dagens samfunn er i stor grad avhengig av å anvende elektrisk kraft til å operere en stor mengde utstyr og teknologier. Selv om dagens nett generelt sett er stabile og sammenkoblede så kan et isolert nett være nyttig for spesielle anvendelser. Noen eksempler er avsidesliggende områder uten infrastruktur, anvendelser som krever høy kvalitet på levert spenning og utnyttelse av småskala fornybar kraft.

Formålet for denne masteroppgaven er å undersøke bruken av en filtrert "back-to-back"-topologi (B2B) til å styre et isolert kraftsystem bestående av en induksjonsgenerator (kortsluttet rotor, 3-10kW) og lokale variable AC-laster. Det er lagt vekt på å designe et system som kan operere generatoren innenfor grenseverdier og som samtidig sikrer en stabil lastspenning av høy kvalitet. Problemstillingen er løst ved å bygge en komplett modell av systemet i MATLAB-Simulink, evaluert ved hjelp av tilhørende simuleringstester. I tillegg utføres eksperimenter på et lab-oppsett av tiltenkt system, og en implementering av et kontrollsystem på kretskortet "Arduino Uno".

Et lengre litteratursøk er utført for å skaffe innsikt i virkemåten til de forskjellige komponentene i systemet, styringsmetoder for induksjonsmaskinen, samt metoder for å lage styresignaler til omformeren. Tilhørende implementering av modeller i MATLAB-Simulink vil bli vist i detalj. Detaljnivået er primært begrenset til elektriske egenskaper. Noen av hovedantagelsene er balansert operasjon, øyeblikkelige tilstandsendringer av brytere/lastere, ingen temperaturavhengighet og ingen prosesseringsforsinkelser.

Modellen av variable laster er bygget fra bunnen, basert på de fundamentale ligningene til resistans, induktans og kapasitans. For induksjonsmaskinen presenteres en stasjonær og dynamisk modell. 2L-3ph VSC (To-nivå trefase spenningskildeomformer) er valgt som omformer på grunn av dens utbredte bruk og operasjonsmulighet i fire kvadranter. En enkel strømbasert modell er presentert. Som filter er en passiv LCL-topologi valgt, med tilhørende designprosedyre funnet i litteraturen. Et batteri er inkludert i systemet for å muliggjøre magnetisering av induksjonsgeneratoren og tilhørende spenningsoppbygging av DC-linken. En enkel vannturbinmodell blir også presentert, basert på et linjert forhold mellom turtall og dreiemoment. Kontrollteorien omfatter metoder som V/f (Skalar kontroll), FOC (Feltorientert kontroll) og DTC (Direkte dreiemoment kontroll). Styresignalmetoder omfatter S-PWM (Sinus pulsbreddemodulasjon), SV-PWM (Romvektor pulsbreddemodulasjon) og hysterese-basert svitsjing.

Kunnskap fra litteratursøket brukes som basis for å designe to styringssystemer for generatoren, med formål om å ivareta DC-link-spenningen i omformeren. Styringssystemene er basert på prinsippene til V/f and FOC, og krever målinger av rotorhastighet og statorstrømmer. En spenningskontroller er også designet for lastene, som krever målinger av lastspenninger. Noen nye bidrag er designet av en hjemmelaget magnetstrømkontroller for FOC-metoden, samt en RMS/DC-funksjon for estimering av levert omformerspenning. En stegvis prosedyre for å dimensjonere komponenter i systemer og stille inn kontrollparametere er også utviklet, and brukes til å lage fire systemkonfigurasjoner basert på induksjonsmaskiner med nominell effekt i området 4-16kW. Lastnettet er definert som 230V (rms) 50Hz. Et mangfold av simuleringstester er så utført for å evaluere ytelse, herunder for å studere effekt av batterispenning, magnetiseringsforløp og spenningsoppbygging, operasjon ved forskjellige laster og forskjellige turtall.

Analyse av simuleringsresultatene viser at dimensjonerings- og designprosedyrene ser ut til å generelt sett fungere bra. Lastpenningen blir godt ivaretatt, med en amplitude innen $\pm$ 2% RMS og THD < 3% (Total harmonisk forvrenging). Høyt nivå av etterslepende (lagging) reaktiv effekt påvirker filteret i negativ forstand, og en økning av referansespenning til DC-linken er foreslått for å heve marginene. Styringssystemet basert på FOC-metodikken presterer best, og det opererer hensiktsmessig under alle tester. Det holder generatorstrømmen innenfor grenseverdier, og viser til lave overskytninger av DC-link spenning (<3%). Det opererer derimot med høye rippler på dreiemomentet, en høy svitsjefrekvens (50kHz) og dets magnetstrømkontroller resulterer i høy tomgangsstrøm. V/f-metodikken viser en mer svingende respons og overskyter i statorstrøm opptil 160% og DC-link-spenning opptil 14%. Revidering av design/parameterinnstilling er anbefalt for å øke ytelse. Til sammenligning med FOC-metodikken operer derimot V/f med lavere rippler av dreiemoment og en lavere svitsjefrekvens (10kHz). Batteriet leverer en arbeidsmengde som generelt sett er meget lav med tanke på de

nominelle maskineffektene. Lavere turtall og høyere batterispenning gir høyere toppverdier av strøm.

Lab-eksperimentet er utført på en 55kW induksjonsmaskin koblet sammen med en 60kVA 2L-3ph VSC og en annen turtallstyrt motor. Det innebygde styringssystemet til lab-omformeren er brukt som gitt. En DC-kilde er koblet i serie med DC-linken. Eksperimenter er utført for forskjellige turtall og initiale DC-link spenninger. Resultatene bekrefter at en lavspent kilde er tilstrekkelig til å magnetisere induksjonsgeneratoren og bygge opp spenning i DC-linken. Systemet evnet dette for initiale spenninger så lavt som 10V ved merketurtall (1000rpm). Lavere turtall krever derimot høyere initialspenninger, opp til 40V. Ingen tydelige trender er observerbare med tanke på DC-kilde strøm, men den virker å generelt være lav og det er tenkelig at et batteri kunne vært en mulig DC-kilde.

En forenklet versjon av V/f-metodikken er implementert på Arduino Uno ved hjelp av MATLAB-Simulink. Sammenligning av måledata mot hva som teoretisk sett er forventet viser at ytelsen er best for referansesignaler med frekvenser under 100Hz. Selv om det er tenkelig at koden kunne blitt optimalisert, så er Arduino Uno sannsynligvis best egnet for enkle applikasjoner som ikke trenger presisjon ned i millisekundområdet.

Acknowledgements

Table of Contents

List of Figures

List of Tables

Abbreviations and symbols

RMS	Root Mean Square
THD	Total Harmonic Distortion
CWT	Continuous Wavelet Transform
pf	Power Factor
EMF	Electromotive Force
IM	Induction Machine
PM	Prime Mover
B2B	Back To Back (converter topology)
VSC	Voltage Source Converter
2L-3ph	Two-level three phase
PWM	Pulse Width Modulation
S-PWM	Sinusoidal Pulse Width Modulation
SV-PWM	Space Vector Pulse Width Modulation
THI	Third Harmonic (in relation to S-PWM)
V/f	Voltage/Frequency (scalar control)
FOC	Field Oriented Control
DTC	Direct Torque Control
#	Index
v_{xs}, V_s, V_ϕ	Phase voltage
ω	Reference frame speed
P_N^G	Nominal generator power (electric)
P_N^{Gm}	Nominal generator power (mechanical)
V_N^G	Nominal generator phase voltage (rms)
I_N^G	Nominal generator current (rms)
f_N^G	Nominal generator electrical frequency
ω_m^G	Nominal mechanical speed (generator)
P_N^L	Nominal load power
V_N^L	Nominal load phase voltage (rms)
I_N^L	Nominal load current (rms)
f_N^L	Nominal load electrical frequency

1 Introduction

1.1 Background

The introduction of electric power has had a prominent impact on society. The modern world has grown a custom of utilizing more electrically powered technologies and are thus becoming more reliant on having an electric power utility available. Today, the grids are a backbone in powering households, industry, transportation and other infrastructure. Having a wide and interconnected main grid provides a generally stable and secure supply. An alternative solution to deliver the power services are isolated grids, utilizing a local energy source. There exist many terms to describe these systems, such as island-mode, off-grid and microgrids. The core principal of an electric grid is however the same, whether it's spanning across several nations or is limited a single household. The definitions are thereby often related to the size/span or amount of power supplied. Some isolated system can also be connected/disconnected to the main grid. In any case, there are several examples of where an isolated system can be useful:

- **Areas without existing grid infrastructure**
  This could be the case for developing countries, and remote locations such as islands and rural unpopulated areas. The cost of extending the main grid might make a more local solution economically viable. Other related examples are mobile systems such as ships or larger vehicles.

- **Poor service quality and self-supply mentality**
  Some applications require voltage of a minimum quality to function. Other applications heavily depend on always having power services available, such as hospitals. If the main grid cannot provide the expected performance, a local system can be the solution. When using the grid service, you must also obey its regulations/laws and expect varying prices. With a local grid, you can limit your dependence on external actors.

- **Utilization of small-scale renewable sources**
  A solution to the problem of climate change and increasing demand for energy is to utilise locally available renewable sources. Motivation for this can be both economical and environmental, and related to the self-supply mentality. An example of such a local system could be a household load with a wind-turbine, battery-storage and controllable grid-connection.

1.2 Problem

1.2.1 Origin

The problem at hand is a inspired by a master's thesis [3], and a continuation of a specialization project [52] conducted in the fall of 2018. The problem originates from "Remote Hydroligth" (`http://www.remotehydrolight.com/`) who have been working with installing micro-hydropower to provide clean electric power in remote locations. In this context, having a simple, robust and cheap system is advantageous, in order make it affordable and maintainable by the local users. The three-phase induction machine (short-circuited rotor) is a very robust machine, as it has no slip rings and no requirement of an additional field circuit. This has made it a very common machine in the industry and marked [4][1], and thus a suitable component in such a remote power system.

1.2.2 Objective/goal
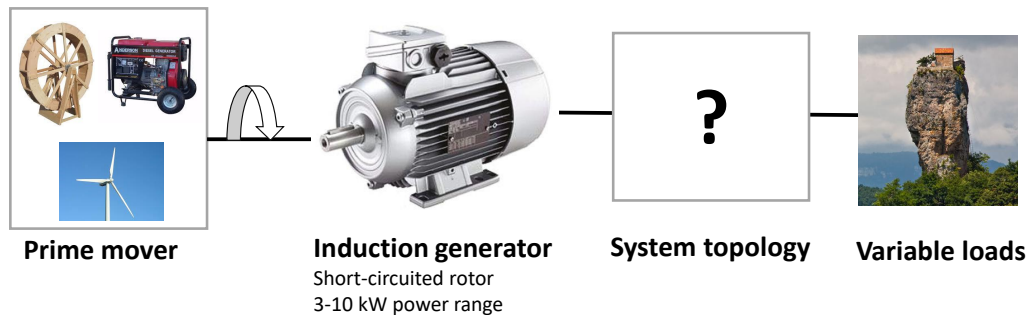
Figure 1.1: System to be solved

The problem/objective of this thesis is to identify and develop a suitable system topology for an isolated electric power system (Figure 1.1). This isolated system (no external grid-connection) is meant to supply local variable loads based on an induction generator (3-10kW) connected to a local prime-mover. A core focus will be the design and development of the appurtenant control system, which should operate the induction machine within rated conditions whilst ensuring a stable supply to the loads. Emphasis is placed on the applicability and performance. This implies that the system than can be easily dimensioned and configured to suit various rotational mechanical sources / induction machines, and that it can provide a stable and high-quality load voltage.

1.3 Method and scope of work

A brief literature study will first be given to present possible system topologies, followed by the reasoning for choosing a filtered back-to-back converter topology (Figure 1.2) in relation to the desired characteristics of the system to be developed. The back-to-back topology forms the basis for the rest of the study.
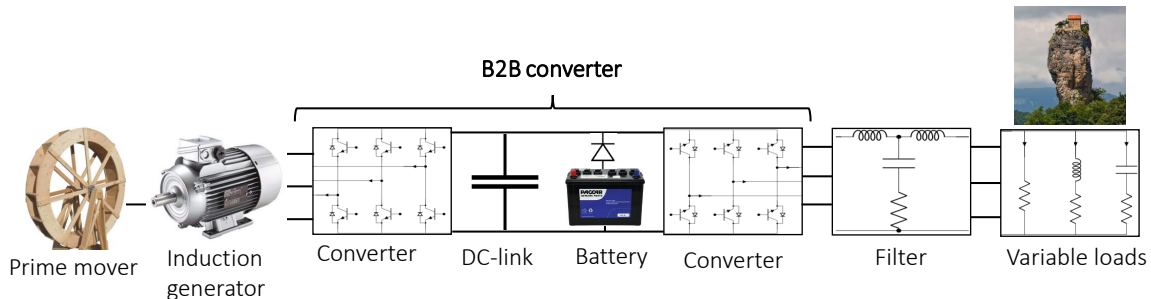
Figure 1.2: Proposed system

Simulation-software is a suitable tool for this type of problem, as it provides an environment that can be used to implement and interconnect control-systems and models of different components to form a complex system. Results are quickly obtained via simulation, where multiple parameters can be inspected and analysed to study the behaviour, which can be used to conduct further adjustments and improvements. MATLAB-Simulink will be used as the simulation-software. To test the theoretical aspects and gain more insight into practical consideration, some experiments will also be conducted with real components.

The problem/objective of this thesis is approached in a chronological manner, covering the following tasks:

- Conduct a literature study to describe the characteristics/behaviour of the components in the system, and implement suitable models into MATLAB-Simulink. The level of detail in the models will mainly be limited to the electrical properties with ideal characteristics. Some of the core assumptions are balanced

operation, instantaneous changes (ideal switching/load-changes) and no thermal/temperature-dependence. The following components will be treated:

  - Variable loads

  - Induction generator

  - Converter

  - Filter

  - Rotational system and prime-mover

  - Battery and DC-link

- Conduct a literature study to present control-methods for induction machines and methods for creating gate-signals to control the converter. MATLAB-Simulink implementation of the latter.

- Develop control-systems for the proposed system at hand with a basis in the presented theory and contribution of own designs. The control-systems are assumed ideal without processing delays. They are intended to operate the induction generator within rated current limits, and provide load-voltage of sufficient quality. Implement the systems into MATLAB-Simulink.

- Develop a generic design/dimensioning-procedure for the components in the system with tuning of the control-systems included.

- Conduct simulation-tests with different configurations of machines to evaluate the performance of the control-systems and the proposed design-procedure. Inspect for various conditions such as voltage build-up and magnetisation, load-changes and different speeds.

- Design a lab-setup of the proposed system and perform experiments to study the voltage build-up in the converter and magnetisation of the machine for variations of initial DC-link voltage and speed. Compare with theoretical results from the simulations.

- Implement a control-system on the low-cost electronic board "Arduino Uno", and study is capabilities and limitations as a processor and controller for a converter.

Further details are presented in the corresponding chapters. This includes the assumptions and limitations of each model and the reasoning for setting up simulations/experiments as done.

1.4   Structure of content

Chapter 2 gives a brief review of possible system topologies, followed by the reasoning for choosing a filtered back-to-back system.

Chapter 3 presents a home-made model of variable AC-loads and its corresponding assumptions and limitations. MATLAB-Simulink implementation is given.

Chapter 4 present an explanation of how induction machines work, including a steady-state and dynamic model. MATLAB-Simulink implementation of the dynamic model is given.

Chapter 5 covers the converter (2L-3ph VSC), presenting its possible states of operation and a simplified current-input based model. MATLAB-Simulink implementation is given.

Chapter 6 relates the converter to different methods of generating gate-signals. This includes methods such as S-PWM and hystereis-controllers (with MATLAB-Simulink implementation) and SV-PWM. A home-made model to control output RMS-voltage is also presented (RMS/DC).

Chapter 7 treats the aspects of filtering output-voltage from converters, followed by a description and MATLAB-Simulink implementation of the series-damped passive LCL-filter. A design procedure found in the literature is presented.

Chapter 8 gathers the modelling and MATLAB-simulink implementation of the rotational system, DC-link and battery. Considerations regarding the prime-mover is presented, with a description of a simple hydro-turbine model.

Chapter 9 presents the limitations and operational aspects of the induction machine, followed by a presentation of three control-methods: Scalar control (V/f), FOC (Field oriented control) and DTC (Direct torque control).

Chapter 10 presents the intent and assumptions regarding the control-systems. Based on the presented theory and the system topology in question, three control systems are designed with their MATLAB-Simulink implementation. This includes two DC-link voltage oriented generator control-systems, based on the principles of the V/f(scalar) and FOC-method. One voltage controller is designed for the loads. Some new contributions are the design of a flux-controller in the FOC-method and an implementation of the RMS/DC-voltage model. A complete list of required parameters for the different control-systems are also given.

Chapter 11 present a home-made procedure to dimension the components of the system. It also includes suggestions on how to tune all control-system parameters based on rated values.

Chapter 12 applies the proposed control-systems and design-procedures at four different machines (system configurations), and presents the setup of several simulation-tests used to inspect the performance. Five types of tests studies the magnetisation/voltage build-up, behaviour during load-changes, the FOC-method's sensitivity to the rotor time-constant, interactions with the hydro-prime mover and the load-voltage quality at different types of loading. The results are analysed to identify patterns, and a comparison is made with respect to the different control-systems and different tested machines (configurations).

Chapter 13 presents the setup and equipment used in a laboratory experiment that resembles the proposed system topology. Tests are conducted to examine the voltage build-up of the converter and magnetisation of the induction machine for different settings of initial DC-link voltage and generator speed. The results are analysed, and compared to the trends observed in the simulation-tests.

Chapter 14 presents technical details and constraints of the "Arduino Uno", followed by a description the setup and equipment used to study its feasibility as a controller. A simplified version of the designed V/f-control system is implemented using MATLAB-Simulink, and measurements are used to compare the output to what is theoretically expected.

Chapter 15 summarises the findings in this thesis and makes a conclusion based on the desired objective. Suggestions for further work is presented.

2   System topology

In the literature, there exists several solutions proposed for problems and systems similar to the one in this thesis. This chapter will give a brief introduction of possible system configurations to control an isolated induction generator with loads, followed by the motivation for choosing the back-to-back converter based approach.

2.1   SEIG

Self-excited induction generator (SEIG) is a common term found in this topic. With some residual magnetism and capacitors connected to the stator terminals, voltage can be built up without the need of a control system. The residual magnetism can induce voltage if the rotor is moving. This induction results in currents flowing in the capacitors, which further builds up the flux in the generator. The build-up eventually stops (reaches a balance) due to saturation, where the voltage increase as a function of magnetizing current becomes non-linear, and intersects with the characteristic line of the capacitors, [4][2] [5][3] [21]. Applying loads to the stator terminals of such a system with fixed capacitors will affect the frequency and magnitude of the system voltage. This is a complex phenomenon, where the characteristics of the prime mover will be of influence, combined with the resistive and reactive nature of the load, [17] [3][1]. Such a system is also in risk of a voltage collapse, which illustrates the benefits of implementing a control system.

2.2   Active controllers

There exist several electrical topologies that can influence the operation of the system. Some examples are STATCOM (Static synchronous compensator), VSC (Voltage source converter), SVC (Static VAR compensator) and ELC (Electronic load controller).

A method of control is to adjust the reactive elements as seen by the system. One example is to use a combination of capacitor banks and thyristor controlled reactors (SVC), [20]. The control can also be realized by switched capacitors and reactors, [16]. Another method is making use of VSCs to function as a STATCOM, [15]. This implies that one can control the reactive power delivered or absorbed to the system. VSCs can also be applied to control the voltage of the system, and aid in the start-up (magnetisation) of the induction generator, [18, 19]. In some systems, it could be desirable to operate the induction generator at fixed speed and active power. With an ELC, a dump load can be used to absorb any unused active power in the system, [3][2].

2.3   Proposed system: Back-to-back converter

The back-to-back (B2B) converter is a topology consisting of two AC/DC converters connected by a common DC-link. This enables a separation of the two AC-sides, which can operate at different voltage frequencies and magnitudes. The power drawn or delivered by either side can also be controlled. This makes it a very versatile topology, with applications such motor drives, interconnecting HVDC and wind turbine generation.

Recall from the objective of this thesis that emphasis is placed upon on developing a system that operates the induction machine within rated conditions whilst providing a stable and high-quality load voltage. The B2B-topology is a suitable candidate to achieve this. The proposed system topology (Figure 2.1) will be composed of two VSCs with four quadrant operation, a battery and a filter at the load output. The reasoning and advantages of this solution are summarized as follows:

- Four quadrant operation is a requirement to operate with reactive power, and it enables a wide range of control. The 2L-3ph VSC is chosen as the converter due to its commonness and conceptually simple structure, making it it easier to implement (Chapter 5).

- The generator and load can be operated at individually controlled AC-grids. This allows for flexibility in terms of speed and voltage of the generator, which does not have to match the required load voltage conditions. Additionally, transient conditions are not directly affecting the load, and vice-versa.

- The DC-link capacitor can act as a energy buffer to smooth out power imbalance, and thus maintain the desired voltage at the load. This can be useful if the prime mover and generator have time-delays for changing operation-points.

- The excitation of the generator can be achieved without the need of three-phase capacitor banks. Some initial voltage on the DC-link provided by a battery could in theory be sufficient for building up the voltage.

- Filters on the load side allows to enhance voltage quality, useful for sensitive loads. LCL-filter is chosen due to it's advantages of high attention from low component-values (Chapter 7).
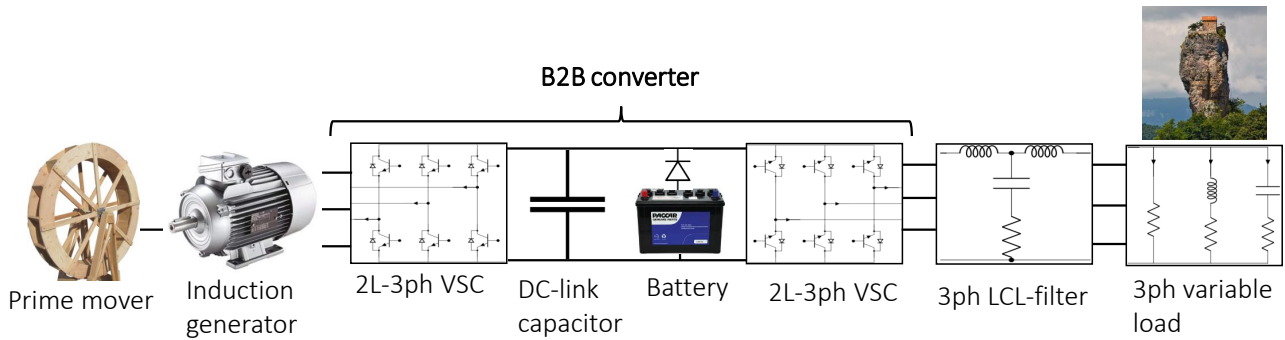
Figure 2.1: Proposed system topology

An alternative solution for the loads could be to define them as DC-loads, which would remove the need for the filter and one of the VSCs. This aspect will however not be treated further, keeping the load-grid defined as AC.

3 Three-phase variable loads

With an assumed three-phase AC grid for the loads, a model to implement variability is useful for studying the operation of the whole system during different types of loading. This chapter will introduce a possible approach for this, with its corresponding MATLAB-Simulink implementation.

3.1 Impedance branches in parallel connection

Under the assumption of three phase balanced loads and a sinusoidal voltage of fixed voltage magnitude and frequency, one can emulate any steady-state active and reactive power by the means of an per phase equivalent impedance. The complex relations are summarised by (3.1), (3.2) and (3.3).

$$\boldsymbol{S^L} = P^L + jQ^L \tag{3.1}$$

$$\boldsymbol{Z^L} = \left(\frac{\boldsymbol{V_\phi}^{\boldsymbol{2}}}{\left(\frac{\boldsymbol{S^L}}{3} \right)} \right)^* \tag{3.2}$$

$$R = \operatorname{Re}\left(\boldsymbol{Z^L} \right), \quad X = \operatorname{Im}\left(\boldsymbol{Z^L} \right) \tag{3.3}$$

Variations of loading can then be realised by adjusting the equivalent impedance ($\boldsymbol{Z^L} = R + jX$). A possible model for this is a per phase parallel R, LR and CR branch, Figure 3.1. For purely active loads, R_L is applied, whereas reactive loads applies the series connection $R_{LL} + L_L$ (lagging) or $R_{CL} + C_L$ (leading). The model takes input of load voltage to provide output of load current. The resistors follow Ohm's law, the inductors voltage is given by $v_L = L\frac{di}{dt}$ and the current of the capacitor is given by $i_C = C\frac{dv}{dt}$. The currents of each branch are expressed in Laplace notation by (3.4), (3.5) and (3.6).

$$I_R = \frac{V_\phi}{R_L} \tag{3.4}$$

$$I_{LR} = \frac{V_\phi - V_{R_{LL}}}{sL_L} = \frac{V_\phi}{R_{LL} + sL_L} \tag{3.5}$$

$$I_{CR} = C_L(V_\phi - V_{R_{CL}})s = \frac{V_\phi}{R_{CL} + \frac{1}{sC_L}} \tag{3.6}$$
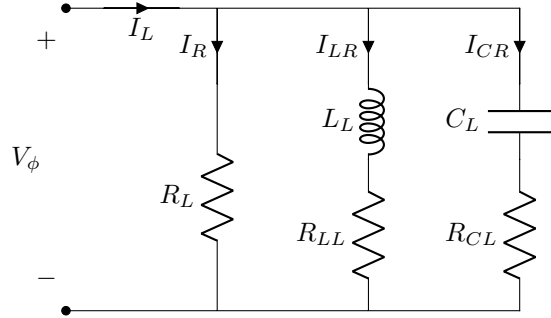
Figure 3.1: Per phase load circuit

3.1.1 Assumptions and limitations

The model assumes ideal components of resistance, inductance and capacitance, i.e. their characteristics are strictly "linear" and the parameter values (of unit: R=ohm, L=henry, C=farad) are unaffected by temperature, frequency, and such. Practical non-ideal inductors and capacitors would have series resistance, which is also included in the model. The main motivation for the inclusion of series-resistance is however related to two considerations:

Firstly: The model uses voltage as input. The capacitor should not have a step change voltage, as this implies an infinitely large current. The resistor is therefore needed for ease in the simulation-implementation.

Secondly: The inductor could have been modelled without a series resistor for this voltage-input approach. The current-response of a pure inductor would however depend on the phase of the step-applied voltage. Figure 3.2

illustrates this, with an inductor of $L = \frac{1}{2\pi}H$ and a sinusoidal voltage ($\sin(2\pi \cdot t - \theta)$) connected at t=1. The current response is sinusoidal for all cases, but can have an apparent DC-offset that would not be "damped". Adding a series resistor will ensure that the response swings toward zero as its symmetrical point, where a larger resistor will give a faster "damping".
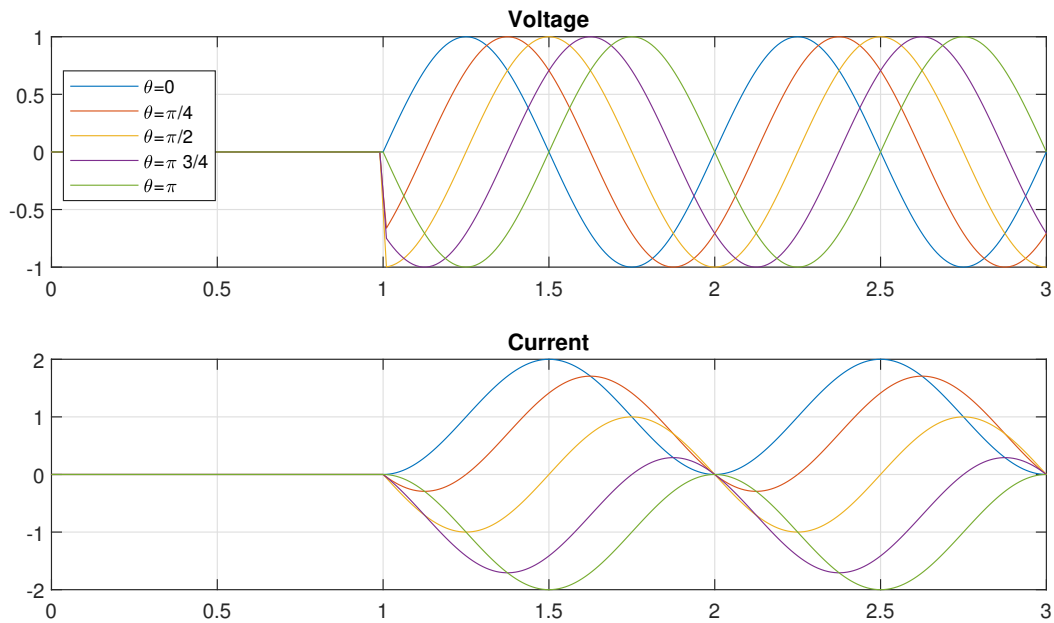
Figure 3.2: Step change of voltage and inductor-current

The model can be used to simulate arbitrary loads, but one must keep in mind the following constraints:

- For reactive power, one will always have belonging active part due to the series-resistors.

- The transient response of an applied load is dictated by the transfer functions given above: (3.4), (3.5) and (3.6).

- The actual apparent power from the impedance-approach will deviate with varying voltage magnitude and inclusion of harmonic components.

- The loads are assumed balanced and star(Y) connected, but modelled as separate individual networks per phase. If unbalanced voltages are applied, the corresponding unbalance of currents are not treated (similar to the dynamic induction machine model, Section 4.5.1)

3.2   Simulink implementation
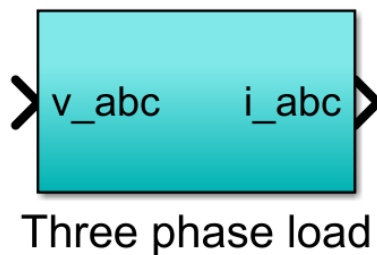
Figure 3.3: Three phase load model block

The impedance-branch based three phase variable load model are made into the custom block, Figure 3.3. It takes input of the phase-voltages to provide the corresponding phase-currents. The inner structure is shown in Figure 3.4, where the phase-voltages are split into their corresponding identical per-phase blocks, Figure 3.5. The yellow quantities (7 in total) represent the required time-series which are used to vary the load. This includes the component values of the three parallel branches (R_L, R_{LL}, R_{CL}, L_L and C_L), and two reset-signals for the inductor and capacitor. The three parallel branches are based on the corresponding transfer-functions, (3.4), (3.5) and (3.6).
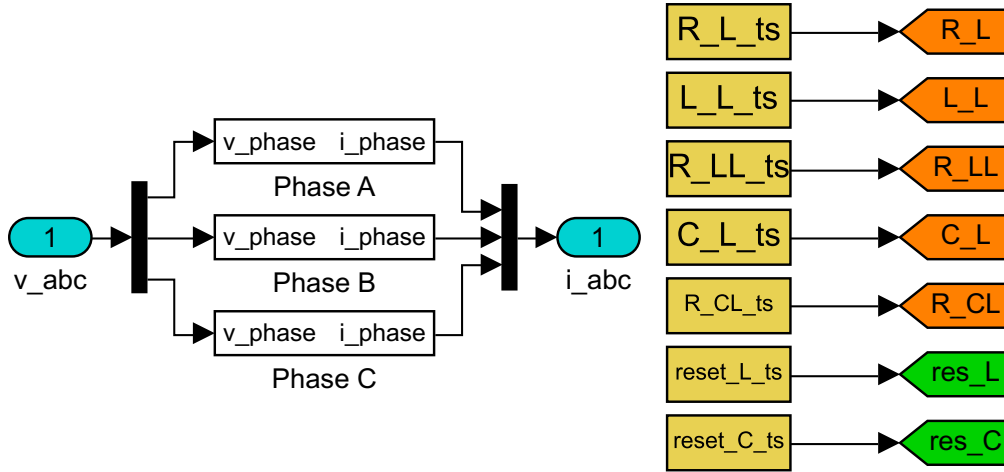
Figure 3.4: Inner structure of three phase load block
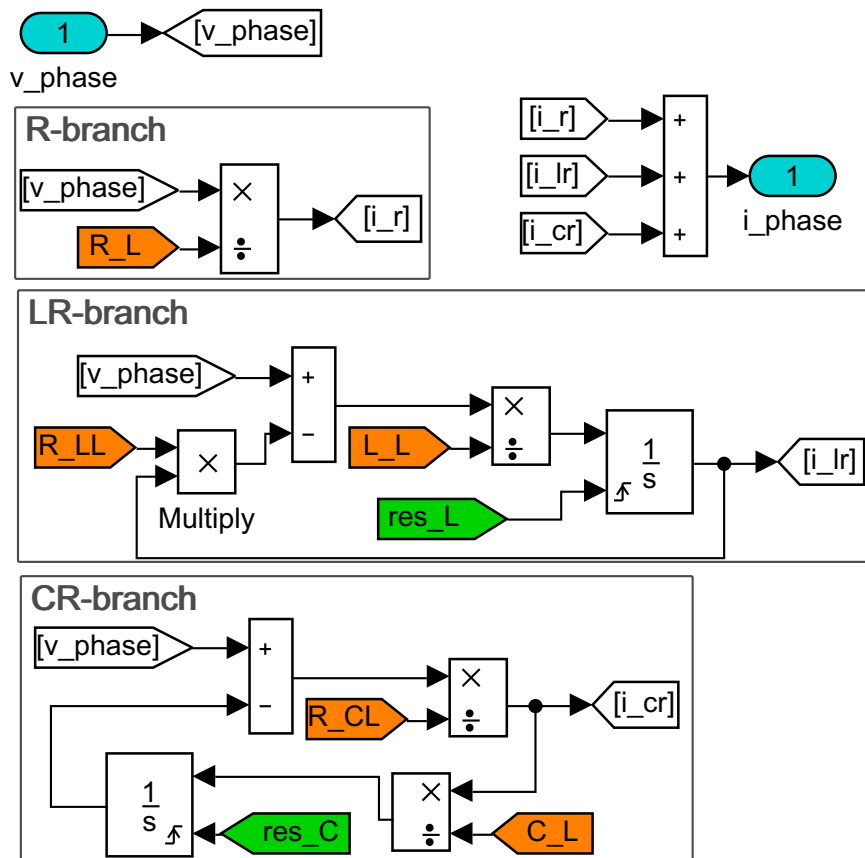
Figure 3.5: Inner structure of phase-blocks

When variables loads are simulated by time-series inputs of resistance, inductance and capacitance, the reset-

9

signals (green) can be used to null the integrators. This effectively resets the current (inductor) or voltage (capacitor) to zero, thus ensuring that no "leftover" conditions are of influence. Though only one of the branches (R, LR or CR) are applied for a given load, all 7 time-series must be defined to run a simulation. The "unused" branches can effectively be defined as open by defining the resistance and inductance/capacitance to a sufficiently large value, such as 10^{10}. The exception is the LR-branch, where R_{LL} should be set to zero as it's used in a multiplication, unlike the other quantities which are used as denominators.

4 The Induction Machine

This chapter is dedicated to the induction machine, covering its working principle and common definitions. A steady-state and dynamic model will be introduced, including a MATLAB-Simulink implementation for the latter.

4.1 Working principle

The induction machine is one of the common types of electric machines. Similar to other electric machines, it consists of an outer non-rotating circuit (stator) and an inner rotating circuit (rotor). To explain its working principles, we consider a simplified representation of the short-circuited (squirrel cage) rotor type [5][1,2]
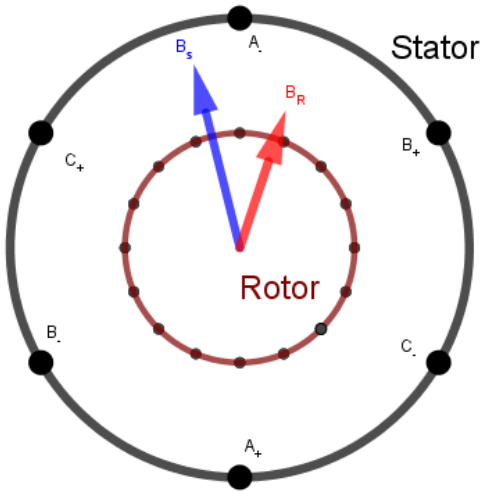
Figure 4.1: 2D cross-section of induction machine
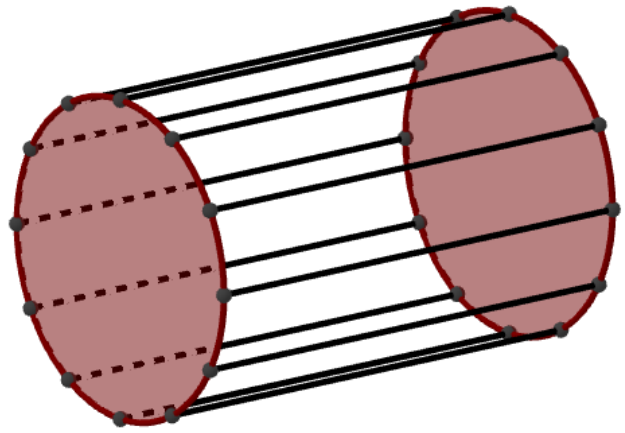
Figure 4.2: Short-circuited rotor

The stator windings can be imagined as three coils displaced symmetrically in space by 120 degrees, Figure 4.1. By applying a balanced sinusoidal three phase current, one obtains a rotating stator magnetic field, $\boldsymbol{B_s}$. It can be represented as a vector of constant magnitude, rotating at speed ω_{sync}. The rotor consists of several conducting bars, short circuited at each end in the axial direction, Figure 4.2. If the rotational speed of the rotor (ω_m) is different from that of $\boldsymbol{B_s}$, voltage is induced in the rotor bars according to Faradays law, $e_{ind} = -\frac{d\phi}{dt}$. This creates currents in the rotor that functions to oppose the changes of magnetic flux, thus introducing the rotor magnetic field vector, $\boldsymbol{B_r}$. These two fields results in a torque on the rotor in a direction that functions to synchronise its speed to that of $\boldsymbol{B_s}$, evident by for instance the Lorentz-Force on a conductor in a magnetic field, $\vec{F} = \vec{i}L \times \vec{B}$. The relation can be derived by using the concepts of co-energy [1][2]. Generally, the converted energy depends upon the relative speeds and applied voltage. In generator-operation, $\omega_m > \omega_{sync}$. Speed-torque characteristic curves are often used to predict suitable operational points. A core characteristic of the IM is that it always consumes reactive power in both motor and generator operation. This is required to maintain its magnetisation, and must be supplied through its utility.

Some commonly encountered parameters/definitions when working with models of the IM are summarised in Table 4.1.

Symbol	Name	Description
n_{pp}	Pole pairs	Number of pole-pairs.
ω_{el}	Electric speed [rad/s]	Angular speed of stator electric currents: $2\pi \cdot f_{el}$
ω_m	Mechanical speed [rad/s]	Angular speed of the rotor shaft
ω_{sync}	Synchronous speed [rad/s]	Angular speed of stator magnetic field: $\frac{\omega_{el}}{n_{pp}}$
ω_r	Electric rotor speed [rad/s]	$\omega_r = \omega_m \cdot n_{pp}$
ω_s	Slip speed [rad/s]	$\omega_{el} - \omega_r$
s	Slip	Normalised relative speed: (4.1)

Table 4.1: IM parameters/definitions

$$s = \frac{\omega_{el} - \omega_r}{\omega_{el}} = \frac{\omega_{sync} - \omega_m}{\omega_{sync}} \tag{4.1}$$

4.2 Steady state model

A common way to model the induction machine is by using the so called "steady state equivalent circuit". It can be derived by considering the similarities of the IM to that of a transformer, giving the per phase representation as shown in Figure 4.3 (short-circuited rotor), [1][3] [5][4]. The rotor is referred to the stator through an fictitious winding-ratio.

4.2.1 Assumptions and limitations

Some simplifications/assumptions are underlying the model, which should be noted to know its limitations:

- The model represent the steady-state operation with balanced sinusoidal supply.

- The model is based on an idealized circuit with three windings in the rotor and stator, symmetrically displaced and concentrated. They are assumed to provide sinusoidally distributed fields.

- The parameters (resistors and inductors) are fixed, i.e. they do not depend on frequency, temperature, voltage, current, etc.

- The air-gap is symmetrical, and there is no reluctance drop in the iron. Losses due to eddy-currents/hysteresis is not included, but might be represented as a resistor in parallel with the magnetising inductance L_m.

- Magnetic saturation is neglected.

- Other non-electric related losses such as friction are also neglected in this representation.

4.2.2 Equivalent circuit
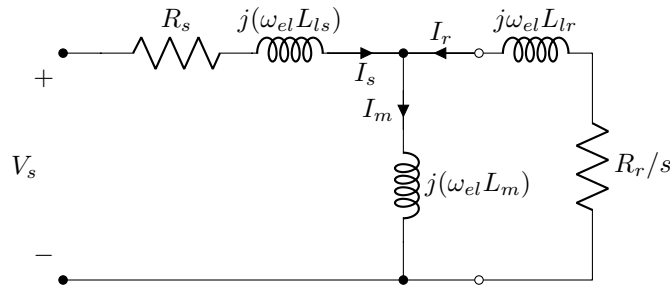
Figure 4.3: Per phase equivalent circuit of IM

R_s	Stator resistance [Ω]
R_r	Rotor resistance (referred to stator) [Ω]
L_{ls}	Stator leakage inductance [H]
L_{lm}	Rotor leakage inductance (referred to stator) [H]
L_m	Magnetizing inductance [H]

Table 4.2: Parameters of the equivalent circuit

The equivalent circuit can be analysed using the common phasor-representation of currents and voltages. With inputs of phase voltage (V_s) and the operational speed expressed by slip (s), all other quantities can be solved for. The stator current (I_s) can be used to determine the per phase active and reactive power. The converted electric to mechanical power (not accounting for friction) can be expressed by (4.2). A positive value corresponds to motor-operation. Note that if $s = 0$, the machine is at synchronous operation, and the resistor R_r/s in Figure 4.3 would approximate ∞. In this condition, no rotor-current would flow, giving $P_{conv} = 0$. A Thevenin-equivalent circuit can be made with the left-facing part of the circuit as seen from the nodes "∘" in Figure 4.3 to simplify the calculation of I_r.

$$P_{conv} = 3 \cdot |I_r|^2 R_r \left(\frac{1-s}{s} \right) \quad [\text{W}] \tag{4.2}$$

$$T_{em} = \frac{P_{conv}}{\omega_m} \quad [\text{Nm}] \tag{4.3}$$

4.3 The fluxes

Commonly encountered terms for the induction machine are magnetic flux related to the stator, rotor and magnetisation. The term "flux" and "flux-linkage" are often use interchangeably, but in principle it describes the amount of magnetic field lines through a surface [Wb], which when varies can result in induced voltage. The concept of flux can be related to inductance in the circuit-domain, as it describes how current-changes through an electric element influences the voltage across it. Inductance might be imagined as a kind of magnetic inertia, which value is determined by the geometry of the element and other nearby sources/materials influenced by magnetic fields.

With the currents as shown in the equivalent circuit, Figure 4.3, identifying that $I_m = I_s + I_r$, we have the definitions of fluxes as shown in Table 4.3. The greek letter ψ is also commonly used to symbolise fluxes.

$\lambda_s = L_{ls}I_s + L_mI_m$	Stator flux linkage [Wb]
$\lambda_r = L_{lr}I_r + L_mI_m$	Rotor flux linkage [Wb]
$\lambda_m = L_mI_m$	Magnetising flux [Wb]

Table 4.3: Definitions of flux-linkage

4.3.1 Analogy to rotational systems

For a rotational system, the kinetic energy is given by $E = \frac{1}{2}J\omega^2$ [J], and for an inductor the stored magnetic energy is given by $E = \frac{1}{2}LI^2$ [J]. Imagine the rotational system as a spinning wheel. If you try to brake down its angular speed, you will have to overcome its resistive force(torque), $T = J\frac{d\omega}{dt}$. An inductor will behave in the same manner, where if you try to alter its current, it will fight back by inducing an voltage, $V = L\frac{dI}{dt}$. The concept of flux ($I \cdot L$) is thereby similar to angular momentum ($J \cdot \omega$).

4.4 Park transformation

For a three-signal system, the Park transformation can be defined by (4.4), i.e. $[\mathbf{x_{dq0}}] = [\mathbf{T_{dq0}}(\phi_\mathbf{d})] [\mathbf{x_{abc}}]$, [1][4]. Its based on a projection of the input signals onto two orthogonal axes: d and q. The input abc-signals correlates to their respective symmetrically 120 degrees displaced axes. The zero-sequence component (0) can be considered a kind of DC-component, which would be equal zero for a balanced sinusoidal three-phase signal. The angle, θ_d, is in the form of (4.4) defined as the leading angle of the d-axis compared to the a-axis. The q-axis further leads the d-axis by 90 degrees. Other definitions of θ_d and the d-q orientations might be used, which should be noted as it influences how the transformation-matrix is defined.

$$\begin{bmatrix} x_d \\ x_q \\ x_0 \end{bmatrix} = \frac{2}{3} \begin{bmatrix} \cos(\theta_d) & \cos\left(\theta_d - \frac{2\pi}{3}\right) & \cos\left(\theta_d + \frac{2\pi}{3}\right) \\ -\sin(\theta_d) & -\sin\left(\theta_d - \frac{2\pi}{3}\right) & -\sin\left(\theta_d + \frac{2\pi}{3}\right) \\ \frac{1}{2} & \frac{1}{2} & \frac{1}{2} \end{bmatrix} \begin{bmatrix} x_a \\ x_b \\ x_c \end{bmatrix} \tag{4.4}$$

Figure 4.4 shows a visual representation of the Park transformation. The a-axis (red), b-axis (blue) and c-axis (green) are shown as vectors pointing in their corresponding direction. Similarly, we have vectors of the d-axis and q-axis in gray. A snapshot of an applied three phase balanced sinusoidal signal is also shown. The sum of the three abc-signal vectors (whose magnitudes are shown by a_m, b_m and c_m) is multiplied by the factor $\frac{2}{3}$ and results in the orange vector abc. Its projection to the dq-axes are indicated by the orange vectors d_m and q_m.

The transformation is useful when handling three-phase systems as it reduces the three inputs to a 2 dimensional dq-reference frame (dq). Further more, the dq-reference can be made to rotate synchronously to the applied signals (by changing θ_d properly), resulting in stationary dq-components (given balanced operation). If the d-axis is aligned with the a-axis ($\theta_d = 0$), (4.4) becomes equal the Clarke-transform.
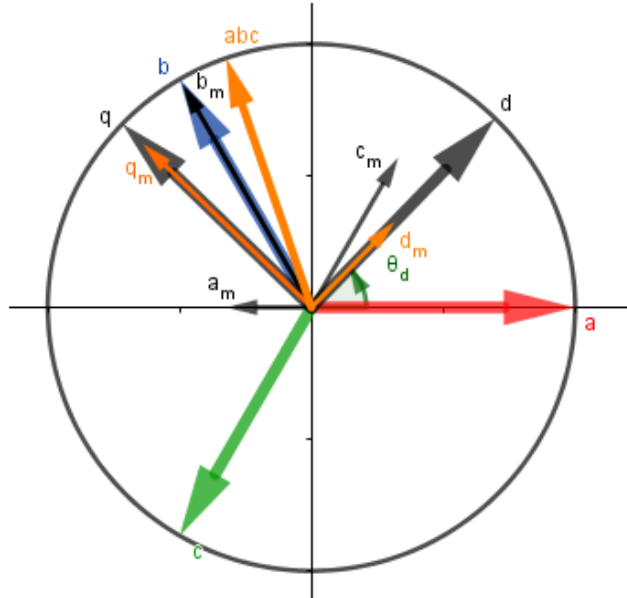
Figure 4.4: Space-vectors of dq0-transformation

4.5 Dynamic model

To study the the details of transient states, a dynamic model is useful, as derived in [1][1] and [2].

4.5.1 Assumptions and limitations

The assumptions and limitations are equal to that of the steady-state-model (Section 4.2.1), expect that it can provide a representation of the IM-behaviour in time-varying conditions with respect to voltage, current, speed and torque. The stator-windings are assumed star(Y)-connected. The model theoretically allows to apply unbalanced voltages, but does not include the considerations of how this voltage imbalance will affect the currents of the three phases. In other words, the stator-phases can be imagined as individual networks with no common connection (or a common ideal ground which can handle unbalanced currents). The short-circuited rotor is modelled in a similar manner. The dynamic model could therefore describe inaccurate behaviour for unbalanced operation. Nevertheless, it provides a useful representation and it's commonly applied with the control-systems used for physical applications.

4.5.2 Principal derivation

With similarities to that of the steady-state-model, the stator (and rotor) can be modelled as three symmetrically displaced coils, Figure 4.5. The position of the stator coils axes are static. For the short-circuited rotor, the three axes are mere fictitious. They are defined to stay symmetrically displaced, and rotate at the electric rotor speed (ω_r). The key to determine the interactions is the relative speed (slip-speed), ($\omega_{el} - \omega_r$). Note that this model applies the number of pole-pairs (n_{pp}) onto a two-pole representation by using the electric speeds. From the perspective of a rotor-bar, ($\omega_{sync} - \omega_m$) is the speed of which the stator-field swipes over them, and thus the cause for the induced voltage [40]. The induced rotor field (B_r) also has a speed of ($\omega_{sync} - \omega_m$) in order to stay in sync with (B_s).
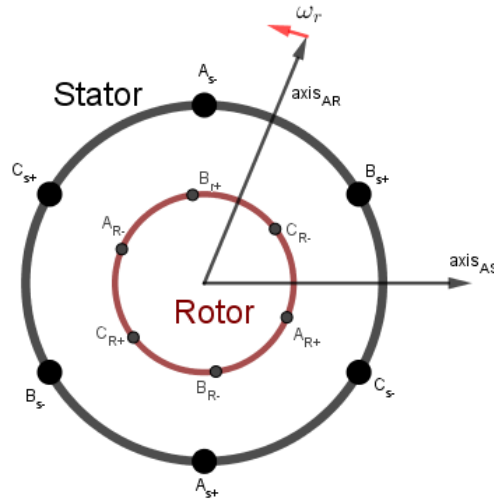
Figure 4.5: Stator and rotor frame for dynamic IM-model

The stator and rotor circuits are modelled per phase with a decomposition of their respective flux-linkages, (4.5) and (4.6). The flux-linkages can be expressed by properly designed matrices of inductance-parameters multiplied with the currents. This will include self-inductance, mutual-inductance and leakage-inductance, for each of the respective fluxes. Because the rotor-circuit reference "coils" constantly change position due to its rotation, the value of mutual inductance becomes position-dependent. This position dependence can however be removed by applying the Park-transformation to the variables. In [1][1], the transformation-matrix is defined as (4.7), where $\omega t = (\theta_d - \frac{\pi}{2})$. Thus, in this form, the q-axis is aligned with the a-axis, which still leads the d-axis by 90 degrees.

$$v_a^s = r_s i_a^s + \frac{d\lambda_a^s}{dt}$$

$$v_b^s = r_s i_b^s + \frac{d\lambda_b^s}{dt} \qquad (4.5)$$

$$v_c^s = r_s i_c^s + \frac{d\lambda_c^s}{dt}$$

$$v_a^r = 0 = r_r i_a^r + \frac{d\lambda_a^r}{dt}$$

$$v_b^r = 0 = r_r i_b^r + \frac{d\lambda_b^r}{dt} \qquad (4.6)$$

$$v_c^r = 0 = r_r i_c^r + \frac{d\lambda_c^r}{dt}$$

$$
\begin{bmatrix} x_d \\ x_q \\ x_0 \end{bmatrix} = \frac{2}{3}
\begin{bmatrix}
\sin(\omega t) & \sin\left(\omega t - \frac{2\pi}{3}\right) & \sin\left(\omega t + \frac{2\pi}{3}\right) \\
\cos(\omega t) & \cos\left(\omega t - \frac{2\pi}{3}\right) & \cos\left(\omega t + \frac{2\pi}{3}\right) \\
\frac{1}{2} & \frac{1}{2} & \frac{1}{2}
\end{bmatrix}
\begin{bmatrix} x_a \\ x_b \\ x_c \end{bmatrix}
\qquad (4.7)
$$

4.5.3   Dynamic model equations (dq0)

By applying the Park-transformation to the model, we end up with the resulting dq0-equations as given below. Upper subscripts, ^{s} and ^{r}, denotes if the parameter is related to the stator or rotor. Lower subscripts, $_d$, $_q$ and $_0$ denotes the component in the dq0-domain. All rotor-related quantities are referred to the stator side through a fictitious winding-ratio, and we can identify the same parameters of resistance and inductance as that of the steady-state-model. The flux linkages can be expressed in the matrix notation as given by (4.8). ω denotes the rotating speed of the dq0-reference frame, which is recommend to be set to zero (stationary) for transient studies.

The currents are defined for motor operation. A negative torque, (4.9), would therefore correspond to generator operation. The expressions for torque are determined by decomposing the instantaneous power for all six "circuits", and subtracting away the terms which accounts for ohmic losses ($r_x i^2$) and change of stored magnetic energy ($\frac{d}{dt}(\lambda_x)i = iL\frac{di}{dt}$).

To apply the model, one must transform the desired input variables (stator phase voltages) into the dq0-domain, (4.7), perform the required calculations, then transform the desired output (stator phase currents) back into the abc-domain.

Stator voltages, dq0

$$v_d^s = \frac{d}{dt}\left(\lambda_d^s\right) - \omega\lambda_q^s + r_s i_d^s$$

$$v_q^s = \frac{d}{dt}\left(\lambda_q^s\right) + \omega\lambda_d^s + r_s i_q^s$$

$$v_0^s = \frac{d}{dt}\left(\lambda_0^s\right) + r_s i_0^s$$

Rotor voltages, dq0

$$v_d^r = 0 = \frac{d}{dt}\left(\lambda_d^r\right) - (\omega - \omega_r)\lambda_q^r + r_r i_d^r$$

$$v_q^r = 0 = \frac{d}{dt}\left(\lambda_q^r\right) + (\omega - \omega_r)\lambda_d^r + r_r i_q^r$$

$$v_0^r = 0 = \frac{d}{dt}\left(\lambda_0^r\right) + r_r i_0^r$$

Flux linkages, dq0

$$\lambda_d^s = (L_{ls} + L_m)\, i_d^s + (L_m)\, i_d^r$$

$$\lambda_q^s = (L_{ls} + L_m)\, i_q^s + (L_m)\, i_q^r$$

$$\lambda_0^s = (L_{ls}) i_0^s$$

$$\lambda_d^r = (L_{lr} + L_m)\, i_d^r + (L_m)\, i_d^s$$

$$\lambda_q^r = (L_{lr} + L_m)\, i_q^r + (L_m)\, i_q^s$$

$$\lambda_0^r = (L_{lr}) i_0^r$$

$$
\begin{bmatrix} \lambda_d^s \\ \lambda_q^s \\ \lambda_0^s \\ \lambda_d^r \\ \lambda_q^r \\ \lambda_0^r \end{bmatrix} =
\begin{bmatrix}
L_{ls} + L_m & 0 & 0 & L_m & 0 & 0 \\
0 & L_{ls} + L_m & 0 & 0 & L_m & 0 \\
0 & 0 & L_{ls} & 0 & 0 & 0 \\
L_m & 0 & 0 & L_{lr} + L_m & 0 & 0 \\
0 & L_m & 0 & 0 & L_{lr} + L_m & 0 \\
0 & 0 & 0 & 0 & 0 & L_{lr}
\end{bmatrix}
\begin{bmatrix} i_d^s \\ i_q^s \\ i_0^s \\ i_d^r \\ i_q^r \\ i_0^r \end{bmatrix}
\qquad (4.8)
$$

$$
\begin{aligned}
T_{em} &= \frac{3}{2} n_{pp} \left(\lambda_d^s i_q^s - \lambda_q^s i_d^s\right) \qquad (4.9) \\
&= \frac{3}{2} n_{pp} L_m \left(i_d^r i_q^s - i_q^r i_d^s\right) \\
&= \frac{3}{2} n_{pp} \left(\lambda_q^r i_d^r - \lambda_d^r i_q^r\right)
\end{aligned}
$$

4.5.4 Simulink implementation
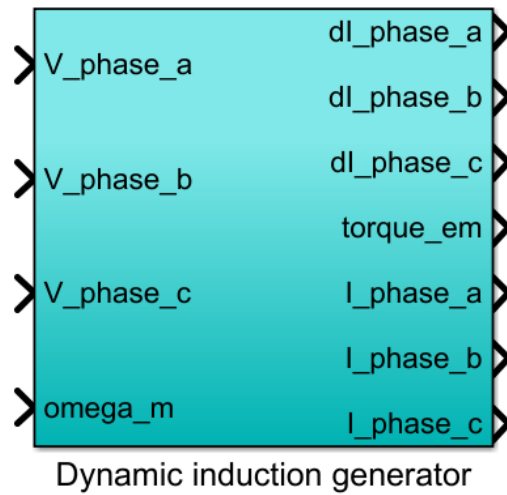
Figure 4.6: Dynamic induction machine model block

Based on the equations in Section 4.5.3, a custom block is made for the dynamic induction machine model, Figure 4.6. It's based on input of stator phase-voltages and ω_m to give the stator currents and shaft torque. The inner details are shown in Figure 4.7 on the next page. The yellow quantities represents required constant parameters (7 in total), namely the machines resistances and inductances, Table 4.2, number of pole pairs, and the speed of the dq0-reference frame (which will be set to $\omega=0$ in the simulations). Briefly explained, the input of stator voltages are transformed into a dq0-representation, which are used to compute the flux-linkages. The currents are found by matrix-calculations using the current_matrix variable, which is the inverse of the inductance matrix in (4.8). The calculated flux-linkages and currents are used as feed-backs.
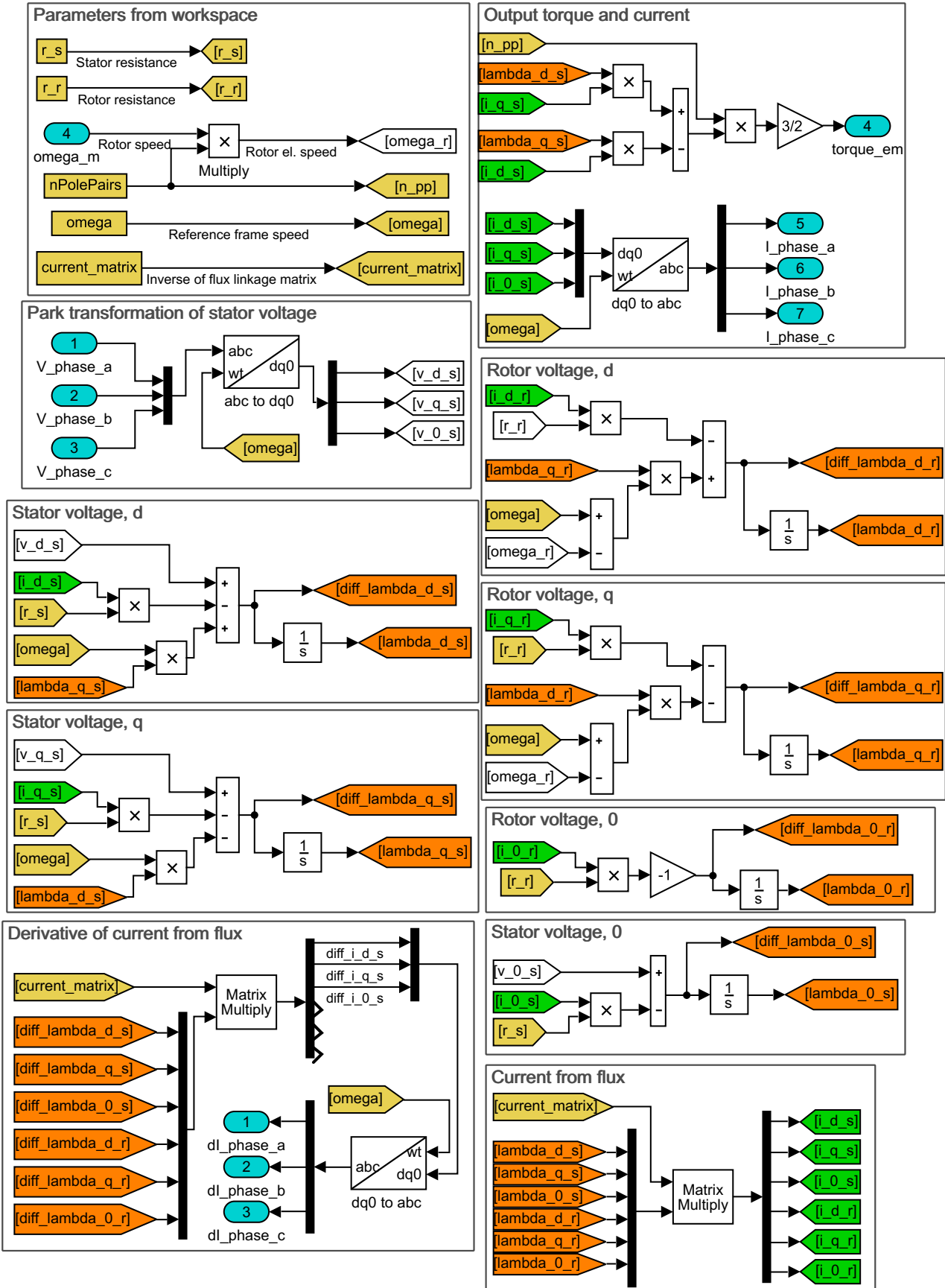
Figure 4.7: Inner structure of dynamic induction machine block

5 Two-level three-phase voltage source converter (2L-3ph VSC)

Transformation of voltage between AC and DC can be achieved by various topologies. The voltage source converters (VSCs) are well suited cadidates, as they can synthesise an arbitrary voltage from a DC-source. Examples are the two-level (2L), three-level (3L) and other modular multilevel converters (MMC). More complex designs can reduce the harmonic distortion of the output, but will require more intricate control-systems. Costs, losses and quality of output are some core considerations when choosing a suitable topology for an application.

This chapter covers the 2L-type, which has a simple structure and widespread usage. The circuit topology will be explained, followed by a simplified instantaneous model and its implementation into MATLAB-Simulink.

5.1 Circuit topology

The circuit topology of the 2L-3ph VSC is shown in Figure 5.1. It connects a DC-circuit to a three-phase circuit through three "legs". Each leg has an upper and lower switch+diode-pair. Each leg is connected to an individual AC-phase in their midpoint, and all the legs connect to the common DC-link (which must be positive as defined). The switches are assumed unidirectional, whose on/off states are determined by a gate signal. The diodes are paralleled with the switches in reverse direction. This enables voltage and currents in all four quadrants of the V-I plane.
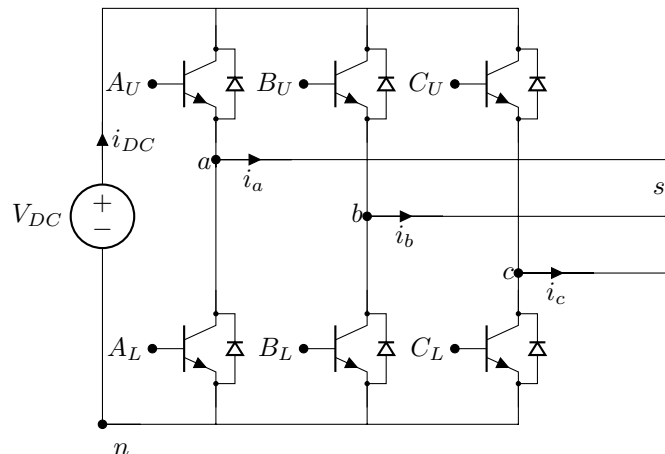
Figure 5.1: 2L 3ph VSC

5.2 Possible states of operation

Each leg has four possible states of operation in terms of controllability. Both switches can be off (X), either the upper or lower can be on (1/0), or both can be on (Y). Keeping both switches on (Y) does however result in a short-circuit of the DC-link, which is undesirable and should be avoided. We can represent the states of all phase legs by S=(a)(b)(c), illustrated by the following examples:

- S=XXX: All switches off

- S=111: All upper switches on

- S=100: Leg "a" with upper switch on, whilst leg "b" and "c" has the lower switches on.

- S=011: Leg "a" with lower switch on, whilst leg "b" and "c" has the upper switches on.

Operating with S=XXX will effectively transform the circuit into a diode-rectifier, which only permit power flowing to the DC-side. All instantaneous power flowing to the DC-side will correspond to a negative i_{DC}, which can only be achieved by phase-currents flowing through the diodes. Likewise, instantaneous power flowing to the AC-side corresponds to a positive i_{DC}, which must go through the switches. Note that S=111 and S=000 would correspond to "transforming" all the switches of the upper or lower parts into "one-way-paths", and in either configuration, the DC-current does not have a path to complete. A balanced three-phase AC-side current would in this state short-circuit within either the upper or lower switches and diodes [22][6].

Choosing to operate only one leg, i.e. S=1XX, S=X0X, etc., would inherit the same problem with no possible path for a positive DC-current. Operation of only two legs, i.e. S=10X, S=X00, etc., would conceptually correspond to a "Full-bridge" converter, which is not the intention of this design. The above considerations of switching leaves us with 8 suitable states of operation, where either the upper or lower switch of a leg should be turned on.

5.3   Instantaneous model

The modelling of the 2L-3ph VSC is based on [23], which provides a simplified representation useful for simulations.

5.3.1   Assumptions and limitations

- Instantaneous switching without losses. No transient states are included.
- Fixed forward voltage and resistive losses in the components (switch/diode) when conducting (i.e. linear operation)
- Balanced AC-side

5.3.2   State determination and phase-voltages

Using the midpoints of each phase, and the neutral point (n) as defined in Figure 5.1, we have the neutral voltage for each phase expressed by v_{an}, v_{bn} and v_{cn}. With instantaneous switching, where either the upper or lower switch of a leg is turned on at any instant, the neutral-voltage depends only on the switch-state [22][1]. Under the balanced assumption, the sum of phase voltages should be zero, $v_{as} + v_{bs} + v_{cs} = 0$. KCL should also hold true, $i_a + i_b + i_c = 0$, in addition that the net current of i_{DC} must be balanced with respect to the upper-legs connector and the lower-legs connector. With this, we can express the phases-voltages to the common AC-side point (s) by (5.1). Identify that $v_{an} + v_{bn} + v_{cn} = 3v_{sn}$, we can rearrange to express the phase-voltages as a function of the neutral voltages, (5.2) [22][5]. If we assume the ideal VSC (no resistance and voltage drops of switches and diodes), it evident that there are six possible outputs phase voltages: $\pm[0, \frac{1}{3}V_{DC}, \frac{2}{3}V_{DC}]$.

$$
\begin{aligned}
v_{an} &= v_{as} + v_{sn} \\
v_{bn} &= v_{bs} + v_{sn} \\
v_{bn} &= v_{cs} + v_{sn}
\end{aligned}
\tag{5.1}
$$

With inclusion of voltage drop parameters for each component (switch/diode), the model results in four possible states for each leg. The neutral voltages are determined depending upon the magnitude and direction of the phase current, the DC-link voltage and the switch-state. Table 5.1 summarises this for phase-leg (a). Subscripts U and L indicates the upper and lower switch/diode pair, where S and D indicates switch and diode. A_U and A_L indicates if the upper or lower switch of phase leg (a) is turned on. R_S and R_D are the conducting resistance of the switch and diode. V_{fS} and V_{fD} are the corresponding forward-voltage drops. The relations in Table 5.1 are similar for the other phases.

$$v_{as} = \frac{2}{3}v_{an} - \frac{1}{3}(v_{bn} + v_{cn})$$
$$v_{bs} = \frac{2}{3}v_{bn} - \frac{1}{3}(v_{an} + v_{cn}) \quad (5.2)$$
$$v_{cs} = \frac{2}{3}v_{cn} - \frac{1}{3}(v_{an} + v_{bn})$$

State	Current path	Neutral voltage, v_{an}
A_U, i_a[+]	S_U	$V_{DC} - V_{fS} - R_S|i_{as}|$
A_U, i_a[-]	D_U	$V_{DC} + V_{fD} + R_D|i_{as}|$
A_L, i_a[+]	D_L	$-V_{fD} - R_D|i_{as}|$
A_L, i_a[-]	S_L	$V_{fS} + R_S|i_{as}|$

Table 5.1: Neutral voltage states for phase-leg (a)

5.3.3 Simulink implementation
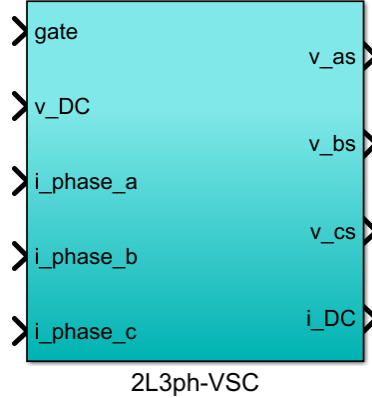
Figure 5.2: Two level three phase VSC model block

The logic of the instantaneous VSC-model is built into a custom block, Figure 5.2. It takes input of DC-link voltage, phase-currents and the 6 switch control-signals (gate), to give out the corresponding phase-voltages and current drawn from the DC-link. The first layer (Figure 5.3) mostly consist of rerouting signals and computing the phase-voltages. It contains three identical leg-blocks (Figure 5.4) where all possible neutral-voltages are calculated, which are fed into a MATLAB-function block that determines the correct output according to Table 5.1. It's important to distinguish between whether the DC-current of a leg is drawn from the upper or lower part, which the MATLAB-function provides as two separate outputs. The sum of DC-link currents from all upper-legs are equal the sum of all lower-legs when the phase-currents are balanced. The sum of the upper-legs are used as output (Figure 5.3) where a positive value corresponds to discharging the DC-link. The yellow quantities in Figure 5.4 represents required constant parameters (4 in total), namely the fixed resistances and forward-voltages of the switches and diodes.

21
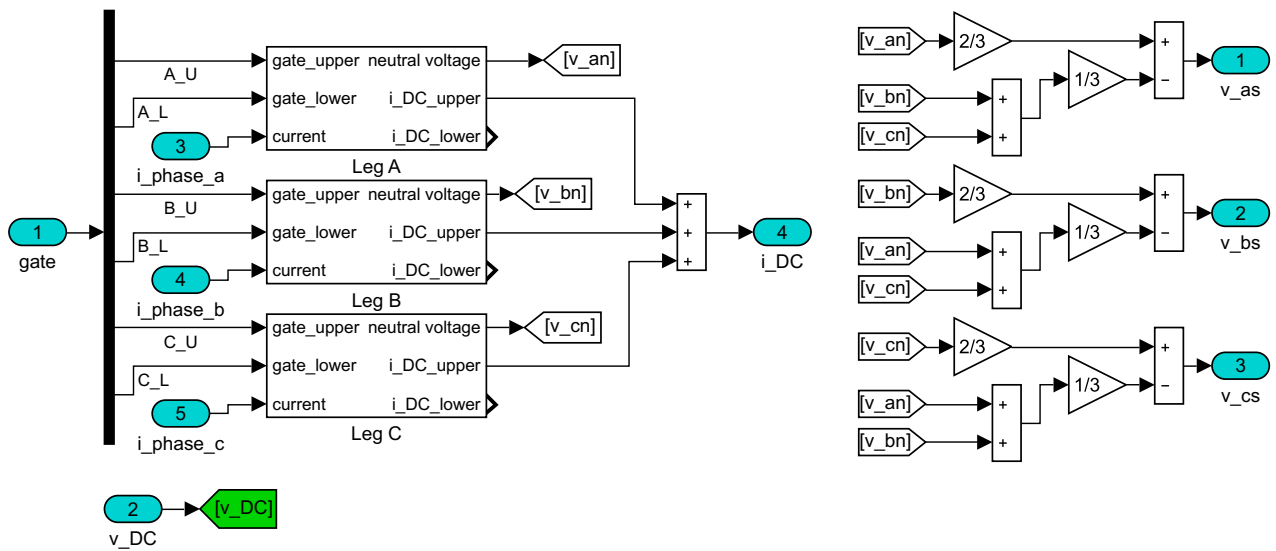
Figure 5.3: Inner structure of VSC block
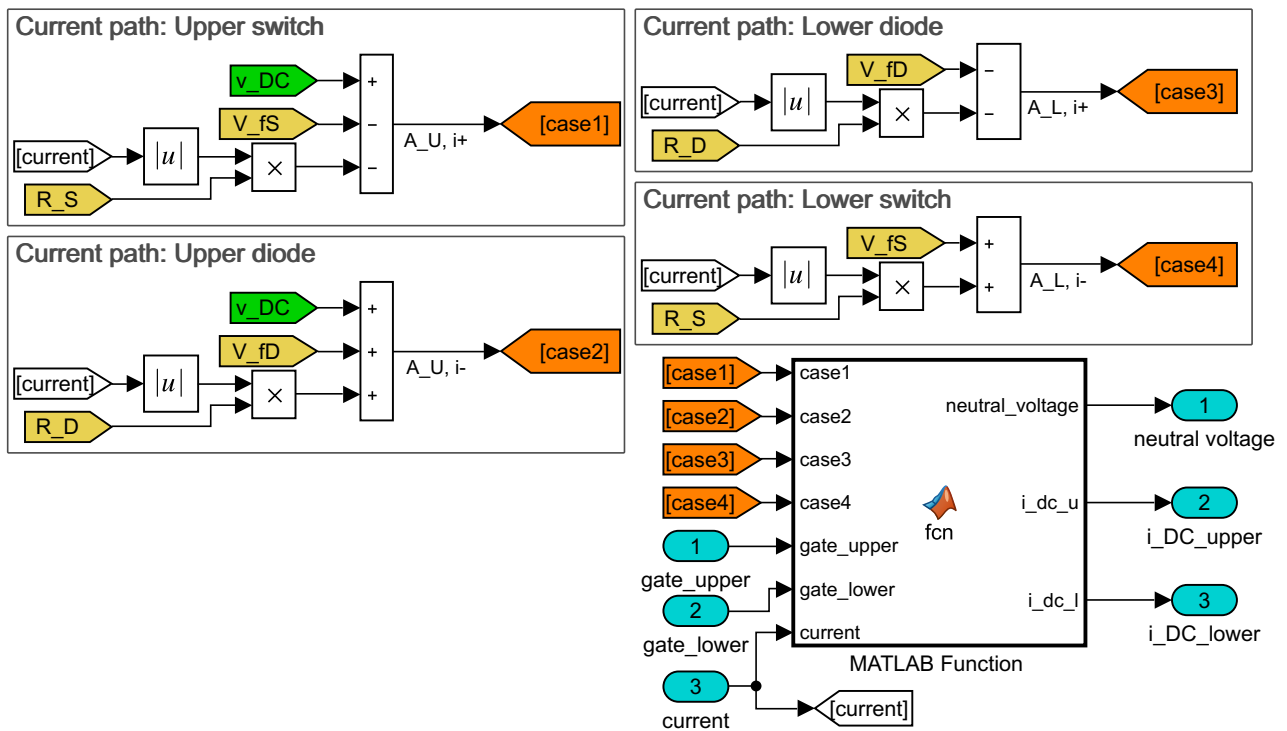
Figure 5.4: Inner structure of VSC-leg block

MATLAB-Function: VSC-leg

```
1  function [neutral_voltage, i_dc_u, i_dc_l]= fcn(case1, case2, case3, case4, gate_upper, gate_lower,
        current)
2
3  neutral_voltage=0;
4  i_dc_u=0;
5  i_dc_l=0;
6
7  if(gate_upper <=0 && gate_lower<=0) %both off
8      if(current>0)
9          neutral_voltage=case3;
10         i_dc_l=current;
11     else
```

```matlab
12          neutral_voltage=case2;
13          i_dc_u=current;
14      end
15  end
16
17  if(gate_upper>0) %upper switch on
18      if(current>0)
19          neutral_voltage=case1;
20          i_dc_u=current;
21      else
22          neutral_voltage=case2;
23          i_dc_u=current;
24      end
25  end
26
27  if(gate_lower>0) %lower switch on
28      if(current>0)
29          neutral_voltage=case3;
30          i_dc_l=current;
31      else
32          neutral_voltage=case4;
33          i_dc_l=current;
34      end
35  end
```

5.4   Practical aspects

For practical converters, the switching functionality is realised by use of transistors. Some examples are BJTs, MOSFETs, GTOs and IGBTs [22][4]. Such real components have non-ideal behaviour, including switching-delays and switching-losses. One must therefore account for the transistors rated limits of voltage, current and the temperature dependence. Heat-sinks/cooling is often required to transfer away the developed heat. Gate-driver circuits are also required to properly change the operational state of the transistors. Blanking time should also be added to the gate-signals to prevent short-circuiting the DC-link [22][2].

6 Gate-signal generation for the 2L-3ph VSC

The 2L-3ph VSC has a total of 6 switches. The on and off-state can be represented simply as either 1 or 0, for each of the corresponding switches: $[A_U, A_L, B_U, B_L, C_U, C_L]$. These gate-signals are the final output of the control-system, which are given to the gate-drivers of the VSC.

This chapter will introduce methods of generating such gate-signals in order to replicate a desired reference in the electrical system. This includes methods such as S-PWM, SV-PWM and hysteresis-based switching. MATLAB-Simulink implementation will also be given for selected methods. The following descriptions assumes ideal switches, and does not consider non-ideal conditions such as the requirement of blanking-time.

6.1 S-PWM

6.1.1 Principle of operation

The sinusoidal pulse-width-modulation is a commonly encountered method, and its favoured for its simple implementation. For a three-phase system, the desired output voltages are represented as three sinusoidal reference-waves. A triangle carrier-wave is then compared with the reference waves, Figure 6.1. When a reference-wave is larger than the carrier wave, the upper switch of the corresponding leg is turned on, and otherwise, the lower switch of that leg is turned on. For periodic references, the frequency of the carrier wave can be related to the reference wave, giving the ratio of frequency modulation, (6.1). The peak values can be related by the amplitude modulation, (6.2). From a control perspective, m_f and m_a can be varied to adjust the output of the VSC.
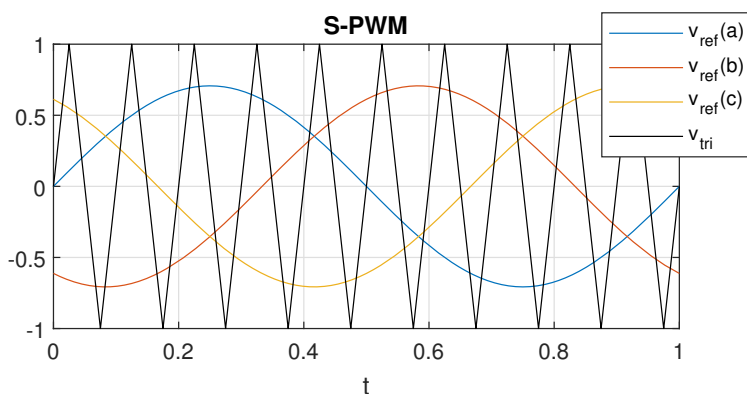
$$m_f = \frac{f_{tri}}{f_{ref}} \qquad (6.1)$$

$$m_a = \frac{\hat{v}_{ref}}{\hat{v}_{tri}} \qquad (6.2)$$

Figure 6.1: S-PWM reference and carrier-waves. m_f=10 and $m_a = \frac{1}{\sqrt{2}}$

6.1.2 Duty cycle

With $m_f \gg 1$, we identify that the S-PWM in principle determines a duty-cycle for the period of the carrier wave. With a carrier wave of peak-value 1, $v_{ref} = 1$ corresponds to 100% duty-cycle, $v_{ref} = 0$ corresponds to a 50% duty-cycle, and $v_{ref} = -1$ corresponds to a 0% duty-cycle.

The carrier-wave does not necessarily need to be a triangle-wave. A saw-tooth could fulfil the same functionality. The duty-cycle could also be determined directly from the reference signal by using (6.3). In this form, we assume that $v_{ref}(x)$ does not exceed the peaks of ± 1.

$$D_x = \frac{v_{ref}(x) + 1}{2} \qquad (6.3)$$

In a more general terms, we can say that larger values of frequency modulation (m_f) increases the switching-frequency, and thus how often the duty-cycles are updated. For periodic references, variation of amplitude modulation determines how far the duty-cycle can vary from 50%. Recall from Section 5.3.2 that for the ideal

VSC, turning on the upper switch of a leg on corresponds to applying a neutral voltage equal V_{DC}. Figure 6.2 and Figure 6.3 shows the corresponding phase-voltages (obtained by (5.2)) when applying gate-signals from S-PWM with three phase balanced sinusoidal references of $f_{ref} = 1$ Hz and $V_{DC} = 1$. With the PWM-switching-patterns, we are able to synthesise the references with the discrete steps of voltage. Lowering m_a gradually reduces the duration of these steps, and with $m_a = 0$, the phase-voltages would also be equal zero.
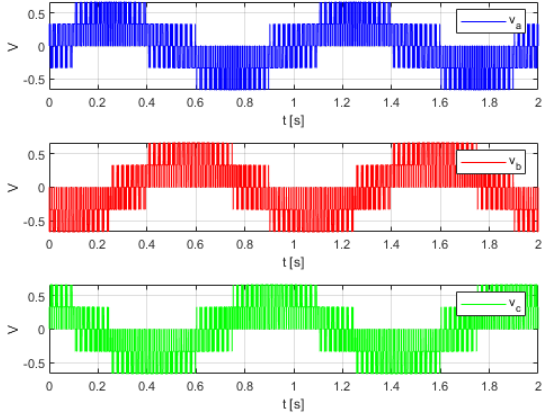
Figure 6.2: Phase-voltage: m_f=100 and $m_a = 1$
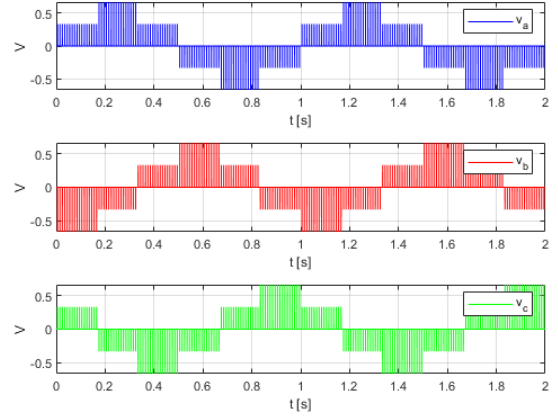
Figure 6.3: Phase-voltage: m_f=100 and $m_a = 0.01$

6.1.3 Modulation and sampling

Operating in overmodulation implies that $m_a > 1$. This could be beneficial for increasing the magnitude of the desired fundamental component of the output voltage. The drawback is introduction of harmonics at lower frequencies, approximating to the distribution of a square wave for sufficiently high m_a, [22][3]. A synchronous PWM implies that m_f is an integer, such that the periodic nature of the carrier and references are matched for every cycle. This can be beneficial for avoiding sub-harmonics [22][2]. For values of $m_f < 21$, it's suggested that m_f should be chosen as an odd integer to cancel even harmonics, and as a multiple of 3 to cancel dominant harmonics of the line voltage [22][1].

Generally, a large m_f is preferred in order to better synthesise the desired reference voltage. When applying the S-PWM to discrete controllers/simulations, the sample-time (ΔT_{samp}) must be considered in relation to the period of the carrier-wave/switching frequency, as this determines the resolution of applicable duty-cycles.

6.1.4 Simulink implementation
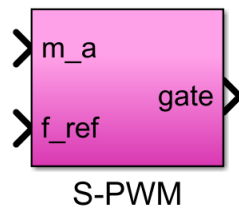
Figure 6.4: S-PWM gate signal generation block

The S-PWM-method is implemented into a custom block, Figure 6.4. It takes input of amplitude and frequency modulation to give out the 6 corresponding gate-signals. The inner details are shown in Figure 6.5. MATLAB-function blocks are used to create the reference signals and detect the intersections of the triangle-carrier wave. The only fixed parameter is the switching frequency (f_{sw}), defined as the frequency of the triangle-wave block. m_f will thereby vary depending upon the input of f_{ref}.

25

Dynamically changing reference-waves are expected from the control-system. To achieve a level of continuity in the wave-forms, the phase-angles are considered. For the periodic reference functions, the phase angle (θ) is calculated and fed back as input for the next time-step, (6.4). This allows for a smooth transition (assuming short time-steps and references not changing to violently). The memory blocks in Figure 6.5 are updated for every step and implements this functionality.

$$\theta[k+1] = \theta[k] + (2\pi f_{ref}[k+1]) \cdot \Delta T_{samp} \tag{6.4}$$
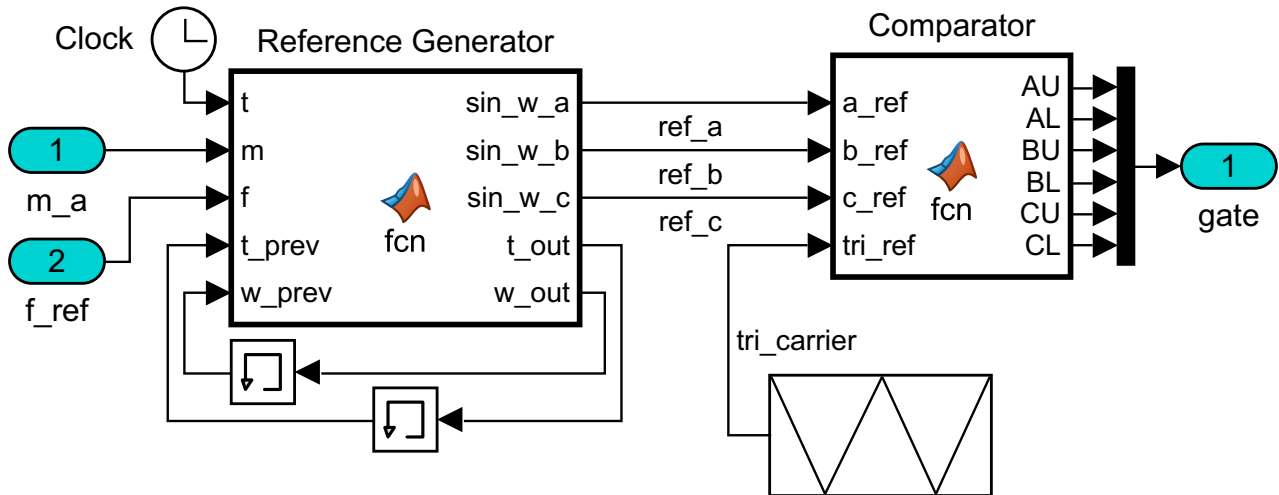
Figure 6.5: Inner structure of S-PWM block

MATLAB-Function: Reference Generator (purely sinusoidal reference waves) ⎯⎯⎯⎯⎯⎯⎯

```
function [sin_w_a, sin_w_b, sin_w_c, t_out, w_out]= fcn(t, m, f, t_prev, w_prev)

t_out=t;

w_out=w_prev+2*pi*f*(t-t_prev);

sin_w_a=sin(w_out)*m;
sin_w_b=sin(w_out-2/3*pi)*m;
sin_w_c=sin(w_out+2/3*pi)*m;
```

MATLAB-Function: Comparator ⎯⎯⎯⎯⎯⎯⎯⎯⎯⎯⎯⎯⎯⎯⎯⎯⎯⎯⎯⎯⎯

```
function [AU,AL,BU,BL,CU,CL] = fcn(a_ref, b_ref, c_ref, tri_ref)

if(a_ref>=tri_ref)
    AU=1;
    AL=0;
else
    AU=0;
    AL=1;
end

if(b_ref>=tri_ref)
    BU=1;
    BL=0;
else
    BU=0;
    BL=1;
end

if(c_ref>=tri_ref)
```

```
20      CU=1;
21      CL=0;
22  else
23      CU=0;
24      CL=1;
25  end
```

6.2 SV-PWM

The space vector pulse-width-modulation is a standard method for switched converters, and it has been a topic of research for some time [24].

6.2.1 Voltage vectors

Consider the ideal 2L-3ph VSC with no current flowing through it. As discussed in Section 5.2, we have 8 feasible switching configurations (2 of which provide zero voltage output). If we apply the Park-transformation to the phase-voltages of these states, with a static reference frame (Clarke-transform) and $V_{DC} = 1$, we obtain the results in Figure 6.6. The subscripts of the voltages indicates the switch state of each leg in the order a-b-c, $V_{abc}=V_{S_A S_B S_C}$, where $S_x = 1 =$[upper switch on, lower switch off] and $S_x = 0 =$[upper switch off, lower switch on]. The states V_{000} and V_{111} results in zero voltage. The six state vectors are of constant magnitude $\frac{2}{3}V_{DC}$, phase shifted by 60 degrees. This create 6 sectors (S1, S2, ...), each bounded by two boundary voltage vectors, V_1 and V_2. All angles (θ, ϕ) are defined as leading from the d-axis. In the static dq-domain, a balanced three phase sinusoidal reference signal (V_{ref}) would be represented as a vector of constant magnitude rotating at the reference frequency f_{ref}.

6.2.2 Imitation by time-division

The idea behind SV-PWM is utilize the possible converter output states to switch in such a way that one can "imitate" the reference vector. By defining a switching frequency of $f_{sw} = \frac{1}{T_s}$, a sample of V_{ref} can be imitated from a voltage·seconds integral using (6.5) and (6.6).
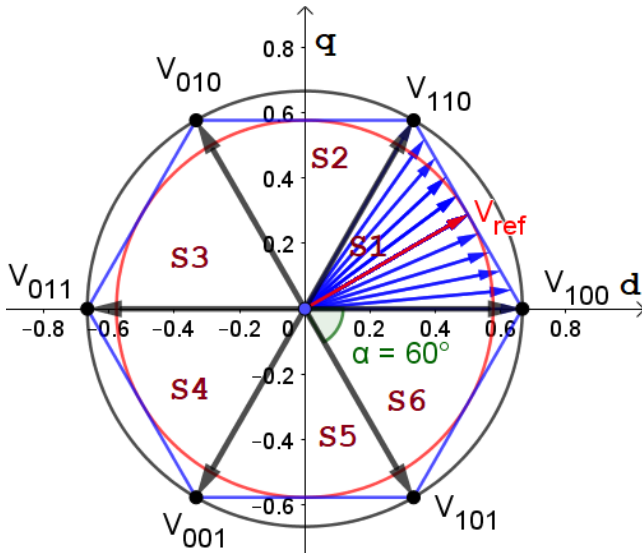
- T_1: Time on for boundary vector 1, $V_1 \angle \phi_1$.
- T_2: Time on for boundary vector 2, $V_2 \angle \phi_2$.
- T_0: Time on for zero vector(s), $V_0 = 0$

$$T_s = T_1 + T_2 + T_0 \tag{6.5}$$

$$V_{ref}T_s = V_1 T_1 + V_2 T_2 + T_0 V_0 \tag{6.6}$$

$$\begin{bmatrix} |V_{ref}| \cos(\theta) \\ |V_{ref}| \sin(\theta) \end{bmatrix} = \frac{2\sqrt{3}}{3} \begin{bmatrix} \cos(\phi_1) & \cos(\phi_2) \\ \sin(\phi_1) & \sin(\phi_2) \end{bmatrix} \begin{bmatrix} T_1 \\ T_2 \end{bmatrix} \tag{6.7}$$

Figure 6.6: VSC dq-voltage vectors and sectors

The maximum voltage reference possible to obtain from V_1 and V_2, with $T_0 = 0$, is indicated by the straight blue lines connecting the voltage vectors, Figure 6.6. The upper limit of $m_a \leq 1$ for "linear operation" can then be defined by the red circle. Normalized such that $m_a[max] = 1$ result in lengths of the converter voltage vectors to be $\frac{2}{3}\frac{3}{\sqrt{3}} = \frac{2\sqrt{3}}{3}$. We can define the phase angle of a sampled V_{ref} as θ. By normalizing such that

$T_s = 1$, the time-division can then be found by the matrix relation (6.7). Similar to the S-PWM method, the output voltage of the VSC can be adjusted by varying m_a and f_{ref}.

6.2.3 Creating gate-signals

Translating time division to gate signals can be done it several ways [24]. To reduce switching losses in a practical application, the transitions from one state to another should imply changed state for one leg only, $\Delta n_u = \pm 1$, [24, 25]. It's evident from Figure 6.6 that each sector has two boundary vectors where one has two upper-switches turned on, $n_u = 2$, and the other has one upper-switch turned on, $n_u = 1$. With a counter-clockwise indexation of V_1 and V_2 for each sector, it can be shown that for odd numbered sectors, $V_1 \rightarrow n_u = 1$, and even numbered sectors, $V_1 \rightarrow n_u = 2$. Each sample is chosen to start and end at a different zero-state vector. T_0 is shared equally, $T_{V_{000}} = T_{V_{111}} = \frac{T_0}{2}$, [24]. By utilizing the property of odd and even numbered sectors and tracking which zero-state that ended the previous sample, one can determine, for each sample, the proper sequence of voltage vectors to achieve $\Delta n_u = \pm 1$.

Similar to the S-PWM method, the controller/simulation sample-time (ΔT_{samp}) must be considered in relations to the switching-period (T_s), as this determines the achievable resolution used for the time-division.

6.3 Sinusoidal references with third-harmonic components

The reference waves shown above for the S-PWM and SV-PWM method are assumed purely sinusoidal. A method for increased utilization of the DC-voltage is to use a sinusoidal reference with an added third harmonic component [26, 27]. The third harmonic components are cancelled in the output line voltage. According to [26], the normalized reference for a phase can be designed as given by (6.8).

$$\frac{v_{ref}(t)}{m_a} = \frac{2}{\sqrt{3}} \sin\left(2\pi f_{ref} \cdot t + \theta\right) + \frac{\sqrt{3}}{9} \sin\left(3(2\pi f_{ref} \cdot t + \theta)\right) \tag{6.8}$$
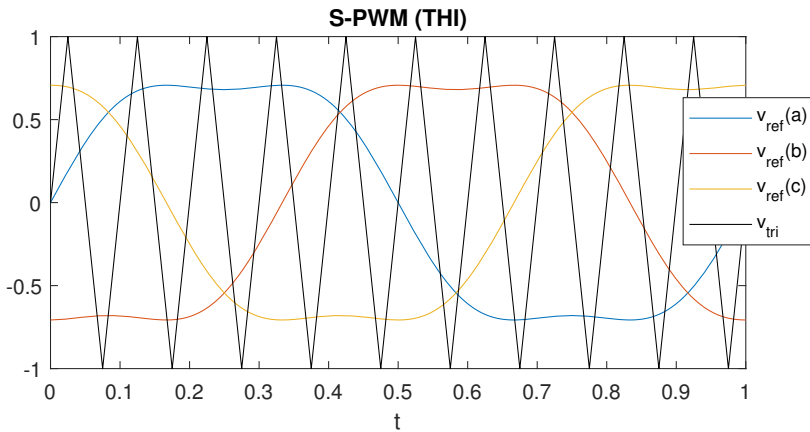
Figure 6.7: S-PWM (THI) with reference and carrier-waves. $m_f{=}10$ and $m_a = \frac{1}{\sqrt{2}}$

6.4 S-PWM vs. SV-PWM

There are several studies available, conducting a comparison of the S-PWM and SV-PWM method [28, 29, 30, 31, 32, 33, 34]. The general differences can be summarised as follows:

For a given switching frequency, $f_{sw} = f_{tri}$ (S-PWM) and $f_{sw} = \frac{1}{T_s}$ (SV-PWM), SV-PWM performs best in terms of DC-voltage utilization. It also gives lower harmonic distortion of the output (measured by THD with a fundamental of f_{ref}). The more strategic method for changing the switch-states in SV-PWM also results in lower switching losses. However, this results in the harmonic content from SV-PWM to be at lower frequencies than that of S-PWM, which is of influence when filtering is desired at the output. Using references with a

third harmonic component increases the DC-voltage utilization of both methods. Operating at lower amplitude modulation, $m_a < 1$, increases the output harmonic distortion for both methods in a non-linear manner when m_a approximates zero.

6.5   RMS-voltage from S-PWM (RMS/DC)

Recall from Section 6.1.2 that the output phase-voltages are synthesised by means of discrete voltage steps when applying the S-PWM-method to the 2L-3ph VSC. We can estimate the RMS-value of the phase voltage (v_ϕ) by means of a discrete integral (6.9). Assuming a constant DC-link voltage, synchronous PWM and $f_{tri} \gg f_{ref}$, the RMS-value of the VSC output voltage per phase is essentially dependent upon the amplitude modulation.

$$v_\phi\,[\text{rms}] = \sqrt{\frac{\Delta t \, \sum_{i=1}^{i=n_{samp}} v_\phi(i)^2}{\Delta t \cdot n_{samp}}} \tag{6.9}$$

Figure 6.8 shows how varying the amplitude modulation (m_a) affects the RMS-values of the output phase-voltage. The phase-voltage shown is normalised to DC-link voltage, i.e. $\frac{v_\phi[\text{rms}]}{V_{DC}}$. The tests are done with the S-PWM-method with both purely sinusoidal and third harmonic components (THI) added to the references. The frequency modulation is set at $m_f = 100$, with $n_{samp} = 10^5$ samples per reference wave period, corresponding to 1000 samples per carrier wave-period.
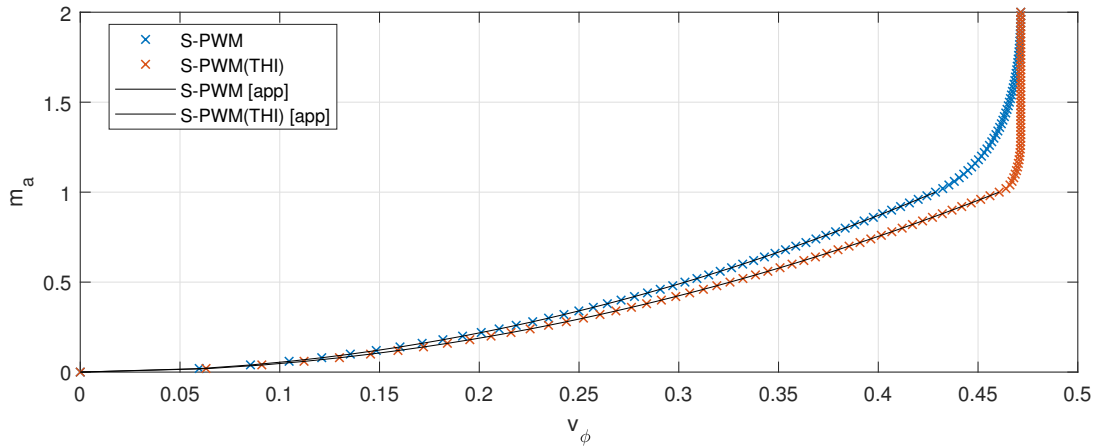
Figure 6.8: m_a vs. v_ϕ for 2L-3ph VSC with S-PWM

The results illustrates the enhanced DC-voltage utilization by adding a third-harmonic component to the reference waves. For sufficiently large m_a, the RMS-value would approximate $\frac{1}{2}V_{DC}$, which corresponds to applying square-wave gate-signals. Limited to linear operation ($m_a \leq 1$) we can express m_a as a function of the normalised phase voltage by an approximated second order function, (6.10), (shown by black lines [app] in Figure 6.8).

$$m_a = \mu_{ma} \cdot v_\phi^2, \quad v_\phi[0, \bar{v}_m] \tag{6.10}$$

$$\begin{aligned} S\text{-}PWM\text{:} \quad & \mu_{ma} = 5.442, \bar{v}_m = 0.4287 \\ S\text{-}PWM\ (THI)\text{:} \quad & \mu_{ma} = 4.714, \bar{v}_m = 0.4606 \end{aligned}$$

6.6   Hysteresis controller

The hysteresis control, also known as bang-bang control, is a method that can provide two output-states: on and off. It consist of an upper (H_U) and lower (H_L) threshold, which are compared to an input H_{in}. The band-gap

is the difference between the upper and lower threshold, $H_B = H_U - H_L$. The upper and lower thresholds are associated with a corresponding output-state (on/off). The controller does not alter its output-state if the input-signal stays within the band. If the input exceeds the band (i.e. $H_{in} > H_U$ or $H_{in} < H_L$), a change of output-state can occur.

Figure 6.9 illustrate the concept. $H_U = 0.5$, $H_L = -0.5$, and H_{in} is a 1 Hz triangle wave. The output is defined to turn off (0) at the upper threshold, and on (1) at the lower threshold.
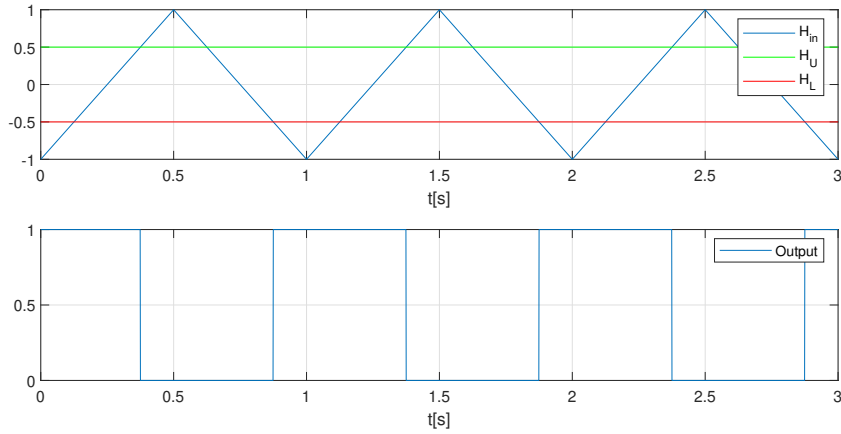
Figure 6.9: Hysteresis controller

Common applications for the hysteresis-controller are thermostats, where the upper and lower threshold are centered around a reference temperature. Whenever the measured temperature drops below the minimum threshold (H_L), the heater is turned on, and kept on until the temperature exceeds the maximum threshold (H_U), where it's turned off.

6.6.1 Current controller

The binary output makes the hysteresis-controller suitable to generate gate-signals for the 2L-3ph VSC. A common application is to control the phase-currents of the AC-side output. Greatly simplified, turning the upper-switch of a phase-leg on applies a positive neutral voltage, which according to (5.2) increases the phase-voltage. This in turn will contribute to an increase of current for the respective phase. The measured phase-currents (i_{abc}) can be subtracted with the references of currents (i^*_{abc}), and the errors for each phase (H_{in}) are fed to a corresponding hysteresis-controller with a band-gap of maximum allowed error (H_B) (centered around 0). Sample-and-hold circuits can be applied between the measurements and hysteresis-controller to impose an upper switching frequency (f_{sw}).

6.6.2 Simulink implementation of current controller
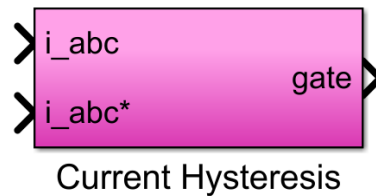
Figure 6.10: Current hysteresis controller block

The hysteresis-controller is built into a custom block, Figure 6.10. It takes input of measured and reference phase-current to provide the 6 gate-signals. The inner details are shown in Figure 6.11. Two constant parameters

are required. The first is the switching frequency (f_{sw}), defined by the period of pulse-generator that triggers the sample-and-hold blocks. The second is the band-gap (H_B) of the three relay-blocks, defining the upper threshold as $\frac{H_B}{2}$ and lower threshold as $-\frac{H_B}{2}$. The hysteresis-controller is defined to turn off (0) at the upper threshold (turns off the upper switch when the current becomes too large), and turn on (1) at the lower threshold (turns on the upper switch when the current becomes too low).
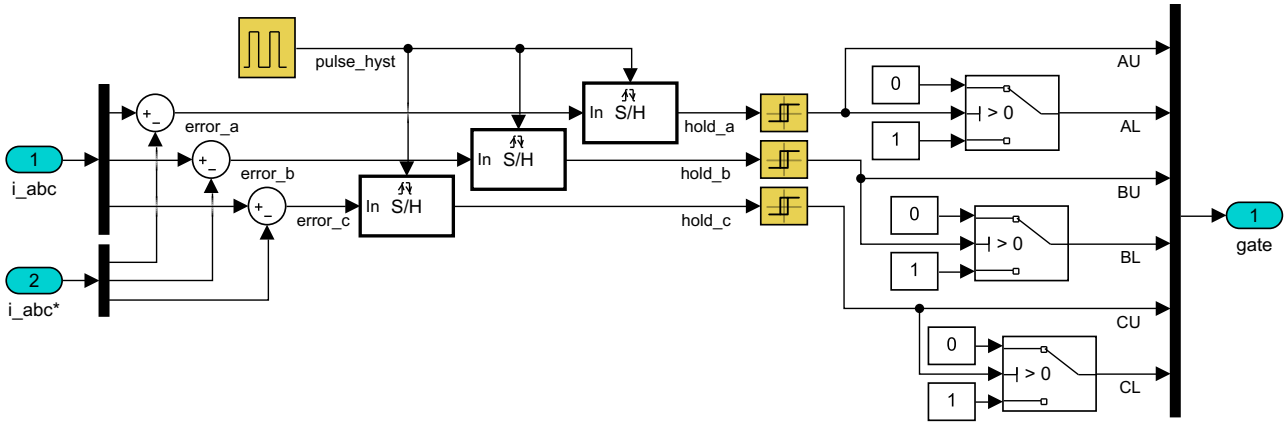
Figure 6.11: Inner structure of hysteresis block

7 LCL-filter

A desired characteristic of the load-grid is voltage of sufficient quality, i.e. a "smooth" sinusoidal shape. The discrete changes of output phase voltage (AC-side) from the 2L-3ph VSC due to high-frequent switching produces voltage waveforms with a variety of harmonic content. To mitigate this, filters are useful. There are several configurations that can be used, which may be divided into active and passive filters. Passive filters are the simplest form, as they have no additional power supply or control system. In general, they are composed of reactive elements (inductors and capacitors), which impedance differs depending upon the the frequency of the applied voltage. Some examples are L, LC and LCL filters.

In relations to the VSC, the voltage drops in the filter and required dimensions of filter components increases for lower switching frequencies. There is thus a trade-off between high switching frequency, DC-voltage utilization and switching losses, [22][1]. Compared to L and LC-filters, the LCL-filter requires lower component values (thus cheaper), and have better attenuation capabilities [35]. This chapter will describe the topology, MATLAB-Simulink implementation and a design-procedure for the LCL-filter.

7.1 Circuit topology

The LCL-filter with damping resistor has the per phase topology as shown in Figure 7.1. The filter can be modelled by the three relations of voltage and current, (7.1), (7.2) and (7.3), in Laplace notation. Similar to the load-model (Section 3.1.1), the components are assumed "linear". The per phase circuits are assumed star(Y)-connected, but modelled as individual networks.
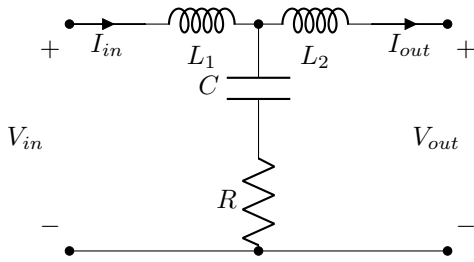
Figure 7.1: Per phase circuit of series damped LCL-filter

$$(I_{in} - I_{out})\left(\frac{1}{Cs} + R\right) = V_{RC} \qquad (7.1)$$

$$\frac{V_{in} - V_{RC}}{sL_1} = I_{in} \qquad (7.2)$$

$$\frac{V_{RC} - V_{out}}{sL_2} = I_{out} \qquad (7.3)$$

7.2 Simulink Implementation

7.2.1 Input/output

The LCL-filter is to be placed in between the VSC and load. Recall from Section 5.3.3 that the VSC-model requires input of phase-currents, namely I_{in}. Recall from Section 3.2 that the load model requires input of phase-voltages, namely V_{out}.

Looking at the model equations, (7.1), (7.2) and (7.3), this is achievable if the LCL-filter has inputs of V_{in} (provided by the VSC-model), I_{out} (provided by the load-model) and $\frac{dI_{out}}{dt}$. Derivative-blocks are thereby required in the simulation. Generally, using derivative-blocks can cause some simulation challenges if the rate of change is large and time-steps (ΔT_{samp}) are small. A workaround could be to model the loads with input of current and output of voltage. This approach has been tested, and comparisons have shown that the two methods provide seemingly identical responses. The approach with using derivative-blocks is thereby chosen as it makes the implementation of variable loads much simpler.

7.2.2 Simulink-blocks
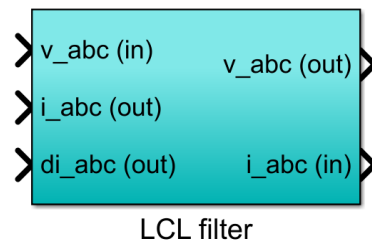
Figure 7.2: LCL-filter model block

The LCL-filter model is built into a custom block, Figure 7.2. The inner structure (Figure 7.3) mostly consist of rerouting the signals to their corresponding identical phase-blocks, Figure 7.4. Yellow quantities (4 in total) represent the required constant parameters, namely the component values of the two inductors, the capacitor and the resistor.
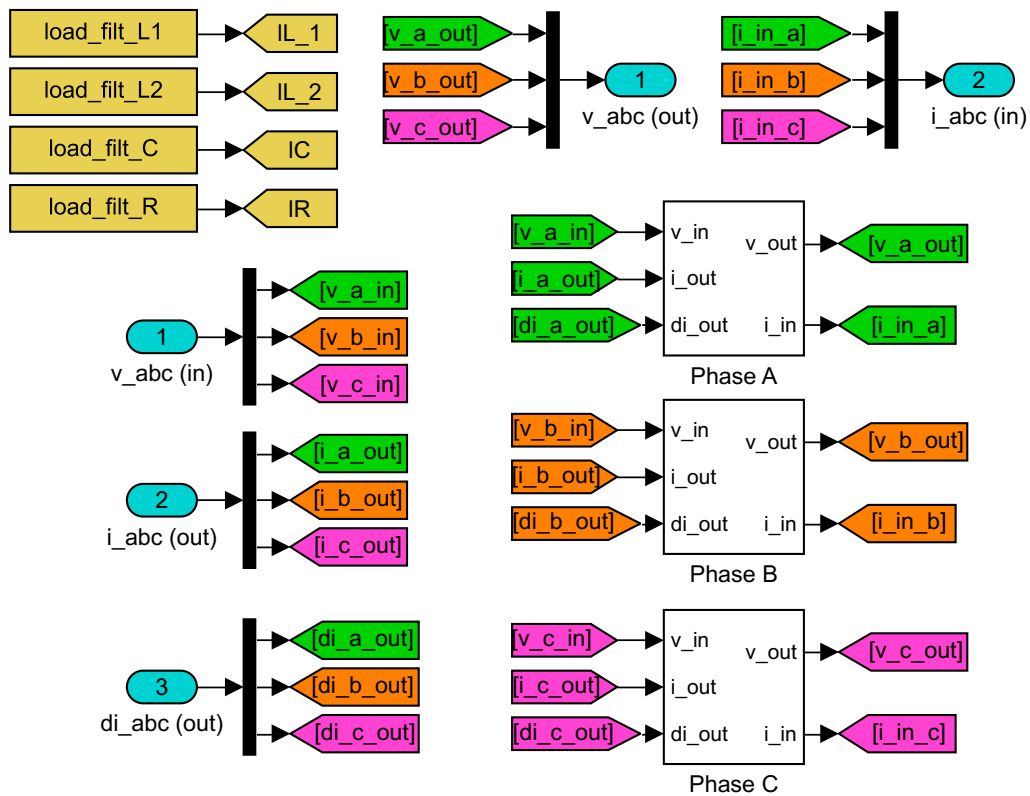
Figure 7.3: Inner structure of LCL-filter block
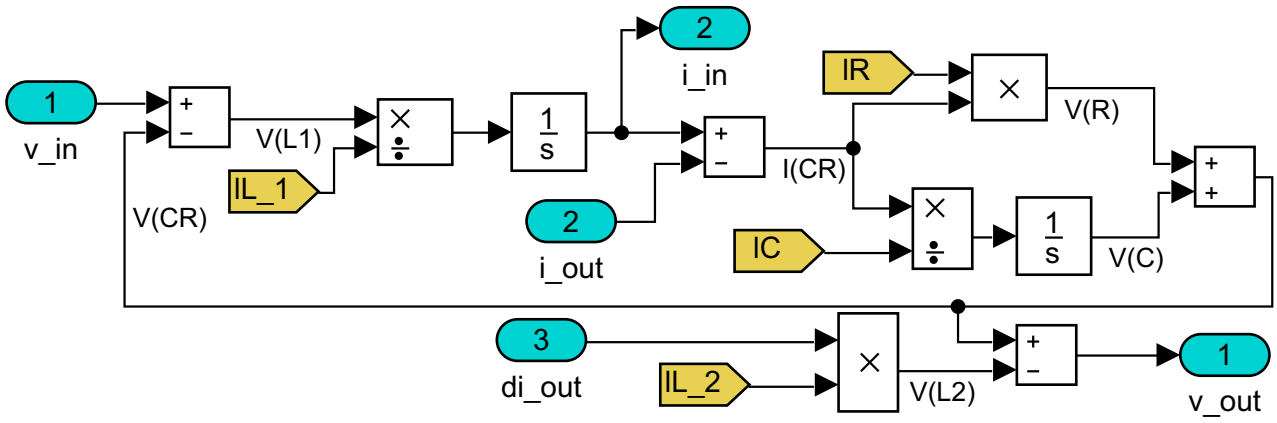
Figure 7.4: Inner structure of phase-blocks

7.3 Component design procedure

Determining suitable component parameters for the filter is a complex task. In the proposed system, the DC-link voltage and load current may vary over time, and a decent design should provide good output voltage quality over this range. Design procedures are available in the literature [36], and an algorithmic approach for determining the component parameters will be used [37]. The full procedure can be found in the filter design script, Appendix B. The script also contains some voltage-drop considerations, further explained in Section 11.1.

The method uses fixed parameters of rated output (voltage, frequency and apparent power), DC-link voltage and the switching frequency to determine the filter components. Three design parameters are also fixed as given in the design example in [37], namely a power-factor variation (x=0.05), attenuation factor (k_a=0.2) and current ripple (delta_i=0.1). The procedure consists of 5 steps, determining the parameters in the order: $L_1 \rightarrow C \rightarrow L_2 \rightarrow R$.

8 Miscellaneous other models

In addition to the models given in Chapter 3-7, some additional minor models are useful for interconnection and simulation-purposes. This chapter will cover the details of the rotational system, prime-mover, DC-link capacitor and battery, with their corresponding MATLAB-simulink implementation.

8.1 Rotational system

In a practical system, the rotor-shaft of the induction machine is connected to a prime-mover (generation) or mechanical load (motoring). A positive net torque, (8.1), is defined to imply an increase of mechanical speed (ω_m). With no gears, we can express the sum of the inertia for the induction machine and prime-mover as J_{tot}. Together with a first-order friction-coefficient (μ_f) we can express the rate of speed-change by (8.2). The inertia is often related to the time-constant H, (8.3), which describes how many seconds of the power P that is stored as rotational energy in the system at nominal speed.

$$\mathrm{T_{net}} = \mathrm{T_{pm}} + \mathrm{T_{em}} \tag{8.1}$$

$$\frac{d(\omega_m)}{dt} J_{tot} = \mathrm{T_{net}} - |\omega_\mathrm{m}|\mu_\mathrm{f} \tag{8.2}$$

$$H = \frac{\frac{1}{2} \cdot J_{tot} \cdot (\omega_m^N)^2}{P} \tag{8.3}$$

8.1.1 Simulink implementation
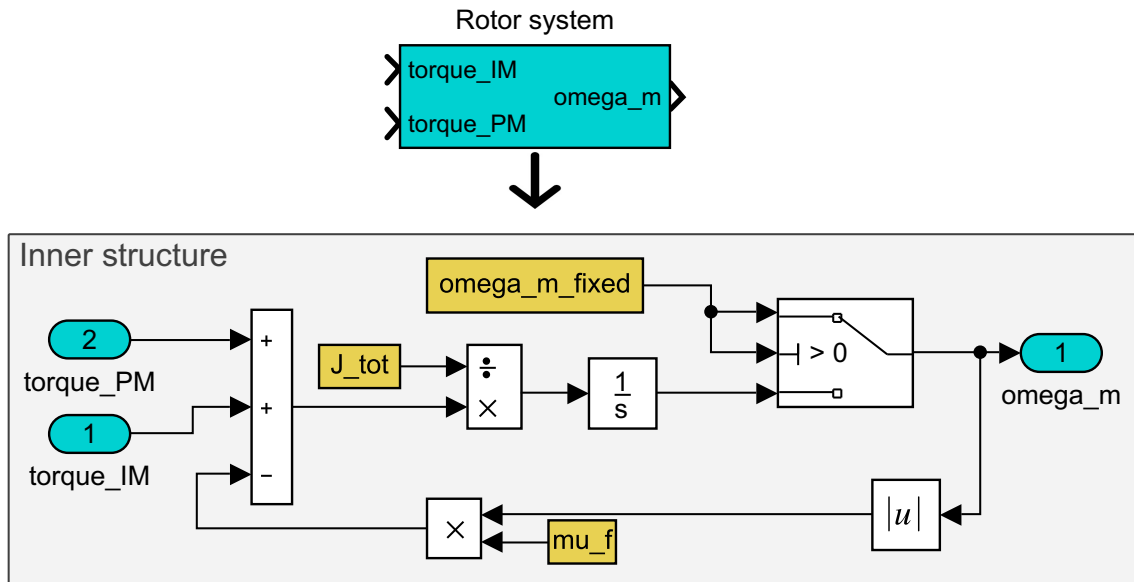
Figure 8.1: Rotational system model block

The rotational system is implemented into the custom block as shown in Figure 8.1. The torque of the prime-mover and induction machine are taken as inputs to provide the mechanical rotor speed as output. Yellow quantities (3 in total) represents the required constant parameters. Fixed speed rotor can be implemented by defining omega_m_fixed larger than 0.

8.2 Prime mover

The prime mover is required to supply the active power to the loads. Energy stored in the system (DC-link and rotational energy) could cope with imbalance, but in the long run, what goes in must eventually come out. The speed-torque characteristics of the prime-mover must be considered in terms of power ($P = T_{pm} \cdot \omega_m [\mathrm{W}]$), together with the capabilities of the induction generator (Section 9.1). Gears can be used to match the power of the generator and prime mover at different speeds, but they will also introduce additional losses. The speed-torque characteristics of the prime mover can vary during operation, and dynamic conditions will be of influence for the performance of the system.

8.2.1 Simple hydro-model

An example of suitable prime-mover is a hydro-turbine, perhaps available from a local river with steady flow. A common model for hydro-power is the linearized transfer function of a hydraulic turbine, where one can represent the incremental change in power output by incremental change in gate-opening [8]. The modelling represents a non-minimum-phase system, caused by inertia of the water in the penstock. This model does however not explicitly express the torque and speed characteristics, which would be desirable for a simulation together with the induction machine.

To keep the complexity low whilst including some of the dynamic properties, a simpler hydro-power model is chosen. Based on [6, 7], the torque can be described by (8.4). For a fixed opening of the valve (T_0), i.e. how much water is supplied, the torque decreases linearly for increasing speeds (ω_m), scaled by the factor $\mathrm{k_{pm}}$. Figure 8.2 illustrates the torque and power-relations. Other more complex models show similarities to this representation of torque and speed [9, 10, 11].

$$\mathrm{T_{pm} = T_0 - \omega_m \cdot k_{pm}} \tag{8.4}$$
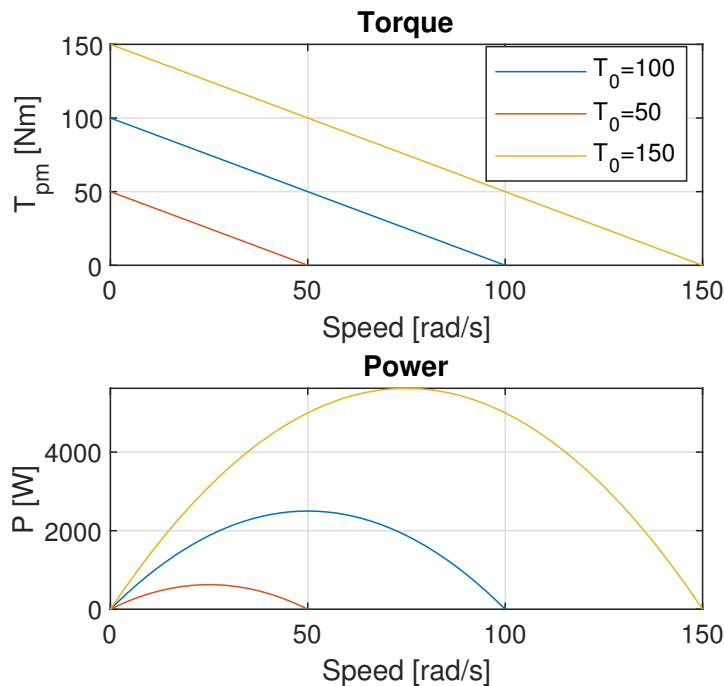
Figure 8.2: Hydro model torque and power as a function of speed. $\mathrm{k_{pm}} = 1$

The parameters (T_0 and $\mathrm{k_{pm}}$) can be scaled by (8.5) and (8.6), when defining a desired power (P_1) at speed (ω_1), and the zero-torque speed (ω_2), where $\omega_2 > \omega_1$. Note that the maximum-power will always be at half the zero-torque speed, $\frac{w_2}{2}$.

$$k_{pm} = \frac{P_1}{(\omega_2 - \omega_1)\omega_1} \tag{8.5}$$

$$T_0 = \frac{P_1}{\omega_1} + \omega_1 k_{pm} \tag{8.6}$$

8.2.2 Simulink implementation
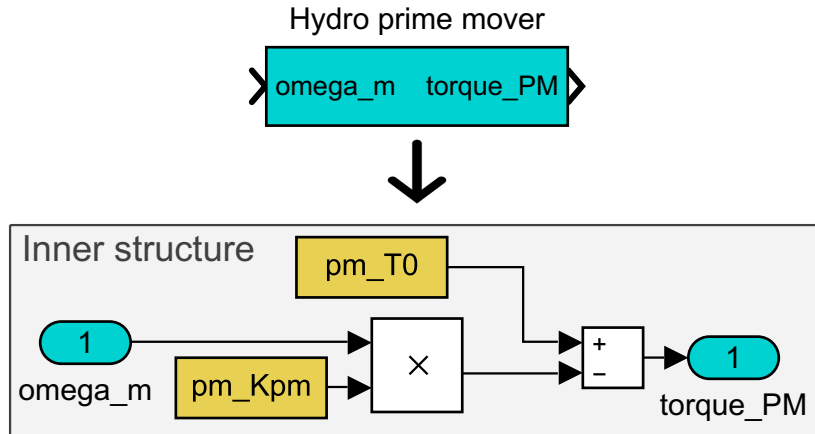
Figure 8.3: Hydro primer mover model block

The simple hydro prime mover model is implemented into the custom block as shown in Figure 8.3. The mechanical speed determines the torque, based on the two fixed parameters of T_0 and k_{pm} (yellow).

8.3 DC-link capacitor

The DC-link capacitor functions as the common voltage-source for the two converters in the system. It's assumed ideal, described by (8.7) in Laplace notation.

$$I_{DC} = C \cdot V_{DC} \cdot s \tag{8.7}$$

8.3.1 Simulink implementation
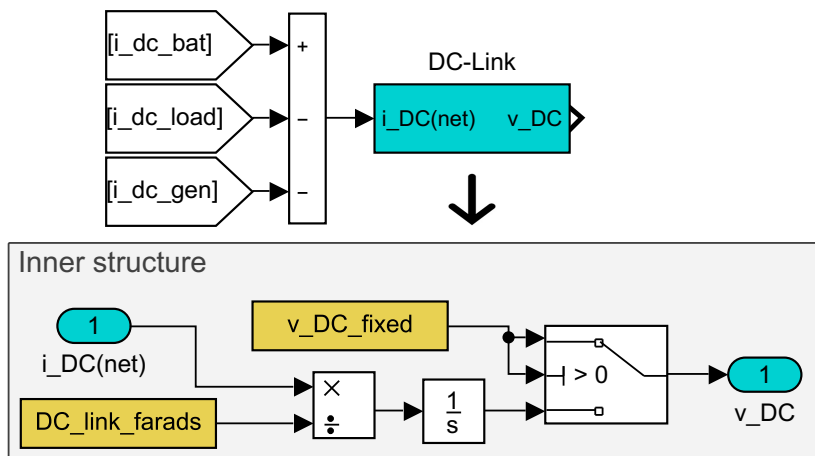
Figure 8.4: DC-link model block

The DC-link model is implemented into the custom block as shown in Figure 8.4. The net current is taken as input to provide the voltage as output. Note the negative signs of the converter currents (i_dc_load and i_dc_gen), who are defined as positive for discharging. The two yellow quantities represents the required constants parameters. DC_link_farads is the capacitance, and a fixed voltage DC-link can be implemented by defining v_DC_fixed larger than 0. The initial charge (in volts) can be set by defining the initial condition of the integrator-block.

8.4 Battery

The proposed system topology requires an initial voltage in the DC-link, to be provided by a battery. The battery is connected to the DC-link through a diode, which functions to prevent reverse-currents when $V_{DC} > V_{bat}$. The diode is assumed ideal (no forward voltage drop, no internal resistance, and perfectly able to block reverse-currents). The battery-current is expressed by (8.8). The internal resistance (R_{bat}) is fixed, and required to limit the current drawn whenever $V_{DC} < V_{bat}$. It also expresses the non-ideal characteristics of a battery as a voltage-source.

$$I_{bat} = \frac{V_{bat} - V_{DC}}{R_{bat}}, \quad I_{bat} \geq 0 \tag{8.8}$$

8.4.1 Simulink implementation
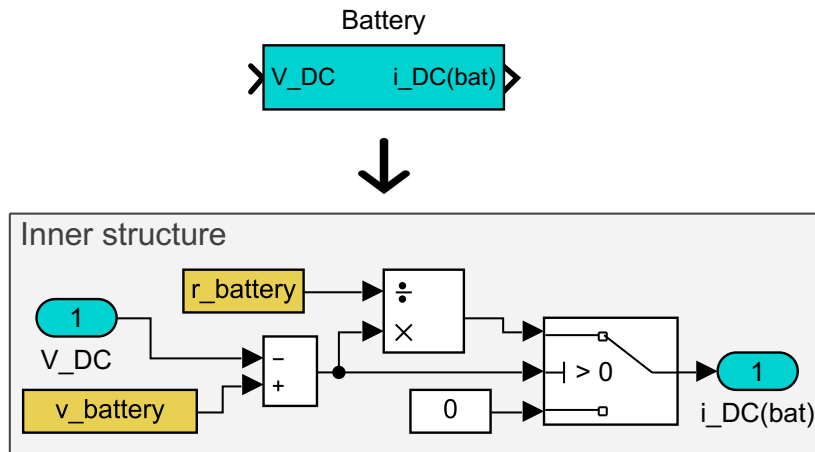
Figure 8.5: Battery model block

The battery model is implemented into the custom block as shown in Figure 8.5. The DC-link voltage is taken as input to provide the battery-current as output. The two yellow quantities represents the required constants parameters, namely the battery voltage (V_{bat}) and resistance (R_{bat}). The switch-block implements the unidirectional properties of the diode.

9 Control methods for induction machines

The art of control lies within observing quantities, and acting on this information to keep the system operating as desired. This chapter will briefly cover the operational limits of induction machines, followed by a theoretical introduction for three commonly encountered control methods, namely scalar control (V/f), field-oriented control (FOC) and direct torque control (DTC).

9.1 Induction machine: Ratings and limitations

Induction machines have limitations in terms of voltage and current. Greatly simplified, the voltage is limited by the insulation of the machines. The limits of currents can be related to magnetic saturation and temperature (heat-development due to losses). Because saturation implies that the efficient use of current vs. torque decreases, most machines are designed to operate near the saturation point. A converter also has limits in terms of voltage and current. These limitations should be considered when the induction machine and converter are to be operated together.

Induction machines rely on magnetic fields to develop the torque, whose origin are the currents. As mentioned, the presented models in Section 4.2 and 4.5 does not account for magnetic saturation in the machine. There are several studies handling this phenomenon, [12, 13, 14], but for the sake of simplicity, this aspect will not be further investigated. The magnetic fields are thus assumed to change in proportion to the fixed parameters of machine inductance. By inspection of (4.3) and (4.9), the upper limit of torque is dependent upon currents, and thus the current-ratings. Current in the rotor of the induction machine will induce voltage back to the stator, dependent upon the speed. With an upper voltage limit of the converter/machine, one must expect a decrease of available for torque for higher speeds, similar to that of the DC-machine. In conclusion (without regarding mechanical limitations), we can say that currents limits the torque, and voltage limits the upper power achievable.

9.2 Scalar control

9.2.1 Constant magnetising flux

Under the assumptions of the steady-state model (Section 4.2), the magnetising-flux of the IM ($\lambda_m = L_m I_m$) can be held constant by properly scaling the "magnetisation" voltage (V_m), i.e. $|\lambda_m| = \text{const} = \frac{V_m}{\omega_{el}}$. With knowledge of the machine parameters, this can be achieved by adjusting the stator voltage magnitude according to applied frequency (ω_{el}) and operational slip (s). Figure 9.1 demonstrates this for a range of frequencies (using the parameters of #M2 in Appendix A). Note that the torque and stator-current characteristics with respect to slip speed (ω_s) becomes equal for all applied frequencies (f_{el}). The required stator voltage increases for higher speeds (back EMF) and slips (larger current). Keeping $|\lambda_m|$ constants gives a predictable and symmetrical motor/generator behaviour, with a defined limit of maximum torque [1][6]. Controlling the magnetisation-flux would require measurements of the quantity. This could be achieved by for instance Hall-sensors, sensing coils, or other indirect estimation methods. Such equipment does however impose additional costs and customisation requirements.
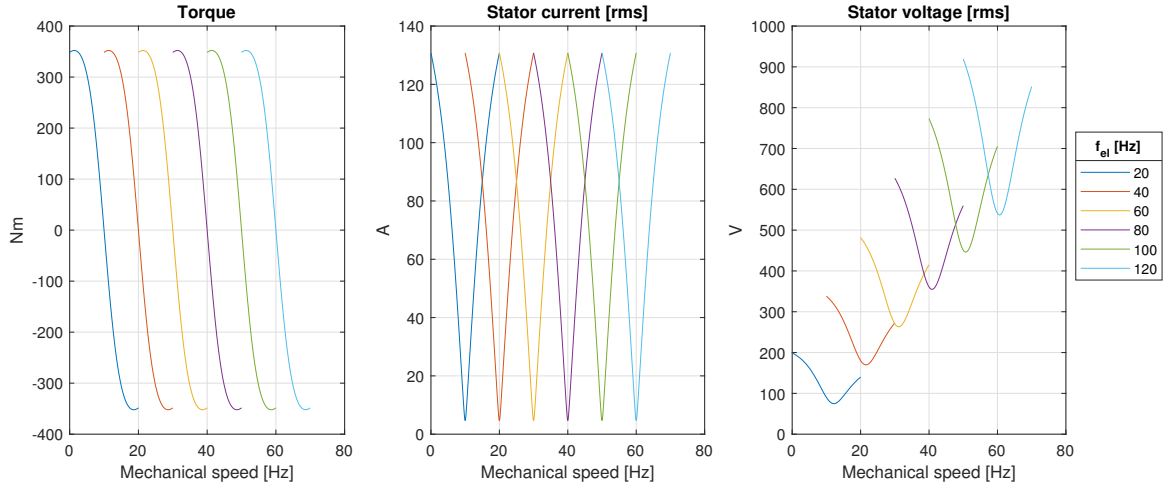
Figure 9.1: Operation of constant magnetisation flux. $V_m = 263.163\text{V}$ [rms], based at $f_{el} = 60$ Hz and $s = -0.016$

9.2.2 Volts/Hertz (V/f)

By inspection of Figure 9.1, we see that the stator-voltage, at a given slip-speed (ω_s), tends to increase somewhat linearly for increasing frequency (f_{el}). From the steady-state model, we can approximate the magnetisation-flux by (9.1), assuming that $L_m \gg L_{ls}$ and that stator restive voltage drops can be neglected. This is the core of the Volts/Hertz-method, also known as "scalar control". It principle is simple: adjust the stator voltage magnitude according to the desired operation of speed.

$$V_s \approx jL_m\omega_{el} \rightarrow \frac{V_s}{f_{el}} = \text{const} \tag{9.1}$$

Figure 9.2 shows the same machine (#M2, Appendix A) when using the V/f principle with rated voltage and frequency as a basis for the constant, (9.1). Compared to Figure 9.1, we notice that the curves of torque and current show a similar pattern, though the simplifications become of influence when operating at lower mechanical speeds (ω_m). Additionally, the pullout-torques are higher in the generator-regions. Figure 9.3 shows the same curves as a function of slip speed (ω_s), ranging from ± 2 times the rated slip speed. The apparent merging of torque and current-characteristics demonstrates the predictability of the V/f control method. Machines are usually operated close to synchronous operation because this region provides the best efficiency in terms of converting between mechanical and electrical power.
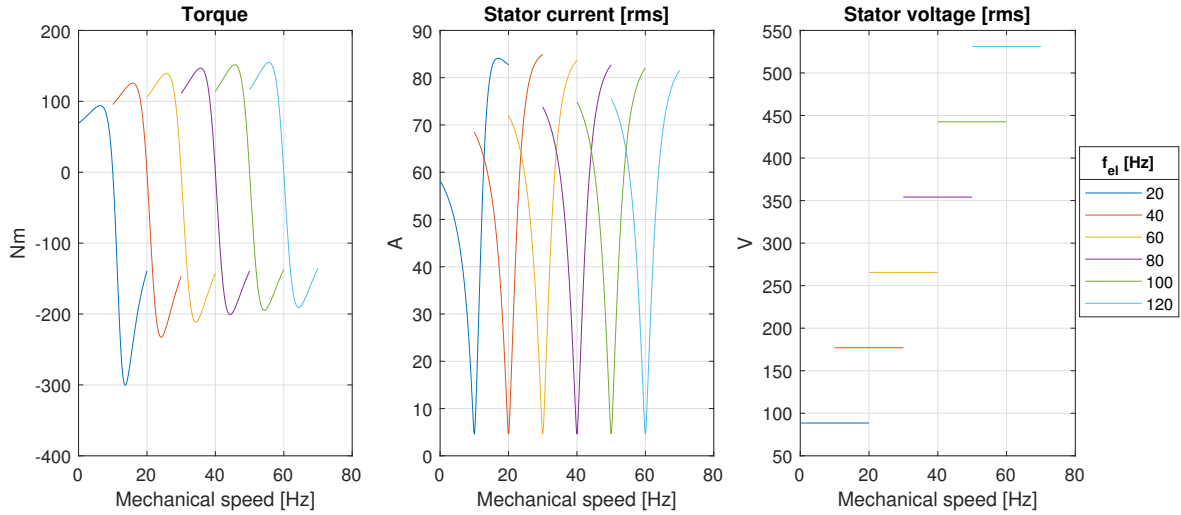
Figure 9.2: Operation of constant V/f-ratio. $c = 4.4263 = \frac{265.58}{60}$
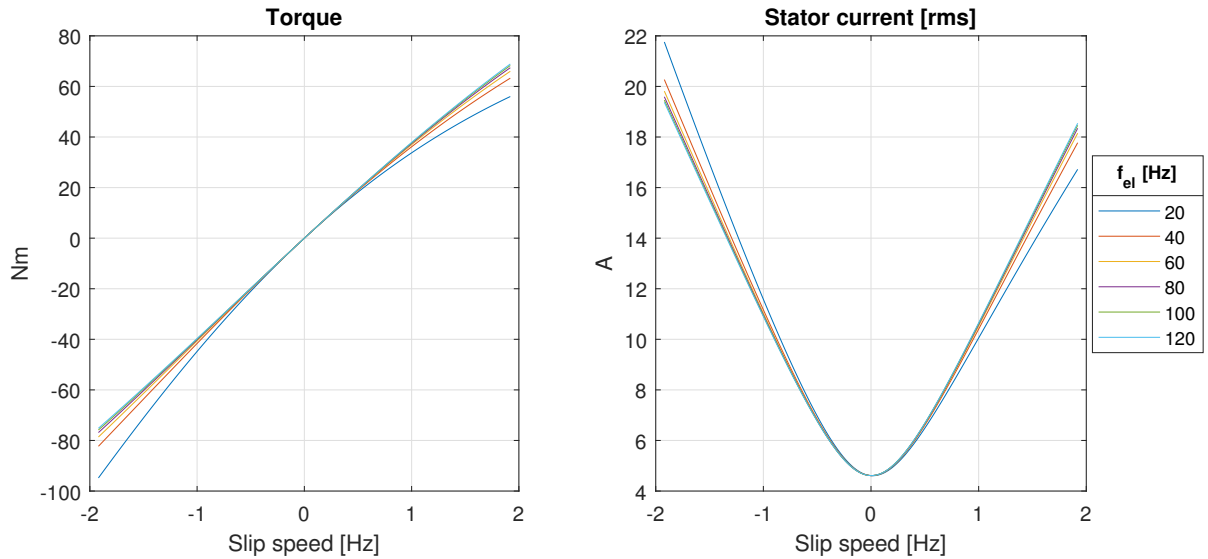
Figure 9.3: Operation of constant V/f-ratio with respect to slip speed

For further adjustment, one can modify the linear V/f-scale to overcome difficulties related to for instance low starting-torque, differences in motor/generator region and different loading conditions [1][7].

9.2.3 Applications and implementation

The simplicity of the V/f control makes it common for predictable low cost applications, such as driving fans and pumps [41][1]. A simple microprocessor could be sufficient for implementing the controls, and inclusion of slip-limits can handle excessive currents/saturation. Some drawbacks are the basis in the steady-state model, which comes at a cost of poor dynamic performance compared to other methods such as FOC.

Open loop:
In an open-loop configuration, no measurements are used as feedback to adjust the references for the converter. This is the simplest and cheapest form, but should require knowledge of the torque/speed characteristics of the load/application to ensure expected performance.

Closed loop:
With closed-loop control, measurements are used to ensure that the references are actually met. The frequency

of the voltage (f_{el}) (in relation to the measured mechanical speed (ω_m)) can be altered as a "speed-control" parameter. Stator current are also important to keep within the rated values, which can be lowered by lowering the voltage or adjusting the frequency closer to synchronous speed.

9.3 Field Oriented Control (FOC)

The FOC-method falls under the term "vector control", which goes deeper into the torque-relations as expressed by the currents and magnetic fluxes. Since the introduction in the 1970s, the method is still a subject of research. Its usage has been widespread due to its advantages for dynamic responses and efficient use of power, driven forward by the introduction of cheaper and faster processors. [41][2] [50].

9.3.1 Working principle

In DC-machine control, the field and armature currents can be adjusted to control the torque. An analogy can be made with the torque in the mechanical domain, $\tau = R \times F$, where the arm-length (R) is the field-current, and the force (F) is the armature-current. To achieve greater torque, both magnitudes can be increased, together with aligning them perpendicular. This is the core idea behind the FOC, and we can demonstrate the mathematics by using the dynamic model for the IM (Section 4.5).

The machine is described in the dq0-domain by using the Park-transformation (4.4) rotating at the same speed as the fluxes. This is achieved by adjusting the d-axis angle in sync with the stator frequency, $\frac{d}{dt}(\theta_d) = \omega = \omega_{el}$. We have three fluxes which could be considered for alignment of the reference frame: λ_m, λ_r and λ_s. We will consider the rotor-flux (λ_r), which has the benefit of a decoupling in terms of torque and flux [43].
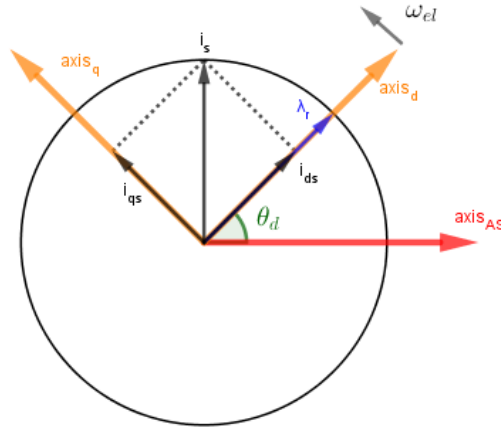
Figure 9.4: FOC Park-transformation

The d-axis of the transformation is aligned with the rotor flux ($\lambda_r = \lambda_d^r$), and thus, $\lambda_q^r = 0$ by definition. This gives an expression for i_q^r, (9.2), which can be inserted into the expression for torque, (9.3). From this we identify that the torque depends upon the magnitudes of i_q^s and λ_d^r.

$$\lambda_q^r = 0 = (L_{lr} + L_m)i_q^r + (L_m)i_q^s \rightarrow i_q^r = -i_q^s \frac{L_m}{L_{lr} + L_m} \tag{9.2}$$

$$\mathrm{T}_{em} = \frac{3}{2}n_{pp}\left(0 \cdot i_d^r - \lambda_d^r i_q^r\right) \rightarrow \mathrm{T}_{em} = \frac{3}{2}n_{pp}\left(\frac{L_m}{L_{lr} + L_m}\right)\lambda_d^r i_q^s \tag{9.3}$$

v_d^r can be rearranged to express i_d^r in Laplace notation by (9.4). Inserted into the equation for λ_d^r yields an expression dependent upon i_d^s, (9.5).

$$v_d^r = 0 = s(\lambda_d^r) - (\omega_{el} - \omega_r) \cdot 0 + r_r i_d^r \rightarrow i_d^r = -\frac{s(\lambda_d^r)}{r_r} \tag{9.4}$$

$$\lambda_d^r = (L_{lr} + L_m)i_d^r + (L_m)i_d^s \rightarrow \lambda_d^r = \frac{L_m}{1 + s\left(\frac{L_{lr}+L_m}{r_r}\right)}i_d^s \tag{9.5}$$

$$\tau_r = \frac{L_{lr} + L_m}{r_r} \tag{9.6}$$

The stator-currents are the measurable quantities which can be used in a control-scheme by decomposition onto the rotating dq-reference frame. The delay of change in rotor flux due to the rotor time-constant (9.6) makes λ_d^r a somewhat "stable" quantity. Thus, for fast torque-control, the stator q-current component (i_q^s) is often chosen as the primary variable, whereas the stator d-current component (i_d^s) is used to maintain a reference magnetisation [42] [2]. In a more general perspective, i_q^s can be dedicated as the active power reference, and i_d^s as the reactive power reference. Note that in steady-state conditions, the magnitude of the torque is scaled by the product of the stator-current components ($i_d^s \cdot i_q^s$). When obeying the limits of rated currents, (9.7), the maximum torque is obtained when $i_d^s = i_q^s = I_N^G$.

$$\sqrt{(i_d^s)^2 + (i_q^s)^2} \leq I_N^G \cdot \sqrt{2} \tag{9.7}$$

9.3.2 Implementation

To apply FOC, one must necessarily have an idea about the position and magnitude of the actual rotor-flux (λ_r) such that one can align the Park-transformation accordingly. There are several methods for doing this, which can be separated into the direct and indirect approach. Common for them is the resulting output references of stator-currents (i_d^s, i_q^s), which can be transformed into the static abc-domain. These references can then be realised with a converter by means of for instance a hysteresis-current controller (Section 6.6), or transformed into voltage references, perhaps with additional decoupling (feed-forward terms) in order to enhance the response. Voltage-references could be realised by for instance the S-PWM or SV-PWM method.

9.3.3 Direct FOC

This methods relies on measurements to determine the rotor flux (λ_r). This can be done by sensing the magnetisation flux (λ_m) by for instance Hall-sensors or search-coils. Another approach is sensing the stator voltage and current, and estimate the rotor-flux by using a model [44].

An example of the magnetisation-flux approach is to acquire measurement of λ_m and the stator currents, which are transformed into the static ($\omega = 0$) dq0-domain. λ_d^r and λ_q^r can now be estimated by using machine parameters L_m and L_{lr}. With these components, we can determine the magnitude and position (in the static reference) of λ_r, which is used to align the system in a rotor-flux oriented dq0-transformation, to be further used in the control-loop [1][5]

Some challenges related to the direct method is the temperature sensitivity and fragile Hall-sensors, and drift of the integration of voltage used to estimate the flux in the sensing-coils. Position control or low-speed operations also becomes more difficult with uncertainty in the rotor-flux estimations. Additionally, more sensors introduce more costs [43] [45]

9.3.4 Indirect FOC

This method mitigates the need for actually sensing/estimating the rotor-flux (λ_r). It's based on measurement of rotor position (θ_m), which is used in a feed-forward manner to determine the rotor flux-position [1][5].

In the rotor-flux aligned reference frame, we have defined $\lambda_q^r = 0$, which should also remain zero, i.e. $\frac{d}{dt}(\lambda_q^r) = 0$. From the expression of v_q^r, this yield the relation as given in (9.8). If we also assume that λ_d^r remains unchanged,

$\frac{d}{dt}(\lambda_d^r) = 0$, we see from the expression of v_d^r, (9.9), that i_d^r must be zero. This property will simplify λ_d^r into (9.10). Using (9.10) and (9.2) into (9.8) yields (9.11).

$$v_q^r = 0 = (\omega_{el} - \omega_r) \cdot \lambda_d^r + r_r i_q^r \rightarrow (\omega_{el} - \omega_r) = -\frac{i_q^r r_r}{\lambda_d^r} \tag{9.8}$$

$$v_d^r = 0 = r_r i_d^r \rightarrow i_d^r = 0 \tag{9.9}$$

$$\lambda_d^r = (L_m) i_d^s \tag{9.10}$$

$$\omega_s = (\omega_{el} - \omega_r) = \frac{i_q^s}{i_d^s} \frac{r_r}{L_{lr} + L_m} \tag{9.11}$$

From (9.11), we identify that the slip-speed (ω_s) is a function of the ratio between the stator current-components when the system is properly oriented. The rotor-flux as described by (9.5) can be treated as a reference, (9.12). This can be combined with the expression of torque as a reference, resulting in (9.13). By applying $(i_d^s)^*$ and $(i_q^s)^*$ into (9.11), we can integrate $(\omega_s)^*$, and add the measured rotor position (θ_m) to obtain the position of the rotor flux (λ_r), which is forwarded to the transformation of dq0-abc static currents references.

$$(\lambda_d^r)^* = \frac{L_m}{1 + s\left(\frac{L_{lr} + L_m}{r_r}\right)} (i_d^s)^* \tag{9.12}$$

$$\mathrm{T}_{em}^* = \frac{3}{2} n_{pp} \left(\frac{L_m}{L_{lr} + L_m}\right) (\lambda_d^r)^* (i_q^s)^* \tag{9.13}$$

The indirect approach has an advantage over the direct as it requires less sensors and can handle operations at lower speeds better. However, it relies on a precise rotor time constant (τ_r) for precise control, and adaptive techniques might be included to tune τ_r during operation.

9.3.5 Current constraints

As mentioned in Section 9.1, operation at higher speeds (ω_m) results in higher back-EMF. Assuming that the available stator-voltage has an upper limit of V_s, we can express the limitations of the dq-voltage components by (9.14).

$$V_s \geq \sqrt{(v_d^s)^2 + (v_q^s)^2} \tag{9.14}$$

Using the expressions given by the dynamic model (Section 4.5.3), the components can be approximated by (9.15) and (9.16) by using the same transformation as presented in Section 9.3.1 and the following assumptions/definitions: [51]

- The fluxes are not varying, i.e. $\frac{d}{dt}(\lambda_s) = \frac{d}{dt}(\lambda_r) = 0$
- The currents are not varying
- $L_s = L_{ls} + L_m$
- $L_r = L_{lr} + L_m$
- $\sigma = 1 - \frac{L_m^2}{L_s L_r}$.
- $i_d^r = 0$
- $\lambda_q^r = 0 \rightarrow i_q^r = -i_q^s \frac{L_m}{L_r}$

$$v_d^s \approx -\omega_{el}(\sigma L_s i_q^s) + r_s i_d^s \tag{9.15}$$

$$v_q^s \approx \omega_{el}(L_s i_d^s) + r_s i_q^s \tag{9.16}$$

Figure 9.5 illustrate the limits of dq-current components for a range of frequencies, using the parameters of machine #M1 (Appendix A), with $V_s = 326.9V$. The rated current-limits are also included (red), as expressed by (9.7). Any feasible operational point at a given frequency must lie within the current circle (red) and voltage ellipse. The voltage-ellipses contract for higher frequencies (ω_{el}), illustrating the effect of the back-EMF. Note that the range of the voltage ellipses tends to be stretched further in the q-current direction. This strehcing is reduced for higher values of σ (σ is small when $L_m \gg L_{ls}$ and $L_m \gg L_{lr}$).
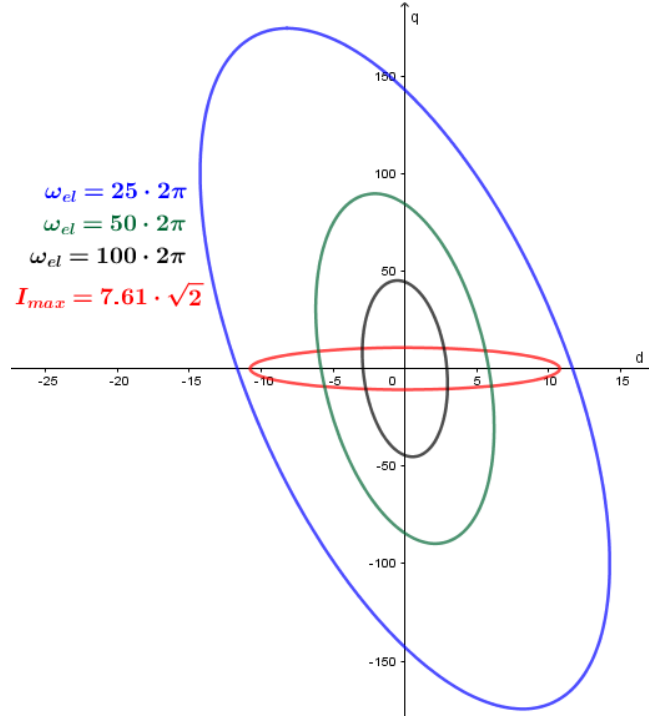
Figure 9.5: dq-current constraints

9.4 Direct torque control (DTC)

Introduced in 1985, DTC has similarities to the FOC-method. It's favoured for its simple implementation and fast response, and has become an industrial standard. It does however have a drawback with ripples of torque, and is, similar to the FOC-method, still a subject of research [41][2].

9.4.1 Working principle

The working principle can be explained by the means of static stator-oriented ($\omega = 0$) Park-transformation. By using the dynamic model (Section 4.5), we can express the stator and rotor related quantities in terms of space vectors pointing in the two dimensions (d and q), as summarised by (9.17), (9.18), (9.19) and (9.20) [42] [46]. Torque can be expressed by the cross-product of $\vec{\lambda}_s$ and $\vec{i}_s$, (9.21), where $\theta_{\lambda i}$ is the angle between them.

$$\vec{v}_s = \frac{d}{dt}(\vec{\lambda}_s) + r_s \vec{i}_s \tag{9.17}$$

$$\vec{v}_r = 0 \approx \frac{d}{dt}(\vec{\lambda}_r) + r_r \vec{i}_r - j\omega_m \vec{\lambda}_r \tag{9.18}$$

$$\vec{\lambda}_s = (L_{ls} + L_m)\vec{i}_s + L_m\vec{i}_r \tag{9.19}$$

$$\vec{\lambda}_r = (L_{lr} + L_m)\vec{i}_r + L_m\vec{i}_s \tag{9.20}$$

$$\mathrm{T}_{em} = \frac{3}{2}n_{pp}|\vec{\lambda}_s||\vec{i}_s|\sin(\theta_{\lambda_s i_s}) \tag{9.21}$$

We can express the stator current $(\vec{i}_s)$ by combining (9.19) and (9.20) to obtain (9.22). (9.22) can be substituted into (9.21) to obtain (9.23). Notice that the cross-product of $\vec{\lambda}_s$ by itself is zero, and that we have defined $L_s = L_{ls} + L_m, \quad L_r = L_{lr} + L_m$ and $\sigma = 1 - \frac{L_m^2}{L_s L_r}$.

$$\vec{i}_s = \frac{1}{\left(L_{ls} + L_m - \frac{L_m^2}{L_{lr}+L_m}\right)}\left(\vec{\lambda}_s - \frac{L_m}{L_{lr} + L_m}\vec{\lambda}_r\right) \tag{9.22}$$

$$\mathrm{T}_{em} = \frac{3}{2}n_{pp}\frac{L_m}{\sigma L_s L_r}|\vec{\lambda}_s||\vec{\lambda}_r|\sin(\theta_{\lambda_s \lambda_r}) \tag{9.23}$$

We can insert (9.22) into (9.20) to obtain (9.24). The rotor current $(\vec{i}_r)$ can be expressed by shifting (9.18) into the Laplace-notation in (9.25). Combining (9.24) and (9.25) yields a relation of stator and rotor flux, (9.26).

$$\vec{\lambda}_r = \sigma L_r\vec{i}_r + \frac{L_m}{L_s}\vec{\lambda}_s \tag{9.24}$$

$$\vec{i}_r = \vec{\lambda}_r\frac{j\omega_m - s}{r_r} \tag{9.25}$$

$$\vec{\lambda}_r = \vec{\lambda}_s\frac{\frac{L_m}{L_s}}{1 + \sigma\frac{L_r}{r_r}s - j\omega_m\sigma\frac{L_r}{r_r}} \tag{9.26}$$

With the mathematics introduced, we can consider the two major assumptions regarding the control method. As seen from (9.26), with its similarities to (9.5), the rotor-flux $(\vec{\lambda}_r)$ is tracking the stator-flux $(\vec{\lambda}_s)$, with a time-delay. Thus, if we assume that $\vec{\lambda}_r$ stays constant for small time steps, the torque can be varied to changing $\vec{\lambda}_s$. The torque (9.23) depends on both the magnitude and angle of $\vec{\lambda}_s$, and the control structure can be divided into two parts: one that maintains the magnitude of $\vec{\lambda}_s$, and one which shifts the position of $\vec{\lambda}_s$ in relation to $\vec{\lambda}_r$ to produce torque. By assuming negligible stator current resistive drops, we have in discrete time steps $\Delta\vec{\lambda}_s \approx \vec{v}_s \cdot (\Delta t)$.

9.4.2 Implementation of DTC

There are several configurations which can function to implement the stator-oriented flux control scheme. At its core, it requires measurements of stator currents and voltages. The voltages can be obtained by considering the DC-link voltage in the converter (VSC), and the present switch-states. Together with knowledge of the stator-resistance, one can then estimate the stator-flux and torque vectors. This is compared to references of torque and flux magnitudes, which in turn determines how the voltage of the converter (VSC) should be applied. With the fixed stator-oriented reference frame, no transformation between coordinate-systems is required, which is an added bonus in terms of computational effort.

The switching states can be made directly by means of considering the possible voltage vectors (Section 6.2). For a given sample, the 6 non-zero voltage vectors can be applied to adjust $\vec{\lambda}_s$. This can for instance be achieved by

hysteresis-bands combined with look-up tables (Direct Self Control), or by applying the SV-PWM-method with $\vec{\lambda}_s$ as a reference [46]. Consequently, the DTC-method does not have a defined fixed switching frequency.

To summarise, DTC has advantages of a fast and a simple control structure that does not require extensive tuning. It does however require a fast-acting processor and precise measurements. Similar to the direct FOC, operation at lower speeds become problematic due to drifting of integrators.

10   Control system designs

The back-to-back system topology consist of two independently controllable VSCs, splitting the generator and loads into two separate AC-networks. This chapter will present MATLAB-Simulink implementations for proposed designs of control-systems, which takes input of measurements to provide references for the appurtenant gate-signal generator. It will cover two methods for the generator (V/f and indirect FOC), and one method for the load (voltage controller).

10.1   Preface

10.1.1   Core assumptions

Some core assumptions are made which applies for the proposed designs. They are summarised as follows:

- The generator (and LCL-filter) can withstand the high-frequency changes of voltage (of magnitude V_{DC}) applied by the VSCs.

- The current limit of the IM is independent upon speed (i.e. the cooling capabilities are not affected by ω_m)

- All measurements are assumed ideal, without filtering and processing-delays.

- There are no processing-delays in the control-system, and the output-references are similarly handled without delay in the gate-signal generators and intended gate-drivers.

- The loads connected are never exceeding the rated limits

For a practical system, there are several faults that could occur from several events. A component might break, a lightening strike could introduce a high voltage, and the load side might be short-circuited for some reason. Additional measurements and breakers might be introduced to the topology for the purpose of detecting and acting upon such errors. The introduced control systems are limited to handle only the "expected" and nominal conditions.

10.1.2   Properties of intent

Two aspects are intended to define the design of the control-systems.

Firstly, the structures should be made adequately general and simple, such that they can function in a kind of "plug-and-play" manner. A standardised "one-fits-all"-control system could be easier to set up, whilst also applicable for a wider range of configurations in terms of rated voltage, current, power, etc. The number of required parameters/measurements are therefore attempted to be kept low. Additionally, tuneable parameters are inteded to be derived by general ratings (Section 11.2).

Secondly, the system should quickly and smoothly react to disturbances, over the full range of operational-conditions. This would define the quality and reliability of the service. Having a generic and simple, yet well-reacting system is no straight-forward task. The full-range capabilities are met by including ad-hoc/special-case structures.

10.1.3   Threshold-based PI-controller

A slightly modified PI-controller is used as a common building brick for the control systems, shown in Figure 10.1. The core idea behind this structure is that a certain error (threshold) would scale the proportional gain into saturation, and the participation of the intregral-part would serve no useful function at these conditions.
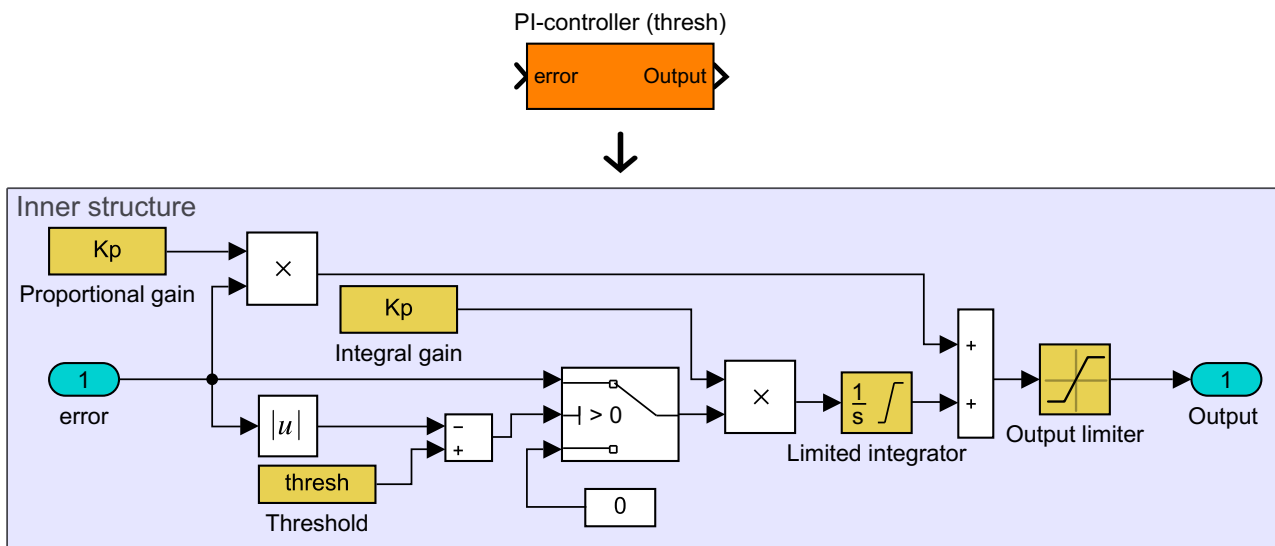
Figure 10.1: Simulink block of threshold PI-controller

The yellow quantities represents required constant parameters (5 in total). The output is limited within defined upper and lower boundaries, which represent the saturation. In other words, the maximum and minimum output is capped as desired. The integrator is defined with the same limits to prevent it to build up excessive values for prolonged errors. This anti-windup allows for a faster response. The threshold for error stops the integral part to participate if the error exceeds the value of "thresh".

10.2 V/f controller (generator)

10.2.1 Overview
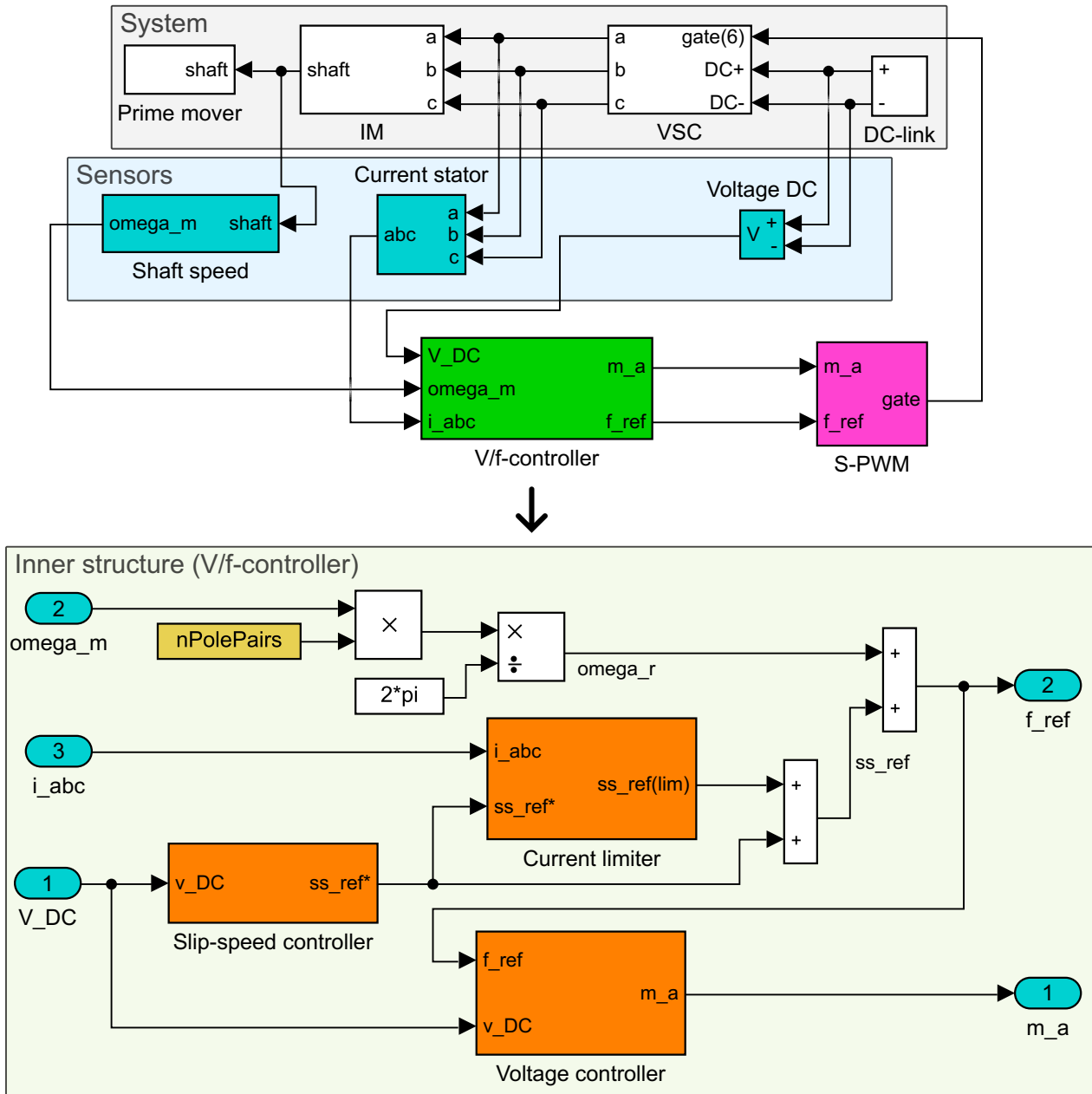
Figure 10.2: V/f-controller overview

Inputs (5)	Outputs (2) [S-PWM]
DC-link voltage, V_{DC} [V]	
Mechanical rotor speed, ω_m [rad/s]	Amplitude modulation, m_a [-]
Stator currents, i_{abc} [A]	Frequency reference, f_{ref} [Hz]

Figure 10.2 shows an overview of the measurements and outputs of the proposed V/f-controller. It's based on the concepts of scalar-control (Section 9.2), with a basis in the steady-state model of the IM. The gate-signals are realised by the S-PWM-method. The SV-PWM-method could also have been used, but the much simpler implementation of S-PWM was favoured, despite the potential benefits in performance by using SV-PWM

(Section 6.4).

The core purpose of this controller is to maintain the DC-link voltage at a reference level. This is achieved by commanding a slip-speed (Slip-speed controller), which effectively determines how much torque/power the IM should extract from the prime-mover. To avoid excessive currents in the stator, the current-limiter block can reduce the commanded slip-speed if necessary. The voltage (Voltage controller) is adjusted by the V/f-ratio scaling, trying to maintain a proper rms-voltage output based on the commanded electric frequency (f_{ref}).

10.2.2 Slip-speed controller

Figure 10.3: Slip-speed controller block

Figure 10.3 shows the structure of the slip-speed controller. Based on a reference DC-link voltage, it utilises the threshold-PI block (Figure 10.1) to give out a commanded slip-speed (ss_ref*). The output is capped to a maximum/minimum allowable slip-speed.

10.2.3 Current limiter

Figure 10.4: Current limiter controller block

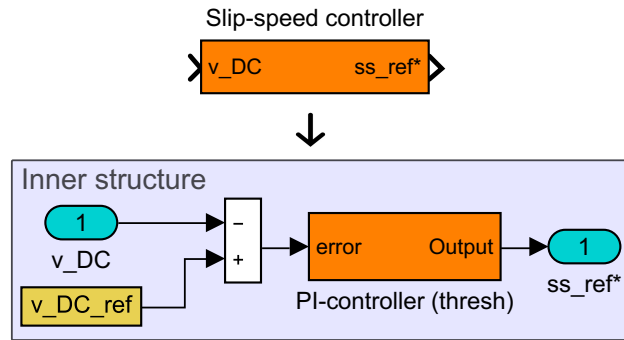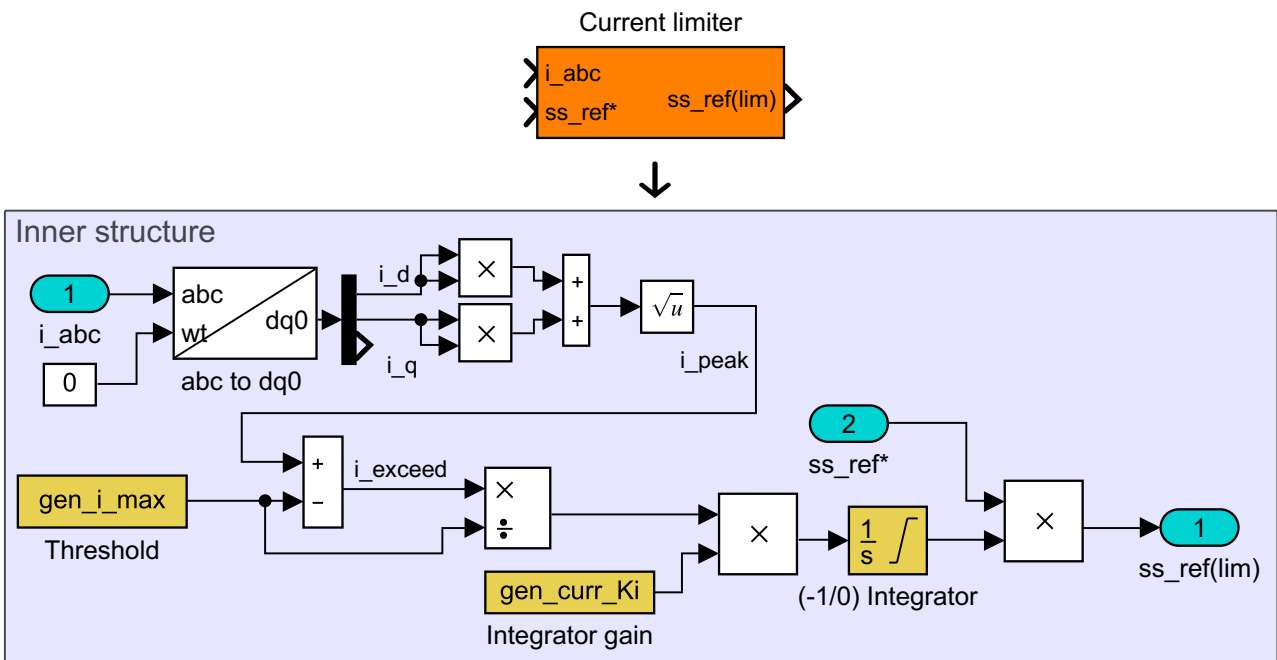Figure 10.4 shows the structure of the current-limiter controller. It uses a static Park-transformation to obtain an instantaneous measurement of the peak-values of the stator-currents. This is compared to the rated peak-value, and fed into an integrator. The integrator is limited to a lower value of -1, and an upper value of 0. Prolonged excessive currents results in the integrator reaching -1, and by inspections of Figure 10.2, this would correspond to the resulting slip-speed command (ss_ref) being zero (i.e. synchronous operation). Whenever the measured currents does not exceed the rated limits, the integrator works toward zero, where no slip-speed adjustment is performed (ss_ref*=ss_ref).

10.2.4 Voltage controller
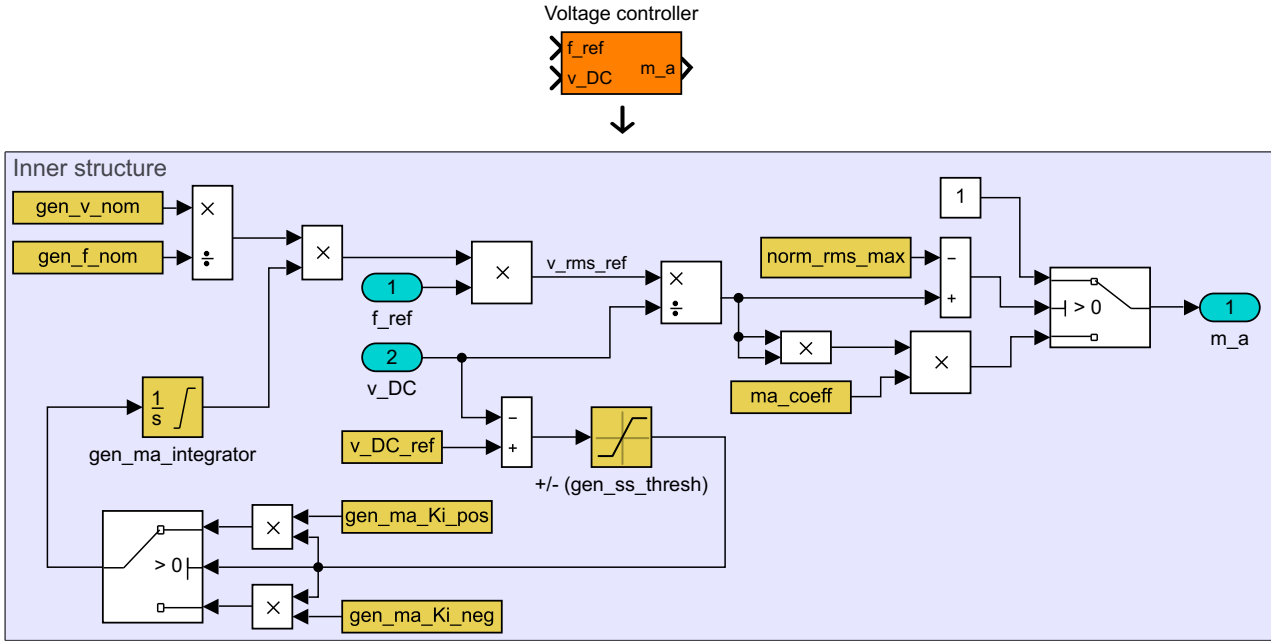
Figure 10.5: Voltage controller block

Figure 10.4 shows the structure of the voltage controller. It uses the rated machine parameters (gen_v_nom and gen_f_nom) to determine a basis frequency-coefficient ($\frac{V_n}{f_n}$) for commanded rms-voltage. The corresponding output of amplitude modulation (m_a) is determined by applying the RMS/DC-model given in Section 6.5, where norm_rms_max = $\bar{v}_m$ and ma_coeff = μ_{ma}.

The block also features a dynamical scaling of the frequency-coefficient, realised by the integrator (gen_ma_integrator). Whenever the DC-link voltage is below the reference value, the integrator can build up through the positive gain (gen_ma_Ki_pos), up to an upper limit (gen_ma_Ki_upper_lim). If the DC-link voltage exceeds the reference, the integrator works toward the lower limit of 1 through the negative gain (gen_ma_Ki_neg). The motivation for this functionality is illustrated by Figure 10.6. It shows the IM shaft-power when the machine #M1 (Appendix A) is operated at nominal speed (1555 rpm), applied with rated 50Hz phase voltage (230.97V rms) from the 2L-3ph VSC ($f_{sw} = 10$kHz) and a purely sinusoidal source. Though both methods apply the same rms-voltage, the resulting power is lower when the switch-based voltage source is used. Therefore, the ability to scale up the frequency-coefficient allows the system to apply a higher rms-voltage to utilise the full potential of the IM.
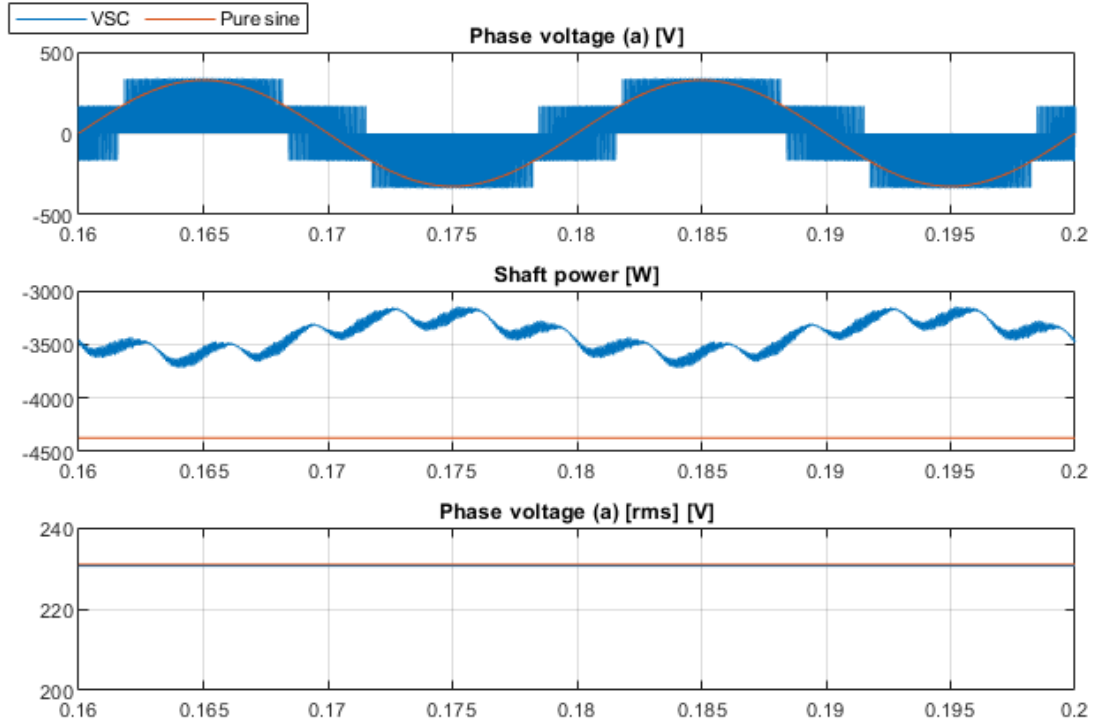
Figure 10.6: Shaft power variation: VSC and pure sine voltage

10.2.5 Parameter list

Name	Features in	Description
f_sw_vf [Hz]	S-PWM	Switching frequency (Section 6.1.4)
v_DC_ref [V]	Slip-speed controller Voltage controller	DC-link voltage reference
nPolePairs [-]	V/f-controller	Number of pole-pairs
gen_v_nom [V]	Voltage controller	Rated generator phase voltage[rms] (V_N^G)
gen_f_nom [Hz]	Voltage controller	Rated generator frequency (f_N^G)
gen_i_max [A]	Current limiter	Rated generator peak current $(I_N^G \cdot \sqrt{2})$
norm_rms_max [-]	Voltage controller	$\bar{v}_m$ (Section 6.5)
ma_coeff [-]	Voltage controller	μ_{ma} (Section 6.5)
gen_curr_upper_lim = 0	Current limiter	Upper integrator limit
gen_curr_lower_lim = -1	Current limiter	Lower integrator limit
gen_ma_Ki_lower_lim = 1	Voltage controller	Lower integrator limit

Table 10.1: Fixed parameters of V/f-controller

Name	Features in	Description
gen_ss_upper_lim [Hz]	Slip-speed PI-controller	Upper limit for integrator and output
gen_ss_lower_lim [Hz]	Slip-speed PI-controller	Lower limit for integrator and output
gen_ss_thresh [V]	Slip-speed PI-controller Voltage controller	Threshold (integral error)
gen_ss_Kp [-]	Slip-speed PI-controller	Proportional gain
gen_ss_Ki [-]	Slip-speed PI-controller	Integral gain
gen_curr_Ki [-]	Current limiter	Integral gain
gen_ma_Ki_upper_lim [-]	Voltage controller	Upper integrator limit
gen_ma_Ki_pos [-]	Voltage controller	Positive error integral gain
gen_ma_Ki_neg [-]	Voltage controller	Negative error integral gain

Table 10.2: Tuneable parameters for V/f-controller
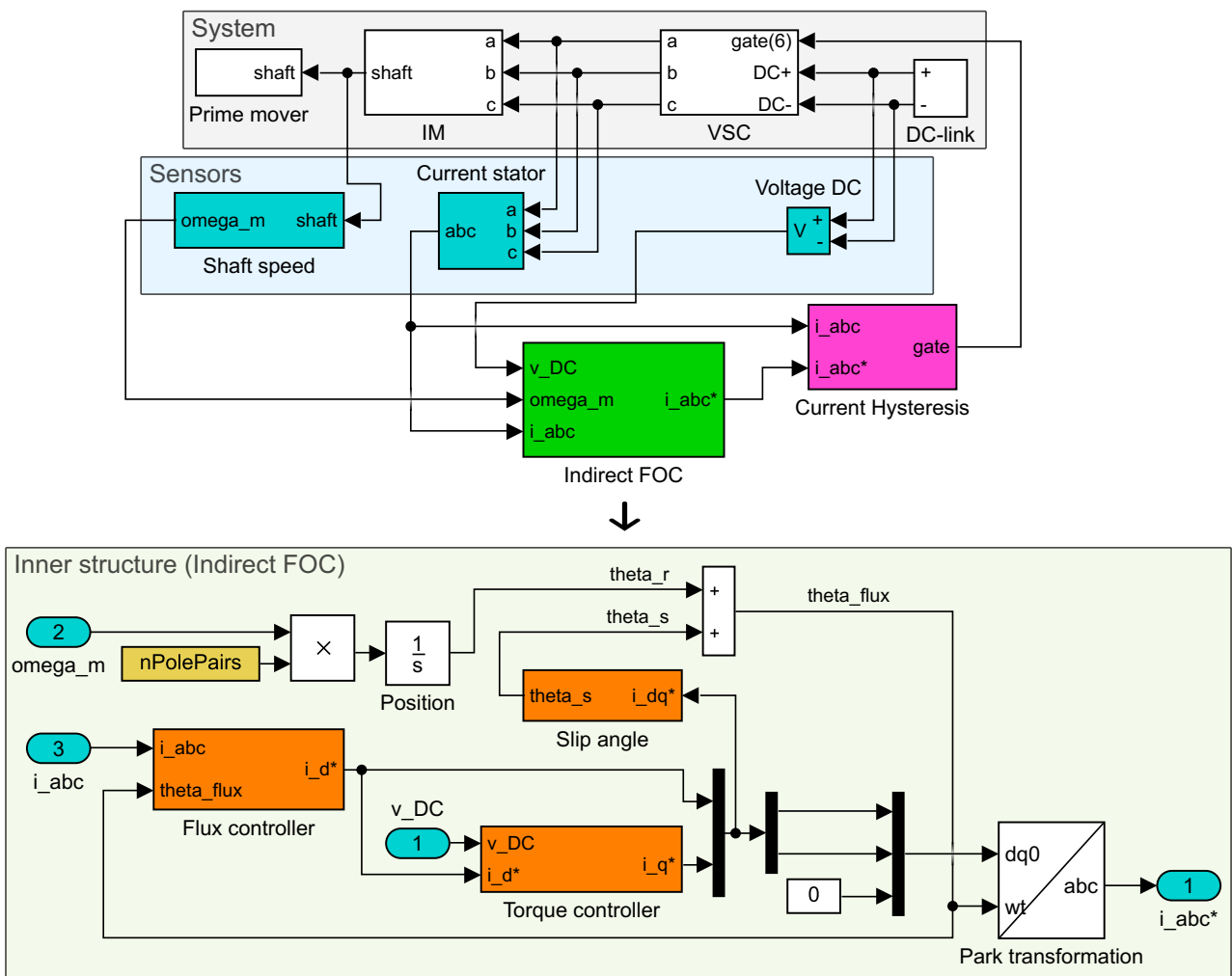
10.3 Indirect FOC (generator)

10.3.1 Overview

Figure 10.7: Indirect FOC overview

54

Inputs (5)	Outputs (3) [Current Hysteresis]
DC-link voltage, V_{DC} [V]	
Mechanical rotor speed, ω_m [rad/s]	Reference stator currents, $i_{abc}*$ [A]
Stator currents, i_{abc} [A]	

Figure 10.7 shows an overview of the measurements and outputs of the proposed FOC. It's based on the concepts of indirect FOC (Section 9.3), with a basis in the dynamic model of the IM. The gate-signals are realised by a hysteresis current controller.

The core purpose of this controller is to maintain the DC-link voltage at a reference level. This is achieved by adjusting the active stator current component (i_q^s) with an PI-controller (Torque controller). The appurtenant reactive stator current component (i_d^s) is given by the flux-controller, whose magnitude is linked to the torque-controller as to not violate the limits of rated stator-current. The commanded current-components are used to estimate the slip-speed angle, and combined with an integration of the shaft speed, this forms a position-estimation of the rotor flux, used to transfer the current-references into static abc-components.

10.3.2 Torque controller
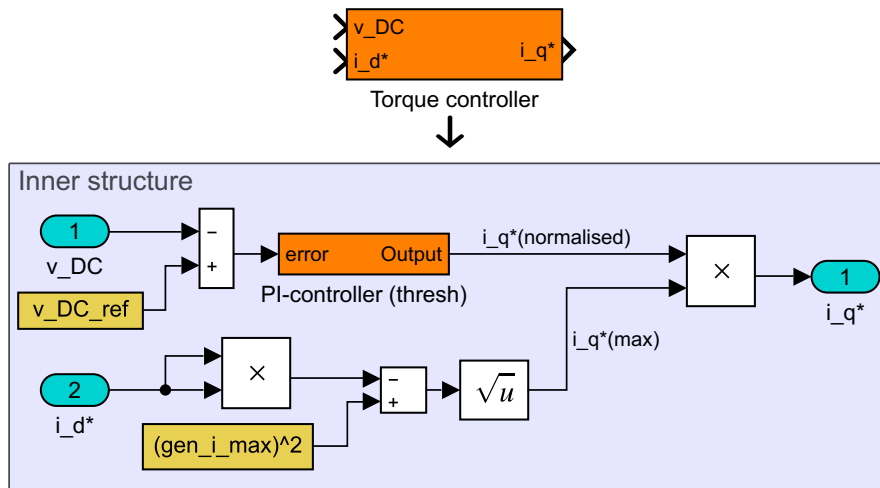
Figure 10.8: Torque controller block

Figure 10.8 shows the structure of the torque controller. Based on a reference DC-link voltage, it utilises the threshold-PI block (Figure 10.1) to give out a commanded active current (i_q*). The output is "normalised" with the internal limits of the PI-controller capped to a maximum/minimum of 1 and -1. The magnitude of the commanded reactive component (i_d*) is used to determine the maximum of i_q*, thus obeying (9.7).
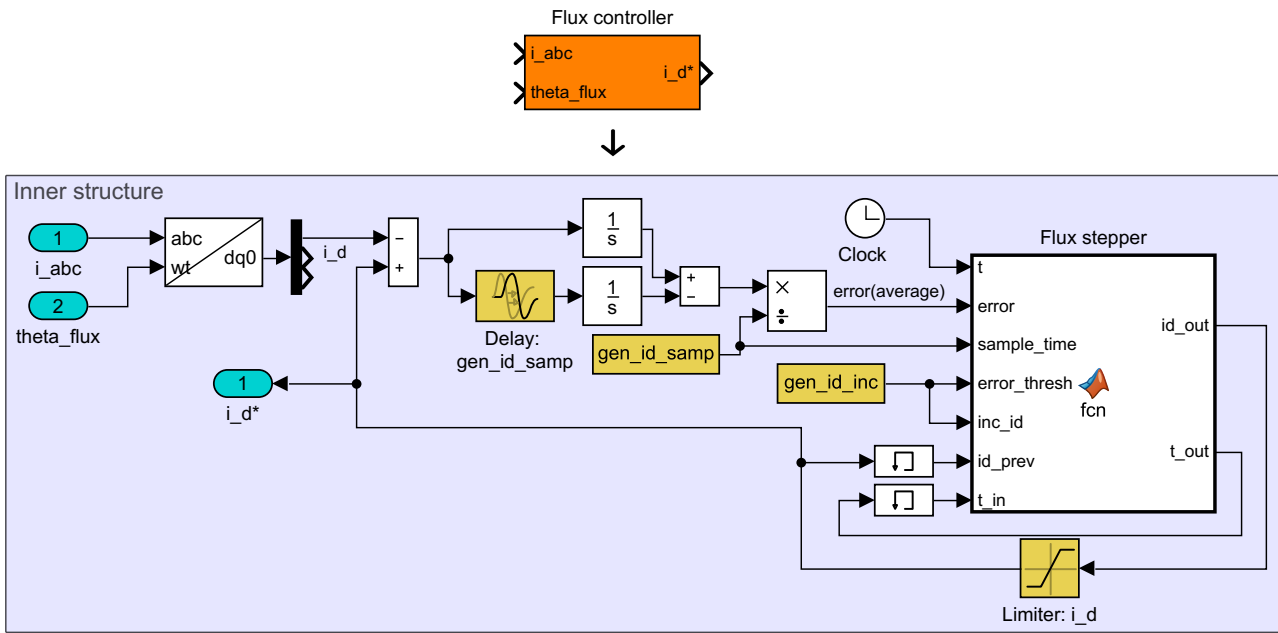
10.3.3 Flux controller

Figure 10.9: Flux controller block

Figure 10.8 shows the structure of the flux controller. The implications of current-constraints (Section 9.3.5) demonstrates that field-weakening (reduction of i_d^s) is required for higher speeds. Assuming a low value of σ, the active reference (i_q*) should not be a problem to achieve if the reactive reference (i_d*) is properly reduced. To mitigate the need of machine parameters to design the flux-controller, an increase/decrease approach is implemented.

The stator-currents and estimate of rotor-flux position are taken as input and Park-transformed to obtain an estimate of the actual d-current component. This estimate is compared to the commanded value (i_d*), and the error is fed into two integrators to provide a moving average for the error of length gen_id_samp. The error is then checked periodically (at intervals of gen_id_samp) by the MATLAB-function block, and if it's below a certain threshold (error_thresh), i_d* is increased by inc_id. If the error is above the threshold, i_d* is reduced by inc_id. The output limiter has an upper limit of $i_d^*[\max] = I_N^G = \text{gen\_i\_max}/\sqrt{2}$, which corresponds to the maximum achievable torque.

This increase/decrease-approach will effectively try to find the highest value of i_d* that can be maintained, and adapt when conditions change. Because the change of rotor-flux is limited by the rotor time-constant, (9.5), trying to maintain i_d* at the highest possible value gives the controller a higher capability to quickly produce high torque, and thus a faster response for sudden changes in the load. The initial value of i_d* is set to $i_d^*[\max]$ in the memory-block corresponding to id_prev.

MATLAB-Function: Flux stepper

```
1  function [id_out, t_out] = fcn(t, error,  sample_time, error_thresh, inc_id, id_prev, t_in)
2
3  id_out=id_prev;
4  t_out=t_in;
5
6  if ((t-t_out)>0)
7      t_out=t_in+sample_time;
8
9      if(error<error_thresh)
10          id_out=id_out+inc_id;
11      else
12          id_out=id_out-inc_id;
```

```
13        end
14    end
```
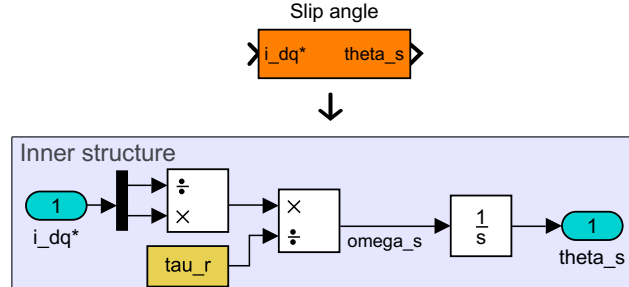
10.3.4 Slip angle

Figure 10.10: Slip angle block

Figure 10.8 shows the structure of the slip angle block. With the commanded magnitudes of i_q* and i_d*, it uses the rotor time-constant (τ_r) to employ (9.11).

10.3.5 Parameter list

Name	Features in	Description
f_sw_foc [Hz]	Current hysteresis	Switching frequency (Section 6.6.2)
v_DC_ref [V]	Torque controller	DC-link voltage reference
nPolePairs [-]	Indirect FOC	Number of pole-pairs
gen_i_max [A]	Torque controller	Rated generator peak current ($I_N^G \cdot \sqrt{2}$)
tau_r [-]	Slip angle	Rotor time constant (τ_r)
gen_iq_upper_lim = 1	Torque PI-controller	Upper limit for integrator and output
gen_iq_lower_lim = -1	Torque PI-controller	Upper limit for integrator and output
gen_id_upper_lim $= (gen\_i\_max)/\sqrt{2}$	Flux controller	Upper limit for output

Table 10.3: Fixed parameters for FOC

Name	Features in	Description
hyst_lim [A]	Current hysteresis	Band gap (H_B) (Section 6.6.2)
gen_iq_thresh [V]	Torque PI-controller	Threshold (integral error)
gen_iq_Kp [-]	Torque PI-controller	Proportional gain
gen_iq_Ki [-]	Torque PI-controller	Integral gain
gen_id_lower_lim [A]	Flux controller	Lower limit for output
gen_id_inc [A]	Flux controller	Step-change and error threshold
gen_id_samp [s]	Flux controller	Sample-time and period for moving average

Table 10.4: Tuneable parameters for FOC
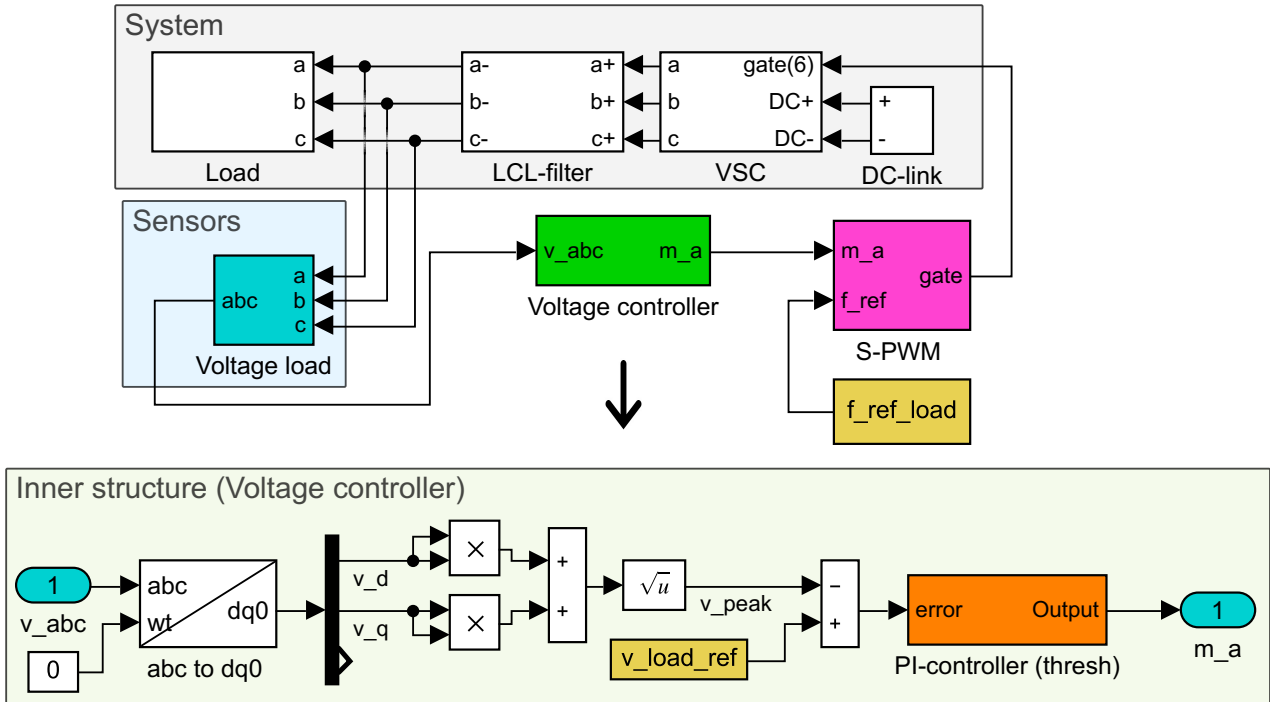
10.4 Voltage controller (load)

10.4.1 Overview

Figure 10.11: Voltage controller overview

Inputs (3)	Outputs (2) [S-PWM]
Stator voltages, v_{abc} [V]	Amplitude modulation, m_a [-]
	Frequency reference, f_{ref} [Hz]

Figure 10.11 shows an overview of the measurements and outputs of the proposed load voltage controller. The gate-signals are realised by the S-PWM-method. The SV-PWM-method could also have been used, but S-PWM was favoured due to simpler implementation, in addition to the considerations of lower filter components (Section 6.4).

The core purpose of this controller is to maintain the load voltage magnitude at a reference level. The measured load phase-voltages (could also be line-line voltage) are fed into a static Park-transformation. With a properly designed filter, the distortions of the load-voltage should be sufficiently low, and thus suitable for providing an instantaneous measurement of the peak-value. The peak-value is compared to the reference (v_load_ref), and the error is fed into the threshold-PI block (Figure 10.1) to create a proper amplitude modulation (m_a). The output is capped to minimum of 0 and maximum of 1 (linear S-PWM operation). The frequency reference is fixed at f_ref_load.

10.4.2 Parameter list

Name	Features in	Description
f_sw_vl [Hz]	S-PWM	Switching frequency (Section 6.1.4)
v_DC_ref [V]	Voltage controller	DC-link voltage reference
f_ref_load [Hz]	S-PWM	Rated load voltage frequency (f_N^L)
v_load_ref [V]	Voltage controller	Rated load phase voltage peak ($V_N^L \cdot \sqrt{2}$)
load_ma_upper_lim = 1	Voltage PI-controller	Upper limit for integrator and output
load_ma_lower_lim = 0	Voltage PI-controller	Lower limit for integrator and output

Table 10.5: Fixed parameters for load voltage controller

Name	Features in	Description
load_ma_thresh [V]	Voltage PI-controller	Threshold (integral error)
load_ma_Kp [-]	Voltage PI-controller	Proportional gain
load_ma_Ki [-]	Voltage PI-controller	Integral gain

Table 10.6: Tuneable parameters for load voltage controller

11 Proposed design procedure

This chapter will introduce a proposed design-procedure, that takes certain input-parameters to fully determine the whole configuration of a isolated power system, ranging from scaling of system components, to the turnings of the VSC-controllers.

The reasoning behind each step/turning is based on a good mix of theoretical analysis, tests, intuition and trial and error. The performance of this procedure (and control-systems) will be investigated with the simulation-study in the next chapter.

11.1 Component ratings

Step 1: Generator power
The starting point is the rated active power of the load (P_N^L). The active power of the induction generator (P_N^G) must be capable to meet this demand and cover the losses in the system (lines, VSCs, LCL-filter, etc.). The losses are accounted through a total efficiency coefficient (η_{tot}).

$$P_N^G = \frac{P_N^L}{\eta_{tot}} \tag{11.1}$$

If the prime-mover is expected to operate at a mechanical speed, $\omega_m(\min)$, that is lower than the rated mechanical speed of the generator (ω_m^G), some "over-rating" is required. The current-limits of the induction generator defines its maximum torque, which must fit the desired minimum speed (11.2). With this determined, we find the required machine rating by (11.3).

$$\frac{\frac{P_N^L}{\eta_{tot}}}{\omega_m(\min)} = T_N^G \tag{11.2}$$

$$T_N^G \cdot \omega_m^G = P_N^G \tag{11.3}$$

Step 2: Switching frequency
Ideally, the switching frequency should be as large as possible to best synthesise the desired output wave-forms. Its therefore suggested to pick $m_f > 100$ for the S-PWM-based methods. As discussed in Chapter 7, there is a trade-off between switching-losses and filter-components.

For the current-hysteresis controller (FOC), it's suggested to pick $m_f > 500$.

$$f_{sw} = f_{ref} \cdot m_f \tag{11.4}$$

Step 3: DC-link voltage reference
Next up is the DC-link voltage (V_{DC}). First we consider the generator, which is assumed to be operated in proximity to its rated speed. The rated phase voltage (V_N^G [rms]) is divided by the capability-coefficient ($\bar{v}_m$), as derived in the RMS/DC-model (Section 6.5). Though the proposed FOC-controller is based on a current-hysteresis gate-signal generator (not S-PWM), the RMS/DC-model is still assumed to provide a reasonable set-point for V_{DC}^G.

$$V_{DC}^G = \frac{V_N^G}{\bar{v}_m} \tag{11.5}$$

Then, consider the load-voltage. The LCL-filter will introduce a voltage drop not accounted for in the RMS/DC-model. As a starting point, we apply the RMS/DC-model and increase the output by the factor μ_s (for instance 10%), obtaining V_{DC}^L.

$$V_{DC}^L = \frac{V_N^L}{\bar{v}_m} \cdot (1 + \mu_s) \tag{11.6}$$

V_{DC}^L is then used as the DC-link voltage in the LCL-filter design script (Appendix B). The resulting inductances are then used to estimate the voltage drop at the rated frequency (f_N^L). If the the condition in (11.7) is not met, μ_s should be increased and the process is repeated.

$$V_N^L \mu_s > (L_1 + L_2) \cdot (2\pi f_N^L) \cdot (I_N^L) \tag{11.7}$$

Finally, the largest DC-link voltage estimate is chosen, and scaled up by 10% for some additional margins.

$$V_{DC} = \max[\mathrm{V}_{DC}^G, \mathrm{V}_{DC}^L] \cdot 1.1 \tag{11.8}$$

Step 4: LCL-filter
The LCL-filter components, (L_1, L_2, C and R) are chosen as given by the design script when the condition of (11.7) is satisfied (Step 3).

Step 5: DC-link capacitance
The DC-link functions as a buffer between the generator and load side. Whenever there is unbalance in the active power produced (generator) and consumed (load), the DC-link voltage will vary. Larger capacitance will provide better resilience, but also make the system cost more.

Based on simulation-tests and the ratings of a similar converter [38], the DC-link is dimensioned to hold $H_C = 0.1s$ worth of rated generator active power:

$$C_{DC} = \frac{0.1 \cdot P_N^G}{\frac{1}{2}(V_{DC})^2} \quad [\mathrm{F}] \tag{11.9}$$

Step 6: Battery
The battery is used to provide the initial DC-link voltage required to excite the IM to further build up voltage. A conventional car-battery able to deliver high current in short periods of time is assumed sufficient, with a voltage-level in the range of approximately 10-50V.

Practical considerations
This study treats the VSCs (with its transistors), DC-link capacitor, lines, gate-drivers, control-system and measurement-sensors as ideal components. Such practical components will have constraints and non-ideal operations in terms of voltage, current, temperature and time-dependence. This must be considered when choosing the actual components to ensure that they can handle what is expected, which is crucial for the performance of the system and expected life-time.

11.2   Control system tuning

This section will show a procedure to setup all control-parameters required in the proposed control-systems, as presented in the corresponding parameter-lists in Chapter 10. Table 11.1 summarises quantities that must be known in advance.

Quantity	Relation	V/f	FOC	Load voltage
Switching frequency [Hz]	f_{sw}=f_sw_(...)	x	x	x
DC-voltage [V]	V_{DC}=v_DC_ref	x	x	
Generator voltage [V]	V_N^G=gen_v_nom	x		
Generator frequency [Hz]	f_N^G=gen_f_nom	x	x	
Pole pairs [-]	n_{pp}=nPolePairs	x	x	
Rated slip-speed [Hz]	$|\omega_m^G \cdot n_{pp} - f_N^G|$=gen_ss_nom	x		
Generator current [A]	$I_N^G \cdot \sqrt{2}$=gen_i_max	x	x	
Rotor time-constant [-]	$\tau_r = \frac{L_{lm}+L_m}{r_r}$=tau_r		x	
Load voltage [V]	V_N^L=v_load_ref			x
Load frequency [Hz]	f_N^L=f_ref_load			x
S-PWM capability-coefficient [-]	$\bar{v}_m$=norm_rms_max	x		
S-PWM ma-coefficient [-]	μ_{ma}=ma_coeff	x		

Table 11.1: Required parameters for control-systems

The proposed control-systems are packed with functions imposing if/else-conditions and saturation. The control-systems thereby exhibit a non-linear behaviour. The system at hand is also quite complex with the gate-signal generators, VSCs, filter and load/generator. Obtaining a properly accurate transfer function of the system response can thus become quite comprehensive. Many of the tuneable parameters are related to proportional (K_p) and integral (K_i) gains, in interaction with upper/lower saturation. The following settings are thereby based on a "rule-of-thumb"-principle. Speed control of a car will be used as an illustrative example:

We define the most positive control output (upper_lim = 1), as the accelerator at max, and the most negative output (lower_lim = -1) as full breaking power. Then, we define a speed-error (thresh = 30 km/h) as justifiable for giving full output. The proportional gain (11.10) is then set to reflect these considerations.

$$K_p = \frac{\text{upper\_lim}}{\text{thresh}} = \frac{1}{30} \tag{11.10}$$

The integrator builds up value over time. We figure that a constant speed-error of 10 km/h (thresh/3) lasting for a period of t = 5 seconds is justifiable for letting the integrator saturate. The integral gain is then set by (11.11).

$$K_i = \frac{\text{upper\_lim}}{\text{thresh/3} \cdot \text{t}} = \frac{1}{5 \cdot 10} \tag{11.11}$$

These steps for tuning allows for a quick determination of decent starting points. It does however require some knowledge about how the system responds to the output, and fine-tuning might be needed for further improvement. Trying to create a generic tuning-procedure that fits various systems enlarges the complexity. The following proposed settings relies on scaling of rated quantities to create thresholds, and periods of frequencies to choose integrator-saturation times.

11.2.1 V/f controller (generator)

Parameter	Setting	Comment
gen_ss_upper_lim	(gen_ss_nom)·2	2x rated slip speed
gen_ss_lower_lim	-(gen_ss_nom)·2	2x rated slip speed
gen_ss_thresh	(v_DC_ref)·0.1	10% DC-voltage
gen_ss_Kp	$-\frac{(\text{gen\_ss\_upper\_lim})}{(\text{gen\_ss\_thresh})}$	Saturate at gen_ss_thresh
gen_ss_Ki	$-\frac{(\text{gen\_ss\_upper\_lim})}{(\text{gen\_ss\_thresh})\cdot\frac{1}{(\text{gen\_f\_nom})}\cdot 2}$	Saturate for 2x periods of frequency
gen_curr_Ki	$\frac{(\text{gen\_curr\_lower\_lim})}{\frac{1}{(\text{gen\_f\_nom})}\cdot 10}$	Saturate for 10x periods of frequency
gen_ma_Ki_upper_lim	$\frac{(\text{v\_DC\_ref})\cdot(\text{norm\_rms\_max})}{(\text{gen\_v\_nom})}$	Shifting V/f-coefficient to upper RMS-capability of S-PWM
gen_ma_Ki_pos	$\frac{(\text{gen\_ma\_Ki\_upper\_lim})}{(\text{gen\_ss\_thresh})\cdot\frac{1}{(\text{gen\_f\_nom})}\cdot 100}$	Saturate for 100x periods of frequency
gen_ma_Ki_neg	(gen_ma_Ki_pos) · 10	10x positive gain

Table 11.2: V/f controller tuning

11.2.2 Indirect FOC (generator)

Parameter	Setting	Comment
hyst_lim	$(\text{gen\_i\_max})\cdot 10 \cdot \frac{(\text{gen\_f\_nom})}{(\text{f\_sw\_foc})}$	1% rated current for m_f=1000.
gen_iq_thresh	(v_DC_ref)·0.1	10% DC-voltage
gen_iq_Kp	$-\frac{(\text{gen\_iq\_upper\_lim})}{(\text{gen\_iq\_thresh})}$	Saturate at gen_iq_thresh
gen_iq_Ki	$-\frac{(\text{gen\_iq\_upper\_lim})}{(\text{gen\_iq\_thresh})\cdot\frac{1}{(\text{gen\_f\_nom})}\cdot 2}$	Saturate for 2x periods of frequency
gen_id_lower_lim	(gen_i_max)·0.1	10% rated current
gen_id_inc	(gen_i_max)·0.01	1% rated current
gen_id_samp	$\frac{1}{(\text{gen\_f\_nom})\cdot 10}$	1/10 of frequency period

Table 11.3: Indirect FOC tuning

11.2.3 Voltage controller (load)

Name	Features in	Description
load_ma_thresh	(v_load_ref)·0.1	10% load voltage
load_ma_Kp	$\frac{(\text{load\_ma\_upper\_lim})}{(\text{load\_ma\_thresh})}$	Saturate at load_ma_thresh
load_ma_Ki	$\frac{(\text{load\_ma\_upper\_lim})}{(\text{load\_ma\_thresh})\cdot\frac{1}{(\text{f\_ref\_load})}\cdot 2}$	Saturate for 2x periods of frequency

Table 11.4: Voltage controller tuning (load)

12   Simulation study

This chapter will cover the results and analysis of a series of simulations performed in MATLAB-Simulink to test the proposed design procedures (Chapter 11) for the isolated system with its appurtenant controllers. The simulation utilises the models introduced in the previous chapters, which are are connected together as shown in Appendix C.

Appendix A contains parameters for four different induction machines in the range of 4-16 kW generated power. These are used as a basis to create four different systems, thus giving a range of configurations that can be compared and used to evaluate how well the design-procedures are made. The component-ratings and settings for the four systems will be presented. Following this are tests that will investigate different aspects of the system, namely the build-up of voltage (Test 1), response to load-change (Test 2), the FOC-method's sensitivity to the rotor time-constant (Test 3), how the systems performs for rotor-speed variations (Test 4) and the LCL-filter performance (Test 5).

12.1   Configuration

12.1.1   Loads

An assumed efficiency of $\eta_{tot} = 0.9$ is used to determine the rated active power of the loads with a basis in the rated electric power (P_N^G) of the four generators. The nominal prime-mover speed is assumed equal the rated mechanical speed of the generator.

To include the possibility to have some additional reactive power in the loads, the current-rating of the loads are set as given by (12.1), i.e. allowing to include $|Q| = P_N^L$ when supplying full active power. The loads are for all cases, defined as a system of phase voltage V_N^L=230V [rms], at a frequency of 50Hz, i.e. the standard of the Norwegian residental grid.

$$I_N^L = \frac{\sqrt{2} \cdot P_N^L}{V_N^L \cdot 3} \tag{12.1}$$

12.1.2   Gate-signal generator, VSCs and battery

For the V/f-controller (generator) and Voltage controller (load), the S-PWM(THI)-method (third harmonic reference waves) is chosen due to its better utilisation of DC-link voltage (Section 6.3 and 6.5). This gives $\bar{v}_m = 0.0460$ and $\mu_{ma} = 4.714$. All studied machines are rated for an electrical frequency of 50/60Hz, and the switching frequency (f_{sw}) is set to a fixed 10kHz for both the V/f and load-voltage controller. This corresponds to m_f of 200/166.66 at rated frequency.

For the current-hysteresis controller, the switching frequency is set to a fixed 50kHz.

The 2L-3ph VSCs are assumed ideal, thus defining $V_{fS} = V_{fD} = R_S = R_D = 0$. The battery is modelled with a fixed resistance of $R_{bat} = 0.01\Omega$.

12.1.3   Resulting parameters from design-procedure

Applying the procedures as given in Chapter 11, we end up with the following component configurations and parameters as given in the following tables. The four different systems are indicated by their corresponding generators (#M1, #M2, #M3 and #M4).

Parameter	Unit	#M1	#M2	#M3	#M4
P_N^L	[kW]	3.58	6.4	9.12	13.92
I_N^L	[A]	7.34	13.12	18.69	28.53
V_{DC}	[V]	605	635	600	600
μ_s	[V]	0.1	0.1	0.092	0.092
C_{DC}	[mF]	2.17	3.53	5.63	8.6

Table 12.1: Load and DC-link parameters

Parameter	Unit	#M1	#M2	#M3	#M4
L_1	[mH]	8.8223	4.935	3.438	2.2524
L_2	[mH]	0.3011	0.1683	0.1182	0.0774
C	[mF]	0.0051	0.0091	0.0129	0.0197
R	[Ω]	2.5242	1.412	0.9908	0.6491

Table 12.2: LCL-filter parameters

Parameter	#M1	#M2	#M3	#M4
gen_ss_upper_lim	3.7	1.92	4	3.1596
gen_ss_lower_lim	-3.7	-1.92	-4	-3.1596
gen_ss_thresh	60.5	63.5	60	60
gen_ss_Kp	-0.0612	-0.0302	-0.0667	-0.0527
gen_ss_Ki	-1.5289	-0.9071	-2	-1.5798
gen_curr_Ki	-5	-6	-6	-6
gen_ma_Ki_upper_lim	1.2066	1.1013	2.1758	2.1758
gen_ma_Ki_pos	0.01	0.0104	0.0218	0.0218
gen_ma_Ki_neg	0.0997	0.1041	0.2176	0.2176

Table 12.3: V/f controller tuning (generator)

Parameter	#M1	#M2	#M3	#M4
hyst_lim	0.1077	0.1811	0.5107	0.8433
gen_iq_thresh	60.5	63.5	60	60
gen_iq_Kp	-0.0165	-0.0157	-0.0167	-0.0167
gen_iq_Ki	-0.4132	-0.4724	-0.5	-0.5
gen_id_lower_lim	1.0767	1.5088	4.2559	7.0274
gen_id_inc	0.1077	0.1509	0.4256	0.7027
gen_id_samp	0.002	0.0017	0.0017	0.0017

Table 12.4: Indirect FOC tuning (generator)

Parameter	#M1	#M2	#M3	#M4
load_ma_thresh	32.5269	32.5269	32.5269	32.5269
load_ma_Kp	0.0307	0.0307	0.0307	0.0307
load_ma_Ki	0.7686	0.7686	0.7686	0.7686

Table 12.5: Voltage controller tuning (load)

12.1.4   Simulink solver

Simulations are performed at fixed discrete time steps of $\Delta T_{samp} = 5 \cdot 10^{-6}$ s. This corresponds to 20 samples per 10kHz switching period (S-PWM). With a triangle carrier wave, we thus have an effective resolution of 0%:10%:100%, i.e. ten steps of applicable duty-cycle outputs. Ideally, this should be larger, but a feasible computational time is also favoured. For the hysteresis-controller (FOC), we have 4 samples per 50kHz switching period.

12.2   Test 1: Magnetisation and DC-link charge-up

12.2.1   Purpose and setup

These tests are performed to study the elapse of the IM-magnetisation, and the corresponding build-up of voltage in the DC-link. The load-side is not included in the tests. The tests are divided into two parts.

The first part is performed with a fixed rated mechanical speed (ω_m^G), where the battery voltage and initial DC-link voltage ($V_{DC0} = V_{bat}$) is varied for two levels (10V and 40V).

The second part is performed for three levels of fixed mechanical speed ($\omega_m^G \cdot 0.5$, ω_m^G and $\omega_m^G \cdot 1.5$), where the battery voltage and initial DC-link voltage are set to 40V.

With four system configurations (machines) and two controller methods (V/f and FOC), a total of 32 simulations are performed.

12.2.2   Plots of #M1 at different speeds

Given below are plots (Figure 12.1-12.6) showing the DC-link voltage, stator currents, torque and controller-outputs for the two controller-methods (V/f and FOC), for the three levels of mechanical speed with $V_{DC0} = V_{bat} = 40V$. These are meant as a reference to visualise the elapses and illustrate differences between the operation of the two control-systems. A more detailed comparison will be given in the next sections by utilisation performance-indicators. From the plots, we can observe how the frequency of the stator-currents increase in relations to the mechanical speeds. Though not clearly visible due to the different scaling of the axes, the FOC-method tends to have a higher torque-ripple than the V/f-method.

For the V/f-controller, we can see how the current-limiter handles excessive currents by scaling down the commanded slip-speed. Because we are in generator-operation, this is observed by the slight increase of f_{ref}. When the DC-link voltage exceeds the reference, the slip-speed controller responds by putting the machine in motor-operation, resulting in a positive shaft torque. The oscillating response of f_{ref} toward a steady-state slip-speed illustrates the behaviour of a typical PI-controller. In terms of amplitude modulation (m_a), we see that the steady-state value increases for higher speeds, as intended by the voltage-controller. In Figure 12.1, notice how m_a abruptly is decreased when the DC-link voltage builds up. This results in a temporary loss of torque.

For the FOC-method, the "actual" current components represented (blue and red) are found by transforming the stator-currents with the estimated rotor-flux angle. Because we have a time-delay for the response of the rotor-flux, and the fact that the system is clearly not at steady-state, they are not accurately representing the current-components since the actual position of the rotor-flux is not known. However, once the references

coincides with the measurements, we can observe that the stator-currents transforms into a less distorted sinusoidal shape. It's pleasing to see that the controller can maintain a generating torque during this transition. We can also observe how i_q* changes in relation to the magnitude of i_d*, and that the achievable magnitude of i_d* is reduced for higher speeds, as illustrated by the voltage-constraints in Section 9.3.5. i_d* is constantly changing in steady-state operation, as a result of the increase/decrease methodology of the flux-controller.
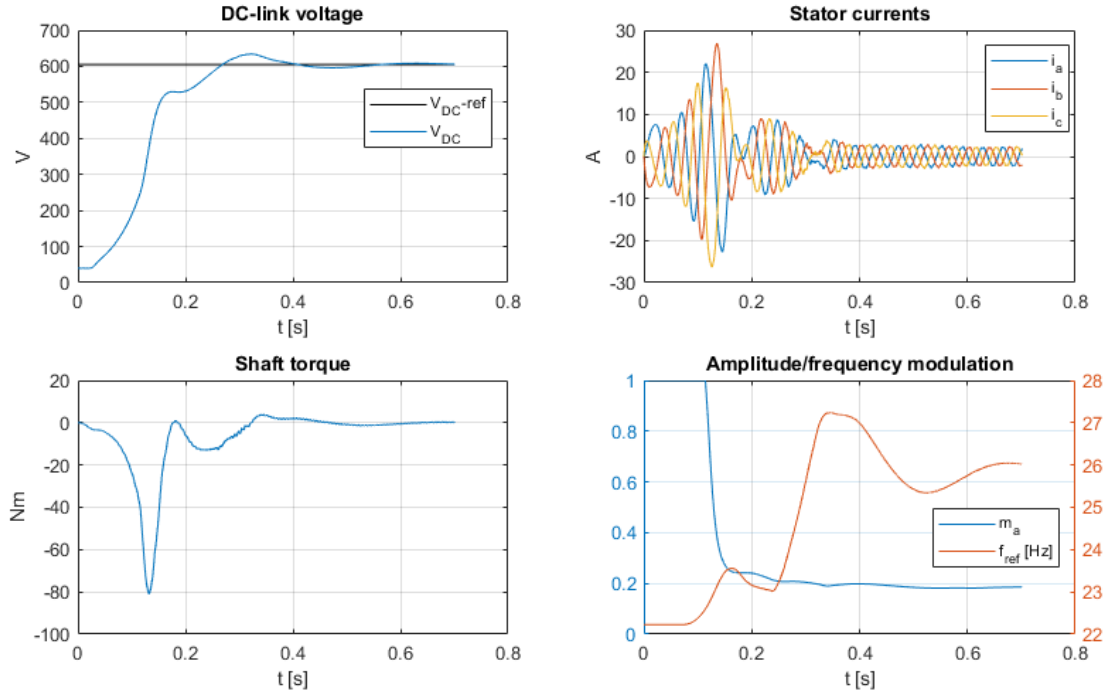
Figure 12.1: #M1, $[\omega_m^G \cdot 0.5]$, (V/f)
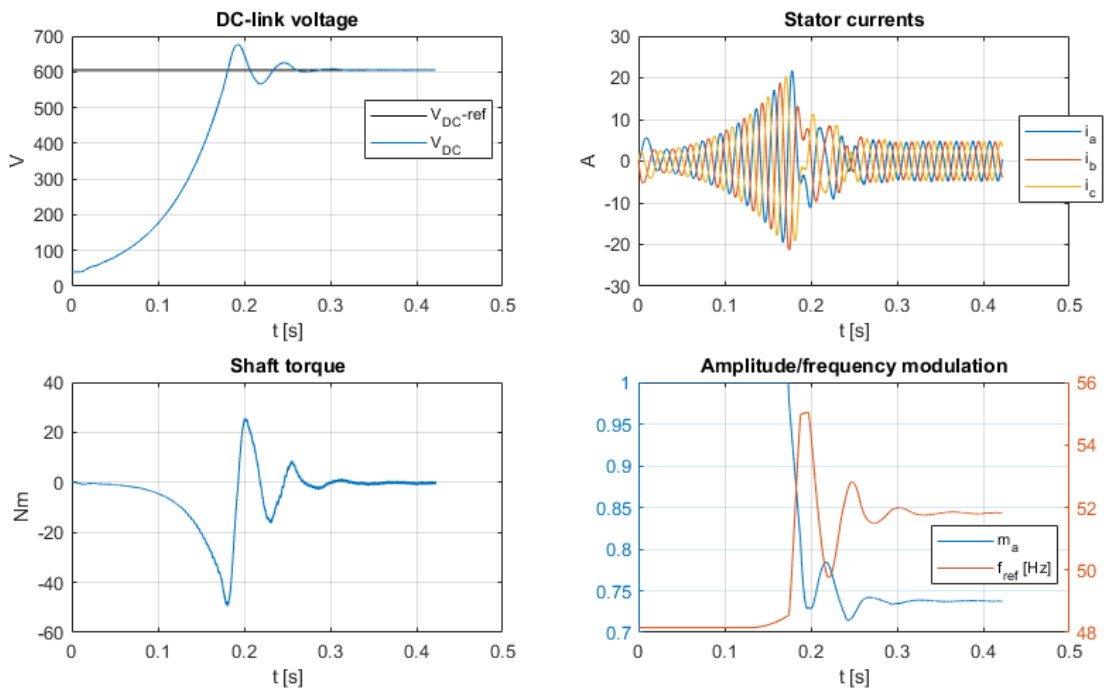
Figure 12.2: #M1, $[\omega_m^G]$, (V/f)
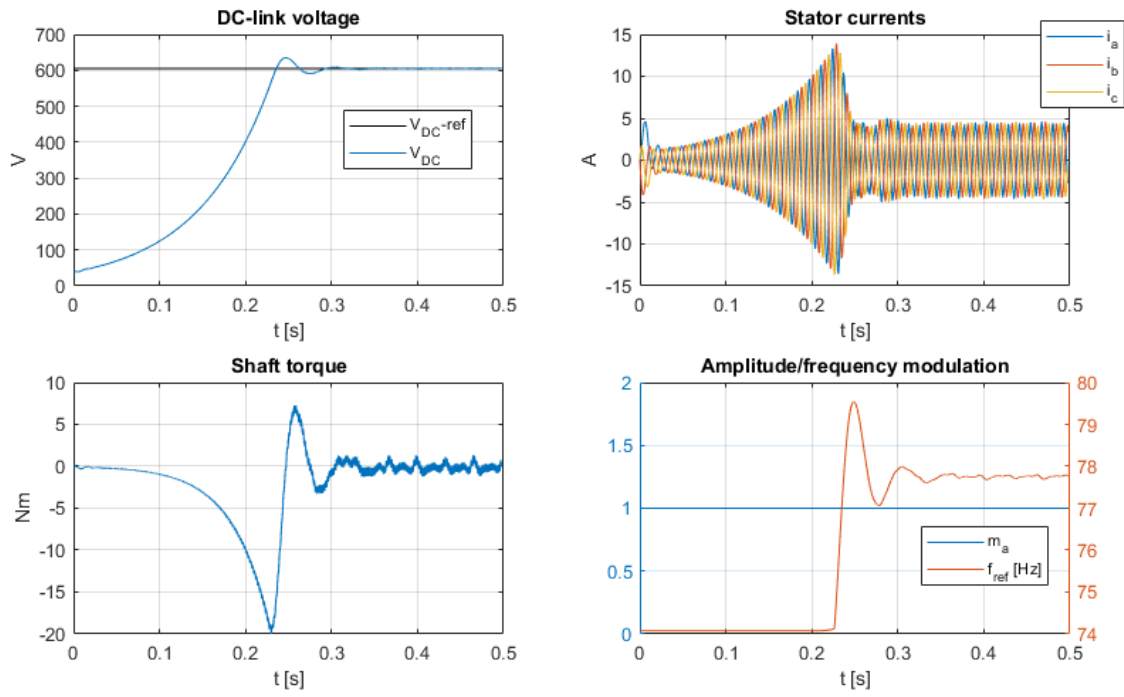
Figure 12.3: #M1, $[\omega_m^G \cdot 1.5]$, (V/f)
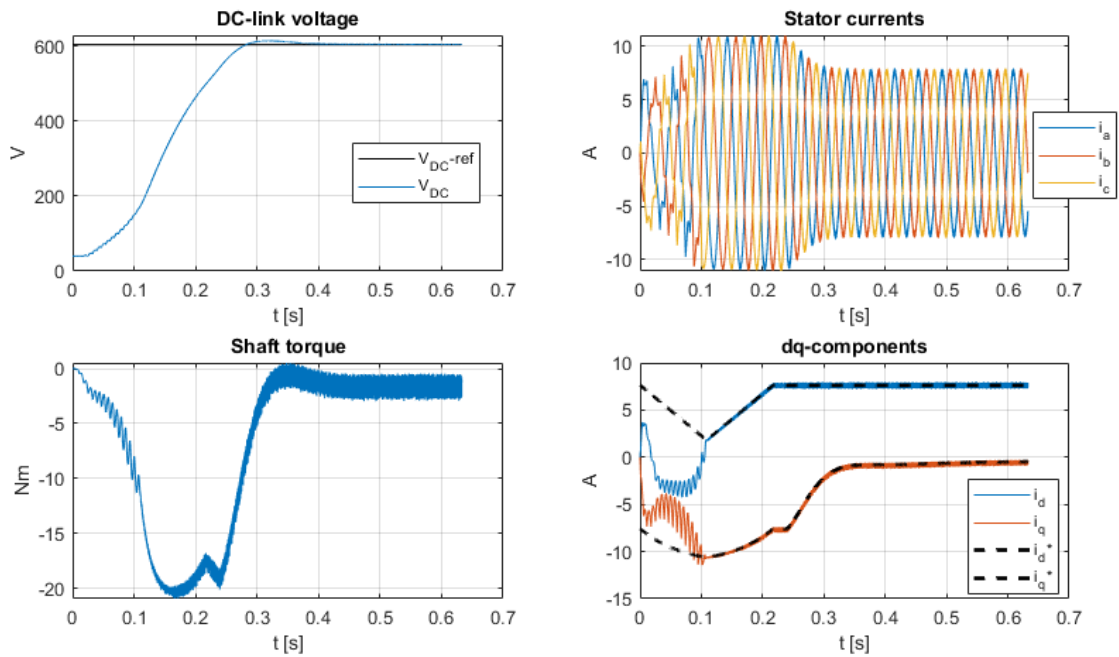
Figure 12.4: #M1, $[\omega_m^G \cdot 0.5]$, (FOC)
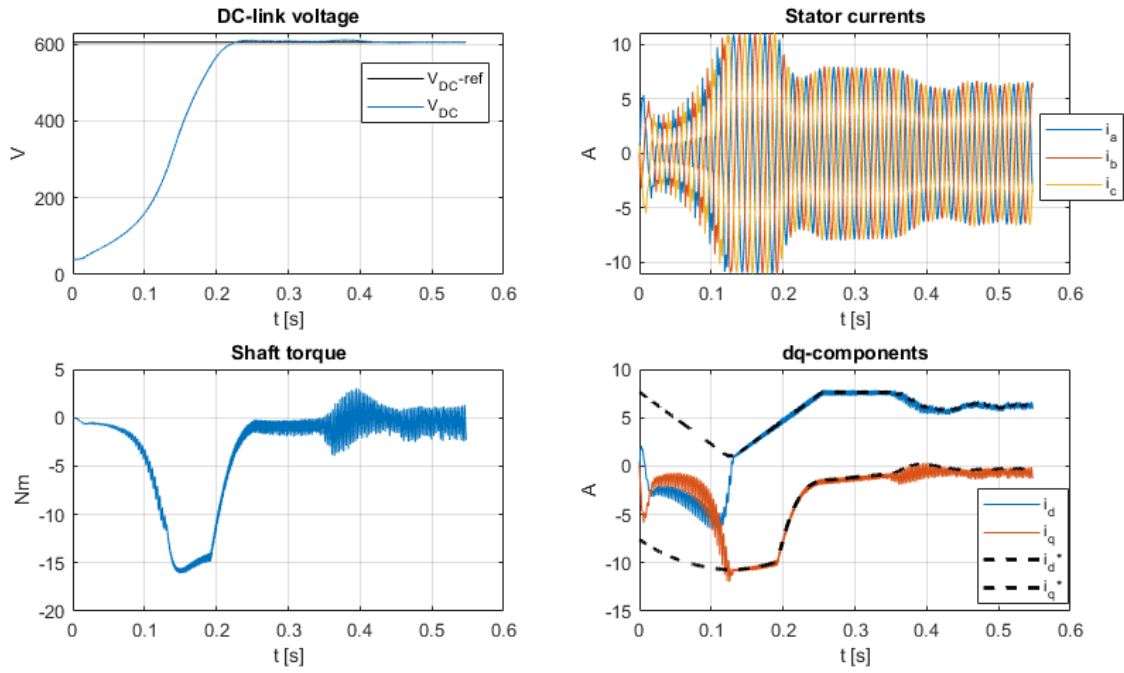
Figure 12.5: #M1, $[\omega_m^G]$, (FOC)
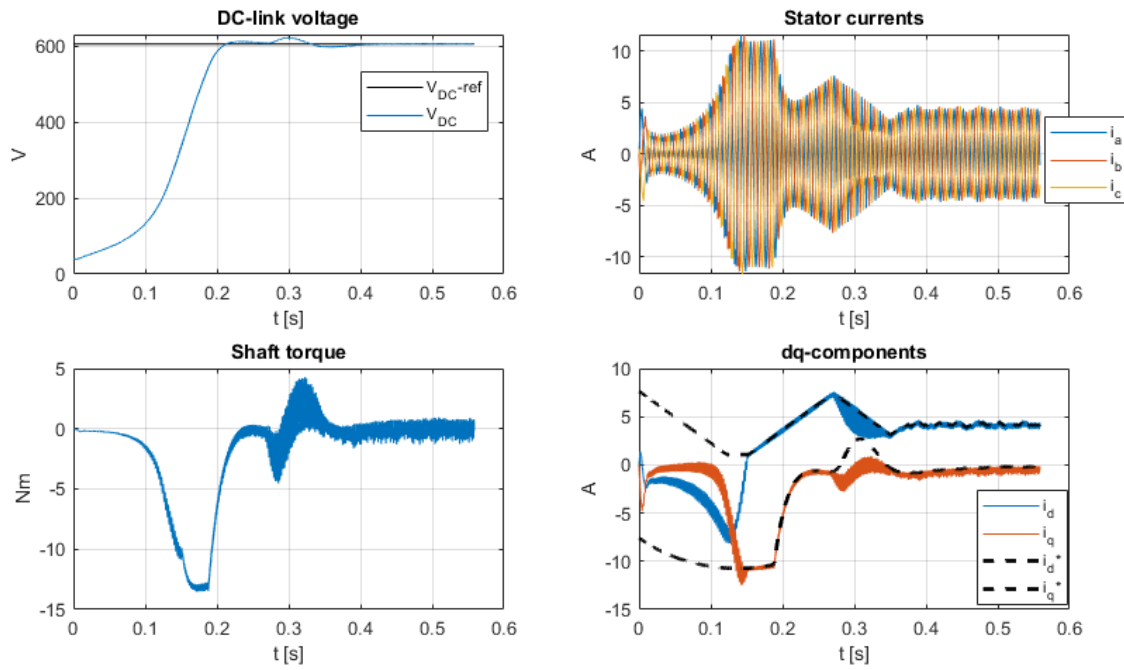
Figure 12.6: #M1, $[\omega_m^G \cdot 1.5]$, (FOC)

12.2.3 Performance indicators
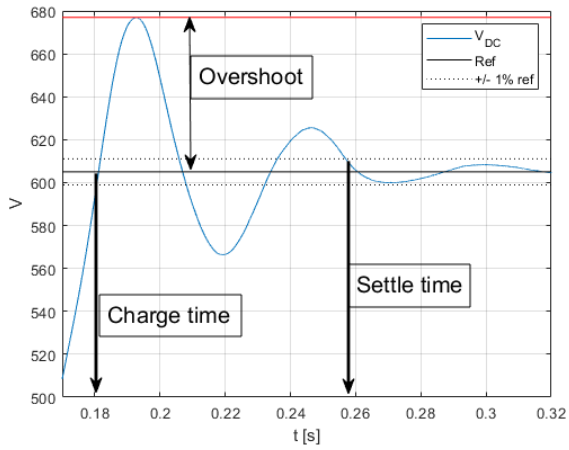
Figure 12.7: DC-voltage indicators
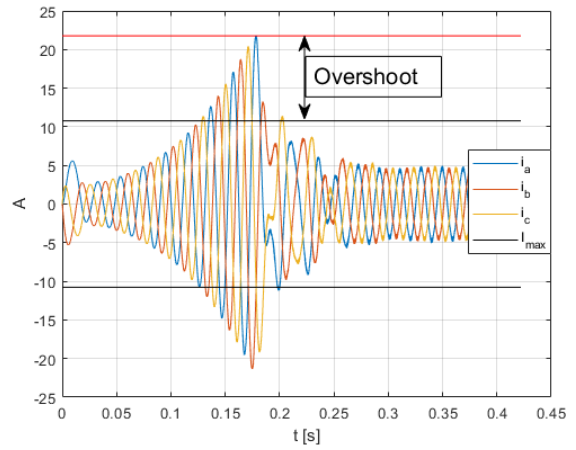
Figure 12.8: Overshoot generator current
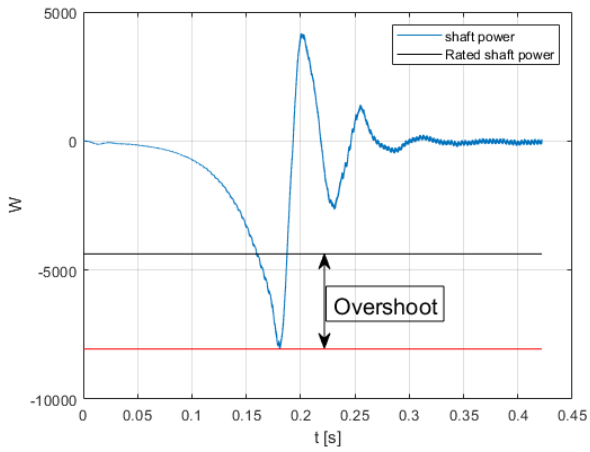
Figure 12.9: Overshoot shaft-power
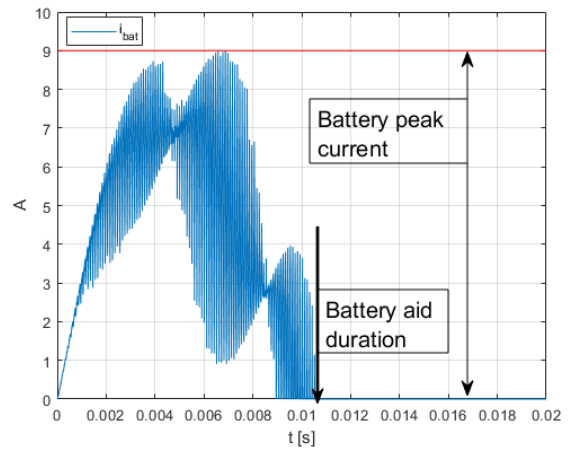
Figure 12.10: Battery indicators

The following two sections will make use of the following performance-indicators to analyse the test-results:

Indicator	Description
Charge-up time	Time required for the DC-link voltage to reach its reference. Figure 12.7
Settle-time	How long it takes for the deviation to settle withing 1% of the reference. Figure 12.7 - Expressed as (Settle-time minus Charge-up time) in the charts
Overshoot DC-voltage	How far the DC-link voltage exceeds the reference. Figure 12.7 - This overshoot is expressed as a percentage of the reference.
Overshoot generator current	How far the stator currents exceeds the maximum rating ($I_N^G \cdot \sqrt{2}$). Figure 12.8 - This overshoot is expressed as a percentage of ($I_N^G \cdot \sqrt{2}$).
Overshoot shaft power	How far the mechanical shaft power exceeds the rating (P_N^{Gm}). Figure 12.9 - This overshoot is expressed as a percentage of (P_N^{Gm}).
Battery aid duration	How long the battery supplies current to the DC-link Figure 12.10
Battery peak current	The highest amplitude of current delivered from the battery. Figure 12.10
Battery work	The integrated power delivered to the DC-link from the battery through the aid-duration.

12.2.4   Effects of varying battery voltage (initial charge)

The following graphs (Figure 12.11-12.16) gives a visual representation of how the two levels of battery-voltage (10V and 40V) affect the magnetisation-elapse. The mechanical speed is fixed at ω_m^G.

The charge-up time (Figure 12.11) is reduced (for all machines) when increasing the initial voltage from 10V to 40V. This makes sense, due to the fact that less work is required to "fill" the remainder of the capacitor, and a higher initial voltage provides a faster magnetisation of the machine. The FOC-method generally has a longer charge-up time compared to the V/f-method. The cause can be found by inspecting Figure 12.14, where we observe that the V/f-method is able to employ significantly larger overshoots of currents in the generator, giving it higher torque and thus more power.

Looking at the settle-time (Figure 12.12) and voltage-overshoot (Figure 12.13, the V/f-method tends to settle faster, with lower voltage overshoots, when the initial voltage in increased. For the FOC-method, this also applies for the voltage overshoots, but no clear pattern is seen with the settle-time.

The battery was, for all cases, only supplying in the first 9-14ms, where the DC-link afterwards has a higher voltage than the battery and becomes "self-sustained". For both control methods, the work delivered to aid the DC-link (Figure 12.15) and peak-value of current drawn (Figure 12.16) increases with machine power-rating. This trend also applies, for both methods, when the initial DC-link voltage is increased. The DC-link dependency is likely due to the fact that a higher voltage enables more current, and thus more work is delivered before the machine becomes self-sustained. The work delivered is quite low compared to the rated power of the machines.
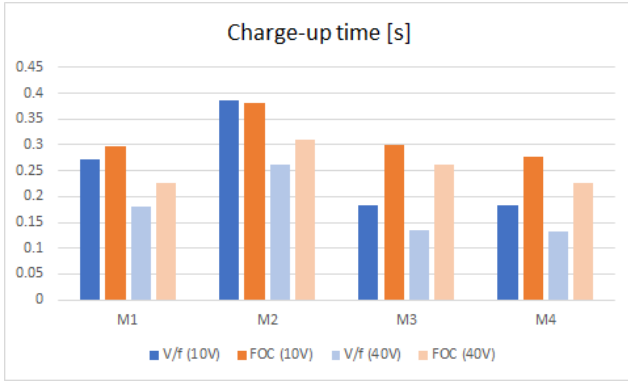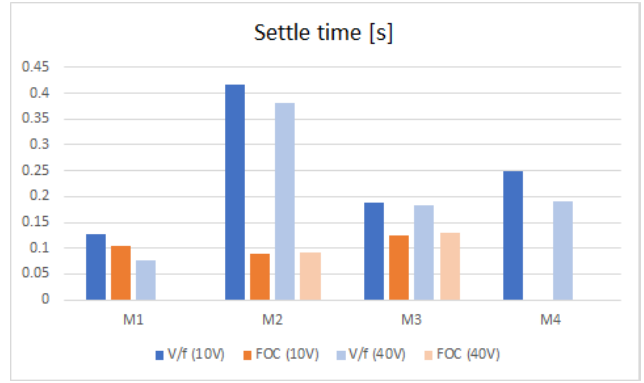
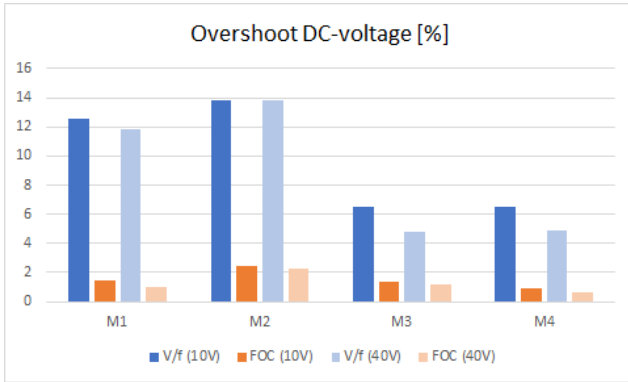Figure 12.11: Charge-up time

Figure 12.12: Settle-time

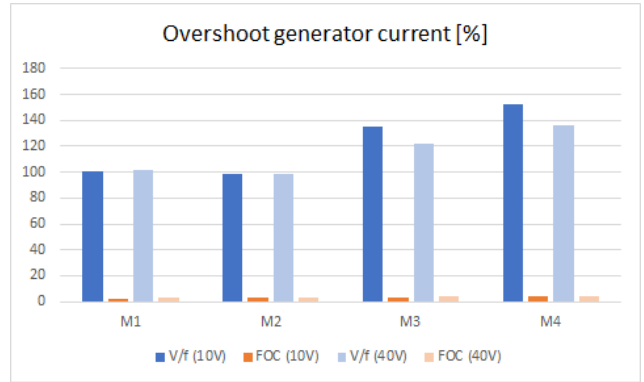Figure 12.13: Overshoot DC-link voltage

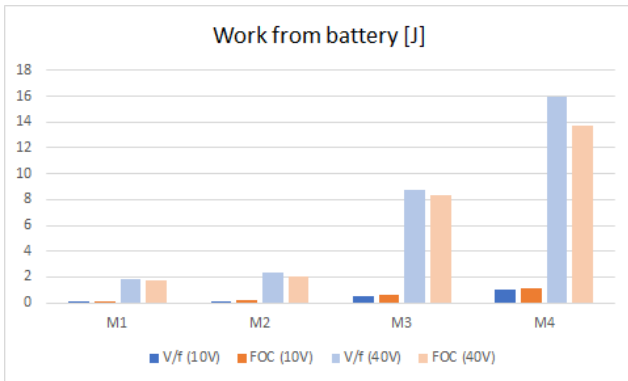
Figure 12.14: Overshot generator current
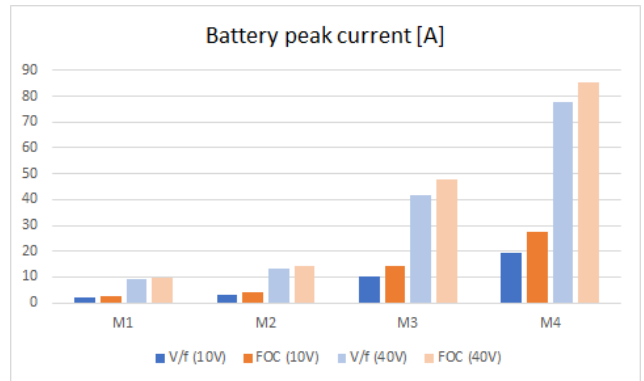

Figure 12.15: Battery work

Figure 12.16: Battery peak current

12.2.5 Effects of varying mechanical speed

The following graphs (Figure 12.17-12.24) gives a visual representation of how the three levels of fixed mechanical speed (x0.5, x1 and x1.5) affects the magnetisation-elapse. The battery-voltage is fixed at 40V.

The charge-up time (Figure 12.17) shows a slightly downwards trend for increasing the speed when the FOC-method is applied. The V/f-method has significantly shorter times at x1 and x1.5 rated speed for #M3 and #M4.

Higher speeds shows shorter settle-times (Figure 12.18) for all machines when the V/f-method is applied. No clear pattern is visible for the FOC-method, but it generally outperforms the V/f-method with its overall lower/zero settle-times. The superiority of the FOC-method is also shown in the DC-voltage overshoot (Figure 12.19), generator current overshoot (Figure 12.20) and shaft power overshoot (Figure 12.21). The V/f-

72

method shows a downward trend in generator current overshoot when increasing the speed, most noticeable for machine #M1 and #M2. The cause could lie in the fact that higher speeds results in higher back-EMFs, thus damping how much excessive current the V/f-method is able to provide in the generator. Note that the overshoots in shaft power are highest for the V/f-method at x1.5 speed for machine #M3 and #M4. This can be linked to the corresponding high values of current overshoot, which gives higher values of peak-torque.

Overall, the FOC-method seems to perform best with the proposed design-procedure and turnings. It should be noted that the generator current and shaft-power exceedings from rated conditions, which the V/f-method generally displays, are temporary, and the steady-state operation would obey the ratings of the generator. The FOC-method is built around references of current and utilises a current-hysteresis controller. This naturally gives it better control of currents. The V/f-method is built on a steady-state model and deals with current indirectly through the slip-speed, with a small integral-gain for the current-limiter function.

Looking at the battery, the patterns are similar for all machines and seemingly independent upon whether the V/f or FOC-method is applied. Lower speed require aid from the battery for a longer durations (Figure 12.22). Similarly, lower speeds results in more work (Figure 12.23) and higher peak currents (Figure 12.24). Two effects could explain this behaviour. Firstly, lower speed gives lower back-EMF, such that a higher current can be drawn from the DC-link. Secondly, at a given torque (which is a function of current for IMs), lower speeds gives lower power, and thus a lower rate of charge back to the DC-link.
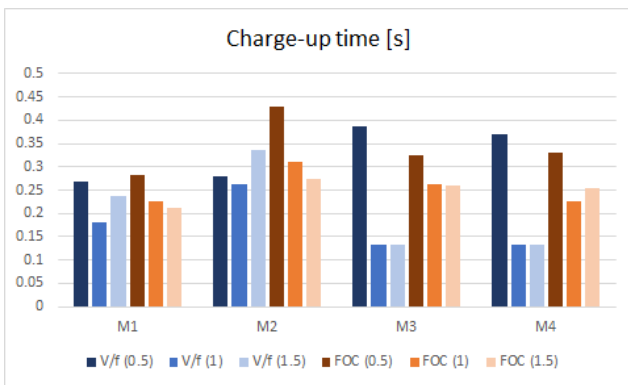

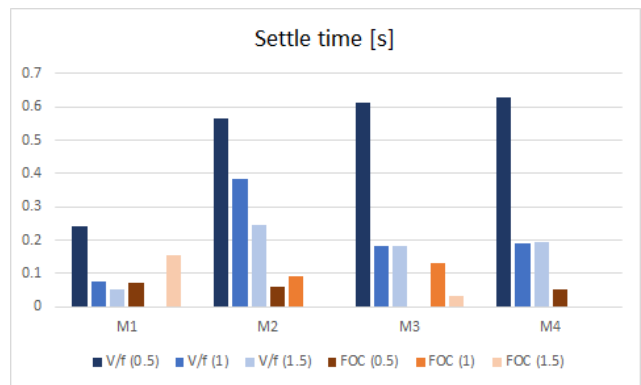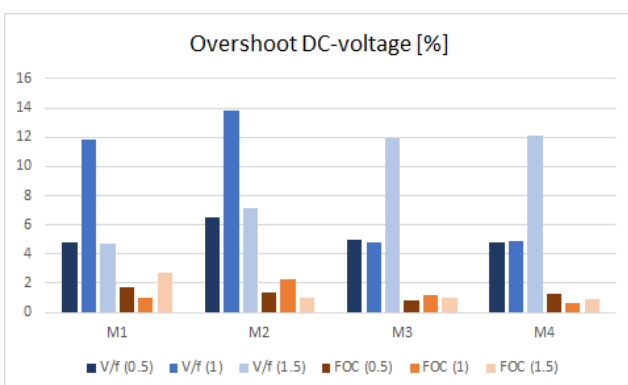Figure 12.17: Charge-up time

Figure 12.18: Settle-time

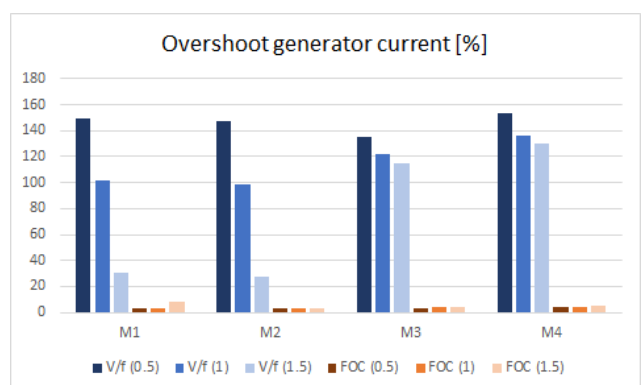Figure 12.19: Overshoot DC-link voltage

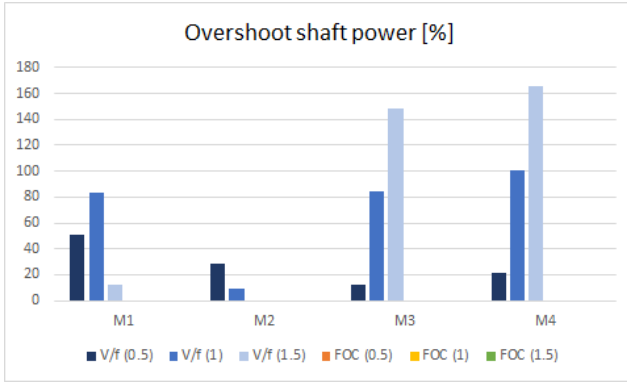Figure 12.20: Overshoot generator current

73

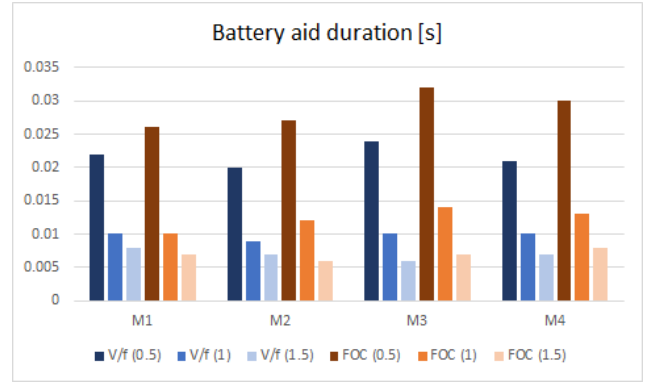Figure 12.21: Overshoot shaft power
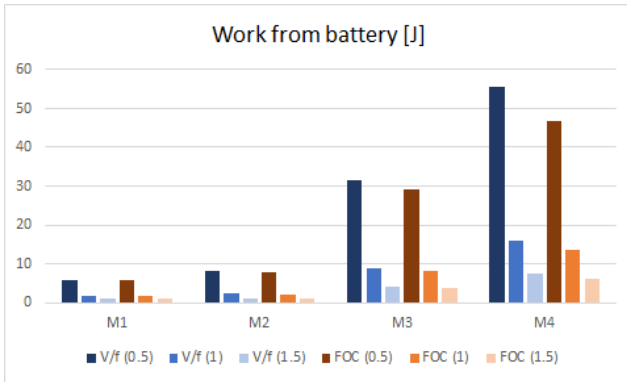

Figure 12.22: Battery aid duration
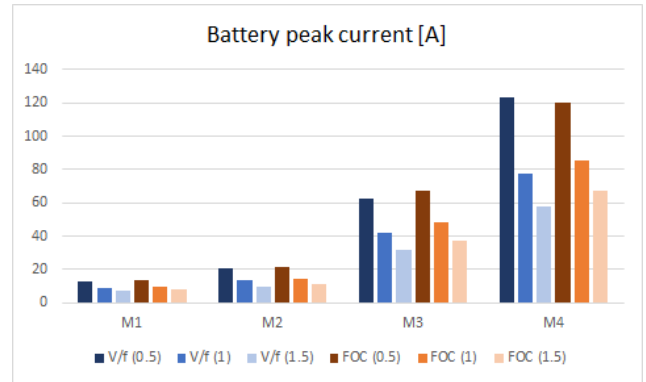

Figure 12.23: Battery work

Figure 12.24: Battery peak current

12.3 Test 2: Step change to full load

12.3.1 Purpose and setup

These tests functions to evaluate the whole systems ability to handle step-change of loads. All simulations are run at a fixed rated mechanical speed (ω_m^G), with a battery and initial DC-link voltage set to 40V. The first 0.5s carry out the magnetisation (i.e. the same as Test 1), where the VSC of the load is disabled. Then, at t=0.5s, the loads are connected in a step corresponding to a purely resisitive load of full active power (P_N^L). The full loads stay connected until t=1s, where they are step-changed down to zero, and the simulation ends at t=1.5s.

With four system configurations (machines), one voltage-controller for the loads and two controllers for the generator (V/f and FOC), a total of 8 simulations are performed.

12.3.2 Results and analysis

Given below are plots (Figure 12.25-12.32), showing the DC-link voltage, stator currents, torque, controller-outputs and RMS+THD of the load voltage. η expresses the average efficiency, defined as full load power divided by the shaft power.

From the results, we see that none of the configurations results in a voltage-collapse, though the V/f-method struggles for #M3 and #M4, where the DC-link voltage drops down to about -150V from its reference, and additionally overshoot with about 100V when the load is disconnected. This in turn also affects the systems ability to maintain the 230V load for a duration of about 0.3-0.4 seconds. For all configuration, we observe a delay from when the load is connected (t=0.5s) until the voltage stabilises at the 230V reference. This is caused by the LCL-filter, which takes some time to "magnetise". Apart from this, the load-voltage seems to be well

maintained within ±1V rms deviations when the DC-link is voltage close to its reference value. The THD (at a fundamental of 50Hz) is generally under 1% with full load, swinging around 2% with no load.

The FOC-method shows the best performance for all machines, with DC-voltage deviations below $\pm$ 40V, and stator-currents staying within the rated limits. The power extracted from the shaft is also quite stable, though with a high-frequent ripple larger than that of the V/f-method.

As observed in the magnetisation-test (Section 12.2), the V/f method tends to overshoot in rated current (and shaft power) during the magnetisation. This overshoot-behaviour is however smaller when the load is connected, seemingly linked to the fact that the amplitude modulation (m_a) is not being drastically reduced from 1 to a lower value in combination with an increase in f_{ref}. #M2 is though an exception, where these control-parameters oscillates quite a lot during the load-change, indicating a poor match between machine and tuning. #M2 is however also the only machine where the machine voltage became the dimensional factor for the DC-link voltage (V_{DC}^G).

Looking at the efficiency (η), the FOC-methods performs best for all configurations. The steady-state current of the V/f-method is however lower during no-loaded conditions due to the fact that it's not, like the FOC-method, trying to maintain the highest possible magnetisation (i_d^s).
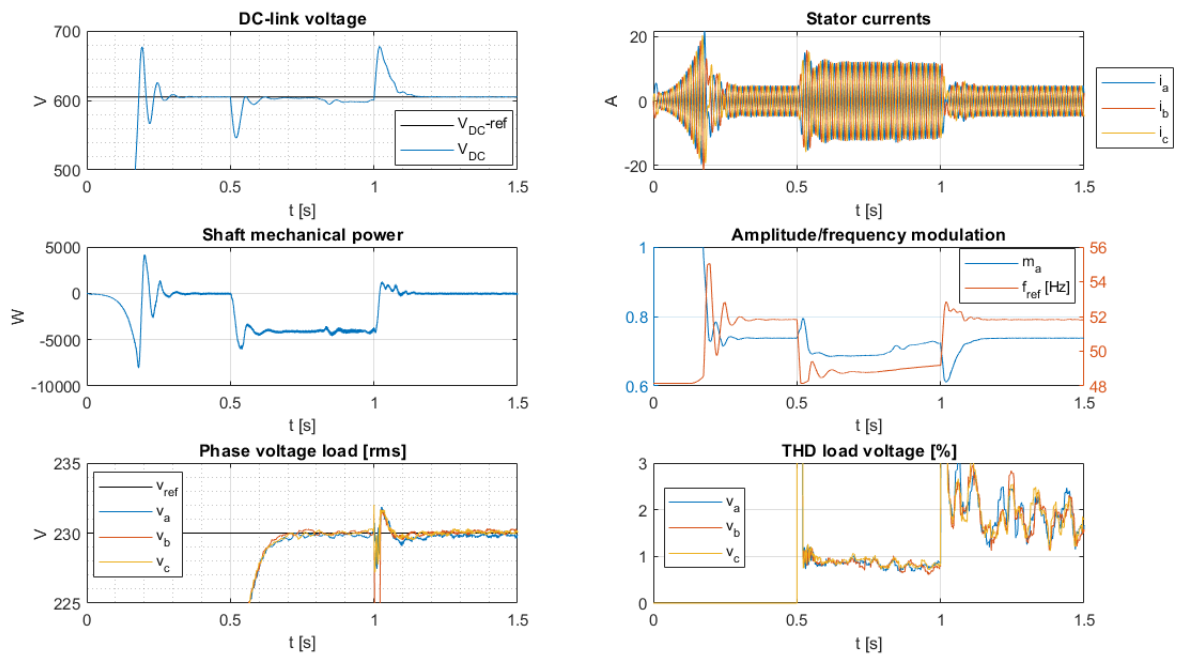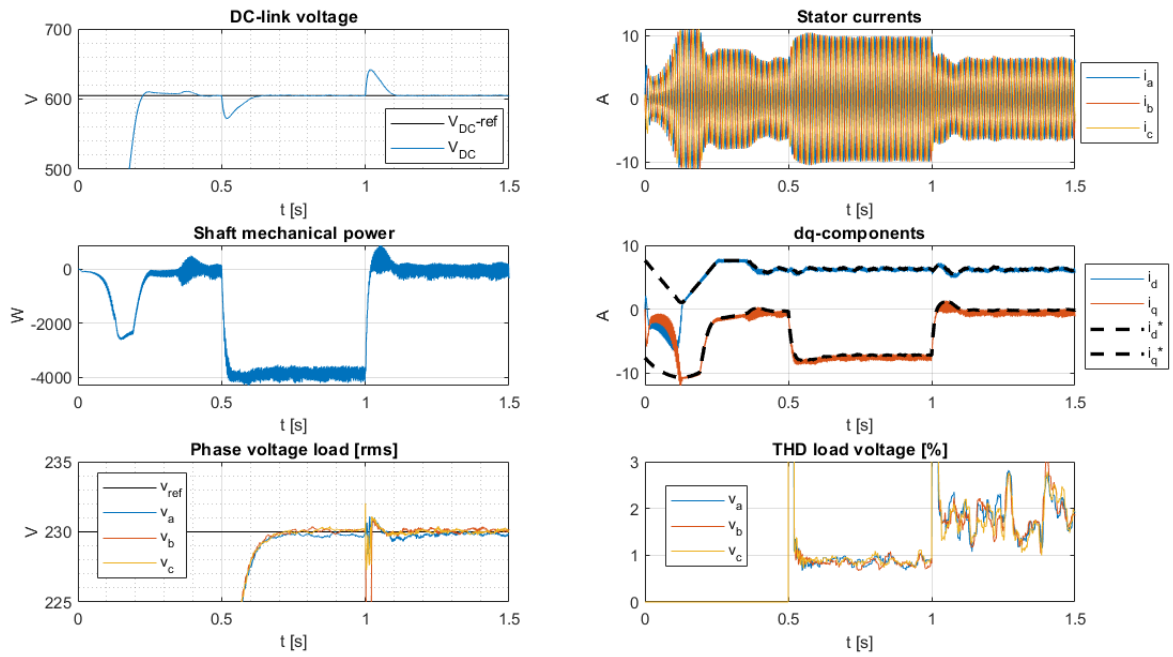

Figure 12.25: #M1, (V/f), $\eta \approx 0.8732$

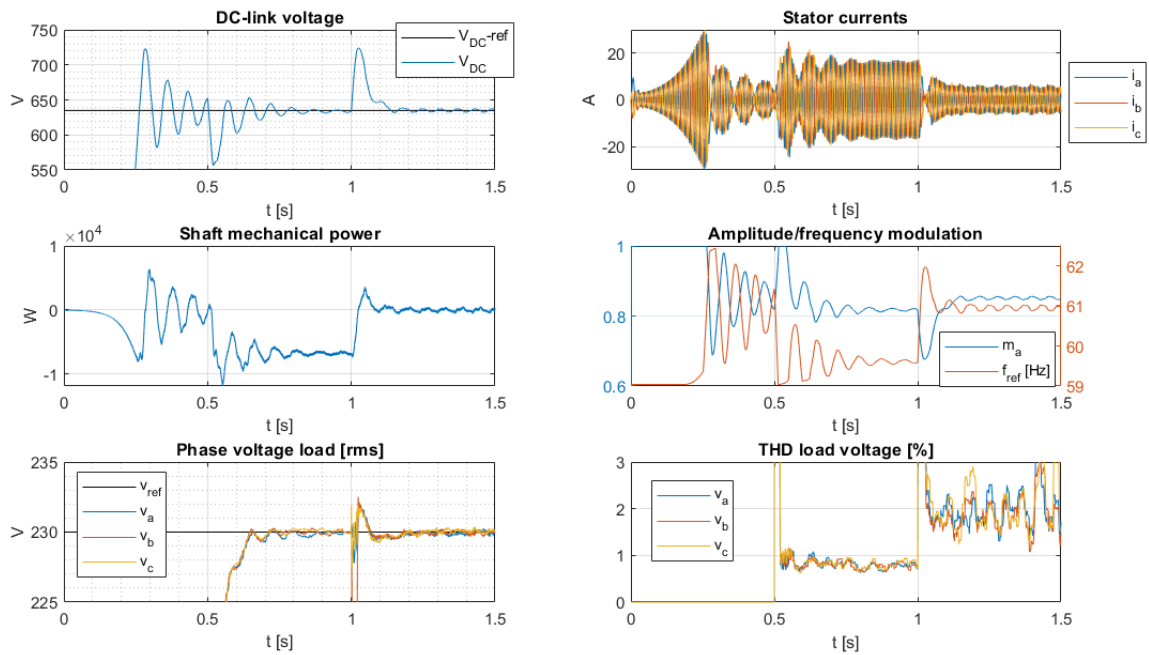Figure 12.26: #M1, (FOC), $\eta \approx 0.9251$

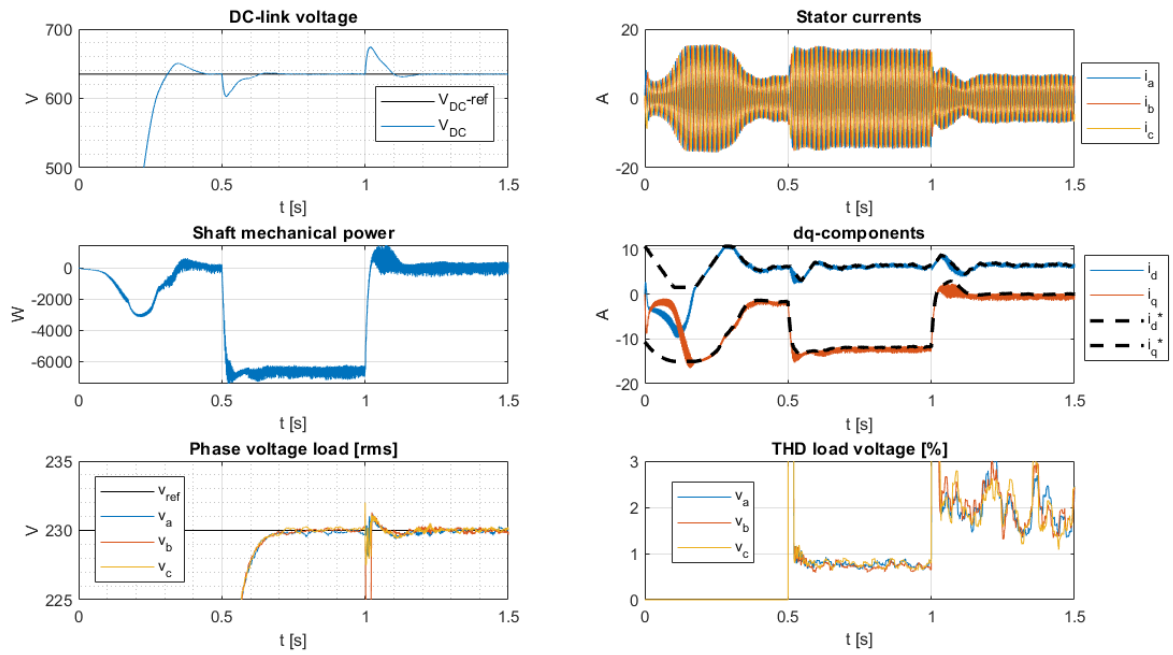Figure 12.27: #M2, (V/f), $\eta \approx 0.9275$

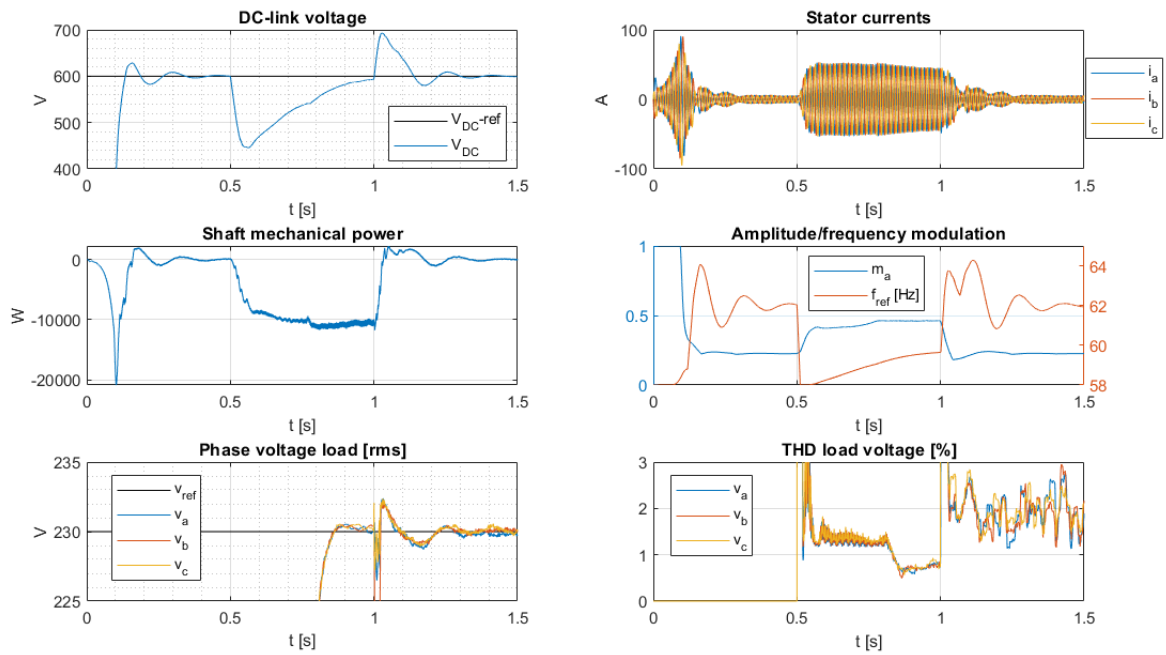Figure 12.28: #M2, (FOC), $\eta \approx 0.9601$

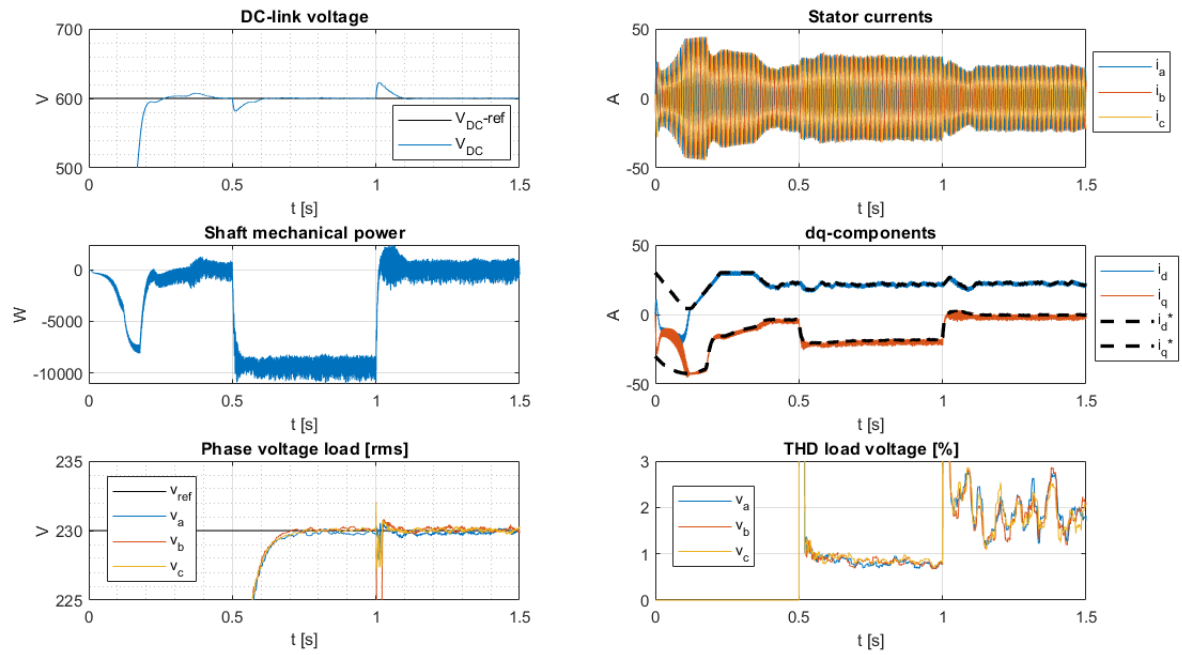Figure 12.29: #M3, (V/f), $\eta \approx 0.8468$
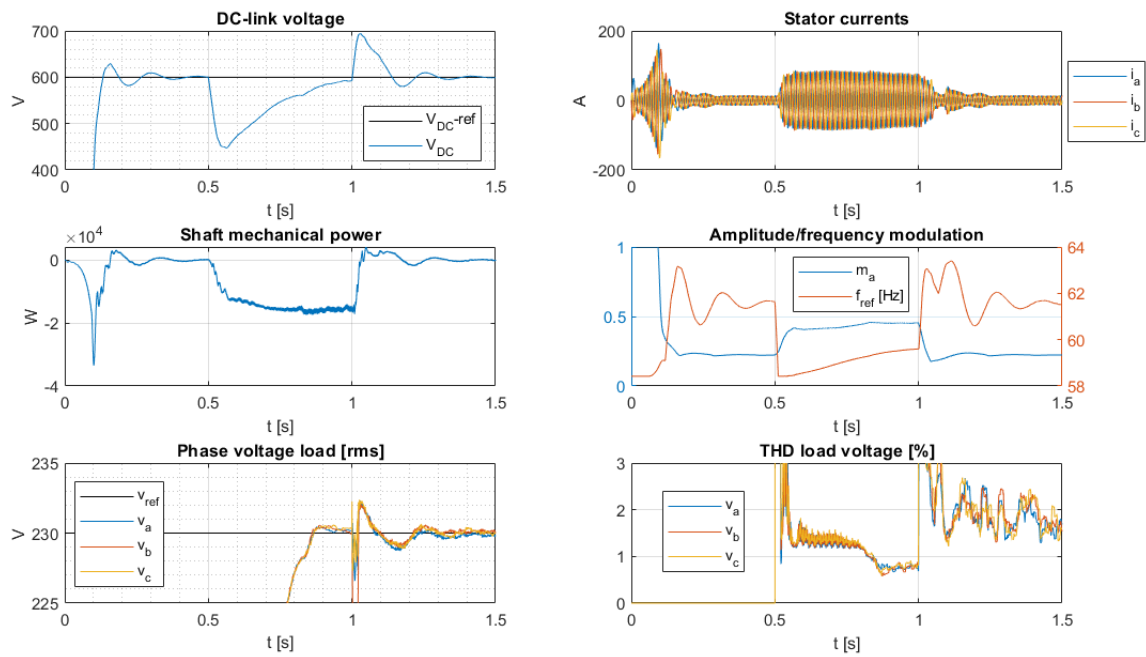
Figure 12.30: #M3, (FOC), $\eta \approx 0.9804$
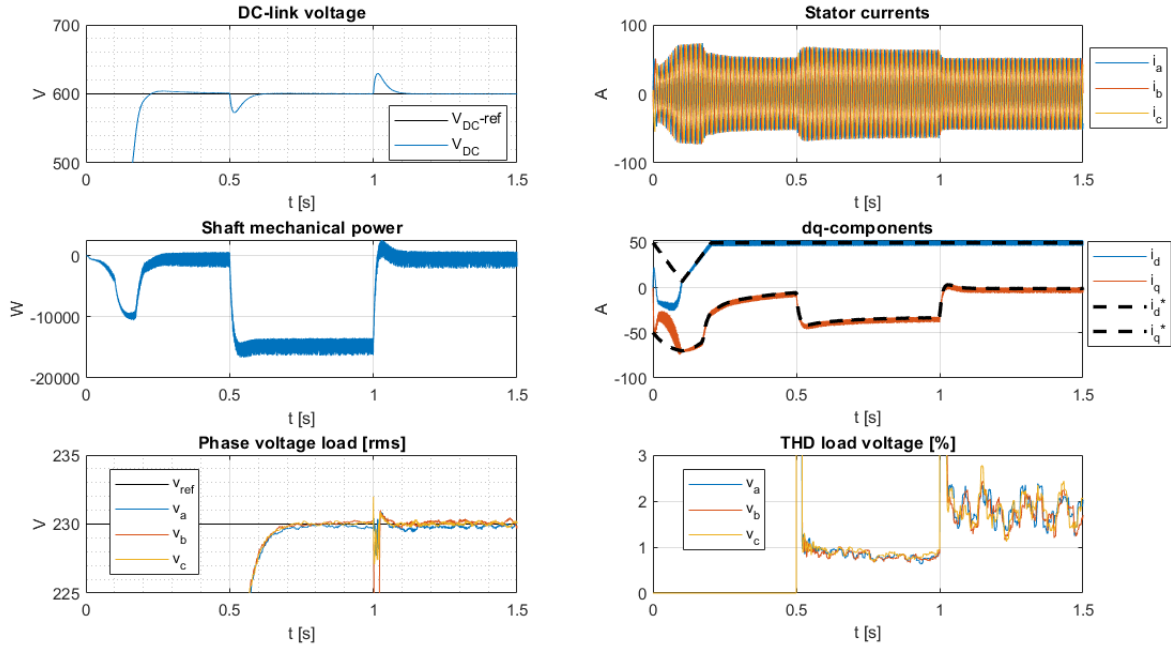

Figure 12.31: #M4, (V/f), $\eta \approx 0.87$

Figure 12.32: #M4, (FOC), $\eta \approx 0.9502$

12.4 Test 3: Sensitivity to rotor time-constant (FOC)

12.4.1 Purpose and setup

Unlike the V/f-method, the FOC-method requires knowledge of the rotor time-constant (τ_r). These tests will study the effects varying τ_r for configuration #M1, with a fixed rated mechanical speed (ω_m^G) and battery and initial DC-link voltage set to 40V. The rotor time-constant is changed down to 25% and up to 400% of its theoretical value. A total of 3 simulations are performed, run in the same manner as the full-load test (Section 12.3): magnetizing for the first 0.5 seconds, and applying a full step active load afterwards.
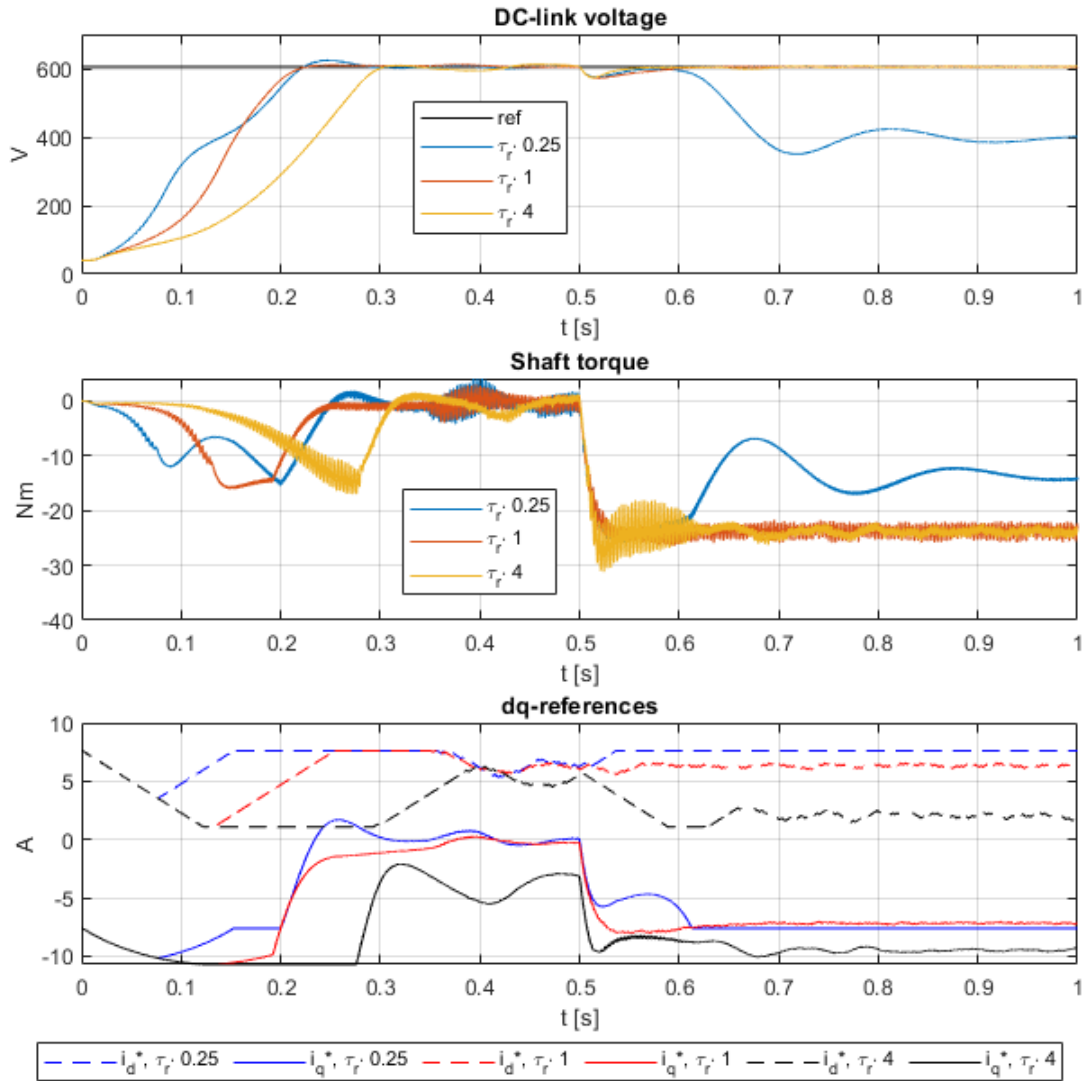
12.4.2 Results and analysis

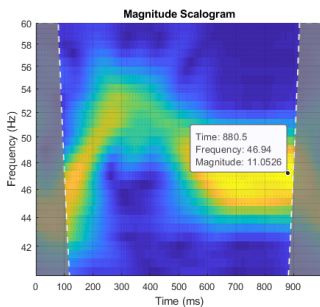Figure 12.33: #M1, Full-load step at t=0.5s, (FOC)

Figure 12.34: CWT: $\tau_r \cdot 0.25$
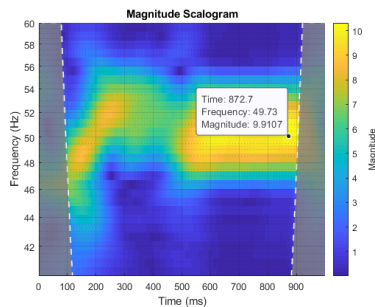
Figure 12.35: CWT: τ_r
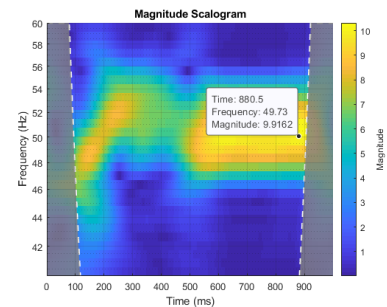
Figure 12.36: CWT: $\tau_r \cdot 4$

Figure 12.33 shows the DC-link voltage, torque and controller references. CWT-analysis of the stator phase "a" currents are also shown in Figure 12.34-12.36. Refer to Section 14.5.1 for more details about the CWT-analysis.

The first thing to note is that with 25% τ_r, the system is unable to produce the required torque to meet the load demand, and consequently gives a stable system at -200V from the reference DC-link voltage. The charge-up

time seems to be the same for 25% and 100% τ_r, but the 25% case has a "bulkier" torque-response in the 0.1-0.2s region. In terms of dq-references, there seems that a larger τ_r gives a slower response, i.e. longer time before i_d* is within the allowed margin of error (as implemented in this control-system). The response of dq-references in the load-region also oscillates more for the 400% τ_r case.

We can also observe that a larger τ_r gives a larger ratio of the active to reactive current components, $\frac{i_q*}{i_d*}$. Looking at the slip-speed relations at steady-state flux, (12.2), this ratio of currents can be described as a kind of compensation to achieve a higher slip-speed. In the simulations, the rotor shaft was fixed at a speed corresponding to $\omega_r = 51.85$ Hz. The CWT-plots (Figure 12.34, Figure 12.35 and Figure 12.36) shows that for the 100% and 400% τ_r cases, the stator current during applied loads stays close to 50Hz, corresponding to rated slip. The 25% case goes down to about 47Hz, thus exceeding the rated slip.

$$\omega_s = \frac{i_q^*}{i_d^*} \frac{1}{\tau_r} \tag{12.2}$$

In practical machines, the rotor time-constant can vary during operation. Increasing temperature increases the rotor resistance, and increasing speeds can alter the self-inductance of the rotor [49]. Inaccurate τ_r will influence the accuracy of the commanded versus actual position of the dq-components. A smaller τ_r (25%) results in the dq-reference leading the actual true axis (larger ω_s). This gives $i_d < i_d*$, and $i_q > i_q*$. With the control-system as implemented, we see from Figure 12.33 that $|i_d*| \approx |i_q*| = I_N^G$. With the control-system unable to compensate by further increasing i_q*, we have a reduction in obtainable torque, which explains why this configuration failed to maintain the DC-link voltage. A larger τ_r (400%) results in the dq-references lagging the actual true axis (smaller ω_s). This gives $i_d > i_d*$, and $i_q < i_q*$. Because the control-system with its margins of error made a reduction of i_d*, and thus allowed a higher i_q*, it was effectively able to compensate for the inaccurate rotor time-constant.

12.5   Test 4: Interaction with prime-mover

12.5.1   Purpose and setup

The previous tests are performed with fixed rotor speed. A well speed-controlled prime-mover would make this a justifiable approximation, but it's also of interest to study how the system work during variable-speed operation. In these tests, the simplified hydro-model (Section 8.2) is included in the simulations. All simulations are run with a battery and initial DC-link voltage of 40V, where the first 0.5 seconds consist of the magnetisation followed by a step-change to full active loads.

The scaling of the prime-mover parameters (T_0 and k_{pm}) are done as suggested in Section 8.2.1, defining $P_1 = 1.1 \cdot P_N^{Gm}$ (10% margin), $\omega_1 = \omega_m^G$ and $\omega_2 = 2 \cdot \omega_m^G$. For the rotational system (Section 8.1), #M4 is assumed frictionless (mu_f=0) because it has no coefficient available (Appendix A). The total inertia (J_{tot}) could in a practical system be increased by choosing a "heavier" hydro-turbine, or adding flywheels to the shaft. Finding realistic values of inertia for small-scale hydro-turbines was not successful. The inertia (J_{tot}) is defined by applying (8.3) with $H = 0.01$, $\omega_m^N = \omega_m^G$ and $P = P_N^{Gm}$. The resulting values are shows in Table 12.6, as a ratio of the IM-inertia. These values are of course unphysical, as they are all lower than intertia of the generator itself. They are however used in the simulation, because larger values of J_{tot} would impose a quite slowly changing rotor speed (ω_m), and this would defeat the purpose of studying operation under variable speed.

#M1	#M2	#M3	#M4
0.252	0.082	0.034	0.004

Table 12.6: $\frac{J_{tot}}{J_{gen}}$

With four system configurations (machines), one voltage-controller for the loads and two controllers for the

generator (V/f and FOC), a total of 8 simulations are performed. The initial mechanical speed is set to $2 \cdot \omega_m^G$ (zero-torque point for hydro-prime mover).

12.5.2   Results and analysis

Given below are plots (Figure 12.37-12.44), showing the DC-link voltage, stator currents, torque, controller-outputs and rotor speed.

All cases with the FOC-method seems to be working well and maintains the DC-link voltages with low over/under-shoots. The rotor speed (referred to by ω_r), dips down during the magnetisation-procedure, and again when the full load is connected. We can also observe how the reactive reference (i_d*) is increased when the speed (ω_r) is reduced, due to lower back-EMF. The quick response of the control-system allows it to find a steady-operational point above the rated speed, and thus draws a steady-state current lower than the rated value.

With the V/f-method, configuration #M1 and #M2 struggles in maintaining the DC-link voltage when the load is applied. The cause seems to be related with the amplitude-modulation controller. After the load is applied, the IM starts to draw more power, and thus reduces the speed of the prime-mover. This is combined with the DC-link voltage overshooting, making the gen_ma_Ki_neg-intral gain reduce the scaling of the frequency-coefficient for voltage reference. This results in a sudden drop and large reduction of m_a. The machine responds to this by an increase of generating torque, reducing the rotor-speed even further. The load is meanwhile drawing power, steadily discharging the DC-link. By the time the controller manages to correct the torque, the speed is increased due to the prime-mover, and this result in a sudden increase of m_a. This increase of m_a increases the torque (the opposite effect as when m_a was reduced), putting the IM towards motor-operation, which discharges the DC-link further.

With the V/f method, #M3 and #M4 managed to handle the speed-variations, but they both exhibit a oscillating response during the magnetisation procedure and high peaks of stator-currents. Their advantages (compared to #M1 and #M2) might be due to their lower voltage-ratings, which effect can be seen by their lower charge-times (below 0.2s) compared to (0.3-0.4s for #M1 and #M2). Having a larger DC-link voltage compared to the machine-voltage ratings seems to be advantageous when operating above rated speeds.

Looking at #M3 and #M4 (where both control-systems managed to maintain the DC-link voltage), the steady-state rotor speed (ω_r) is slightly higher for the FOC-method. The cause can be a combination of the FOC-method operating with lower stator currents (thus lower torque), and the improved efficiency of the FOC-method compared to V/f (as observed in Section 12.3.2). In terms of speed-dip during magnetisation, the #M1 and #M2 cases show similar dips, whereas for #M3 and #M4, the dips are slightly higher for the V/f method.
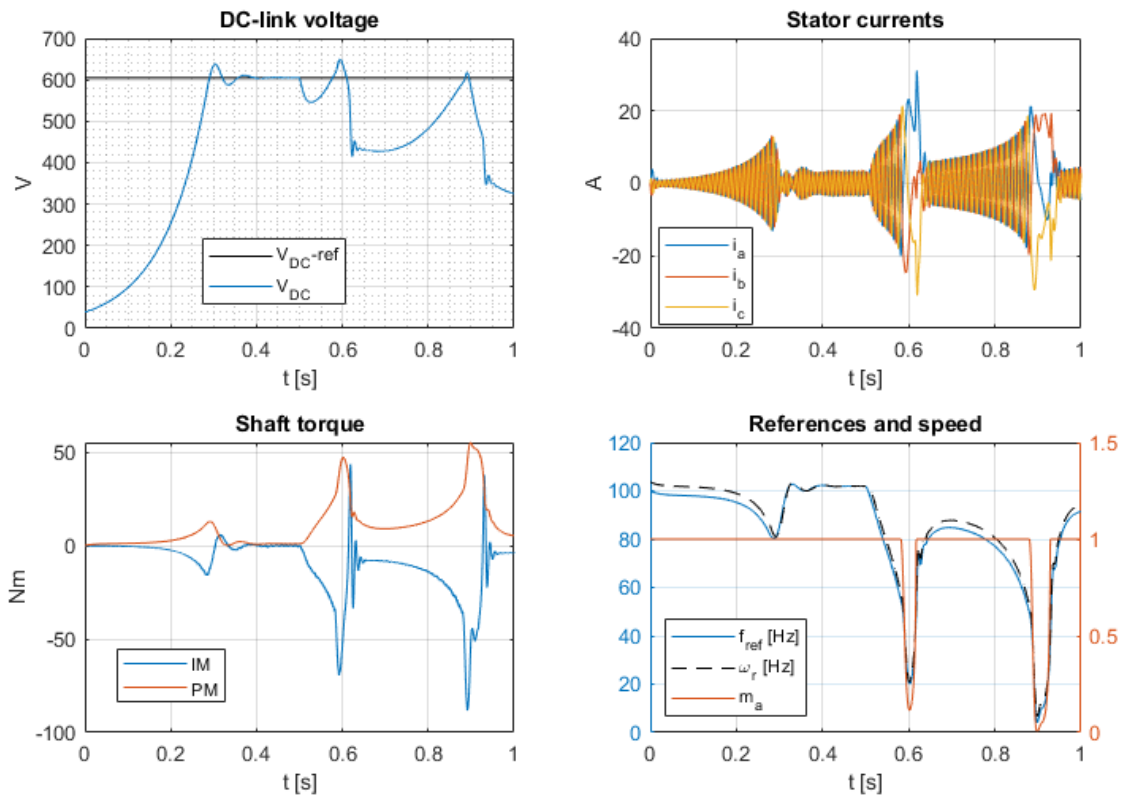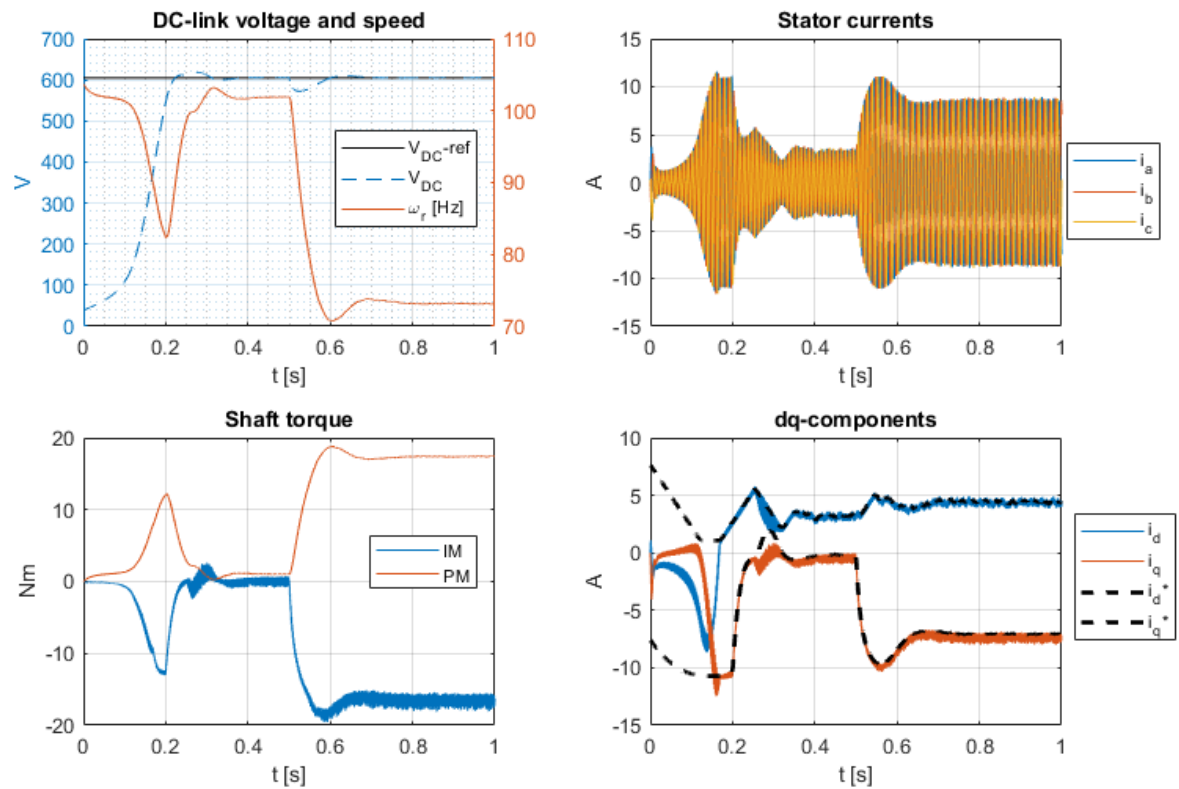
Figure 12.37: #M1, Hydro PM, (V/f)
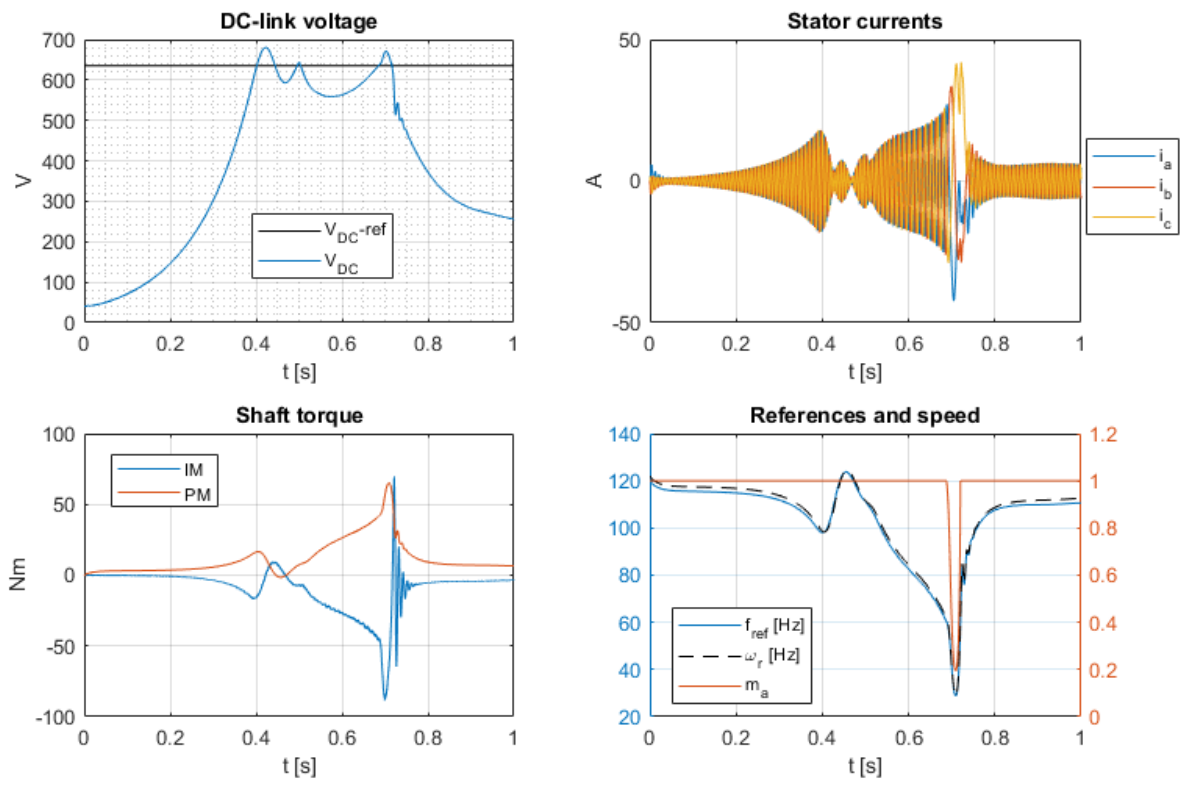

Figure 12.38: #M1, Hydro PM, (FOC)
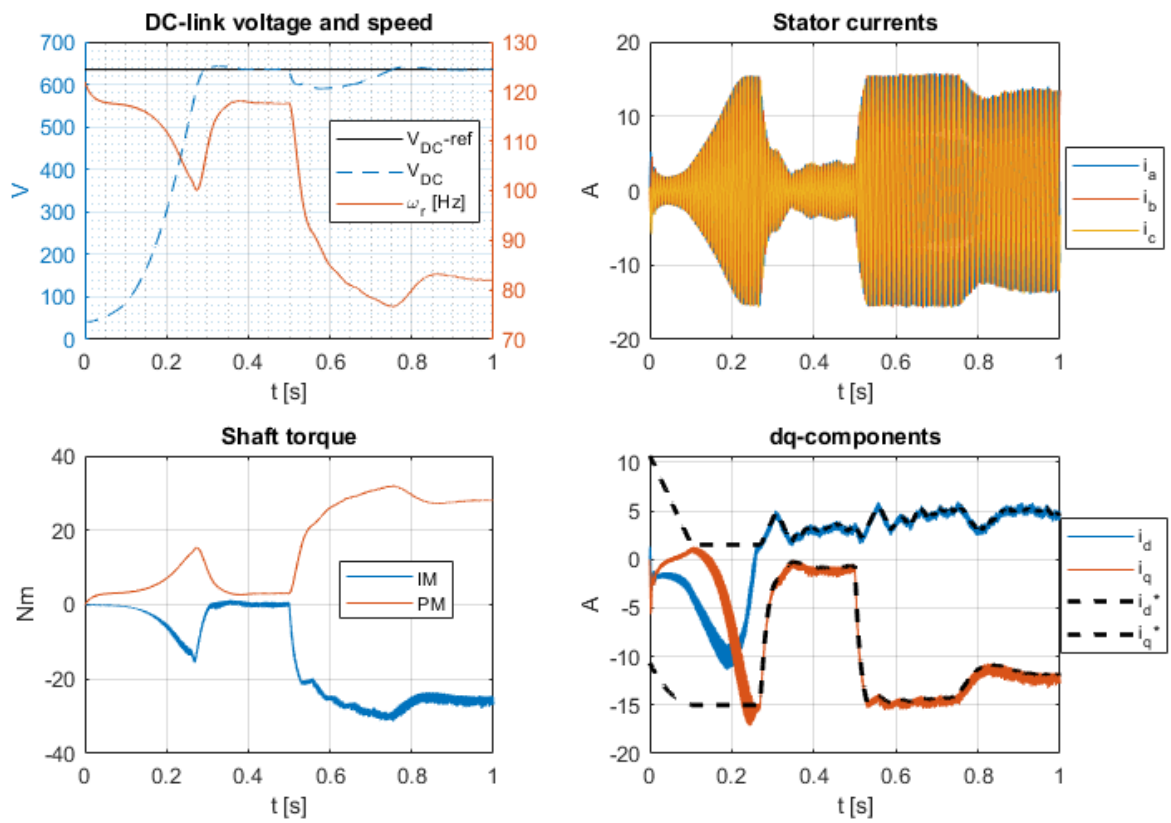
Figure 12.39: #M2, Hydro PM, (V/f)
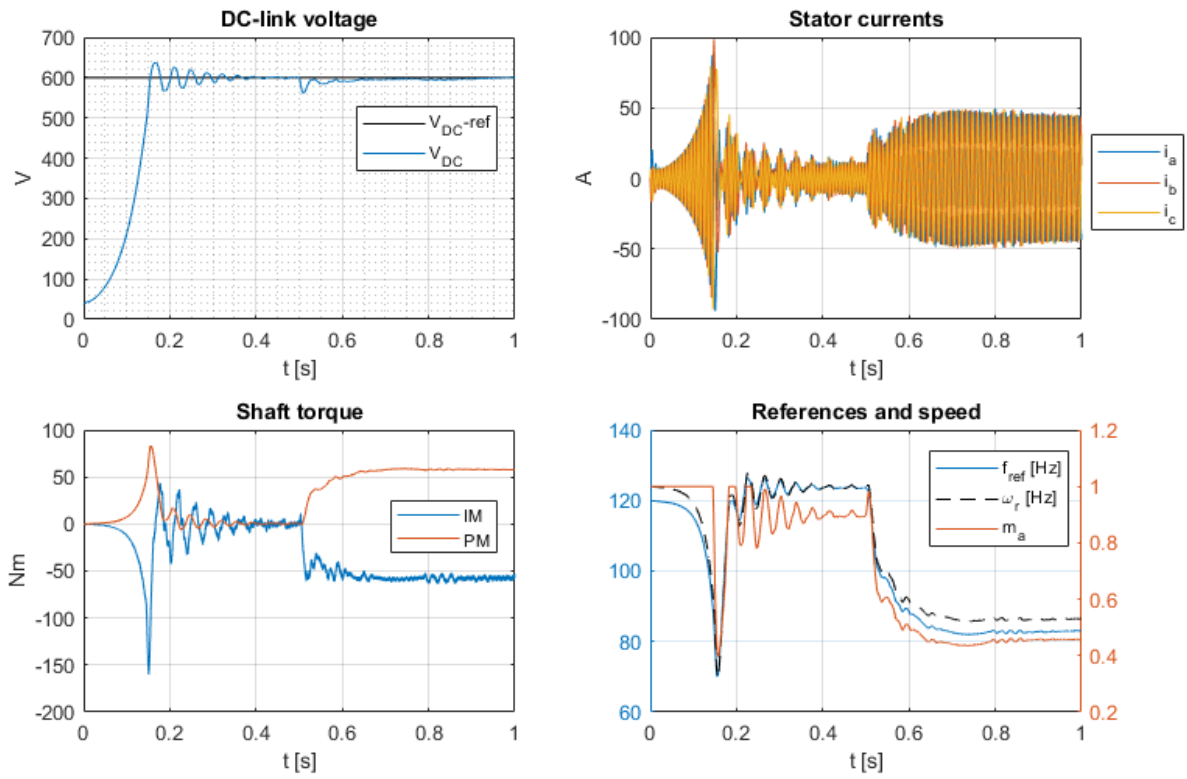

Figure 12.40: #M2, Hydro PM, (FOC)
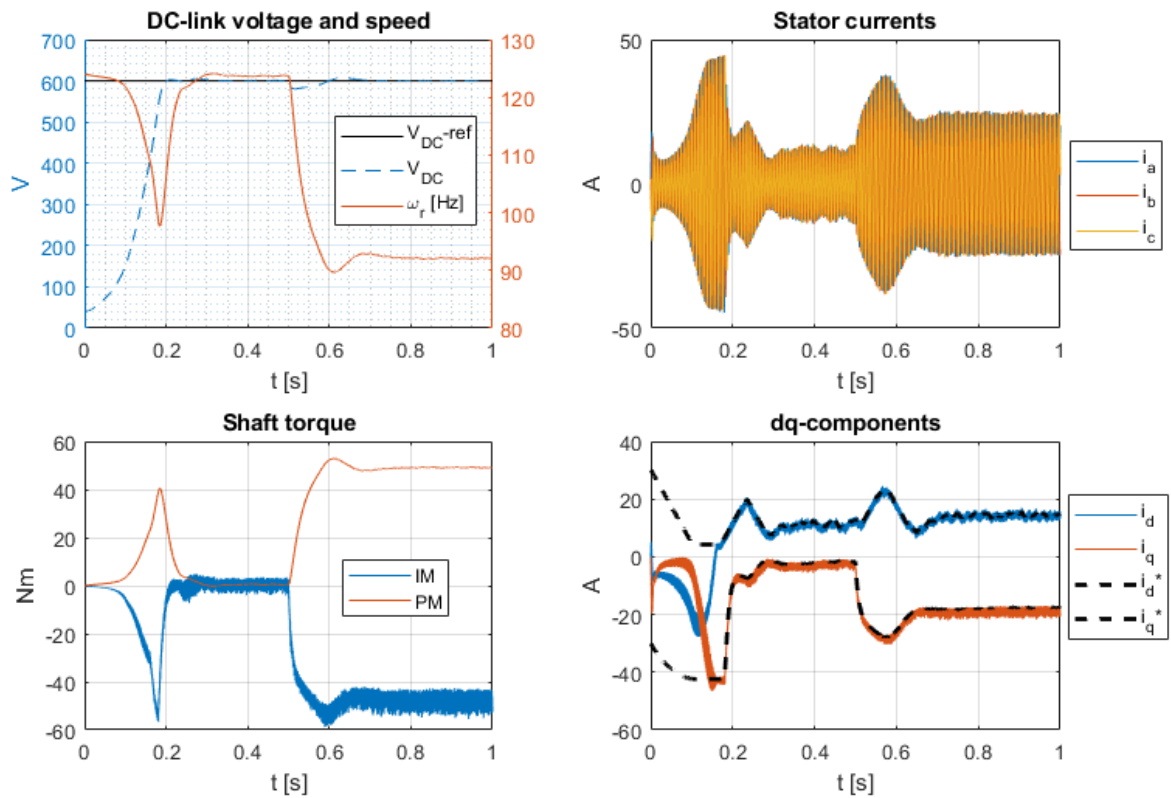
Figure 12.41: #M3, Hydro PM, (V/f)

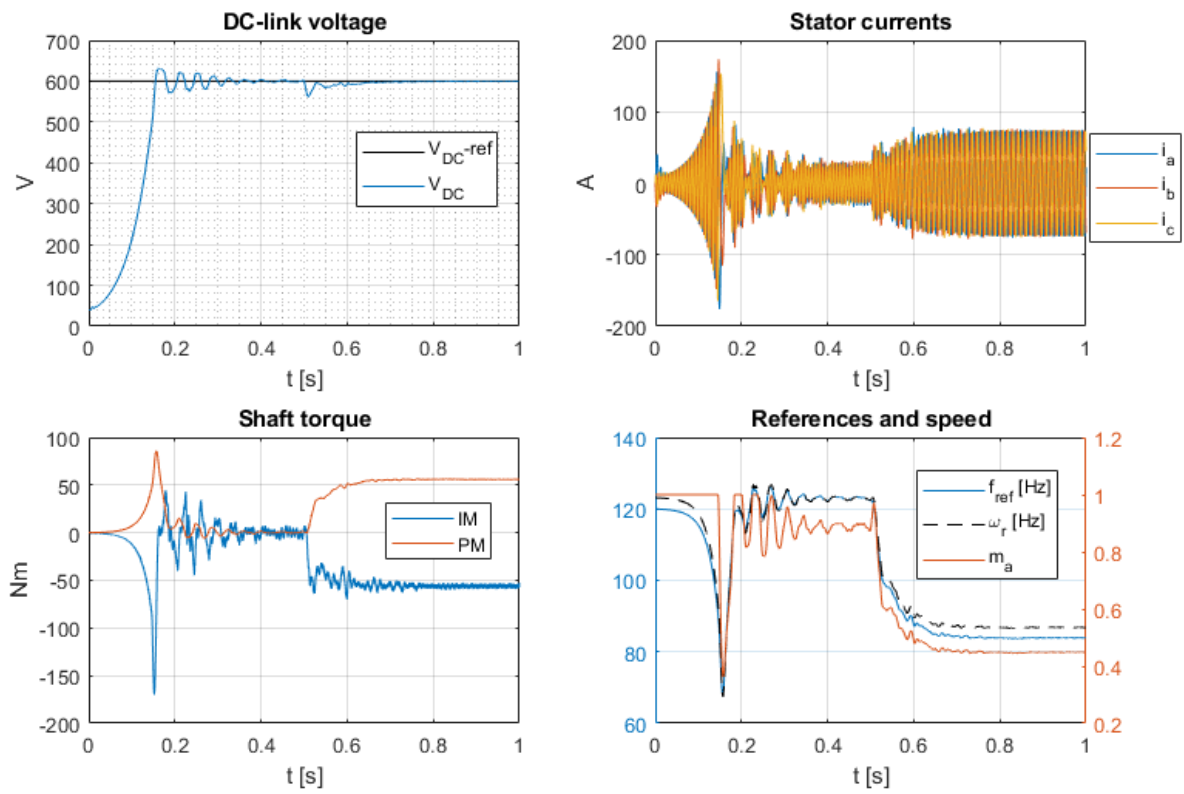Figure 12.42: #M3, Hydro PM, (FOC)

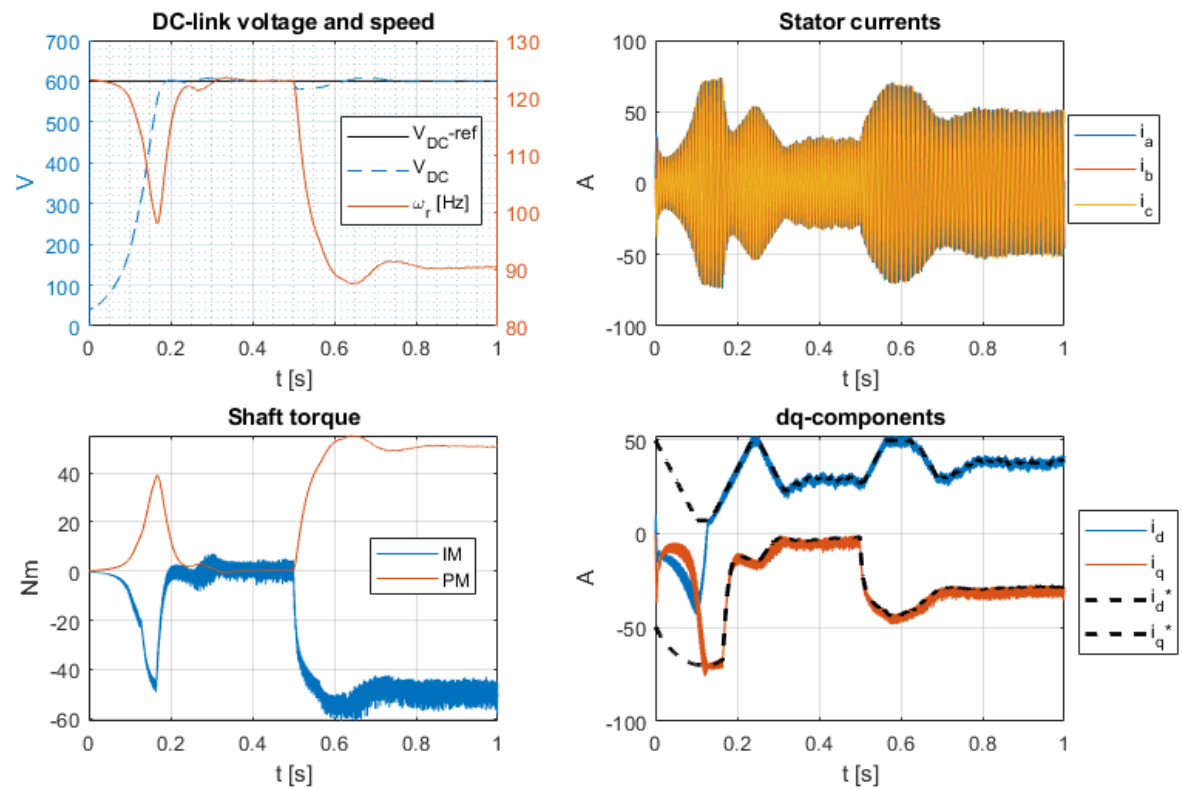Figure 12.43: #M4, Hydro PM, (V/f)

Figure 12.44: #M4, Hydro PM, (FOC)

12.6   Test 5: Filter performance at different loads

12.6.1   Purpose and setup

These tests functions to study the performance of the LCL-filter with its design procedure. This will be evaluated by inspecting the the quality of the load voltage (magnitude and THD) during different types of loading.

These tests are run without the generator-side. The DC-link voltage is fixed at the reference corresponding to its respective configuration (#M1, #M2, #M3 or #M4). The load-current is varied in five step [100%, 75%, 50%, 25% and 5%] of the rated current (I_N^L). For each of these levels, the power-factor is changed from 0.99 down to 0.1, in steps of $\Delta \text{pf} = 0.1$, changed every 0.1 second (5 periods of the 50Hz voltage reference). This is done for power-factors corresponding to both lagging (positive reactive power) and leading (negative reactive power) loads. With an upper active power limit ($P_N^L = \frac{S_N^L}{\sqrt{2}}$), as defined in Section 12.1.1, some power-factors are reduced for the high-current levels.

With four system configurations (machines), one voltage-controller for the loads and to types of power factor (lagging and leading), a total of 8 simulations are performed.

12.6.2   Results and analysis

Given below are plots (Figure 12.45-12.52), showing the commanded load currents and power factor, with the corresponding RMS and THD (50Hz fundamental) of the load voltage.

The sudden spikes of RMS and THD seen in all plots are due to the discrete changes of loads throughout the simulation. This is especially present for the cases of leading power-factors, casued by the fact that the output current of the CR-block (Figure 3.5) is changed instantaneously ($\frac{V_{R_{CL}}}{R_{CL}}$) when a new load is applied, whereas the LR-block has a integrator before this output ($\frac{V_{L_L}}{s \cdot L_L}$).

For all cases with leading reactive power, the phase-voltage is well maintained around its 230V reference for all types of loading. We can also observe that larger amounts of leading reactive power reduces the THD. For all leading configurations, the THD drops below 1% when the current is set to 100% and 75%, and otherwise, the THD stays between 1-2%.

For all cases with lagging reactive power, the THD seems to remain fairly unchanged, centred around approximately 2%. We do however observe some exceptions in the RMS when the load draws currents of 100% and 75% for configurations #M1, #M3 and #M4. For 100% current, the system is unable to maintain the 230V reference, and this effects is worsened for larger amounts of lagging reactive power, down to a deviation of about 5V (2%). Recall that #M2 is the only configuration where the rated machine-voltage determined the dimensioning DC-link voltage.
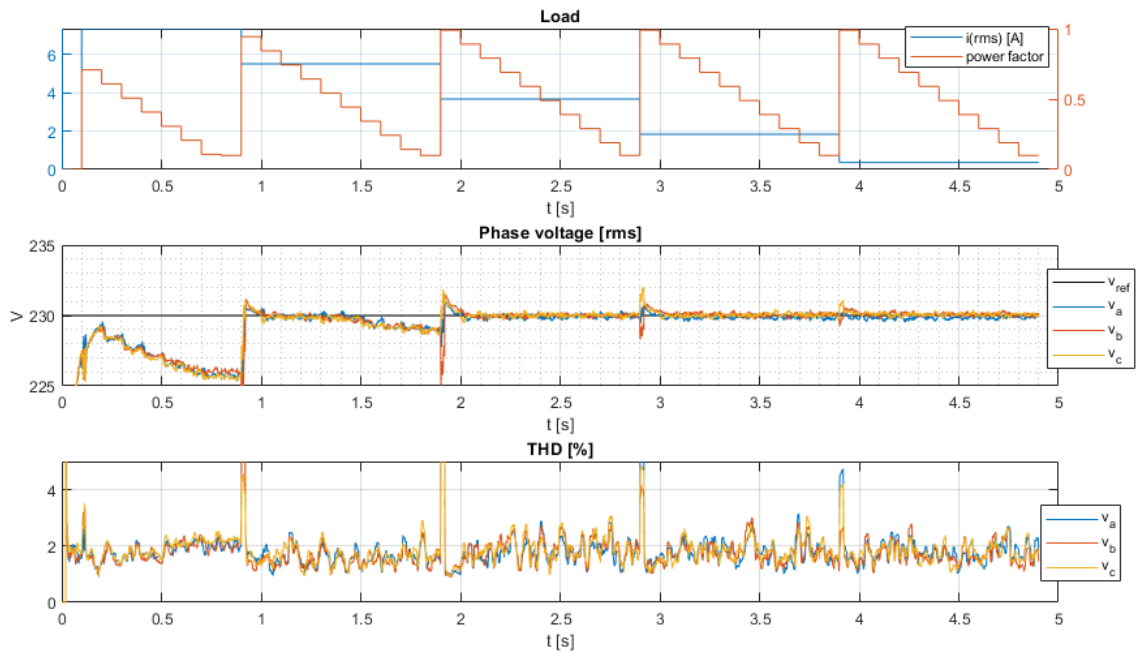
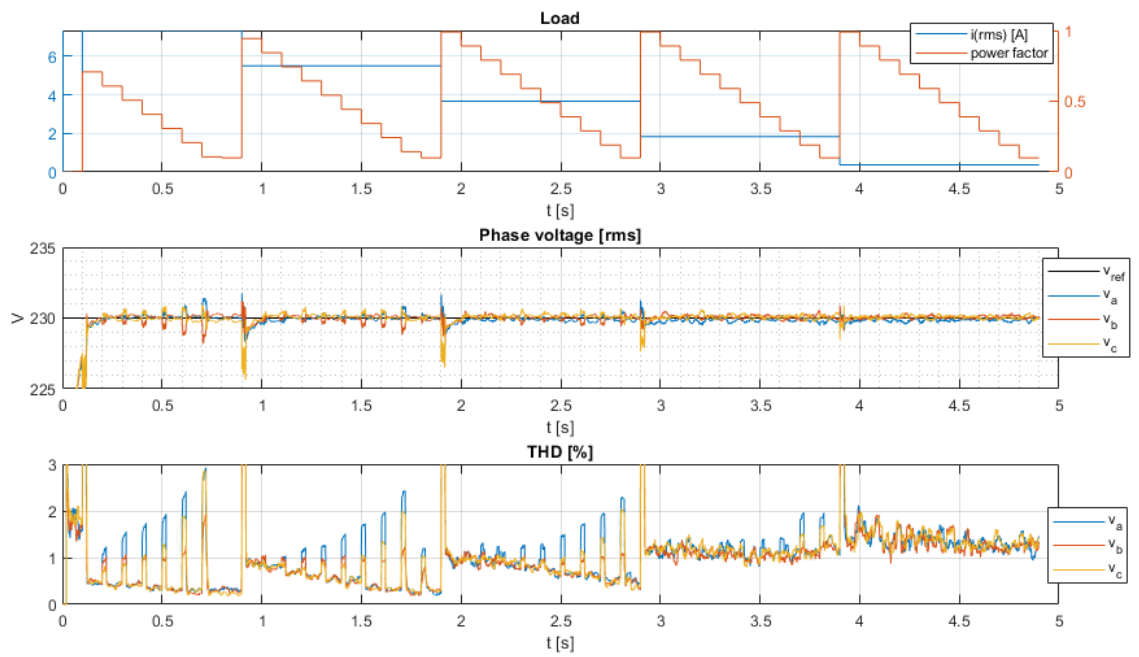Figure 12.45: #M1, Lagging pf

Figure 12.46: #M1, Leading pf
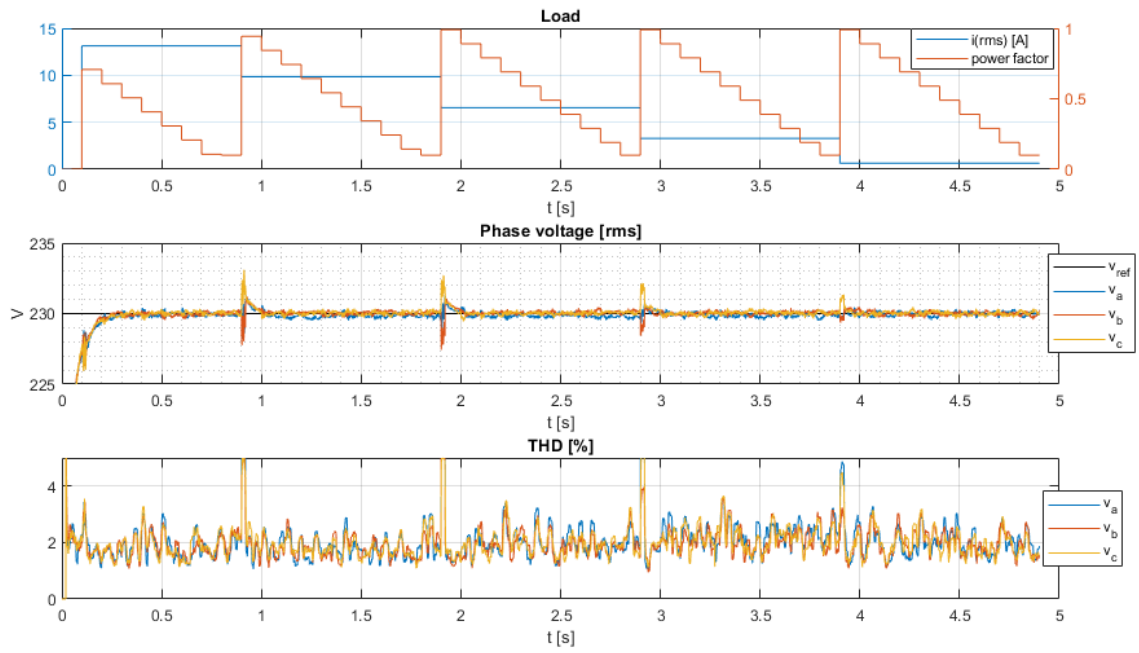
Figure 12.47: #M2, Lagging pf
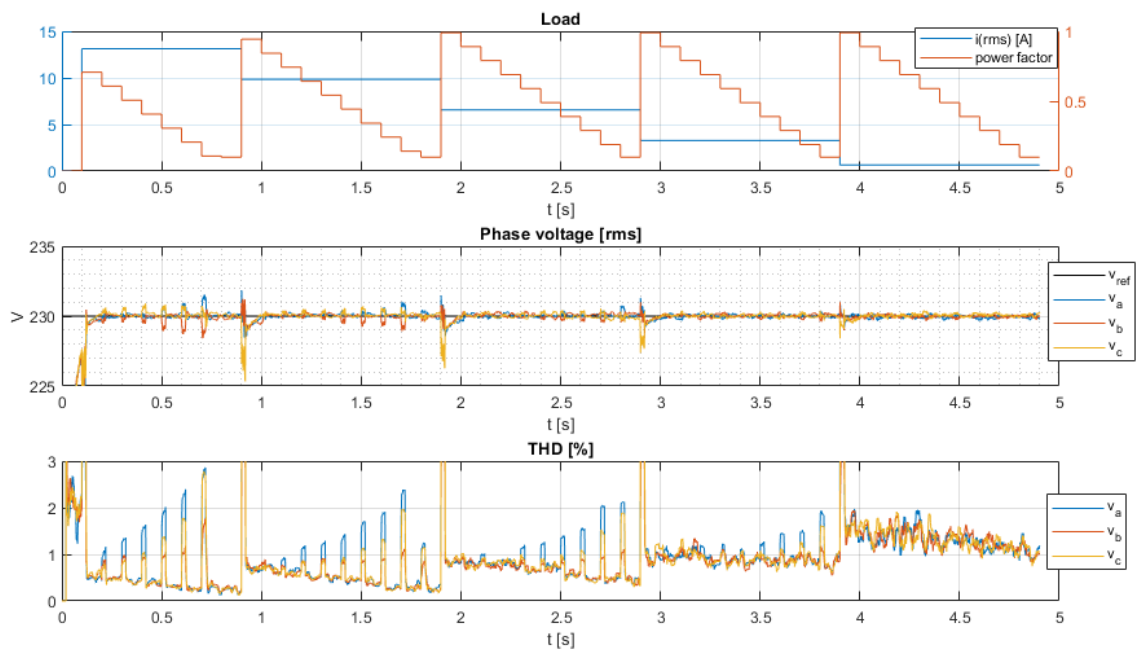
Figure 12.48: #M2, Leading pf
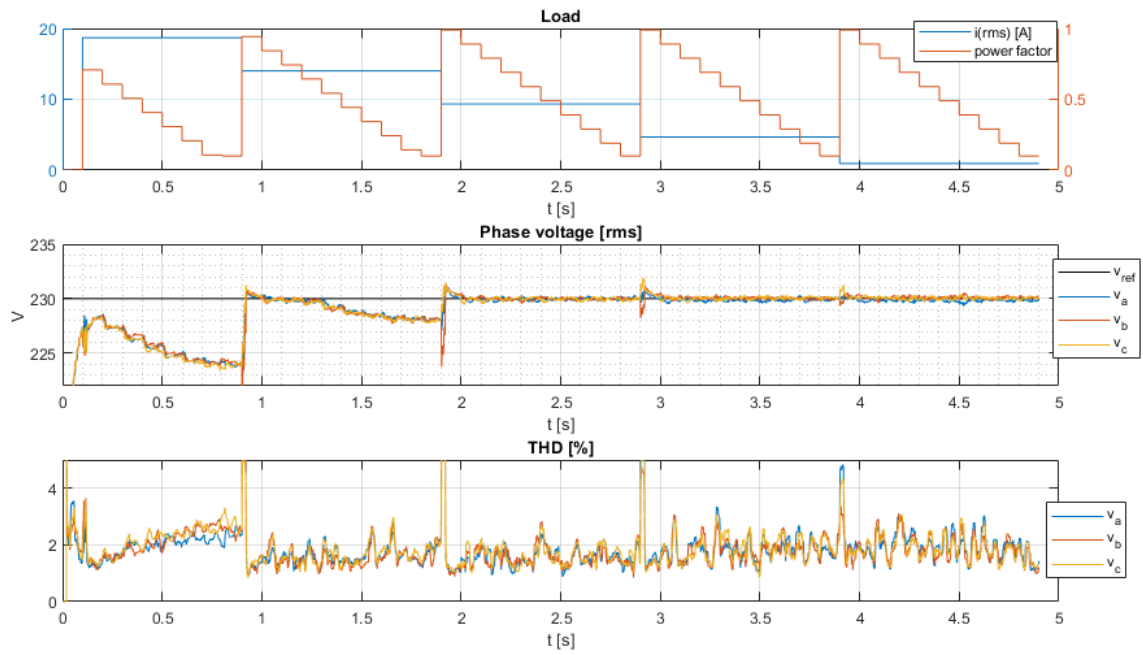
Figure 12.49: #M3, Lagging pf
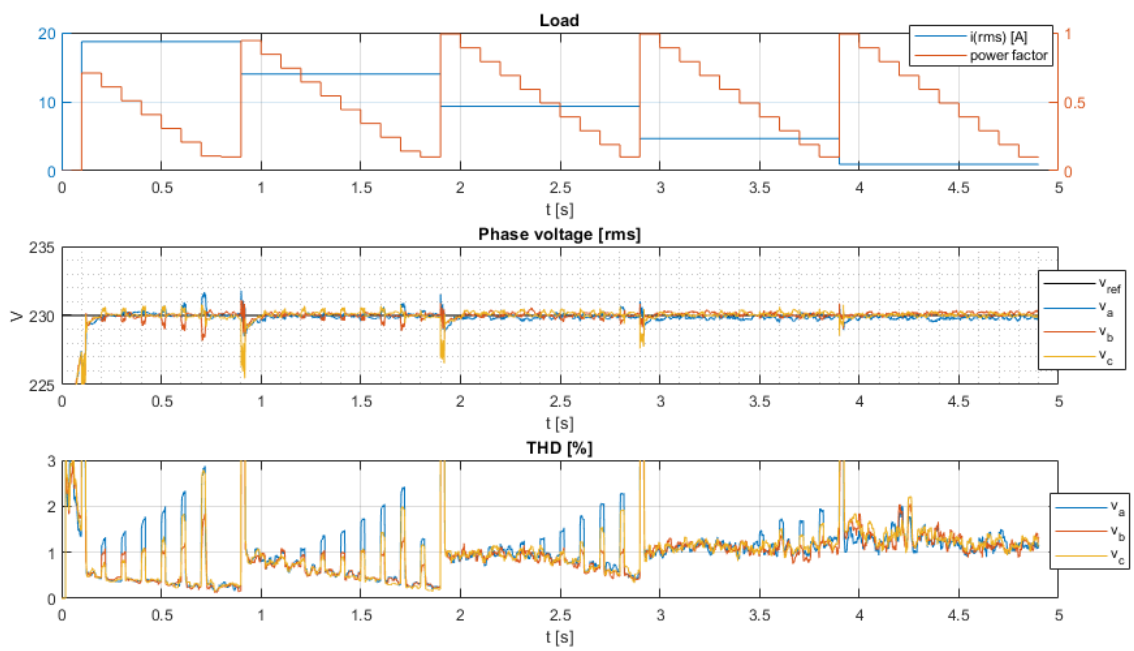
Figure 12.50: #M3, Leading pf
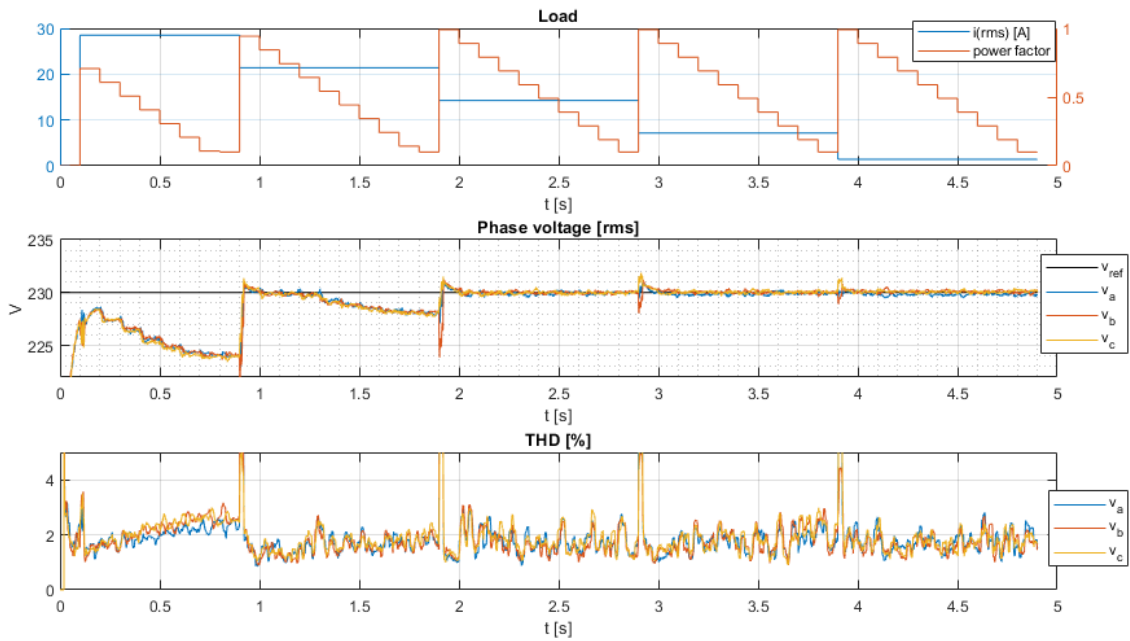
Figure 12.51: #M4, Lagging pf
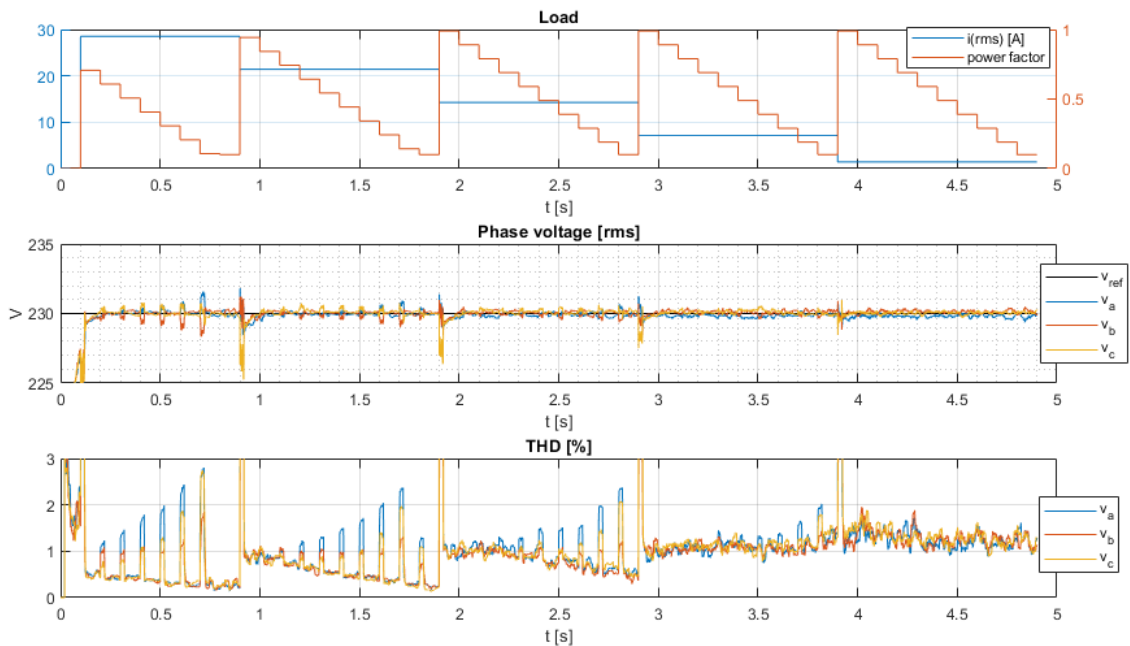
Figure 12.52: #M4, Leading pf

12.7 Conclusion

Load voltage

The dimensioning of DC-link voltages was mostly determined by the load-voltage rating (#M1, #M3 and #M4). This results in an operation of m_a (load-controller) close to 1, which is favourable for a reduction of THD (Section 6.4). The LCL-filter performed best (Test 5) in terms of THD for larger amounts of leading reactive loads. For larger amounts of lagging reactive loads and no-loaded conditions (Test 2), the THD reaches

its highest levels of about 2-3%. The lagging loads are the only case of which an unmet steady-state RMS-voltage was observed, up a to a 2% deficit. Figure 12.47 seems to show than an increase of the DC-link voltage reference could improve the RMS-performance when the margins are small. With the Norwegian quality-requirements for low-voltage grids given at $\pm 3\%$ RMS and 5% THD [39], the design is however within the bounds as is. The response of the voltage-controller works satisfactory, and its composed of only 3 tunable parameters.

Magnetisation and overshoots

In terms of magnetisation (Test 1), all configurations managed to perform a successful charge-up at different fixed speeds. All configurations tend to settle at the DC-link voltage reference within 1 seconds. The dimensioning of DC-link capacitance as a function of rated electrical power seems to substantiate this predictability. The FOC-method generally displays low/zero settle-time, and low overshoots of current ($<7\%$) and DC-link voltage ($<3\%$). In comparison, the V/f-method has higher overshoots of current ($<160\%$) and DC-link voltage ($<14\%$), and in the worst case, it exceeded the rated mechanical shaft power by 160%. In defence for the V/f-method, induction machines can draw large starting currents, up to 7-8 times the rated value during start-up $[1]^1$. The exceeding of the V/f-method might therefore be approved if the machine is designed to handle such large currents for a limited period.

Battery

The work delivered from the battery during magnetisation (Test 1) is generally low, and it supports for periods no longer than 2x the rated machine frequency. Machines with higher power-ratings requires more work and higher peaks of battery current (up to 120A for #M4, $V_{bat} = 40V$), but this is reduced for higher rotor speeds (ω_m). Higher speeds also reduced the support-time of the battery. Higher battery voltage gives shorter charge-up times, but also higher peaks of current and more work delivered. Note that only one battery-resistance was used ($R_{bat} = 0.01\Omega$). The observed patterns should however remain for variations of R_{bat} if the DC-link capacitance design is kept as is.

FOC-method

Compared to the V/f-method, the FOC-method excels in both the full-load study (Test 2) and variable-speed study (Test 4). With DC reference-voltages in the range of 600-635V, its deviations hardly swing further than $\pm 40V$, and it stabilises the voltage smoothly. The produced torque/power is sleekly changed, and the hysteresis current-controller enables it to always stay within rated current limits. The increase/decrease method for the reactive reference (i_{d*}) based on an estimate of the actual reactive current component seems to detect the upper achievable limits well. The intended default of a high flux seems to pay off in term of dynamic performance and efficiency when producing power, but it comes at a cost of higher steady-state current during light/no-load conditions. The torque-ripple is also larger for the FOC-method, and it utilised a switching-frequency 5x higher than the V/f-method, which would result in more switching-losses for a practical converter. The defined(tuned) band-gap of the hysteresis-controller could be of influence to this torque-ripple. Taken into consideration that the V/f-method and FOC-method requires the same measurements, the better performance and lower number of tuneable parameters (7) makes FOC the better option. It does however require knowledge of the rotor time-constant (τ_r). If its inaccurate (Test 3), the performance is reduced. It has margins to compensate, but a too low τ_r could put it out of play.

V/f-method

Looking at the V/f-method, from the full-load study (Test 2) and the variable-speed study (Test 4), the over-shoots of current are smaller during changes of loads compared to the magnetisation (Test 1). Higher rotor speed (ω_m) also naturally reduces the overshoot due to higher back-EMF. The DC-link voltage overshoots up to +100V from the reference. Some cases illustrate weaknesses in the controller-design. In the case of #M3 and #M4 during the full load study (Test 2), the DC-link voltage deviates so low that the system is unable to deliver the rated load voltage for an extended period. In the case of #M1 and #M2 during the variable-speed study (Test 4), the controller was unable to stabilise the DC-link voltage. The voltage-controller and corresponding output of amplitude-modulation (m_a) seems to be the sinner. The rated voltages of machine #M1 and #M2 are higher than #M3 and #M4. With the design of DC-link voltage and tuning as given, the commanded m_a is generally lower for the low-voltage machines (#M3 and #M4), giving a slower response to load-changes (Test

2). The opposite is true during the variable-speed operation (Test 4), where the tight margins leads to sudden drops of m_a, resulting in violent oscillations of torque for #M1 and #M2. It should however be noted that the inertia (J_{tot}) used in these simulations was quite small and unphysical. With a basis in the steady-state model, the slip-speed as a torque-controller works in theory but the performance is mediocre with oscillating response during dynamic conditions. The appurtenant poorly designed/tuned voltage-controller does not help. The integral-gain in the current-limiter function was also made small as to not further contribute to oscillating responses, which comes at a cost of larger overshoots of current. There is perhaps room for improvement by increasing the DC-link capacitance and revise the tuning procedure for the 9 tunable parameters. However, the complexity due to the numerous functions and the goal of making a tuning-procedure that fits a wide range of configurations might suggest that the whole V/f control-structure should be redesigned.

Summary

As an overall review, the design-procedures functions well. The load-controller and LCL-filter seems to be a good match, giving a load-voltage of good quality. The FOC-method and corresponding tuning show the best capabilities in terms of response and applicability to various configurations. The V/f-method generally manages to succeed aswell, but it has room for improvement. As a final note, recall that the models employed in the simulation assumes balanced currents, and that the dynamic IM model, variable loads and LCL-filter treats the phases as "individual networks". Throughout the simulations performed, this conditions was check by inspecting the sum of the currents ($i_a + i_b + i_c$), and it never exceeded values larger than 10^{-10}, indicating that the results should be realistic. But of course, all the simplifications and assumptions taken in all the models will ultimately limit the validity and applicability of the results obtained and conclusions taken.

13 Lab experiments: Magnetisation of IM with VSC

A core assumption in the proposed topology for operation of an isolated power system is that the IM can be magnetised by means of a low-voltage source such as a battery. The results of the simulation study in the previous chapter substantiates that this should work in theory. This chapter will describe a laboratory set-up used to study the magnetisation and DC-link voltage build-up, with corresponding analysis of the results obtained.

Due to limited time and practical challenges, an implementation of the proposed control-systems (Chapter 10) was sadly not possible to achieve. The already implemented control-structure of the VSC was used a provided. The following results of are thereby not representing the proposed control-structures, but still subject to how a converter with its control system operates in relations to an IM driven by a speed-controlled prime mover.

13.1 Setup and equipment

The experimental setup and tests are done at the National Smart Grid Laboratory at NTNU Gløshaugen in Trondheim. Figure 13.1 shows a schematic of the components. The AC supply grid provides power for the variable DC voltage-source and AC-driver. The DC-source is connected to the VSC's DC-link through a diode which functions to ensure that the DC-link cannot discharge power back into the DC-source. The VSC is configured through its interface and is, as a module, fully equipped with measurement sensors internally. The only external signal needed is that from the position-encoder. The oscilloscope (OSC) is used to capture and store the various measurements, aquired from current probes, voltage probes connected to the VSC and from the built-in BNCs on the VSC. The setup consist of two induction machines, connected by a common shaft (no gears). IM is connected to the VSC, and functions as the generator. PM is connected to the AC-driver with speed-control, making it the equivalent of a fixed speed prime mover.

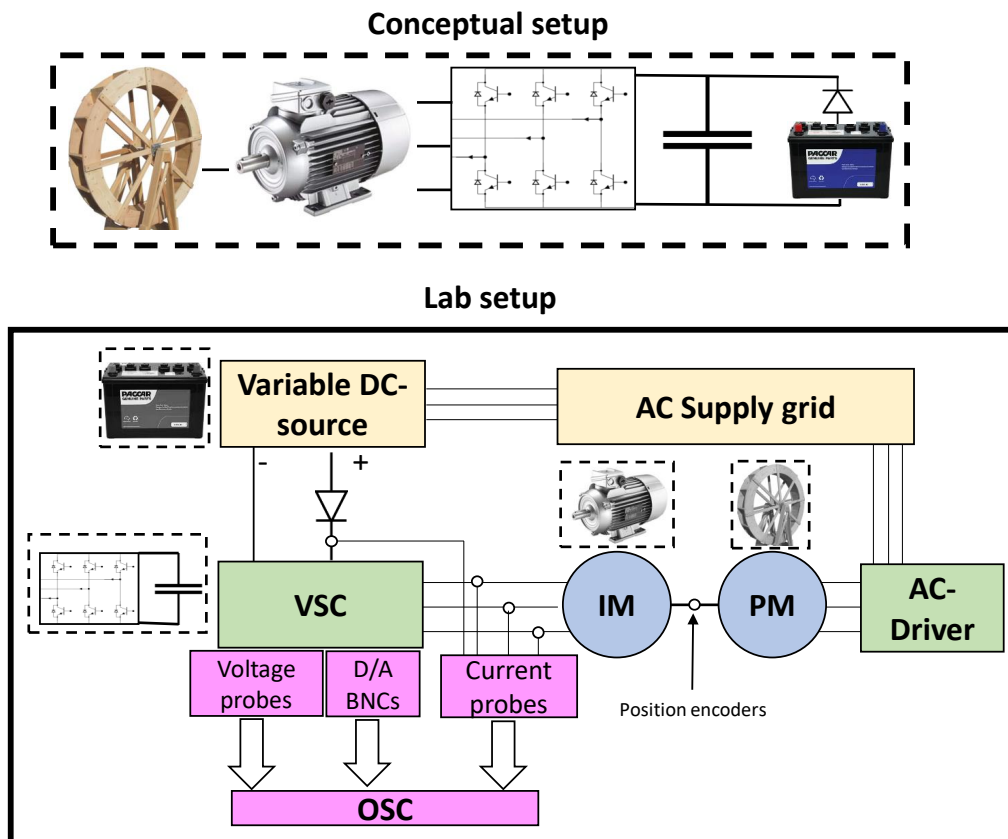Component details and pictures are given in the next section.

Figure 13.1: Lab setup

13.1.1   Component details

AC Supply grid ——————————————————————————
Three phase grid. 400V (line-line rms), 225A (rms), 50Hz
(NTNU-Elkraft Archive ID: B03-0538)

Variable DC-source ——————————————————————
DELTA ELEKTRONIKA: DC power supplies (SM500-CP90)
0-500V, ±90A
(NTNU-Elkraft Archive ID: B02-0737)

Diode ——————————————————————————————
IXYS: Standard Rectifier Module (MDD95-16N1B)
V_{RRM}: 1600V, A_{FAV}: 120A, V_F: 1.13V
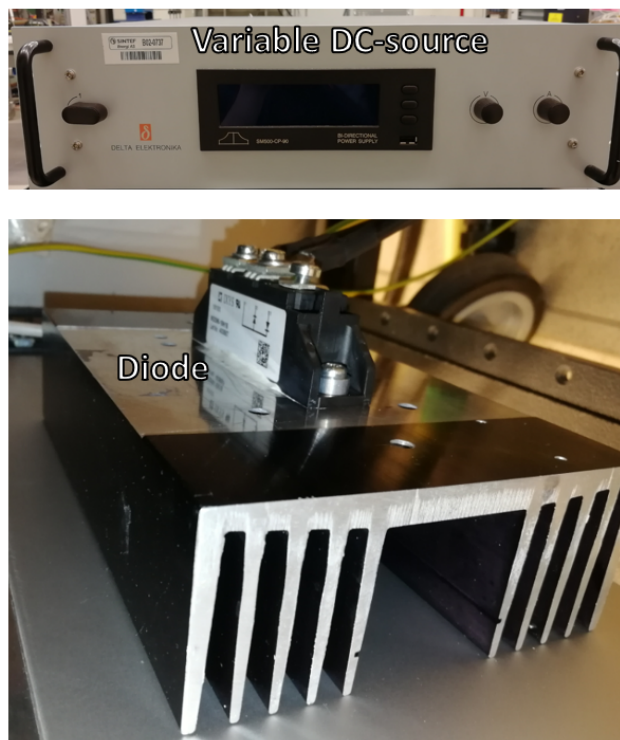
Figure 13.2: Variable DC-source (top) and diode (bottom). The diode is mounted to a heat exchanger.

IM ————————————————————————————————
Strömberg: Three phase asynchronous machine. (HXUR 565G3 B3)
380V(Y) (line-line, rms), 110A (rms), 55kW, 50Hz, 990 rpm
(NTNU-Elkraft Archive ID: A03-0106)
Position encoder: Heidenhain ERN 420 (2048 ppr)

PM ————————————————————————————————
Vem Motor: Three phase asynchronous machine. (KMER 280 M6)
220V(Y) (line-line, rms), 179A (rms), 55kW, 50Hz, 980 rpm
(NTNU-Elkraft Archive ID: A03-0105)
Position encoder: Leine&Linde (1024 ppr)

Figure 13.3: Induction machines

Figure 13.4: Position encoders for induction machines. IM not connected in picture.

VSC _____

60 kVA 2L-3ph AC-DC Inverter. 400 V(AC, line-line, rms), 650V (DC), 100A (rms)

(NTNU-Elkraft Archive ID: B03-0488)

This multi-purpose 2L-3ph VSC is based on a three phase IGBT and diode rectifier module (Semikron SEMIKUBE IGDD6-2-428-D1616-E1F12-1DH-FA). Amongst other things, its integrated with a gate-driver for the IGBTs (SEMIKUBE Board GD11) and a FPGA based controller processor board (Xilinx Virtex5). Set up in a "motordrive"-configuration, its DC-link is powered directly from a DC-source. The IGBTs (SKM400GB126D) are rated for 1200V, 400A. The DC-link is composed of electrolyte capacitors rated 14 mF. The converter has a user interface with an LCD-display, 4x D/A BNC-ports to extract internal parameters and shrouded banana contacts for voltage measurements of the DC-link and the midpoints of the three IGBT-legs.

AC-Driver _____

ABB: Frequency converter (ACS 600)

400V (line-line, rms), 145A (rms)

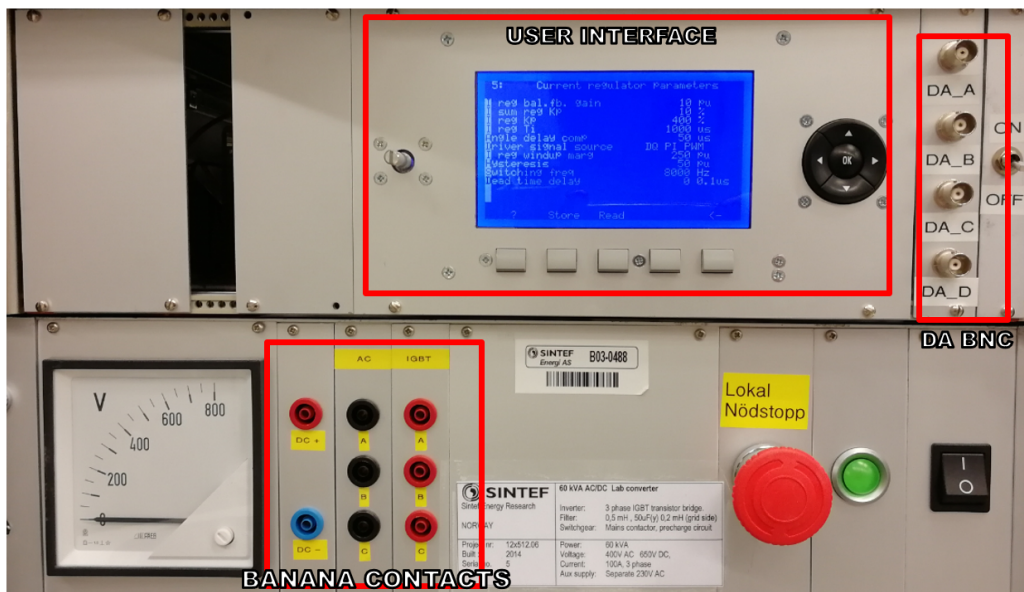(NTNU-Elkraft Archive ID: B03-0551)

Figure 13.5: Converters

Figure 13.6: Interface of VSC

OSC

Tektronix: Mixed signal oscilloscope (MSO 2014)
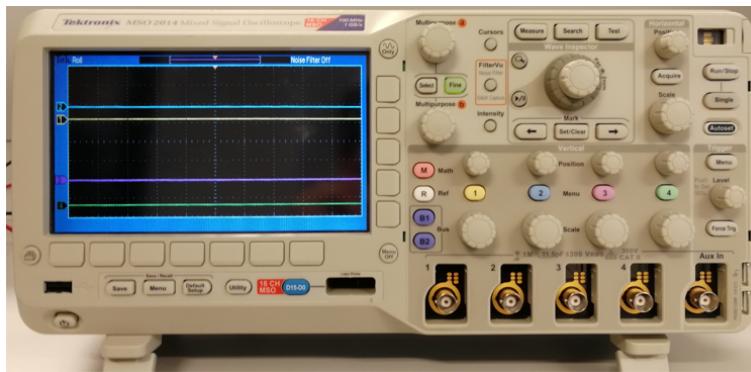
16Ch, 1GS/s, 100MHz

Figure 13.7: Oscilloscope

Current probes (AC)

Fluke: AC current probe (i1000s)

0.1-1000A rms, 5Hz-100kHz

Current probe (DC)

Fluke: AC/DC current probe (80i-110s)

0.1-100A, 0-100kHz

Voltage probes

Tekronix: High-voltage Differential Probe (P5200A).

±1300V peak, 50MHz, x50/x500 attenuation

Figure 13.8: Measurement-probes

13.2 Configuration

Variable DC-source:

The levels of voltage and current can be freely set within the rated range. For all tests, the current was set to an upper limit of +90A.

AC-driver:

Controlled through a button+display interface allowing to set the prime-mover reference speed in rpm.

Current probes (AC):

For measurement of the IM phase-currents, clamped around corresponding cables. For all tests, configured in the 10mV/A mode.

Voltage probes:

For measurements of DC-link voltage and phase-voltages (midpoints of IGBT-legs). Connected to the banana-contacts (Figure 13.6). For all tests, configured with 1/500 attenuation.

Current probe (DC):

For measurements of DC-source current, clamped around corresponding cable. For all tests, configured in the 100mV/A mode.

Oscilloscope:

All inputs are set to "DC-coupling" mode. The length of captured time-series varies depending upon what is being measured. The oscilloscope has four BNC-inputs, limiting the number of signals possible to capture per take.

13.2.1   VSC configuration

The built-in processor, sensors and user interface of the VSC allows for a range of adjustable operational modes. Due to the vast range of input-parameters such as PI-controller gains, filter-time constants, etc. , the following description will focus on the most relevant parameters.

The control structure is built on current-control of d- and q-components with a rotor position feedback, i.e. the indirect FOC method. The converter is set to work in the DC-link voltage control mode (except for Lab Test 1, Section 13.3), which is also the main control variable for the proposed generator control-systems as presented in Chapter 10. PI-controllers adjust the references of current. The reference for field current (i_d^s) is variably adjusted according the DC-link voltage and speed. An increase in speed above the nominal value, and lower DC-link voltage results in reduction of the field-current reference. Similar to the proposed FOC-method (Section 10.3), a current hysteresis-controller is used to create gate-signals. The current references are however compared with measurements the dq-domain, which errors form the basis of a per-phase duty-cycle when converted to the abc-domain. A PWM-modulator of fixed frequency then generates the switching-signals based on these duty-cycles.

Some core parameters in the setup are as follows:

- Rotor time constant: 0.9s

- Excitation (field-current): Rated: 30%, Max: 100%, Min: 5%

- Max slip speed: 10Hz

- Rated current: 110A. Trip-level: 245A.

- Number of poles: 6

- Switching frequency: 8000Hz

- Dead time delay 0.1 μs. (Added delay to control signals when a leg is conducting, aka blanking-time)

- Hysteresis: 5% of rated current

- Pulses per revolution of position encoder: 2048

- Speed: Trip-level: 1400 rpm

- DC-link voltage reference: 400V

13.3 Lab Test 1: Output voltages at steady state

13.3.1 Purpose and setup

These tests functions to inspect the voltage-waveforms applied to the IM and the corresponding switching-patterns. The prime-mover (PM) is disconnected from the AC-driver, and the VSC is set to speed-controller operation, drawing power from the DC-source. The IM is thus operated as a motor. At steady-state, the phase-neutral voltages are measured for all three phases by connecting the voltage-probes between the AC-contacts (A, B and C) and DC-, Figure 13.6. The last slot of the oscilloscope is used for a measurement of a phase-current. Table 13.1 summarises the configuration and data-quality of the samples.

Control mode	Speed
Speed reference (ω_m)	500 rpm
DC-source voltage	100 V
Sample frequency	1.25 MHz
Measurement length	0.1 s
Resolution	1V, 0.4 A

Table 13.1: Lab Test 1

13.3.2 Results

Figure 13.9 shows a sample of measured phase-neutral voltages. By closer inspection (Figure 13.10) we can identify the PWM-patterns with a switching-frequency of 8000Hz. The voltage changes in seemingly discrete steps of approximately 100V (V_{DC}). To obtain an approximation of the phase-voltages, we can apply (5.2) (2L-3ph VSC model). The results are shown for two samples, Figure 13.11 and Figure 13.12. The dashed lines (- -) marks the $\pm \frac{2}{3} V_{DC}$ boundaries. The plots show the expected phase-shifts of the three phase-voltages, with shapes similar to that of Figure 6.2. They are periodic, with a frequency of approximately 25Hz (as expected for this IM with $n_{pp} = 3$ operated at 500rpm). One phase current is also shown per plot, seemingly lagging its phase-voltage, which coincides with the inductive nature of the IM.
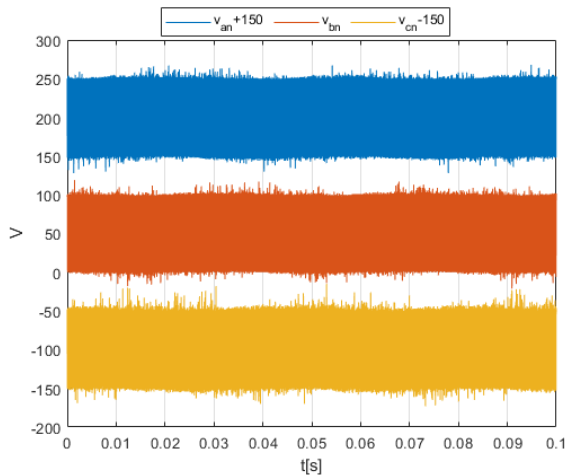
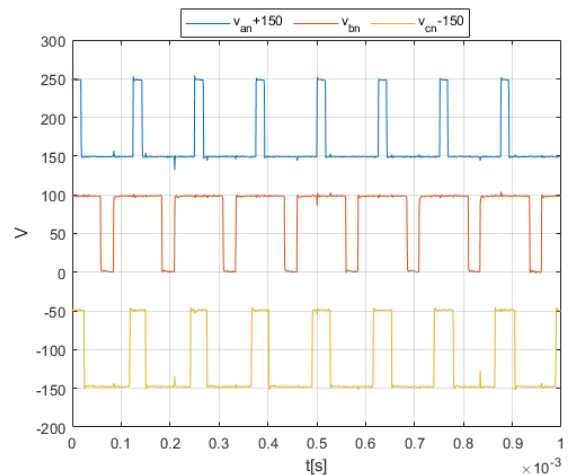

Figure 13.9: Phase-neutral voltages
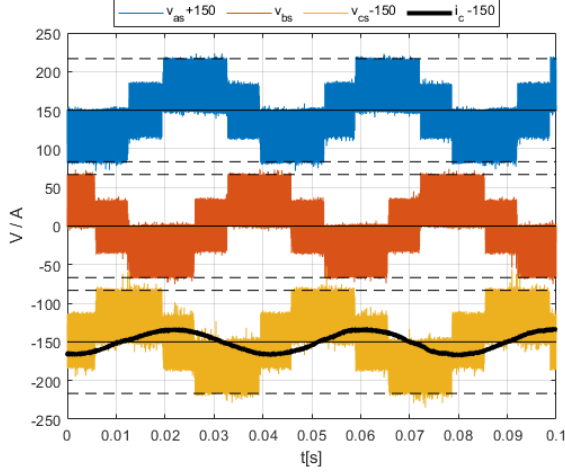

Figure 13.10: Phase-neutral voltages (zoomed in)

100

Figure 13.11: Calculated phase voltages and i_c [30]
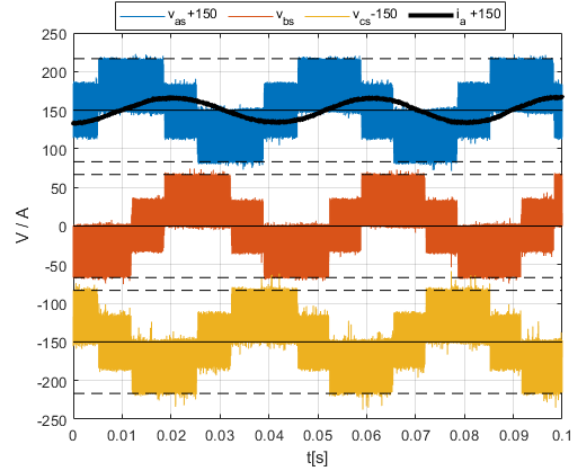

Figure 13.12: Calculated phase voltages and i_a [31]

13.4   Lab Test 2: Magnetisation for different speeds and initial DC voltages

13.4.1   Purpose and setup

The purpose of these tests are to study how the VSC and IM interacts when operated in the DC-link voltage control mode ($V_{DC\mathrm{ref}} = 400V$). The aspects of interest are similar to that of the magnetisation test in the simulation study (Section 12.2). Performance indicators such as the charge-up time, settle-time, generator peak current, DC peak voltage, DC-source peak current and work will be used to analyse the effects of varying the initial DC-link voltage (V_{DC0}) and the PM speed reference (ω_m).

For all samples in this test, the following setup applies:
The PM is connected to the AC-driver, set to follow a specified speed (ω_m). The variable DC-source is set to a fixed initial voltage (V_{DC0}). When the speed has stabilised and the DC-link voltage of the VSC is equal the DC-source voltage ($V_{DC0} = V_{DC}$), the control-system of the VSC is activated, and up to 4x quantities are sampled with the oscilloscope.

13.4.2   Overview of samples and corresponding measurements

With the configuration (controller-setup) of the VSC kept fixed for all samples, there are two references in the experimental conditions than can be varied (V_{DC0} and ω_m). Because the oscilloscope is limited to 4x input signals, some references are replicated for the purpose of gathering measurements of other quantities.

The samples can be classified into four types, based on the measured quantities. Table 13.2 shows the indexations and corresponding measurements. The 51 samples are mapped according to their references in Table 13.3. The measurements of active (i_q*) and reactive (i_d*) current-reference, and the speed (ω_m) are fetched for the VSC itself, using the D/A BNC-contactors (Figure 13.6).

Index	Measurements	Number of samples
#1	i_{abc}, V_{DC}	15
#2	i_b, i_q*, i_{DC}, V_{DC}	30
#3	i_b, i_q*, i_d*, V_{DC}	3
#4	i_b, ω_m, V_{DC}	3

Table 13.2: Sample classifications

V_{DC0}(V) ↓ | ω_m(rpm) →	200	400	500	600	800	1000
10					#1.11 #2.19 #2.20	#1.14 #2.25 #2.26
20						#1.13 #2.23 #2.24
30				#1.8 #2.13 #2.14		
35	#1.2 #2.3 #2.4					
40	#1.1 #2.1 #2.2	#1.4 #2.29 #2.30		#1.7 #2.11 #2.12	#1.9 #2.15 #2.16	#1.12 #2.21 #2.22
42	#3.1 #4.1		#3.2 #4.2			#3.3 #4.3
100	#1.3 #2.5 #2.6	#1.5 #2.7 #2.8		#1.6 #2.9 #2.10	#1.10 #2.17 #2.18	#1.15 #2.27 #2.28

Table 13.3: Samples and corresponding references of V_{DC0} and ω_m

The samples of type #1 was first performed to determine, for various speeds, the minimum initial voltage at which the VSC and IM would be able to charge up the DC-link. For each speed, the starting-point was $V_{DC0} = 10V$, which were increased in steps of 5V until the lowest successful initial voltage was found. Only successful charge-ups are noted in Table 13.3. The additional measurements of type #1 at higher V_{DC0} are included to study the influence of varying the initial DC-link voltage at different speeds. The type #2 samples are performed at the same references as the type #1 samples, but the measurement of i_a and i_c are replaced with i_{q*} and i_{DC}. The type #2 samples are also performed twice, giving some room to study the variability of the results at a given reference-configuration.

The samples of type #3 and #4 are all taken at $V_{DC0} = 42V$, for three different speeds (200rpm, 500rpm and 1000rpm). Their main purpose is to study the controller-references and speed-variations.

All the samples in Table 13.3 (except #1.5 and #2.26) are of measurement length t=4 seconds, with a corresponding sample frequency of 31.25 kHz. This length was required to capture the full duration of the magnetisation. For #1.5, t=2s at 62.5 kHz, and for #2.26, t=10s at 12.5 kHz. To keep the data-files and saving-times low (Oscilloscope), a compromise was made with respect to the vertical resolutions, which are given in Table 13.4.

Measurement	Resolution
i_{abc}	2A
V_{DC}	4V
i_{DC}	0.08A
i_{q*}	0.8% (of rated current)
i_{q*}	0.4% (of rated current)
ω_m	8 rpm

Table 13.4: Measurement resolutions

13.4.3 Minimum initial DC-link voltage

Looking at Table 13.3, the minimum DC-link voltages from type #1 samples are shown in Figure 13.13. Although the amounts of data-points are limited, there seems to be a trend that lower speeds requires higher initial DC-link voltage to successfully charge up the capacitors. The $V_{DC0} = 40V$ at 400 rpm does however make this trend questionable, but it could also be the result of pure chance. During the acquirement of the type #2 samples, some of the minimum-voltage conditions required several attempts to be replicated.
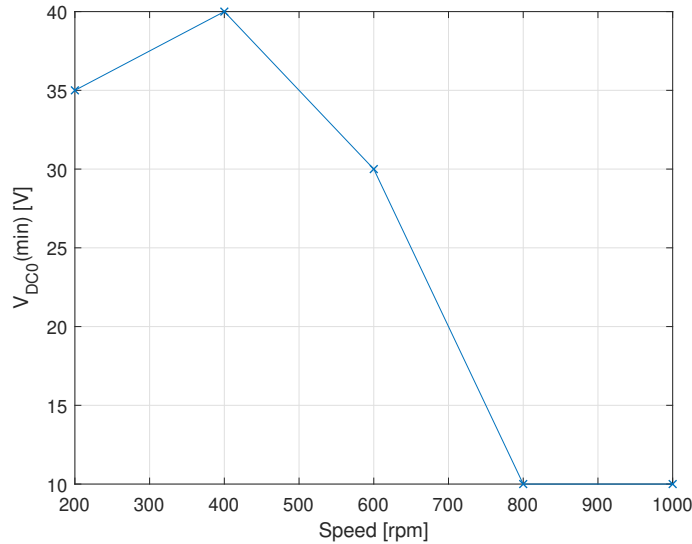
Figure 13.13: Speed and minimum DC-link voltage

Figure 13.15 shows a failed charge-up attempt ($V_{DC0} = 24V$), with Figure 13.14 for reference ($V_{DC0} = 40V$). In terms of stator-currents, the configurations show similar development. In Figure 13.14, V_{DC} have some tiny spikes before it gets traction at about t=1.5s. Interestingly, a similar positive change of V_{DC} is seen in Figure 13.15, but it dies out. In this operation, the VSC is draining power from the variable DC-source to maintain the current, which in fact is almost at the trip-limit. Somehow, it is still unable to produce the required torque, and this might be related to the inner working of the VSC control system. A possible explanation could be that the VSC (with a low voltage) is not able to properly decompose the stator current into active and reactive components, such that the resulting torque (and power at this given speed) can overcome the heating-losses as a result of the currents themselves. With this logic, higher speeds gives more power for a given amount of torque, in combination with higher back-EMF that limits the drawable current, and thus also heating-losses. This trade-off might be the cause for the observed lower required initial voltages at higher speeds.
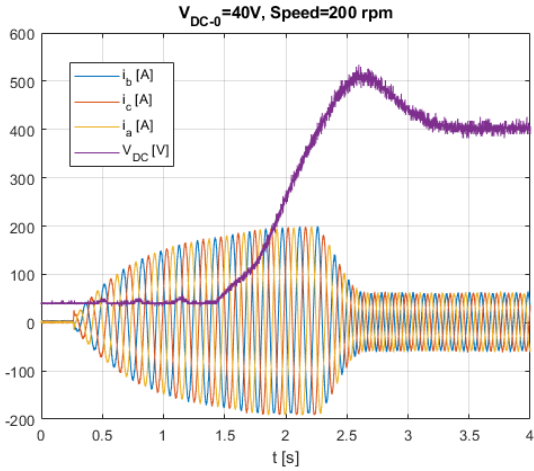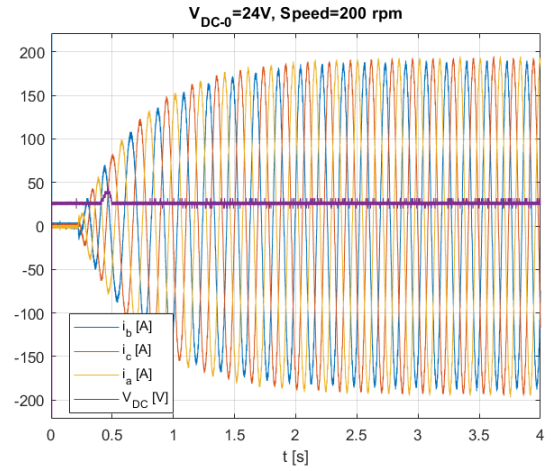
Figure 13.14: Sample #1.1

Figure 13.15: Failed charge-up

13.4.4 Charge-up and settle-time

The following results are based on visual inspection of the type #1 and #2 samples. The charge-up time is defined as the time from which the VSC is engaged, until the DC-link voltage crosses the 400V reference. The settle-time is the time required for the voltage to stabilise at this reference (minus the charge-up time). Figure 13.16 and Figure 13.17 shows the results. The dots marks individual samples, and the lines connects the average-values of samples taken at the same references of V_{DC0} and ω_m.

Finding any clear and credible patterns is limited by the data available. The variability also tends to be high for samples taken at low values of V_{DC0}. With this being said, two trends seems to emerge from the plots. Firstly, increasing V_{DC0} tends to reduce the charge-up and settle-time. Secondly, the charge- and settle-times seem to be speed-dependent, with an optimum (lowest) point somewhere between 200-1000 rpm. Working toward the optimum from either direction will decrease the times, and this fictious optimum might be dependent upon V_{DC0}.
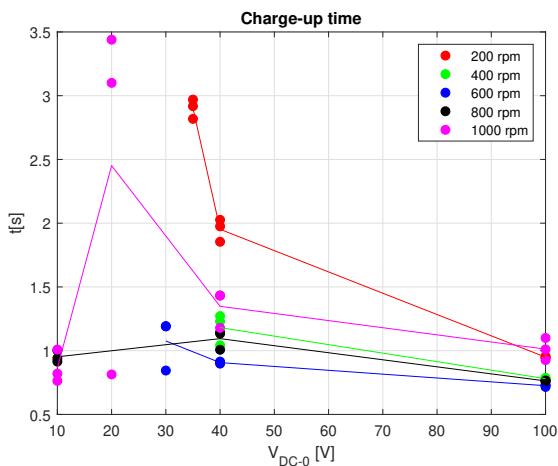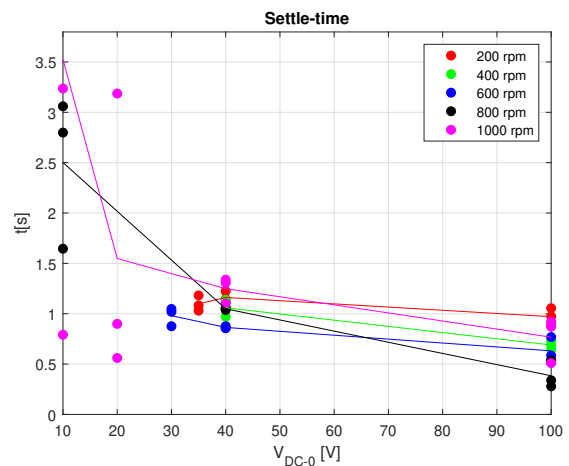

Figure 13.16: Charge-up time

Figure 13.17: Settle-time

13.4.5 Peak values

Similar to the previous section (Section 13.4.4), the following results are based on visual inspection of the type #1 and #2 samples. Both #1 and #2 contains measurements of atleast one stator-current and the DC-link voltage, which can be used to find their corresponding peak-values during the magnetisation, Figure 13.18 and Figure 13.19. #2 also contains i_q*, with the peaks shown in Figure 13.20.

With similarities to the charge-up and settle-time, the variability is higher for lower values of V_{DC0}, and we observe that the peak-values tend to decrease for higher V_{DC0}. Also note how all the peak-values tend to descend for increasing speeds when $V_{DC0} = 100V$. For lower V_{DC0}, this pattern seems to shift towards a lowest "optimum" at 600rpm.
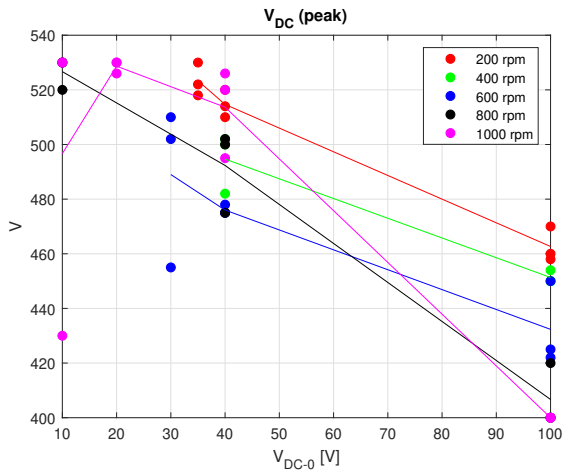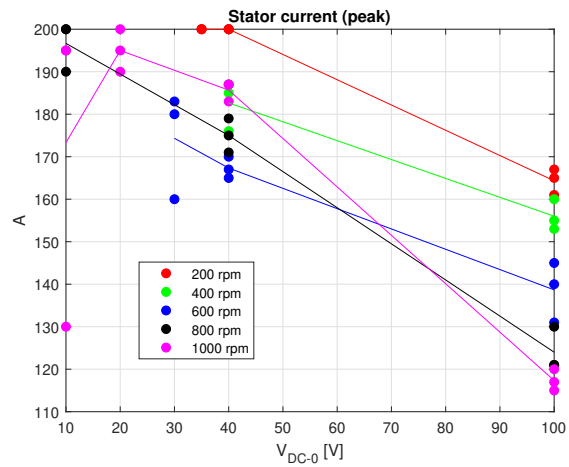

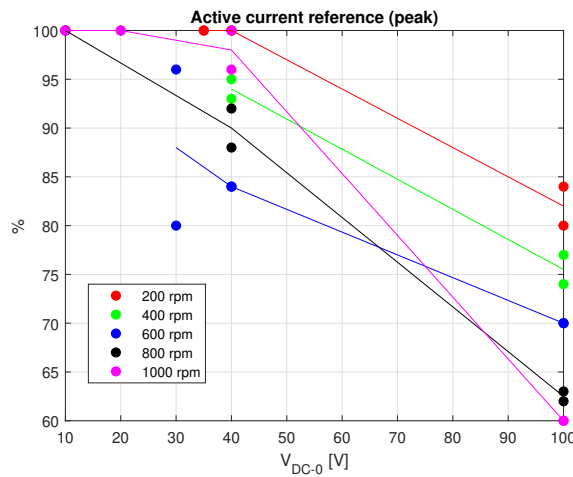Figure 13.18: DC-link voltage peak

Figure 13.19: Stator current peak

Figure 13.20: Active current reference peak

13.4.6   DC-source current and work

The following results are based on inspection of the type #2 samples. The DC-source peak current (Figure 13.21) is obtained by visual inspection. The DC-source work (Figure 13.21) is estimated by integrating the product of $i_{DC}(t) \cdot V_{DC0}$. The dots in the plots marks individual samples/estimations, and the lines connects the average-values of samples/estimations at the same references of V_{DC0} and ω_m.

Before we inspect the graphs, it should be noted that for some samples, i_{DC} exceeded the range of the oscilloscope-input (see Figure 13.23). This applies for #2.1-#2.4, #2.29, and #2.30, which was performed for speed references 200rpm and 400rpm, with V_{DC0} at 35V and 40V. The validity of these samples are thereby limited. Because these conditions are in the low-speed and low initial-voltage range, we might claim that a decrease of ω_m and V_{DC0} results in higher peak-values of current.

Looking at Figure 13.21, no evident pattern is observed. The peak-values seems to be independent upon speed when $V_{DC0} = 100V$, with a common peak at $V_{DC0} = 40V$. High speeds combined with low V_{DC0} also seems to result in lower peak-values. In terms of DC-source work, the full scale of the 200rpm graph is not shown, but

its maximum work at V_{DC0} was 800J. For the 200rpm and 400rpm case, there seems that higher V_{DC0} reduces the required work. The opposite is true for the 600rpm-1000rpm estimations.
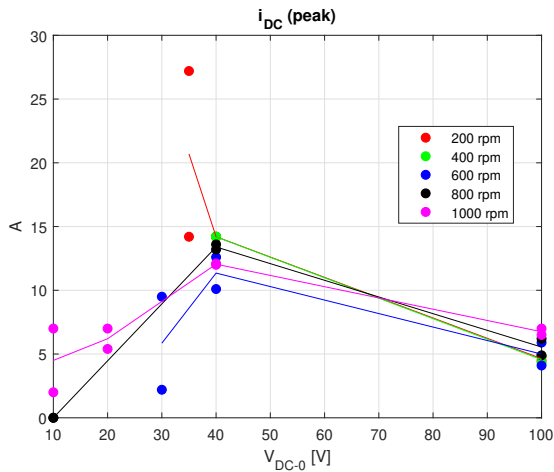

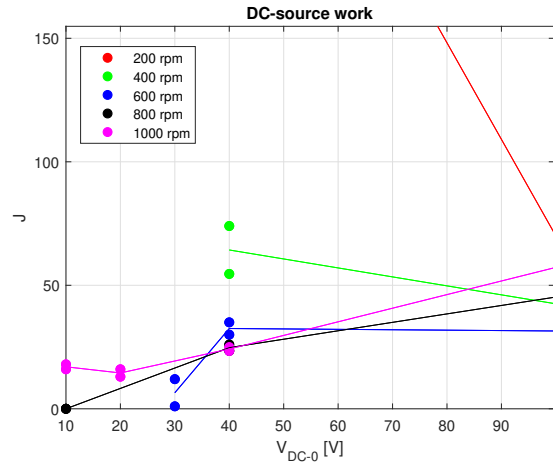Figure 13.21: DC-source current peak

Figure 13.22: DC-source work

13.4.7 Plots of the magnetisation elapse

The previous analysis has been heavily based on indicators and ambiguous graphs. Below are ten plots (Figure 13.23-Figure 13.32) of the type #2 samples, given to provide for a more visual representation. They correspond to the five levels of tested speeds, shown for the corresponding minimum V_{DC0} and $V_{DC0} = 100V$.

Generally, the stator-currents grows steadily in magnitude, and they are consequently reduced to a steady-state magnitude when the DC-link voltage approximates its reference value. This pattern seems to be concurrent with the active reference (i_q*). Starting with the minimum V_{DC0} seems to prolong the duration of high currents, especially noticeable for the speed of 200 rpm (Figure 13.23 and Figure 13.24). It seems that for the speeds of 600-1000rpm, the build-up of V_{DC} starts at lower values of stator-current when the minimum V_{DC0} is applied (compared to $V_{DC0} = 100V$). The build-up of V_{DC} is not always smooth, and the oscillations seems to be more prominent for the cases with the minimum V_{DC0}. With a generally smooth i_q*, the cause could lie in the reactive reference (i_d*).
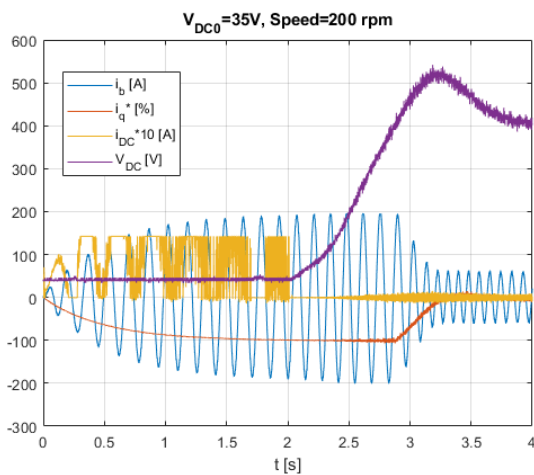

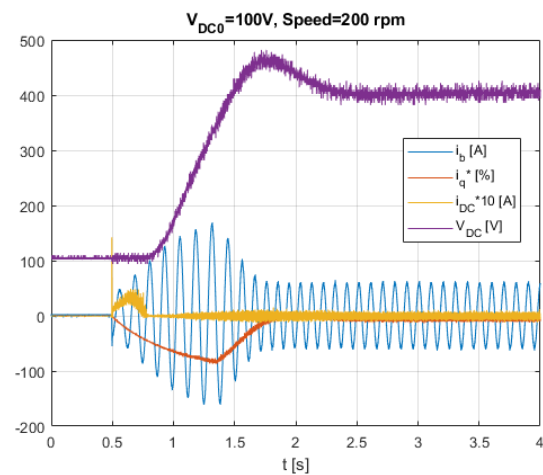Figure 13.23: Sample #2.3
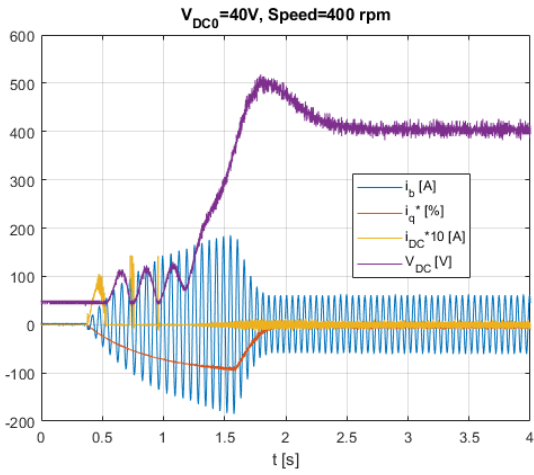

Figure 13.24: Sample #2.5
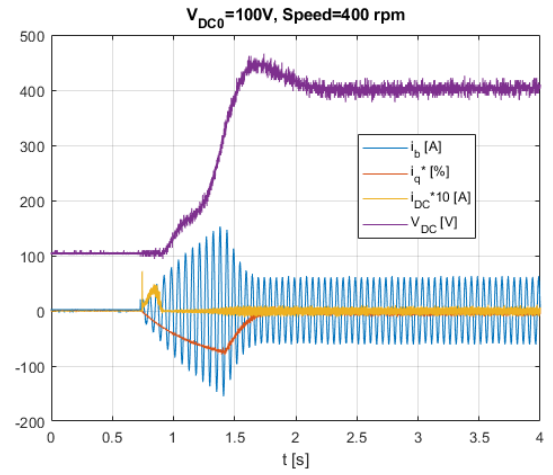
Figure 13.25: Sample #2.29
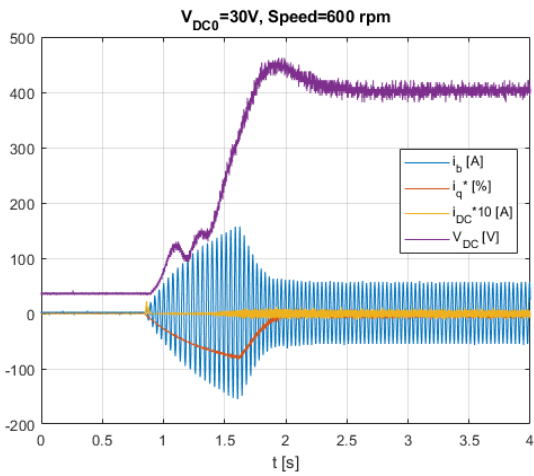

Figure 13.26: Sample #2.7
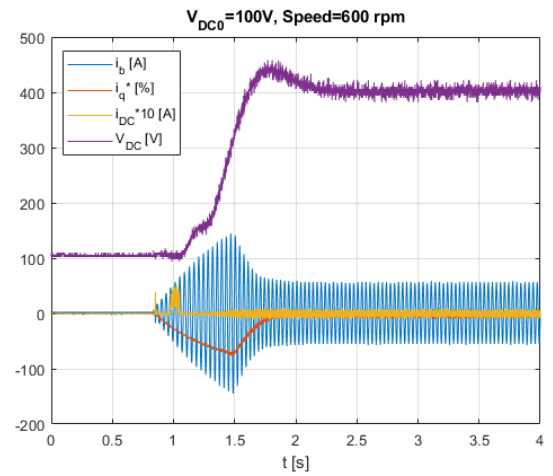

Figure 13.27: Sample #2.13
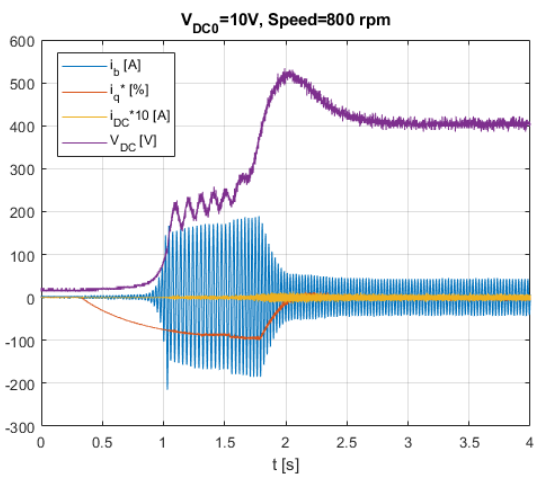

Figure 13.28: Sample #2.9
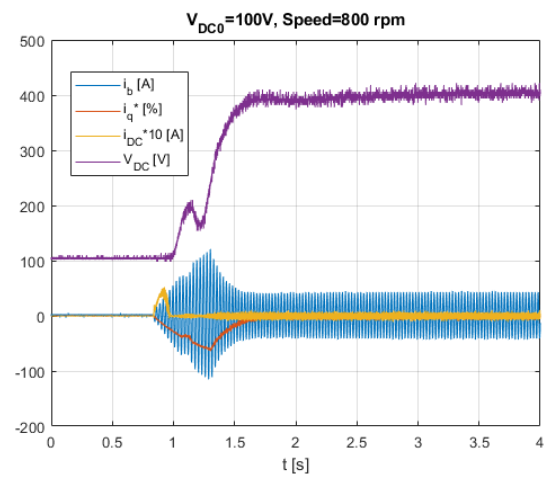

Figure 13.29: Sample #2.20
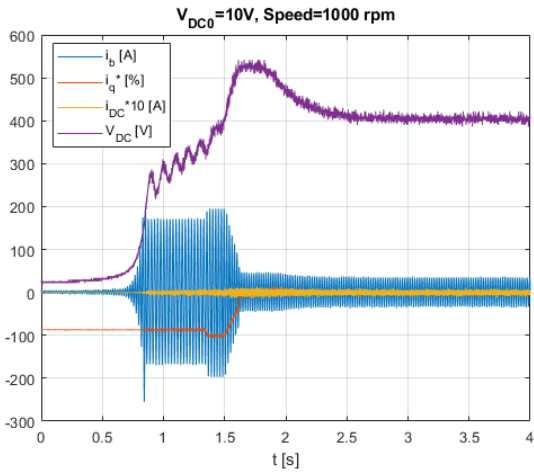

Figure 13.30: Sample #2.17
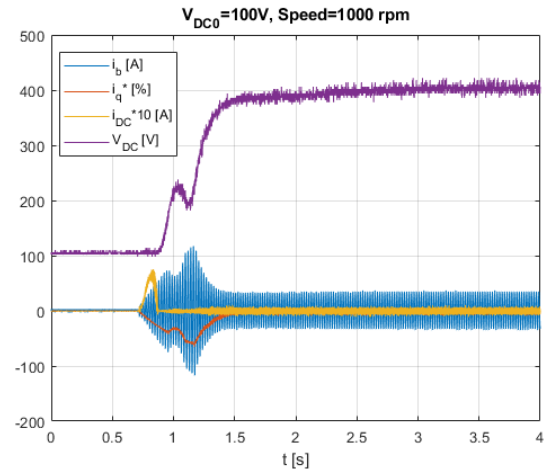
Figure 13.31: Sample #2.25

Figure 13.32: Sample #2.27

13.4.8 Speed deviation and controller references

Given below are plots of the samples of type #3 and #4 (Figure 13.33-Figure 13.38).

The active reference is negative because the IM is working as a generator during the magnetisation. For all three speeds, we can identify how the reactive reference is steadily increasing according to the available DC-link voltage. For increasing speeds, the adaptation of i_{d*} seems to be suboptimal, as it causes some oscillations in the DC-link voltage. The reactive reference stabilises at 30% for 200rpm and 500rpm, which is equal the rated excitation the VSC is configured for. For 1000rpm, i_{d*} stabilises at around 18% (field weakening). i_{q*} steadily approaches the 100% limit for the 200rpm and 500rpm speed. For 1000rpm however (Figure 13.37), we can observe what seems to be a temporary upper limit, which is further increased during the final stage of the magnetisation.

Though very coarse in resolution, the speed seems to dip down to about -60rpm, -20rpm and -18rpm for the speed-references of 200rpm, 500rpm and 1000rpm respectively. The cause is the sudden negative torque of the IM which the PM (and AC-driver) is unable to perfectly compensate for. A higher speed-deviation for lower speed-references is also expected since the rotational kinetic energy stored in the system is lower.
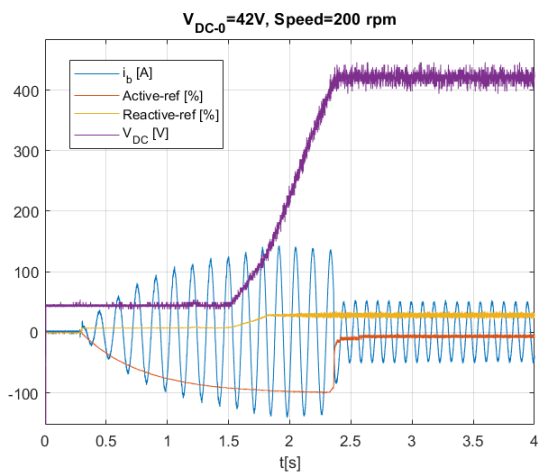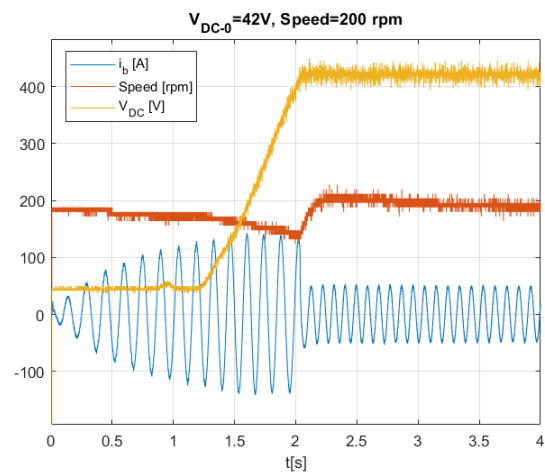

Figure 13.33: Sample #3.1
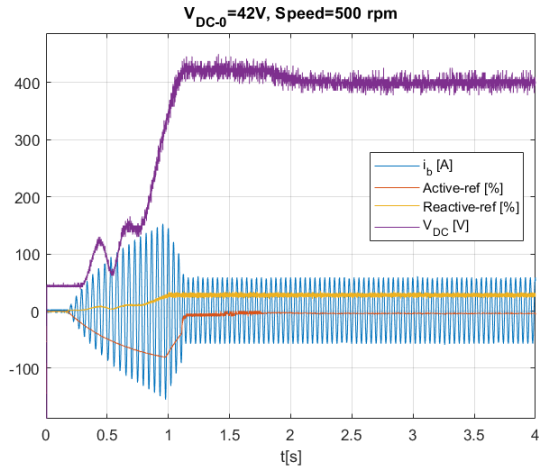

Figure 13.34: Sample #4.1
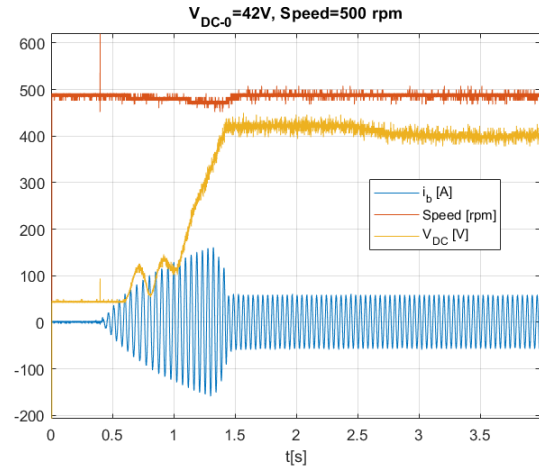
108

Figure 13.35: Sample #3.2
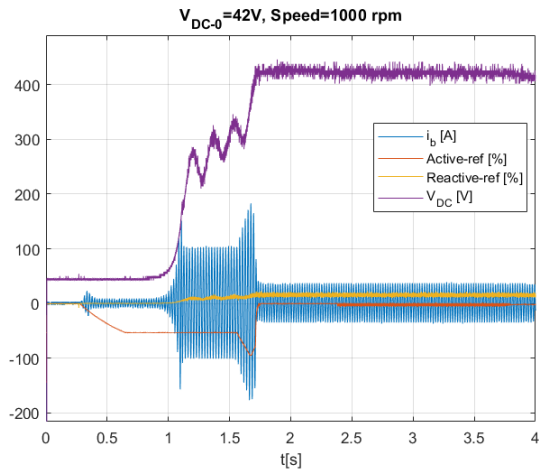

Figure 13.36: Sample #4.2
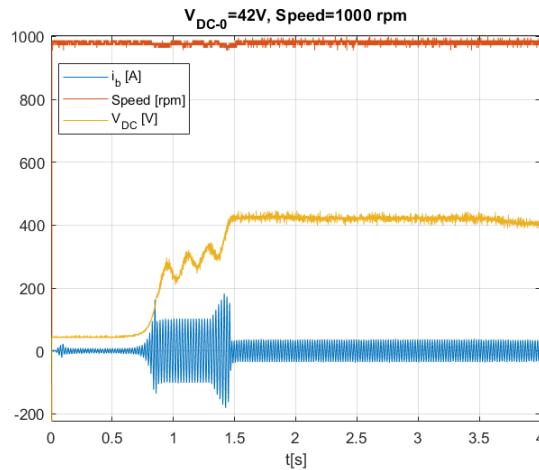

Figure 13.37: Sample #3.3

Figure 13.38: Sample #4.3

13.5 Conclusion

The magnetisation-tests performed has shown that a rotating induction machine can be magnetized by means of a VSC and some initial help from a low-voltage source. Although the rating of the IM (55kW) and converter (60kVA) are unquestionably higher than the power range of interest (3-10kW), the configuration managed to charge up the DC-link to the 400V reference (within 1 second) with initial-voltages as low at 10V at rated speed (1000rpm), drawing DC-currents no larger than 15A. Operation at lower speed does however required larger initial-voltages, up to 35V at 200rpm.

Sources of error and review of tested conditions

The VSC was operated with its built-in indirect FOC control system. Although the parameter-settings was kept fixed during all the tests and different configurations, the analysis (in Lab Test 2) shows that the performance varies when tests are repeated for same conditions of initial voltage (V_{DC0}) and rotor speed (ω_m). There could be several reasons for this. The machine is for instance expected to heat up after prolonged testing, which would alter its electrical characteristics. The full details of how the VSC operates is also not known, and there might be some quirks or unknown variables not accounted for that causes the apparent inconsistencies. Although a total of 45 samples was used as basis for studying the magnetisation and DC-link charge-up, they only cover a limited range of speeds and initial voltages. Looking at Table 13.3, there should have been more measurements for V_{DC0} in the 40-100V range. The lower range of speeds (200-600)rpm did not successfully charge up with voltages lover than 30V, and thus, there is also no data for comparison to the higher speeds (800-1000)rpm.

Measurements for speeds above 1000rpm could also have given more insight. Finally, some of the most used measurements (stator currents and DC-link voltage) had a quite coarse resolution (2A and 4V). This influences how accurate the analysis can be made.

Comparison to simulation-results

With the above considerations stated, we can make a comparison of the results and analysis of this lab experiment to the theoretical observation made in the simulation (Chapter 12). Again, note that this is <u>not</u> a direct comparison of how a specified (i.e. identical design) control-system performs in simulations vs. real-life.

In terms of controller performance (FOC), the lab-results shows that the generator currents never exceed the trip-level of 245A, but compared to rated current, it exceeds up to 30%, compared to 7% in the simulation. The same goes for the DC-link voltage overshoot, up to 33% compared to 3% in the simulation. The time-constant used in the simulations to determine the capacitance (H_C=0.1s) is however larger than the one in lab-configuration (H_C=0.02s, based on $C_{DC} = 14$mf, $V_{DC} = 400V$ and $P_N^G = 55$kW). The sum of charge-up and settle times in the simulations lies below 1 second. It was also observed that higher V_{DC0} gave shorter charge-up times. The same trend is observed in the lab-results, but the sum of charge-up and settle times can vary between 1-6 seconds, despite the lower relative H_C. Losses in the physical system could be a contributing factor.

Conceptually, any $V_{DC0} > 0$ could result in a successful magnetisation in the simulation study. This was not the case in the lab-results. The battery peak current and work delivered was increased for lower speeds and higher V_{DC0} in the simulation. No clear pattern is shown in the lab-results, and some of the inaccurate measurements of i_{DC} limits the validity. If anything, the lab-result seems contradict the simulation due the apparent decrease of DC-source peak-current for $V_{DC0} > 40V$. Omitting the results of 200rpm and 400rpm, the peak-currents of this 55kW machine seems to stay below 15A, with a work up to a maximum of 60-70J. This is low compared to the largest machine in the simulations, #M4 (16.7kW), which drew up to 120A with a work of 50J. However, the internal resistance of the battery in the simulation was also chosen arbitrarily.

The current references (i_q* and i_d*) of the lab-VSC seems to be increased gradually during magnetisation. The reactive component is dynamically scaled according to the DC-link voltage and kept at the rated excitation when speeds are not too high. The implemented FOC-method in the simulation exhibits a similar behaviour, but the increase/decrease method starting a high level of i_d* gives distorted currents in the start. The current produced by the lab-VSC was generally smooth straight from the start. Additionally, it uses a switching frequency of 8kHz, compared to 50kHz in the simulation. There is thus room for improvement in the hysteresis current-controller used in the simulation. The simulated FOC-method did show some minor oscillations of DC-link voltage when the rotor time-constant (τ_r) was not defined correctly, but it's hard to say that this is the cause for the oscillations of V_{DC} observed in the lab-results.

14   Arduino Uno as a controller

The Arduino Uno (A000066), Figure 14.1, is an low-cost open-source electronics board. It's based on the Atmel ATmega328P 8-bit micro controller, with a 16MHz clock speed (quartz crystal), 14 digital I/O-ports, 6 analog I-ports and a USB-connection. It's well documented, with MATLAB-support packages for integration with Simulink.

A converter-controlled application would require a processor to take in measurement from sensors, execute the control-system and give out gate-signals. This chapter will study the suitability and limitations of the Arduino Uno as a low-cost option for use as a VSC-controller. A simplified version of the proposed V/f-control method is implemented, and the performance is evaluated by measurements from an oscilloscope.
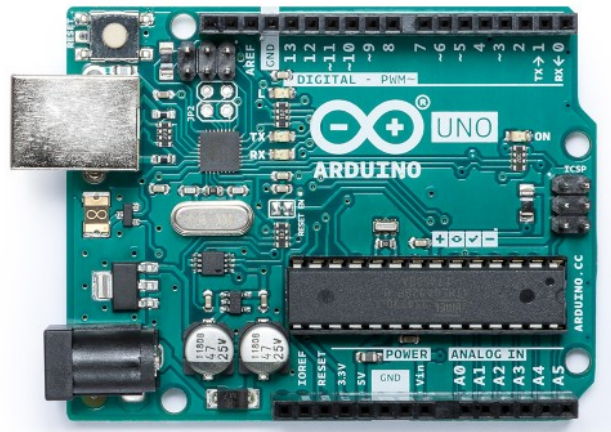

Figure 14.1: Arduino Uno layout. Source: `https://store.arduino.cc/arduino-uno-rev3`

14.1   Technical details

14.1.1   Processing capabilities

The processor and layout of the board sets the limit for its operational and computational capabilities. Although a 16MHz clock-speed provides a theoretical possibility to handle calculations in small time-ranges, the built-in functions requires several clock-cycles to execute. For instance, the digital-write function takes up 56 clock cycles, and a sample of analog-read requires about 0.1ms (10-bit resolution) [47]. The speed of the digital-write can be increased by removing built-in protection in the functions, and the analog-read sample rate can be increased at the cost of lower resolution. For instance, a open-source project on GitHub demonstrate the possibility to implement a S-PWM scheme with a switching frequency of 10kHz [48].

Nevertheless, assigning more task to be done per loop (single threaded) by the processor requires longer time to execute the calculations (T_{ex}). The defined sample time (ΔT_{samp}), which is how often the loop should be executed, should therefore be equal or larger than execution time ($\Delta T_{samp} \geq T_{ex}$). This is important for time-sensitive tasks such as producing periodic S-PWM gate signals.

14.1.2   Pins and ratings

To keep the employment simple, the following implementation will be limited to the available options in the Simulink support-package. The specifications and rated values of the pins are summarised as follows:

- Voltage range: 0-5V

- Built-in voltage sources: 3.3V and 5V

- Digital I/O current: ± 20mA

- Analog input resolution: 10 bit

- Analog minimum ΔT_{samp} (Simulink support package): $1 \mu s$

The digital pins 3, 5, 6, 9, 10 and 11 have the ability to be operated in a built-in PWM-mode, with a duty-cycle of 8-bit resolution. The switching frequency is approximately 490Hz, with an exception of pin 5 and 6, which operates at approximately 980Hz.

14.2 Implementation and setup

The simplified V/f control loop will consist of two fictitious measurements, DC-link voltage (V_{DC}) and mechanical speed (ω_m). These will be fed to a PI-controller to adjust the frequency reference (by adding a slip-speed) and the amplitude modulation (by employing the RMS/DC model). The sine-references are finally made into gate-signals by the S-PWM-method.

A realistic test-setup would involve continuously varying input-measurements as a function of the controller output and other variations at the intended application (like a VSC connected to an IM). This experiment is however defined to study only the suitability and limitations of the Arduino Uno as a controller. The performance will be evaluated by measuring the output-signals directly from the board and compare them to what is theoretically expected. The input-measurements will be made into different levels by means of series-connected resistors and thus kept constant (i.e. non-varying) during the tests. Keeping the input-measurements fixed allows for better predictability of expected controller output, and a simpler comparison of different configurations.

14.2.1 Hardware constraints

For input-measurements, the analog-in pins must be used. The input must be conditioned to the range of 0-5V. The resolution of $2^{10} = 1024$ levels, divided by the range of the physical quantities measured, limits the control-range accuracy. With a total of 6 analog input pins, it's possible to acquire all the required signals proposed in the "full" version of the V/f-method (V_{DC}, ω_m, i_a, i_b, i_c).

The 2L-3ph VSC requires 6x gate-signals. The digital ports are suited for this, providing on/off states. All gate-signals should be in the same switching frequency range to obtain balance in the output voltage frequency spectrum. By writing directly to the digital-out pins, this is employable. By using the built-in digital PWM-modes, the board lacks the sufficient number of supported pins (x6) of the same switching frequency. To study both options, the implementation is thereby chosen to produce only three digital gate-signals, one for each phase, where the on-state represent turning the upper switch of a leg on, and the off-state represents turning the lower switch of a leg on. We thus have two output-pin modes:

- **Mode 1:** Using built-in PWM-mode, with 490Hz switching frequency at 8-bit duty-cycle resolution

- **Mode 2:** Writing directly to output-pins

14.2.2 Equipment setup

Figure 14.2 shows a schematic of the circuit-layout used in the following tests. The program code is generated with MATLAB-Simulink and uploaded via the USB-connection (which is also used to power the Arduino board). The details of the control system is shown in Section 14.3. Using the on-board 5V source, 5x 1kΩ resistors are connected in series, which are used to create fictions input-measurements. The analog inputs (A0 and A1) can be connected to one of the red ports indicated in Figure 14.2, giving a measurable range of 0-5V with steps of 1V. Voltage probes are connected over the three digital-out configured pins (9, 10 and 11) and GND. Each digital-out pin is connected to a LED in series with a resistor, used for visual inspection of the output-signals.

OSC: Tektronix: Mixed signal oscilloscope (MSO 2014)
16Ch, 1GS/s, 100MHz

Voltage probes: Tektronix: (P2220)
200MHz, 10x/1x

220Ω LED

~9

220Ω LED

~10

220Ω LED

~11

V: A

V:B

V:C

GND

5V

A0

A1

Arduino Uno
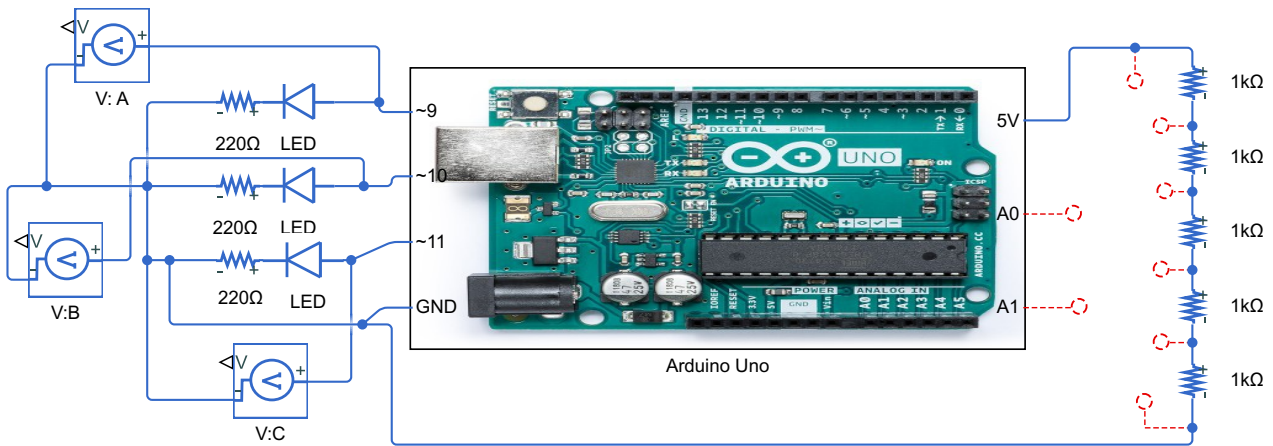
1kΩ

1kΩ

1kΩ

1kΩ

1kΩ
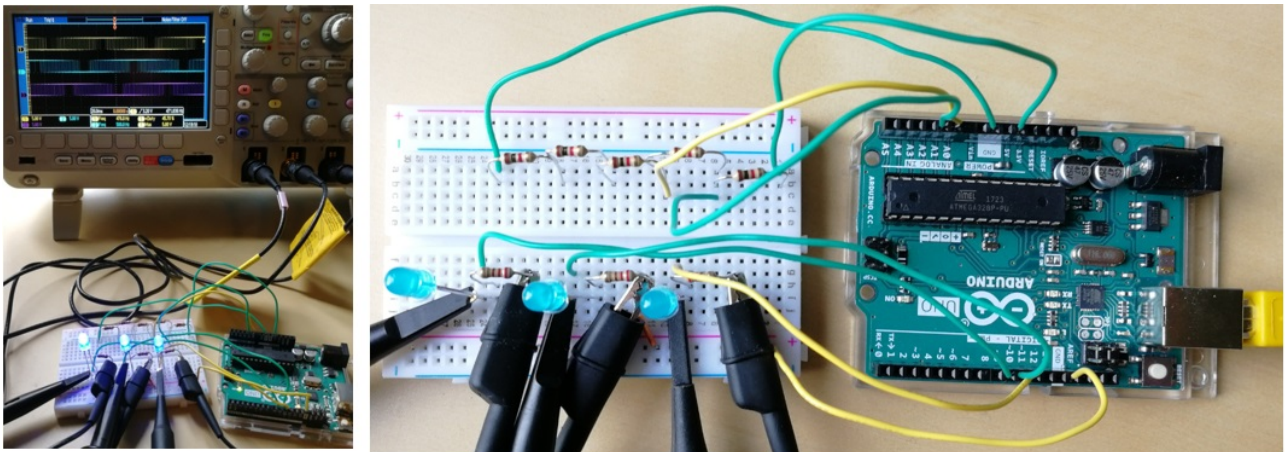
1kΩ

Figure 14.2: Schematic of circuit setup

Figure 14.3: Physical setup

14.3 Simulink control model

The control system is based on the proposed V/f-controller (Section 10.2), but some simplifications and modifications are made for the implementation to the Arduino. The current-measurement are for instance not included, which results in some simplifications of the slip-speed controller and voltage-controller. Figure 14.4 shows an overview (Mode 1). With a 10-bit based analog-read input, the measurements are scaled according to a fictions upper limit of voltage (DC_max) and speed (f_max). The slip-speed controller (Figure 14.6) uses a discrete integrator (forward-euler). Additionally, it does not inherit the error-threshold limits for integral gain. The voltage-controller (Figure 14.7) employs the RMS/DC-model, but with a fixed frequency-coefficient (ma_scale).

The major difference between Mode 1 and Mode 2 (Figure 14.5) lies in the method of generating gate-signals, and corresponding digital output blocks. Mode 1 creates the duty-cycles directly from (6.3). Looking at Figure 14.8, note that the denominator of (6.3) is represented by a gain (255/2) that scales the duty-cycle output according to the 8-bit PWM-resolution. Mode 2 (Figure 14.9) uses a triangle carrier wave of frequency f_sw to detect intersections. Both modes are based on purely sinusoidal references.

The phase-calculation function (code in Section 14.3.1) is similar to the "Reference generator" (as described in Section 6.1.4), but with a fixed sample time (t_samp) defined internally. Its outputs (sin_a, sin_b and sin_c)

are actually of unit time (seconds). This is because the sine-references are calculated by means of look-up table approach, which requires input of time (u → sin(2*pi*u)), placed as seen in Figure 14.8 and Figure 14.9. These look-up table blocks were the only seemingly available option that the compiler could build onto the Arduino.

A fixed global sample time (t_samp) is defined for all blocks in the control-structure. This includes the input-rate of the measurements and the rate of the digital outputs.

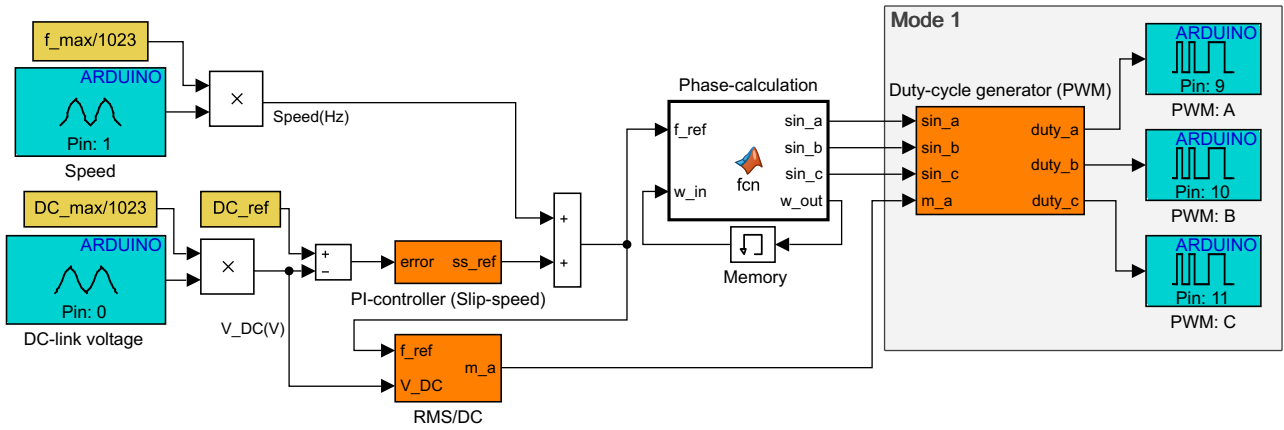### 14.3.1 Images and code

Figure 14.4: Overview of Arduino control structure (Mode 1)
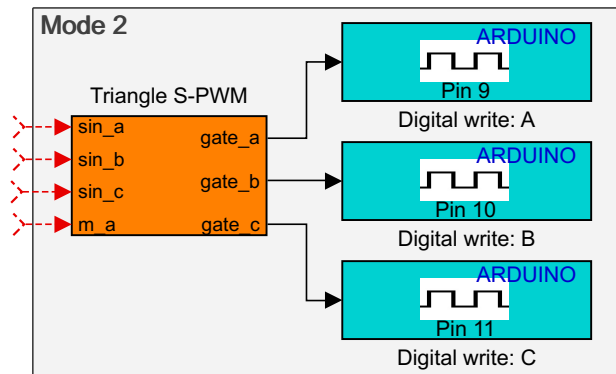
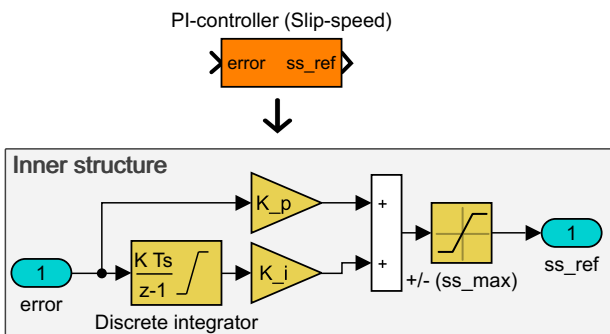

Figure 14.5: Gate-signal generation (Mode 2)
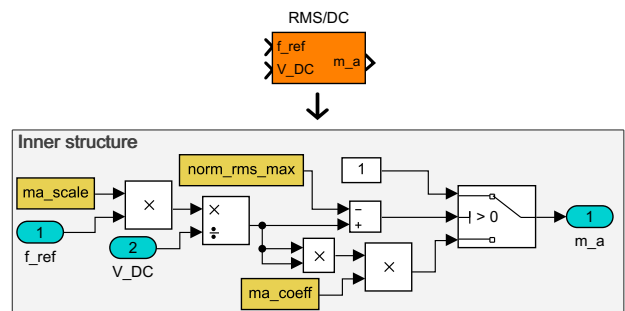

Figure 14.6: Slip-speed controller

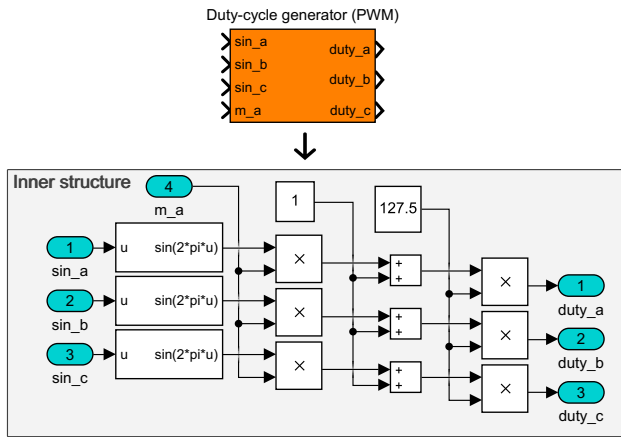Figure 14.7: Voltage controller (m_a)
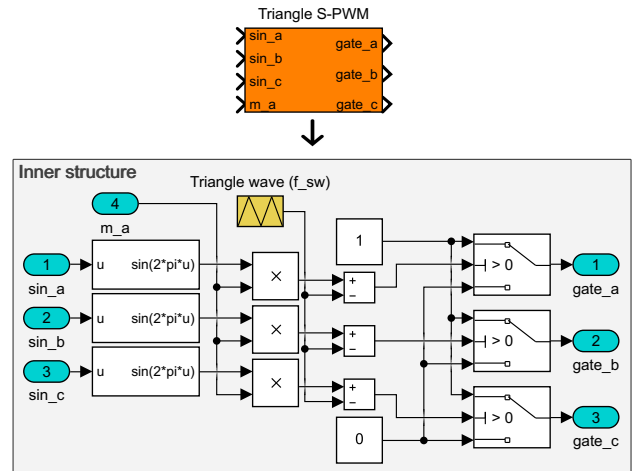
Figure 14.8: Duty-cycle generator (Mode 1)

Figure 14.9: S-PWM (Mode 2)

MATLAB-Function: Phase-calculation

```matlab
1  function [sin_a, sin_b, sin_c, w_out] = fcn(f_ref, w_in)
2
3  t=2*10^(-3); %sample time
4
5  w_out=w_in+t*f_ref*2*pi;
6
7  if(w_out>(2*pi))
8      w_out=w_out-2*pi;
9  end
10
11  sin_a=(w_out)/(2*pi);
12  sin_b=(w_out-2/3*pi)/(2*pi);
13  sin_c=(w_out+2/3*pi)/(2*pi);
```

14.3.2 Parameters

The various parameters defined in the controller (yellow blocks) are summarised in the following tables. Only the variable parameters (Table 14.2) will be modified throughout the following tests.

Parameter	Setting	Comment
DC_max	100V	Maximum fictitious DC-link voltage measurable
norm_rms_max	0.4287	$\bar{v}_m$ (Section 6.5)
ma_coeff	5.442	μ_{ma} (Section 6.5)

Table 14.1: Fixed parameters

Parameter	Comment
t_samp [s]	Sample-time (ΔT_{samp})
f_sw [Hz]	Switching frequency (Mode 2)
f_max [Hz]	Maximum fictitious speed measurable

Table 14.2: Variable parameters

Parameter	Setting	Comment
DC_ref	(DC_max)·0.5	50%
ss_max	(f_max)·0.1	Maximum slip-speed (10%)
K_p	$-\frac{(\text{ss\_max})}{(\text{DC\_ref})}$	Saturate at DC_ref
K_i	$-\frac{(\text{ss\_max})}{(\text{DC\_ref})\cdot 0.5}$	Saturates after 0.5s with error DC_ref
ma_scale	$\frac{(\text{norm\_rms\_max})\cdot(\text{DC\_ref})}{(\text{f\_max})\cdot 0.5}$	$m_a = 1$ when $V_{DC} = \text{DC\_ref}$ and $\omega_m = \text{f\_max} \cdot 0.5$

Table 14.3: Derived parameters

14.4 Test configurations

It's of interest to study the performance of the Arduino with the implemented control-system when both of the input-measurements are varied. The tests will be performed in two classes of speed: f_max=10Hz and f_max=100Hz. For each of these classes, two levels of measured speed (1V and 4V) and DC-link voltage (2V and 3V) are emulated by connecting the analog ports (A1 and A0) in between the resistors (Section 14.2.2). With the two different controller modes of the output-pins (Mode 1(#1) and Mode 2(#2)), we have a total of 16 test configurations, with indexations as shown in Table 14.4.

V_{DC} (**A0**) ↓/ Speed (**A1**) →	**1V** (1/5)	**4V** (4/5)
2V (2/5)	#1.1 [100Hz]	#1.3 [100Hz]
	#1.5 [10Hz]	#1.7 [10Hz]
	#2.1 [100Hz]	#2.3 [100Hz]
	#2.5 [10Hz]	#2.7 [10Hz]
3V (3/5)	#1.2 [100Hz]	#1.4 [100Hz]
	#1.6 [10Hz]	#1.8 [10Hz]
	#2.2 [100Hz]	#2.4 [100Hz]
	#2.6 [10Hz]	#2.8 [10Hz]

Table 14.4: Overview of measurement configurations and indexation of samples

The fixed levels of DC-link voltage input-measurement (A1) corresponds to a constant error of $\text{DC\_ref} - \text{V}_{DC} = \pm 10$V. With the gains (K_p and K_i) and maximum slip-speed (ss_max) for the slip-speed controller as defined in Table 14.3, f_{ref} would saturate after t=2 seconds. The expected values of f_{ref} and the steady-state normalised RMS-voltage outputs are summarised in Table 14.5 and Table 14.6.

Index	V_{DC} (**A0**)	Speed (**A1**)	f_{ref} (t=0)	f_{ref} (t=2)	RMS/V_{DC} (t=2)
#1.1, #2.1	2/5	1/5	18 Hz	10 Hz	0.1072
#1.2, #2.2	3/5	1/5	22 Hz	30 Hz	0.2144
#1.3, #2.3	2/5	4/5	78 Hz	70 Hz	0.4287 ($m_a = 1$)
#1.4, #2.4	3/5	4/5	82 Hz	90 Hz	0.4287 ($m_a = 1$)

Table 14.5: Expected outputs (f_max=100Hz)

Index	V_{DC} (**A0**)	Speed (**A1**)	f_{ref} (t=0)	f_{ref} (t=2)	RMS/V_{DC} (t=2)
#1.5, #2.5	2/5	1/5	1.8 Hz	1 Hz	0.1072
#1.6, #2.6	3/5	1/5	2.2 Hz	3 Hz	0.2144
#1.7, #2.7	2/5	4/5	7.8 Hz	7 Hz	0.4287 ($m_a = 1$)
#1.8, #2.8	3/5	4/5	8.2 Hz	9 Hz	0.4287 ($m_a = 1$)

Table 14.6: Expected outputs (f_max=10Hz)

Measurements of the three output gate-signals are sampled for all 16 configurations (Table 14.4) by using the oscilloscope in the setup as described in Section 14.2.2. The code is updated in the Arduino whenever a new speed-class or output-pin mode is to be studied. The on-board reset push-button is used to reset the controller for a new sample, and each sample has a measurement length of 4 seconds. The sample frequency is 31.25 kHz, and the resolutions of the gate-voltage measurements are 0.04V.

14.5   Mode 1

The PWM switching frequency of approximately 490Hz corresponds to a switching period of approximately 2ms. Updating the duty-cycle more frequently that this does not serve much purpose, so the sample time (t_samp) is defined as 2ms for the controller in Mode 1.

14.5.1   Results

The measured gate-signals can be related to the phase-neutral voltages in the Lab Test 1 (Section 13.3). Looking at them directly does not provide much insight into what frequency (f_{ref}) they are trying to synthesize. They are therefore shown in the following plots as phase-voltages by using (5.2), where v_{an}=V:A (pin 9), v_{bn}=V:B (pin 10) and v_{cn}=V:C (pin 11).

In addition, a CWT-analysis (Continuous wavelet transformation) is performed for the calculated v_{as} voltage from each sample. The CWT-analysis provides a visual representation of the dominant frequency components of a signal over time, and is in this context useful to determine if the control-system manages to produce the expected frequencies (f_{ref}) in the gate-signals. The level of detail is limited by the length of the measurement, which results in a indistinct results for #1.5 (Figure 14.19) and #1.6 (Figure 14.21). The CWT-analysis is run with the "bump"-method and VoicesPerOctave=48. Refer to the MATLAB-documentation for more details: `https://se.mathworks.com/help/wavelet/ref/cwt.html`

The RMS-values of the three calculated phase-voltage (v_{as}, v_{bs} and v_{cs}) are also found by using the discrete integral as defined by (6.9), for the data-points past t=2s. The values are then averaged (for all three phases), and divided by the equivalent "DC-link" voltage of the Arduino (5V). The results are shown in Table 14.7.

Figure 14.10-Figure 14.25 shows the calculated phase voltages and CWT-analysis for the Mode 1 results.
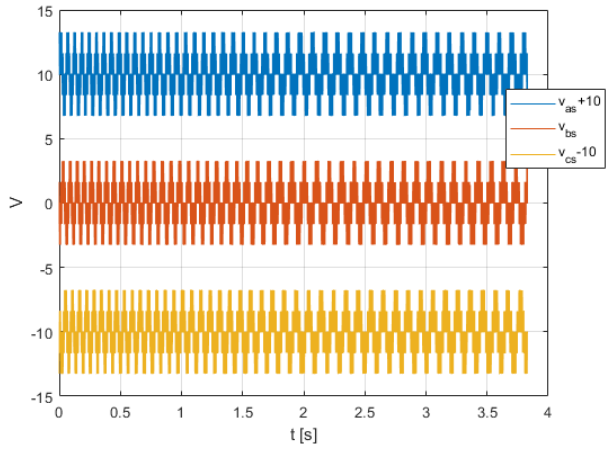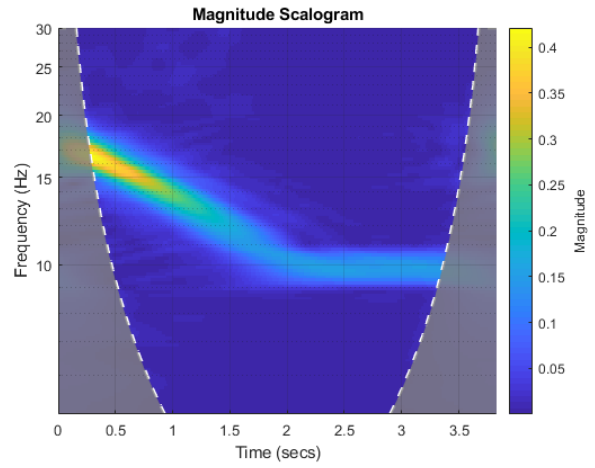
100Hz class:

Figure 14.10: Phase voltage (#1.1)

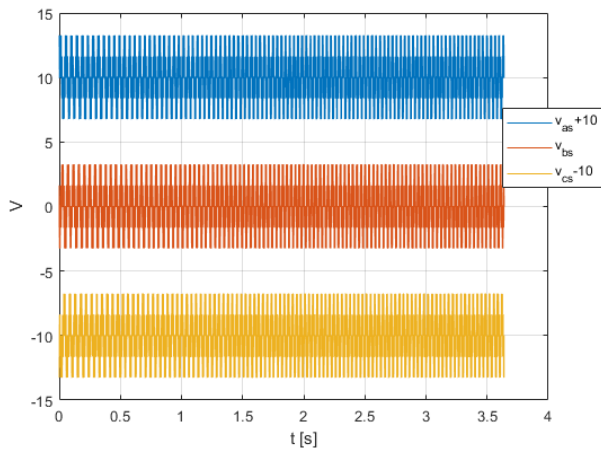Figure 14.11: CWT of v_{as} (#1.1)

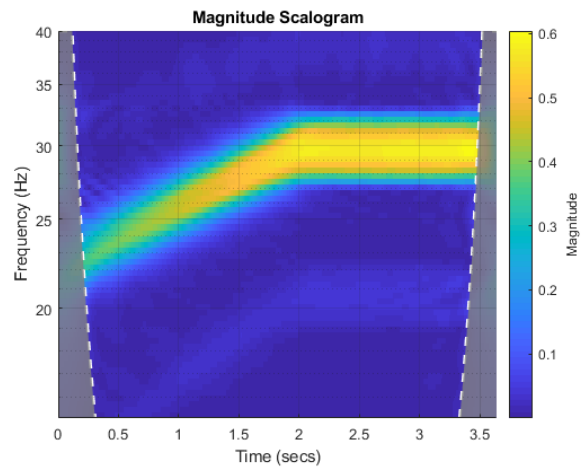Figure 14.12: Phase voltage (#1.2)
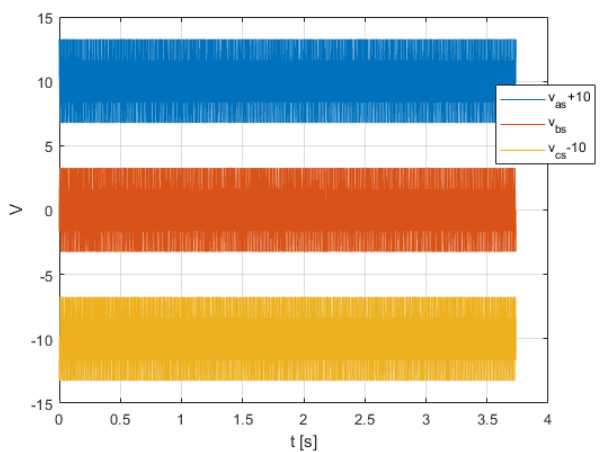

Figure 14.13: CWT of v_{as} (#1.2)
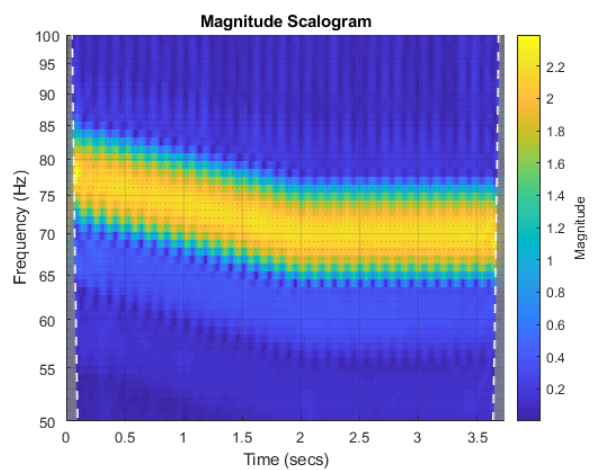

Figure 14.14: Phase voltage (#1.3)

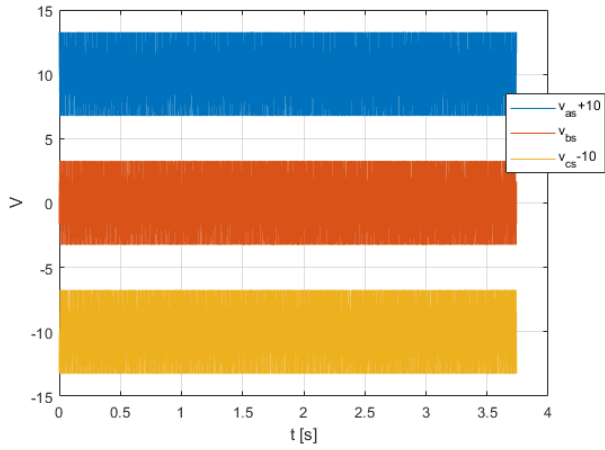Figure 14.15: CWT of v_{as} (#1.3)

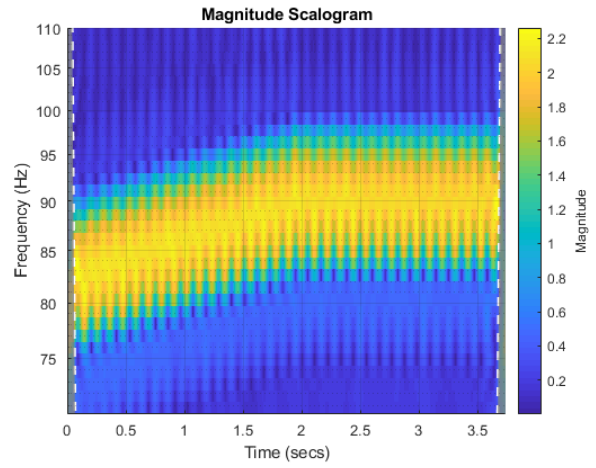Figure 14.16: Phase voltage (#1.4)

Figure 14.17: CWT of v_{as} (#1.4)
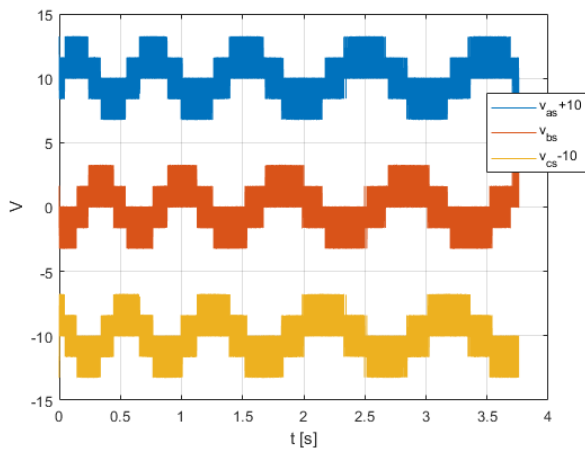
10Hz class:
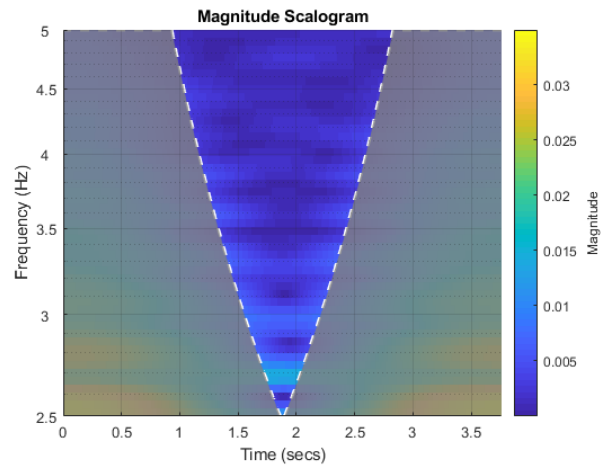

Figure 14.18: Phase voltage (#1.5)
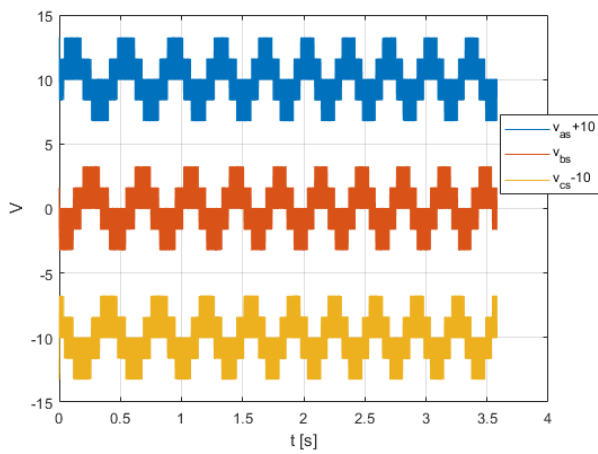

Figure 14.19: CWT of v_{as} (#1.5)

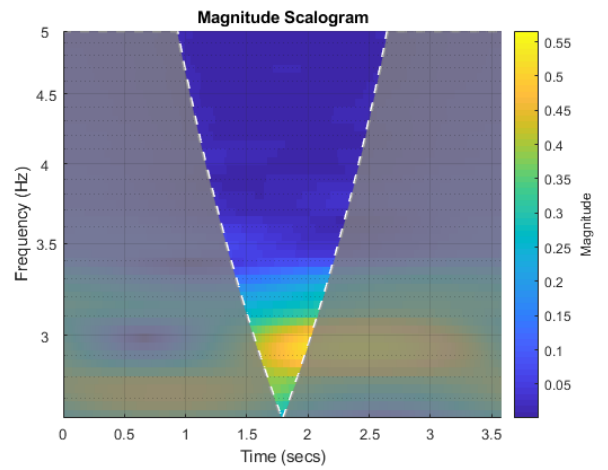Figure 14.20: Phase voltage (#1.6)

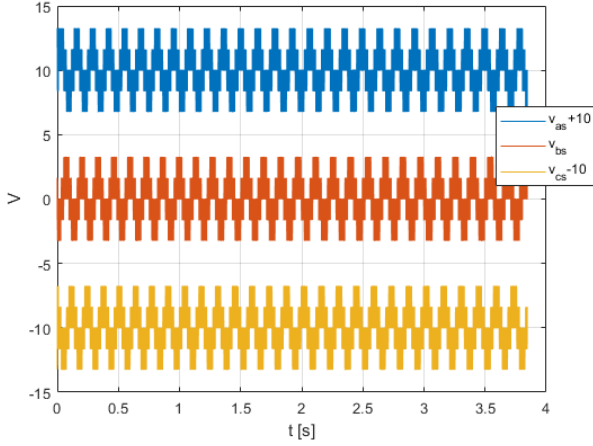
Figure 14.21: CWT of v_{as} (#1.6)

Figure 14.22: Phase voltage (#1.7)
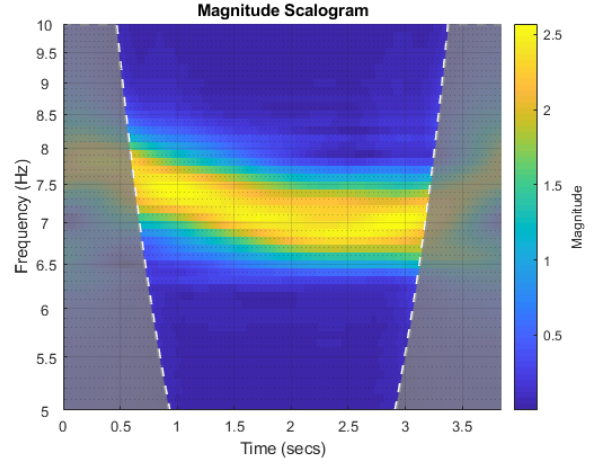
Figure 14.23: CWT of v_{as} (#1.7)
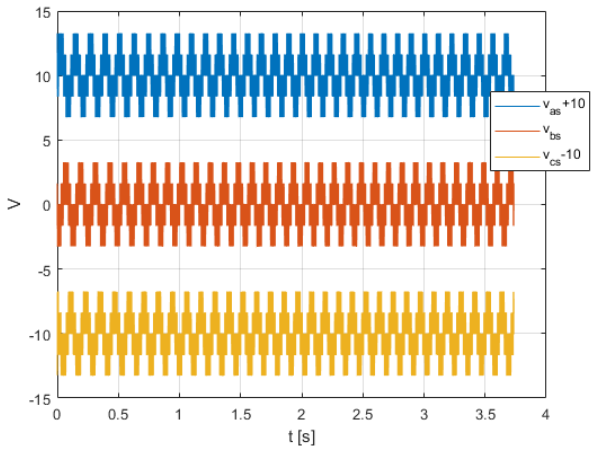
Figure 14.24: Phase voltage (#1.8)
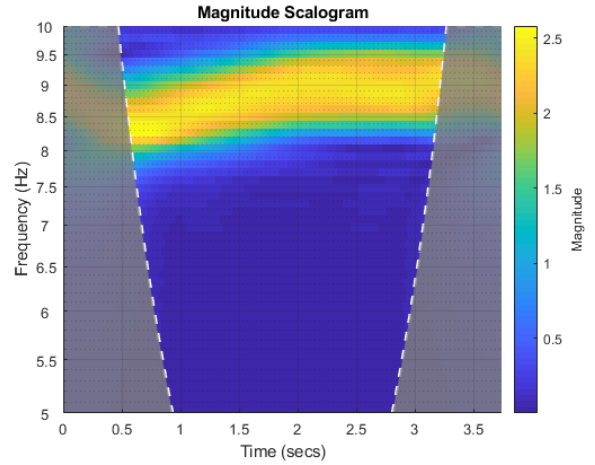
Figure 14.25: CWT of v_{as} (#1.8)

14.5.2 Analysis

From visual inspections of the CWT-plots, we see that the expected results of f_{ref} in Table 14.5 and Table 14.6 coincides quite well. The dominant frequency-components increase/decrease in a linear manner between t=0 to t=2s, which is expected when the slip-speed integrator has a constant error. The CWT-plot of sample #1.1 (Figure 14.10) is somewhat dim after t=2s, perhaps caused by the corresponding low value of RMS/V_{DC}. Though the CWT-analysis of sample #1.5 (Figure 14.19) and #1.6 (Figure 14.21) does not show much, a visual inspection of the corresponding phase-voltages (Figure 14.18 and Figure 14.20) shows frequencies as expected.

Looking at Table 14.7, the reference and measured(calculated) RMS-voltages seems to coincides quite well for both the 10Hz and 100Hz speed class. This is especially interesting for the #1.4 sample: With a frequency reference of 90Hz and a switching frequency of 490Hz, we have low number of duty-cycle updates per period ($m_f \approx 5.4$), yet the RMS-voltage is still able to be produced within good accuracy.

Figure 14.26 shows shows a zoom-in of v_{as} for the different samples. Higher f_{ref} results in a coarser pattern, as expected when considering the corresponding m_f ratio. Samples with low values of RMS/V_{DC} also shows lower durations of voltage-steps, similar to Figure 6.3.

Sample	RMS/V_{DC} (measured)	RMS/V_{DC} (reference)
#1.1	0.1043	0.1072
#1.2	0.2077	0.2144
#1.3	0.4176	0.4287
#1.4	0.4160	0.4287
#1.5	0.1039	0.1072
#1.6	0.2089	0.2144
#1.7	0.4183	0.4287
#1.8	0.4206	0.4287

Table 14.7: RMS/V_{DC} output voltage (Mode 1)
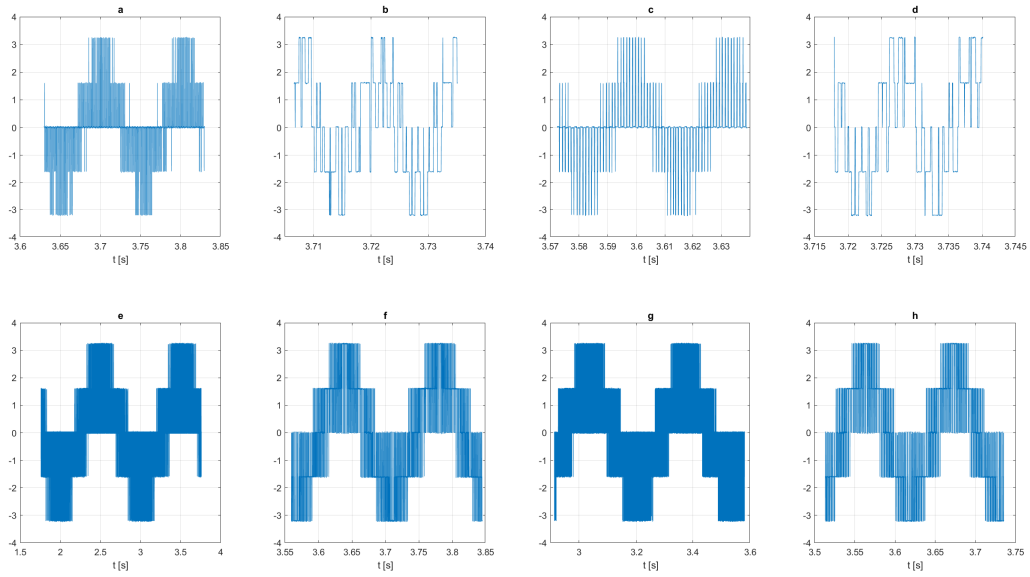
Figure 14.26: Enhanced view of v_{as} (Mode 1)

Top (100Hz) $\rightarrow$: #1.1 (a), #1.3 (b), #1.2 (c), #1.4 (d)
Bottom (10Hz) $\rightarrow$: #1.5 (e), #1.7 (f), #1.6 (g), #1.8 (h)

14.6 Mode 2

When using the triangle-wave based S-PWM, the defined switching frequency ($f_{tri} = f_{sw}$) must be scaled according to the chosen sample time (ΔT_{samp}). We must therefore first determine the lowest sample-time of which the Arudino can manage to perform the required computations ($\Delta T_{samp} = T_{ex}$).

Multiplying the amplitude-modulation (m_a) inside the Triangle S-PWM block (Figure 14.9) with zero does not significantly affect the amount of computation that the Mode 2 controller must perform. With this tweak, we have effectively fixed the duty-cycle of the gate-signal outputs at 50%. The switching-frequency of the triangle-wave (f_sw) is set at 10Hz, and for various t_samp, the gate-signal frequencies are observed with the oscilloscope. Figure 14.27 shows the results. When t_samp is to small, the frequency of the gate-signals starts to decrease, illustrating that $T_{ex} > \Delta T_{samp}$. The breaking-point is at about 1.5ms, which is chosen as the sample-time (t_samp) to be used for the controller in Mode 2. This corresponds to a sample frequency of $\frac{1}{1.5 \cdot 10^{-3}} = 666.67$Hz.
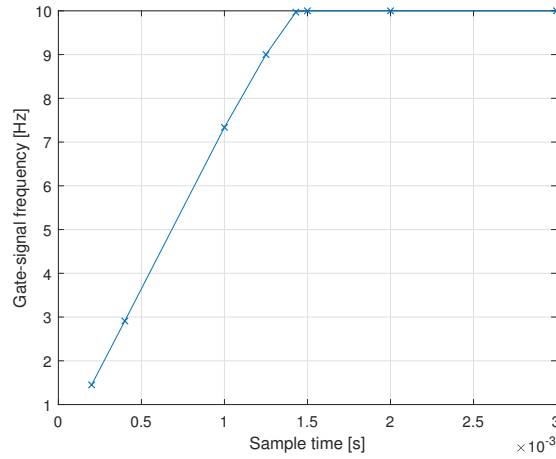
Figure 14.27: Sample time vs. gate-frequency

We define the sample to switching frequency as m_d, (14.1). Choosing a low m_d would result in the triangle carrier-wave being poorly represented, with corresponding low resolution of applicable duty-cycles. Choosing a larger m_d comes at a cost of lower f_{sw}, which will limit the frequency-range of sine-waves that the S-PWM-method can properly synthesise.

$$m_d = \frac{1}{\text{t\_samp} \cdot \text{f\_sw}} \tag{14.1}$$

With the defined speed classes of 10Hz and 100Hz, a point in between is chosen. m_d is set to 10, giving f_sw=66.67Hz for the Mode 2 controller.

14.6.1 Results

The samples of measured gate-signals for Mode 2 are treated in the same manner as for Mode 1, described in Section 14.5.1.

Figure 14.28-Figure 14.43 shows the calculated phase voltages and CWT-analysis. The calculated RMS-values are given in Table 14.8.

100Hz class:
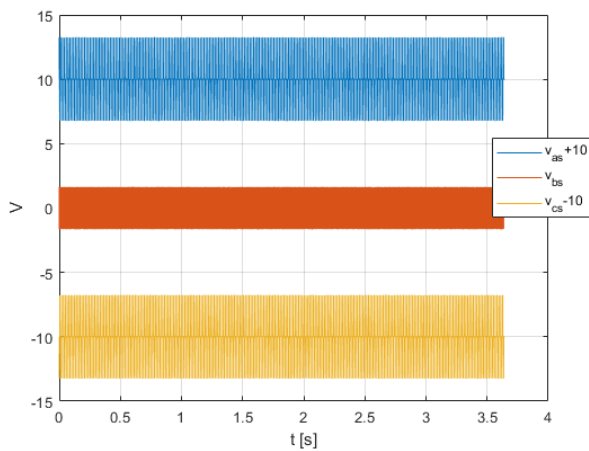
Figure 14.28: Phase voltage (#2.1)
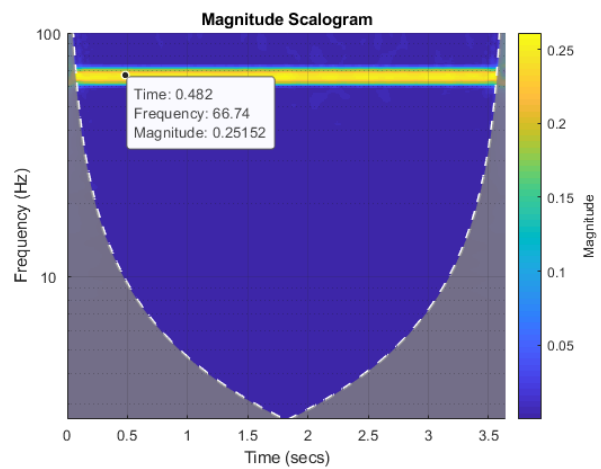
Figure 14.29: CWT of v_{as} (#2.1)

122

Figure 14.30: Phase voltage (#2.2)

Figure 14.31: CWT of v_{as} (#2.2)

Figure 14.32: Phase voltage (#2.3)

Figure 14.33: CWT of v_{as} (#2.3)

Figure 14.34: Phase voltage (#2.4)
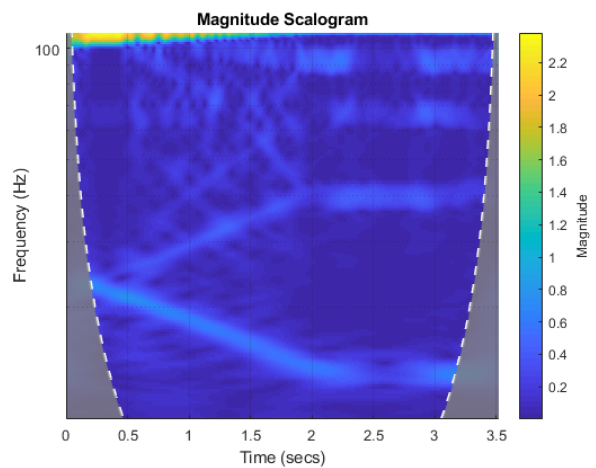
Figure 14.35: CWT of v_{as} (#2.4)

10Hz class:
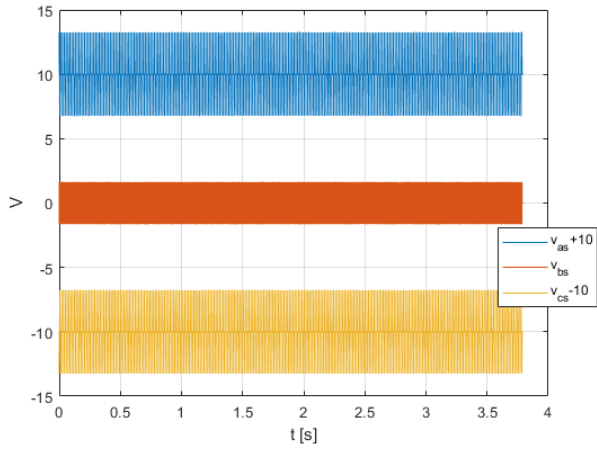
Figure 14.36: Phase voltage (#2.5)
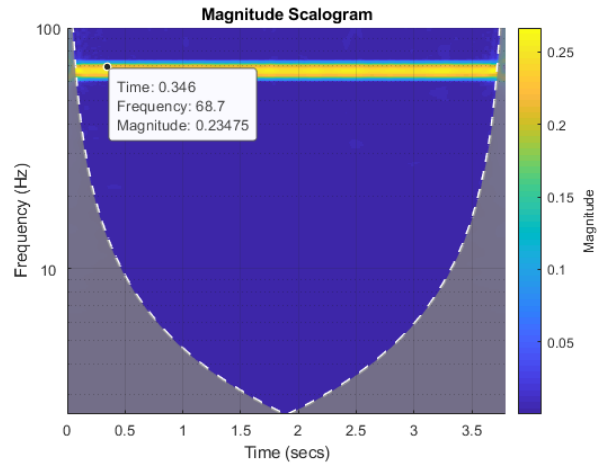
Figure 14.37: CWT of v_{as} (#2.5)
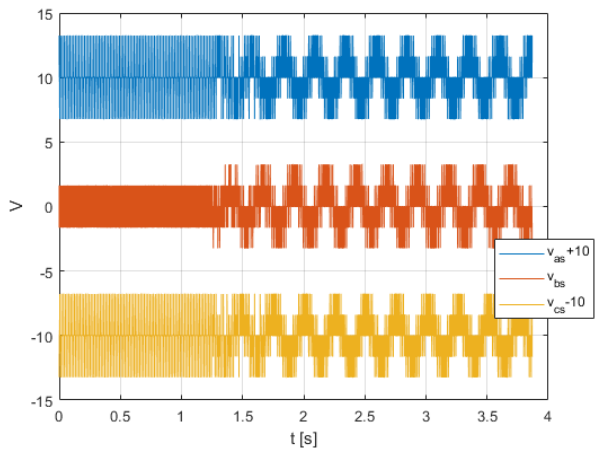
Figure 14.38: Phase voltage (#2.6)
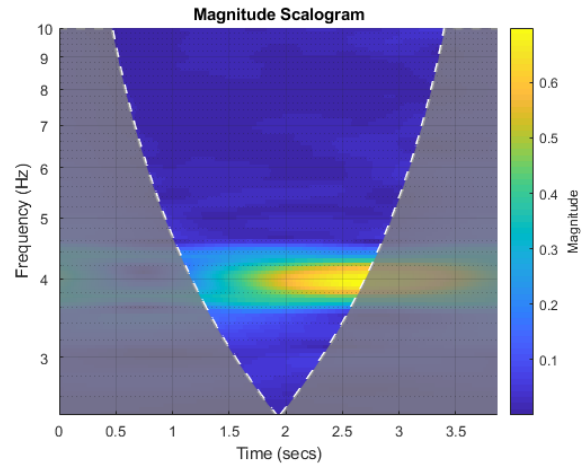
Figure 14.39: CWT of v_{as} (#2.6)
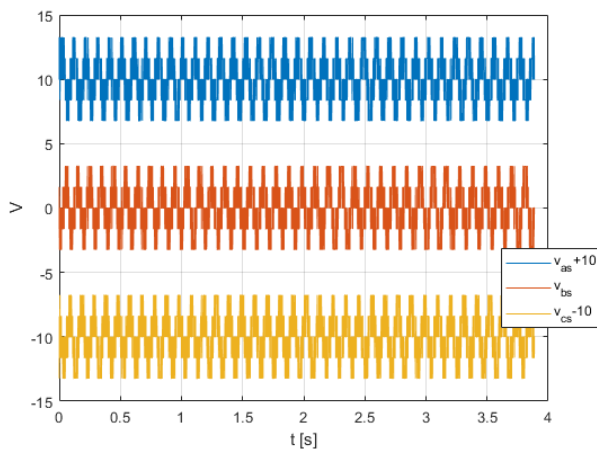
Figure 14.40: Phase voltage (#2.7)
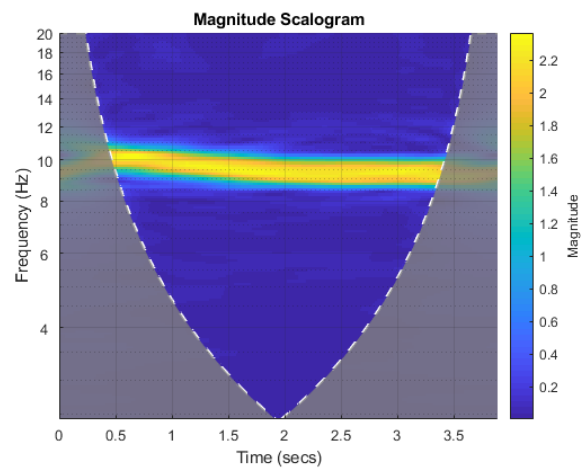
Figure 14.41: CWT of v_{as} (#2.7)
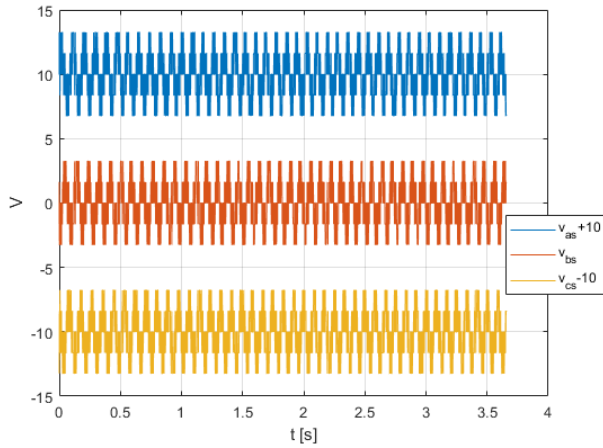
Figure 14.42: Phase voltage (#2.8)
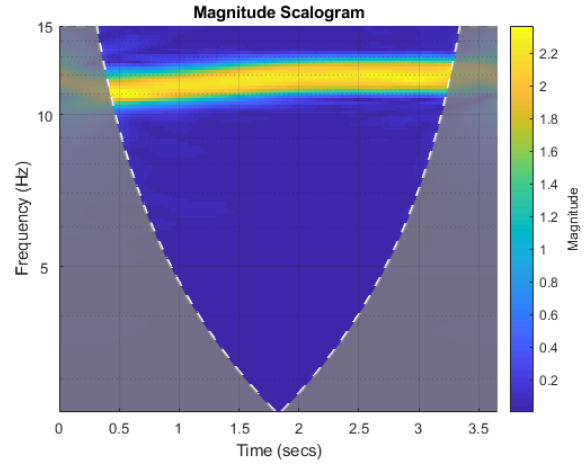
Figure 14.43: CWT of v_{as} (#2.8)
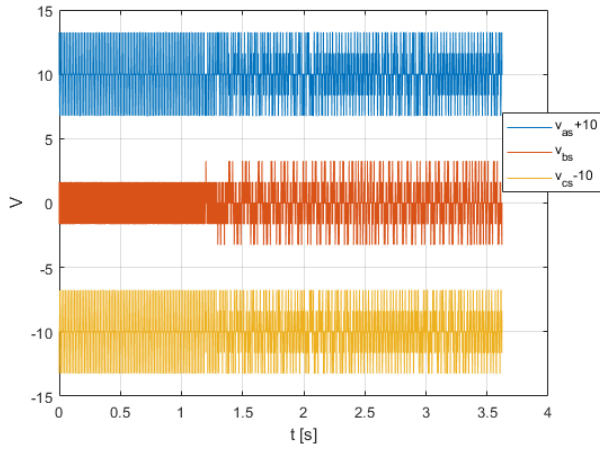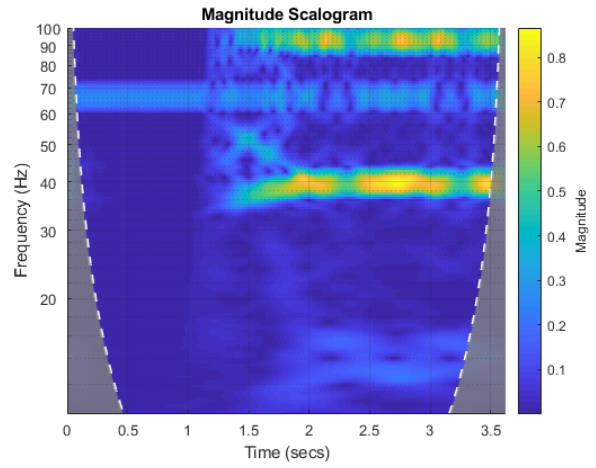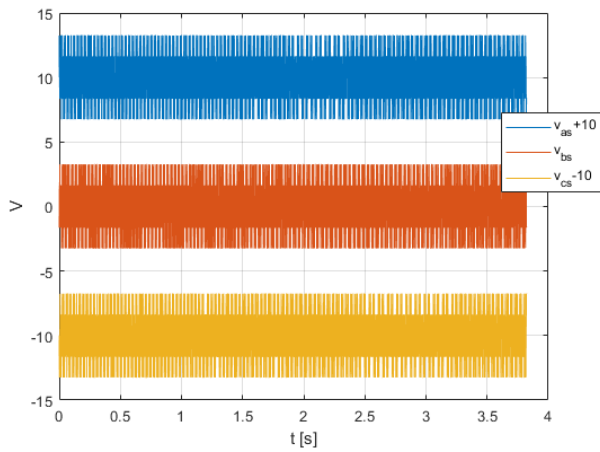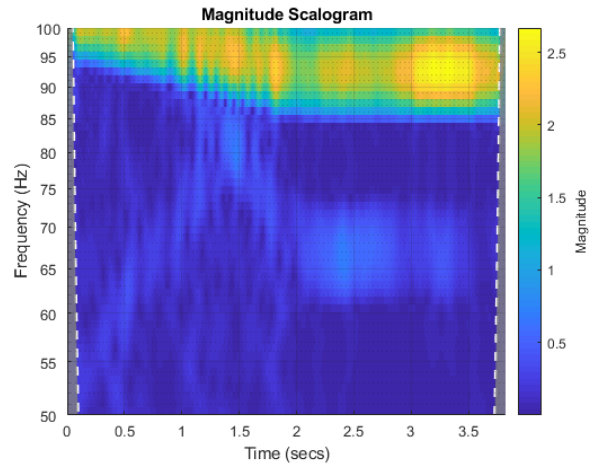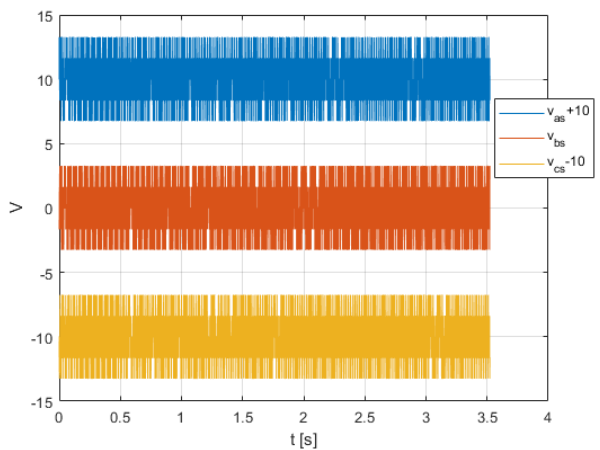
14.6.2 Analysis

This mode generally performs poorly when inspecting the CWT-plots compared to the expected results in Table 14.5 and Table 14.6. Some of the samples (#2.6, #2.7 and #2.8) in the 10Hz-class are in proximity to their expected f_{ref}, but seemingly a bit to large. The 100Hz-class samples are generally ambiguous, as expected due to the fact that the switching frequency (f_sw) of 66.67Hz results in a low ratio of frequency modulation (m_f). The effect of a larger m_f and the ability to synthesize the reference voltage waveforms is illustrated in Figure 14.44.

For sample #2.1 (Figure 14.29) and #2.5 (Figure 14.37), the switching frequency (66.67Hz) dominates the CWT-plots. This is likely related to the appurtenant low RMS/V_{DC} reference in combination with the coarse triangle-wave resolution ($m_d = 10$), resulting in sine-references that fails to intersect which gives an apparent 50% duty-cycle of the gate-signals. The effect of a low RMS/V_{DC} reference can also be seen in the phase-voltage plots during t=0 to t=1.5s of sample #2.2 (Figure 14.30) and #2.6 (Figure 14.38).

In Mode 1, sample #1.4 seemed to perform well with a frequency modulation of $m_f = 5.4$ ($f_{ref} = 90$Hz). The duty-cycle resolution of the PWM-modulator in Mode 1 is however much larger (8-bit = 256 levels) compared to $m_d = 10$ in Mode 2. Although this resolution ($m_d = 10$) is equal the one used in the simulation study (Section 12.1.4), the simulation study could compensate with a larger m_f.

Looking at Table 14.7, the reference and measured(calculated) RMS-voltages seems coincide, but not as good as in Mode 1. The coarse resolution of the triangle-wave is likely of influence.

Sample	RMS/V_{DC} (measured)	RMS/V_{DC} (reference)
#2.1	0.1039	0.1072
#2.2	0.2330	0.2144
#2.3	0.4043	0.4287
#2.4	0.4047	0.4287
#2.5	0.1036	0.1072
#2.6	0.2316	0.2144
#2.7	0.4094	0.4287
#2.8	0.4097	0.4287

Table 14.8: RMS/V_{DC} output voltage (Mode 2)
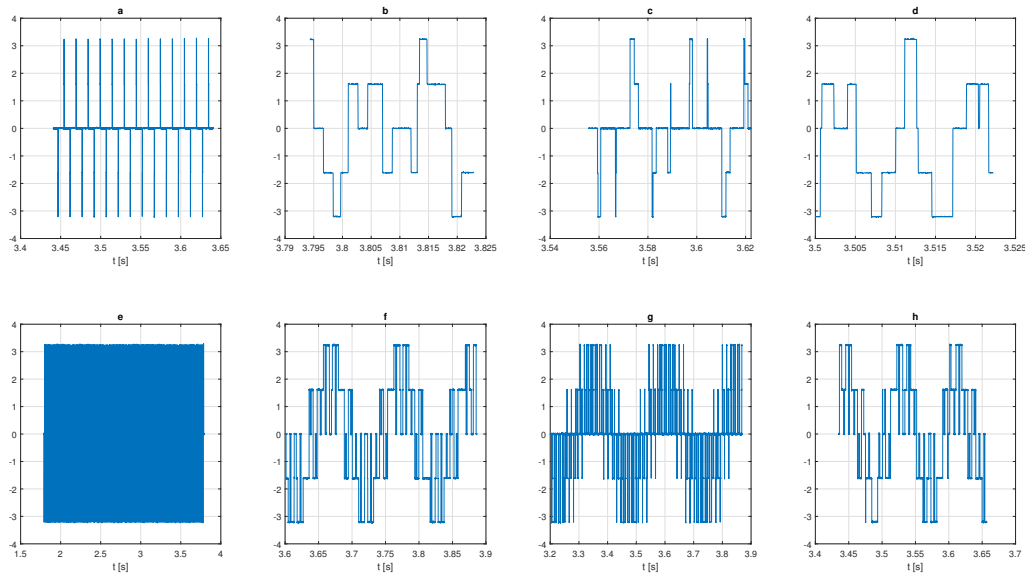
Figure 14.44: Enhanced view of v_{as} (Mode 2)

Top (100Hz) $\rightarrow$: #2.1 (a), #2.3 (b), #2.2 (c), #2.4 (d)
Bottom (10Hz) $\rightarrow$: #2.5 (e), #2.7 (f), #2.6 (g), #2.8 (h)

14.7   Conclusion

Through this experiment, a simple type of a 2L-3ph VSC-control system (intended for an induction machine) is implemented on the Arduiono Uno through MATLAB-Simulink. The control system consists of two analog input-measurement and three digital gate-signal outputs. It was tested with various configurations of fixed input-measurements, with output voltage references in a 1-100Hz frequency range. The performance is evaluated by inspecting the frequency-components and RMS-values of the corresponding phase-voltages that the gate-signals would produce in an ideal VSC.

The performance was generally good when using the built-in PWM functions (Mode 1), with a switching frequency of 490Hz and sample-time of 2ms. The 8-bit duty-cycle resolution allows to synthesize output RMS-voltage references well. The fixed switching-frequency of 490Hz does however limit the ability to synthesize high-frequency references, making this mode best suited for references below 100Hz. Using the built-in PWM functions is not an option if one requires 6x digital outputs.

Writing directly to the digital output-pins by employing the triangle-wave S-PWM (Mode 2) significantly reduced the performance compared to Mode 1. Tested for a switching frequency of 66.67Hz and sample-time of 1.5ms, it struggled to synthesise the reference sinusoidal waveform at the correct frequencies. This can be explained by the low switching frequency, and corresponding coarse resolution of the triangle carrier-wave due to the limitation of how low the sample-time could be set.

For use in a practical system, more functionality is probably required in the controller, with an extension to 6 digital outputs. This added workload could further increase the required sample-time, but it might be possible to counteract this with a more optimised code. The Arduino Uno is cheap and easy to program, but its limited computational power might only make it viable for simple control-systems in a low-frequency reference range.

15 Conclusion

This thesis has taken a basis in a filtered B2B topology with a start-up battery as a solution to control an isolated induction machine and supply local variable AC loads. MATLAB-Simulink has been used as the simulation-environment to implement the models and test the control-systems. The implementations have been shown down to the fine details with the purpose and giving full insight into how the results are obtained.

Results obtained via simulations are ultimately limited by the simplifications and assumptions taken in all the models. The simulation-test were intended to cover a wide range of conditions and study multiple aspects, but limitations had to be made in order to have a comprehensible amount of results to analyse. Also note that the aspects of the prime-mover have only been briefly included in the simulations, whereas most of the results are based on a fixed speed rotor.

Several characteristics was intended to define the system, which we can inspect based on the results of the simulation-tests:

Applicability to various configurations
The proposed design procedure (Chapter 11) was created in step-by-step manner, utilizing the LCL-filter design found in the literature and the home-made RMS/DC-model to dimension components. Neglecting the rotor time-constant of the FOC-method, the procedure (with tuning of controllers included) only requires general ratings of the generator and loads, such as power, voltage, frequency, speed and current.

This procedure quickly determines how the components should be dimensioned and reduces the need for extensive tuning. Accompanied to the proposed B2B-system, it substantiates its characteristic as an easily applicable design. The simulink-tests were performed for four different machines (4-16 kW) using the design-procedure, and the following aspects of load voltage quality and generator operation evaluates its success.

Supply variable loads with a stable and high-quality voltage
For various levels of current and powerfactor of the loads ($S_N^L = \sqrt{2} \cdot P_N^L$), the LCL-filter never exceeded 3% THD (fundamental of 50Hz). The filter performs better for leading reactive loads, and worse for lagging reactive loads. The RMS-voltage did deficit up to 2% due to high levels of lagging reactive power. The voltage-controller for the loads is a simple structure that performed well with only 3 tuneable parameters, requiring three input-measurements of voltage.

If we consider the quality-requirements for Norwegian low-voltage grid ($\pm 3\%$ RMS, THD<5%)[39], the results seem to show that the system indeed provides a high-quality voltage. The DC-link voltage reference should however be increased slightly to overcome the deficits during high levels of lagging reactive load. Higher levels of capacitance could also give more redundancy.

Operate the generator within rated conditions
The two proposed generator control systems (V/f and FOC) used the same input measurements: mechanical speed and stator-currents. Though both control-methods had their advantages, the FOC-method is the better option as it hardly exceeds the rated current. It also handled all the various tests with ease and low overshoots of DC-link voltage (contrary to the V/f-method). The home-made flux-controller showed decent performance, even with an inaccurately defined rotor time-constant. This flux-controller does not require intricate machine parameters to be tuned, but it results in larger currents drawn during light/no-loaded conditions, and thus more losses. The V/f-method needs improvement in the tuning or a redesign to be viable competitor, but it does demonstrate some qualities, such as no need for a rotor time-constant, lower torque-ripples and operation at lower switching-frequency.

So, does the control-systems operate the generator within rated conditions? The FOC-method seems to do so if we assume that the torque-ripple is acceptable. Its current-hysteresis controller does however operate at a high switching-frequency, and improvement might be necessary to reduce switching-losses and match the controller to VSCs with lower rated switching-frequencies. If we dismiss the failed performance of

the #M1 and #M2 configuration in the prime-mover test and assume that the generator can withstand excessive current for a shorter duration, we could qualify the V/f-method as well. Note that a core assumption in this evaluation is that the induction machine can withstand the high-frequent changes of voltage at the magnitude equal V_{DC}.

Magnetisation by means of a low-voltage source

With an isolated system, the battery was included to make the energization of the induction machine possible. The lab-experiment (at a 55kW machine) demonstrates that a low-voltage DC-source would be sufficient, down to 10V initial voltage at rated speed (1000 rpm). The requirement was however increased for lower speeds, up an initial voltage of 40V.

The results obtained from the lab-experiment did show some inconsistencies, which could be due to unknown information about how the FOC-based control system is operated, or physical factors such as heating of the IM during operation. More testing for a wider range of initial voltages and speeds could shed more light on the performance and behaviour of the converter and machine used in the setup. The quality of the measurements could also be improved.

When comparing to the simulation-results, it must be noted that the control system in the lab-VSC is not identical to the ones used in the simulation-tests. In theory, the initial DC-link voltage could be any value >0. The simulation-test revealed that the charge-up time is reduced for higher initial-voltages, and a small amount of energy (compared to machine rating) is needed to "kick-start" the system. Higher initial voltage and lower speeds both contributed to larger peak-values of battery current. The results of the lab experiment coincide with shorter charge-up times for higher initial voltages, but not clear pattern is identified with regards to required work and peak-values of DC-source currents. The low values of peak currents drawn from the DC-source in the lab-experiments does however suggest that a battery could be a suitable DC-source. The time required to charge-up and stabilise the DC-link voltages stayed within the 1 second range in the simulation-tests, and around 1-6 seconds in the lab test. This suggests that the proposed system topology quickly could go from being fully discharged to delivering power to the loads.

Arduino Uno as a controller

The Arduino Uno is cheap, well documented and easy to implement functionality on. Although there is probably room for pushing its capabilities further than what was achieved in the control-system implementation test, it seems to be best suited for its intended use: Simple control-loops that are not critical in the milli-seconds range.

15.1 Suggestions for further work

- Improvement of the proposed FOC-method in order to reduce the torque-ripple. Perhaps related to the home-made flux-controller or the band-gap of the current-hysteresis controller. Investigate the effects of lowering the switching-frequency.

- The economic aspects. Cost will play an important role when choosing a system for a desired application. Technological maturity and production volume influences the costs and ratings of available components. This could be analyzed to see if the solution is worth paying for/within a budget, and determine optimal crossings of costs and sufficient system performance characteristics. Possibilities of reducing costs by defining a DC-grid for the loads.

- Conduct more experiments of the lab-setup to study the magnetisation of the induction generator and charge-up of DC-link voltage. Try to replace the DC-source with a battery and compare performance.

- Design a lab-setup of the proposed system in the intended power range (3-10kW) and implement the control-systems.

  - Implement/design practical safety-features in the control systems. This should be included if the system are to operate in the real world.

– Analyse the distortions/quality of the load voltage. Will a physical system perform better or worse compared to simulations? How does non-ideal conditions in the LCL-filters (such as saturation and losses) influence?

– Evaluate the overall performance of the proposed design-procedure and corresponding tuning. How does the practical implementation of sensors and measurement conditioning, inclusion of blanking-time, processor, gate-drivers, VSC and a physical induction machine influence aspects such as time-delays, power-losses/efficiency, settling time and overall control-accuracy?

References

[1] C. Ong. (1998). *Dynamic Simulation of Electric Machinery : using Matlab/Simulink*. New Jersey: Prentice Hall.

    [1] Three-phase induction machines, pp. 167-180

    [2] Developed torque of a uniform airgap machine, pp. 138-140

    [3] Steady state model, pp. 183-189

    [4] Space vectors and transformations, pp. 150-158

    [5] Field oriented control, pp. 433-440

    [6] Constant airgap flux operation, pp. 420-422

    [7] Constant volts/hertz operation, pp. 422-426

    [8] Project 2 motor, pp. 441

[2] R. Nilsen. (2018). *Compendium TET4120 - Electric Drives*, pp. 177-217. Department of Electric Power Engineering: NTNU.

[3] A. Andersson and E. Bye. (2016). *Analysis of Self-Excited Induction Generator for use in Rural Area with Electronic Load Controller and Additional Compensation Methods* (Master's thesis). Department of Electric Power Engineering: NTNU.

    [1] SEIG with loads, pp. 22-29

    [2] ELC Design options, pp. 37-45

[4] D. P. Kothari and I. J. Nagrath. (2010). *Electric Machines*, 4th ed. New Delhi: McGraw-Hill.

    [1] Induction machine - Introduction, pp. 593

    [2] Induction generator, pp. 667-670

[5] S. J. Chapman. (2003). *Electric Machinery Fundamentals*, 4th ed. New York: McGraw-Hill Higher Education.

    [1] The rotating magnetic field, pp. 238-241

    [2] The development of induced torque in an induction motor, pp. 384-385

    [3] The induction generator, pp. 460-464

    [4] The equivalent circuit of an induction motor, pp. 388-394

[6] Gunt Hamburg. *Basic principles of water turbines.*
https://www.gunt.de/images/download/hydroturbines_english.pdf (27.11.18).

[7] C. P. Ion and C. Marinescu. (2012). *HYDRO TURBINE EMULATOR FOR MICRO HYDRO POWER PLANTS*. Buletinul AGIR 4(2012), pp. 143-148.

[8] P. Kundur. (2006). *Power System Stability and Control*, pp. 377-386. Mc Graw Hill India.

[9] A. Izena, H. Kihara, T. Shimojo, K. Hirayama, N. Furukawa, T. Kageyama, T. Goto and C. Okamura (2006). *Practical hydraulic turbine model.* 2006 IEEE Power Engineering Society General Meeting.

[10] M. Andreica, S. Bacha, D. Roye, I. Exteberria-Otadui and I. Munteanu. (2008). *Micro-hydro water current turbine control for grid connected or islanding operation.* 2008 IEEE Power Electronics Specialists Conference, pp. 957-962.

[11] D. Borkowski. (2013). *Laboratory Model of Small Hydropower Plant with Variable Speed Operation*. Zeszyty problemowe – Maszyny Elektryczne, Nr 3(100)(pt 1), pp. 27-32.

[12] H. Ouadi, F. Giri and L. Dugard. (2011). *Accounting for magnetic saturation in induction machines modelling.* International Journal of Modelling, Identification and Control, Inderscience, 2011, 14 (1/2), pp.27-36.

[13] A. Alfarhan, S. M. Gadoue, B. Zahawi, M. Shalaby and M. A. Elgendy. (2016). *Modelling of magnetizing inductance saturation in self-excited induction generators.* 2016 IEEE 16th International Conference on Environment and Electrical Engineering (EEEIC), pp. 1-6.

[14] O.I Okoro, B. Weidemann, B. R. Oswald. (2005). *Dynamic Modelling and Simulation of Squirrel-Cage Asynchronous Machine with Non-Linear Effects.* Journal of ASTM International, Vol. 2, June.

[15] S. Ryvkin, M. Valiyev, S. Fligl and J. Bauer. (2014). *Control of island mode working induction generator based on state space controller.* 2014 16th International Power Electronics and Motion Control Conference and Exposition, pp. 527-532.

[16] M. Taoufik, B. Abdelhamid and S. Lassad. (2017). *Stand-alone self-excited induction generator driven by a wind turbine.* Alexandria Engineering Journal, 2018, 57(2), pp. 781-786.

[17] P. Aree and S. Lhaksup. (2014). *Dynamic simulation of self-excited induction generator feeding motor load using Matlab/Simulink.* 2014 11th International Conference on Electrical Engineering/Electronics, Computer, Telecommunications and Information Technology (ECTI-CON), pp. 1-6.

[18] K. D. Birendra and M. Kanungo. (2011). *Analysis, Voltage Control and Experiments on a Self Excited Induction Generator.* Renewable Energy & Power Quality Journal ISSN, 1(9), pp. 220-225.

[19] M. G. Simões, S. Chakraborty and R. Wood. (2006). *Induction Generators for Small Wind Energy Systems.* IEEE Power Electronics Society NEWSLETTER, Third Quarter, pp. 19-23.

[20] E. Touti, R. Pusca, J. F. Brudny and A. Chaari. (2017). *Self-excited Induction Generator in Remote Site.* In: N. M. Tabatabaei, A. J. Aghbolaghi, N. Bizon and F. Blaabjerg. (eds). *Reactive Power Control in AC Power Systems.* Springer, Cham.

[21] J. Björnstedt. (2009). *Island Operation with Induction Generators - Frequency and Voltage Control* (Licentiate Thesis), pp. 11-23. Lund University, Department of Measurement Technology and Industrial Electrical Engineering.

[22] N. Mohan, T. Undeland and W. Robbins. (2003). *Power electronics: Converters, Applications, and Design*, 3rd ed. Hoboken, NJ: John Wiley & Sons.

    [1] Three-phase inverters, pp. 225-229

    [2] Effect of blanking time on voltage in PWM inverters, pp. 236-239

    [3] Pulse-width-modulated switching scheme, pp. 203-210

    [4] Controllable switches, pp. 20-24

    [5] Ripple in the inverter output, pp. 231-232

    [6] PWM-operation, pp. 235-236

[23] D. C. Pham. (2017). *Modeling and simulation of two level three-phase voltage source inverter with voltage drop.* 2017 Seventh International Conference on Information Science and Technology (ICIST), pp. 317-322.

[24] D.O. Neacsu. (2001). *Space vector modulation - An introduction - Tutorial at IECON2001.* The 27th Annual Conference of the IEEE Industrial Electronics Society.

[25] H. W. van der Broeck, H-C. Skudelny and G. V. Stanke. (1988). *Analysis and realization of a pulsewidth modulator based on voltage space vectors.* IEEE Transactions on Industry Applications, 24(1), pp. 142-150.

[26] K.R. Padiyar. (2007). *FACTS controllers in power transmission and distribution*, pp. 514-515. New Delhi New York: New Age International.

[27] J. A. Houldsworth and D. A. Grant. (1984). *The Use of Harmonic Distortion to Increase the Output Voltage of a Three-Phase PWM Inverter*. IEEE Transactions on Industry Applications, IA-20(5), pp. 1224-1228.

[28] A. Omeiri and B. Farid. (2009). *A Study of New Techniques of Controlled PWM Inverters*. European Journal of Scientific Research, 32(1), pp. 78-88.

[29] K. B. Nagasai and T. R. Jyothsna. (2016). *Harmonic Analysis and Application of PWM Techniques for Three Phase Inverter*. International Research Journal of Engineering and Technology (IRJET), 3(7), pp. 1228-1233.

[30] K.V. Kumar, P.A. Michael, J.P. John and S.S. Kumar. (2010). *Simulation and comparison of SPWM and SVPWM control for three phase inverter*. ARPN Journal of Engineering and Applied Sciences, 5(7), pp. 61-74.

[31] B. Belkacem, L. Abdelhakem-Koridak and M. Rahli. (2017). *Comparative study between SPWM and SVPWM control of a three level voltage inverter dedicated to a variable speed wind turbine*. Journal of Power Technologies, 97(3), pp. 190-200.

[32] X. Cao, C. Zhang, Y. Zhang, Z. Gan, H. Li, W. Ni and J. Wang. (2018). *The simulation study of the modulation method for PV grid-connected system*. Energy Procedia, 145, pp. 122-127.

[33] Ö. Türksoy, Ü. Yılmaz, A. Tan and A. Teke. (2017). *A Comparison Study of Sinusoidal PWM and Space Vector PWM Techniques for Voltage Source Inverter*. Natural and Engineering Sciences, 2(2), pp. 73-84.

[34] Y-H. Kim and S-J. Kim. (2015). *Prediction of 2-level PWM inverter efficiency using MATLAB/Simulink*. International Journal of Electronics, 102(10), pp. 1735-1753.

[35] U. P. Yagnik and M. D. Solanki. (2017). *Comparison of L, LC & LCL filter for grid connected converter*. 2017 International Conference on Trends in Electronics and Informatics (ICEI), pp. 455-458.

[36] M. Liserre, F. Blaabjerg and S. Hansen. (2005). *Design and control of an LCL-filter-based three-phase active rectifier*. IEEE Transactions on Industry Applications, 41(5), pp. 1281-1291.

[37] A. Reznik, M. G. Simões, A. Al-Durra and S. M. Muyeen. (2012). *LCL filter design and performance analysis for small wind turbine systems*. 2012 IEEE Power Electronics and Machines in Wind Applications, pp. 1-7.

[38] LEYBOLD DIDACTIC GMBH. (1996). *Instruction sheet - Universal Converter 3 x 230 V, 735 297*. `https://www.ld-didactic.de/documents/de-DE/GA/GA/7/735/735297de.pdf` (29.05.19).

[39] Lovdata. *Forskrift om leveringskvalitet i kraftsystemet - § 3.1-3.10: Krav til leveringspålitelighet og spenningskvalitet*. `https://lovdata.no/dokument/SF/forskrift/2004-11-30-1557` (01.06.19).

[40] B. Robyns, B. Francois, P. Degobert and J. P. Hautier. (2012). *Vector Control of Induction Machines - Desensitisation and Optimisation Through Fuzzy Logic*, pp. 36-38. Springer-Verlag London.

[41] J. Yu, T. Zhang and J. Quian. (2011). *Electrical motor products: International energy-efficiency standards and testing methods*. Woodhead Publishing.

    [1] Scalar control, pp. 150

    [2] Vector control, pp. 150-151

[42] F. Wang, Z. Zhang, X. Mei, J. Rodríguez and R. Kennel. (2018). *Advanced Control Strategies of Induction Machine: Field Oriented Control, Direct Torque Control and Model Predictive Control*. Energies 2018, 11, 120.

[43] Y. Ayman and A.M Samir. (2015). *Review on Field Oriented Control of Induction Motor*. International Journal for Research in Emerging Science and Technology (IJREST), 2.

[44] B. S. Nayak. (2014). *Comparison of Direct and Indirect Vector Control of Induction Motor*. International Journal of New Technologies in Science and Engineering 2014, 1(1).

[45] B. T. Venu Gopal. (2017). *Comparison Between Direct and Indirect Field Oriented Control of Induction Motor*. International Journal of Engineering Trends and Technology (IJETT) 43(6), pp. 364-369.

[46] G. Buja, D. Casadei and G. Serra. (1997). *Direct Torque Control of induction motor drives*. IEEE International Symposium on Industrial Electronics, 1. TU2 - TU8 vol.1

[47] S. Robinson (2015). *Speeding Up Arduino.* `https://stackabuse.com/speeding-up-arduino/` (06.05.19).

[48] "Terbytes". (2016). *Implementation of an sPWM signal on Ardunio and Atmel micros.* `https://github.com/Terbytes/Arduino-Atmel-sPWM` (06.05.19).

[49] S.H. Kim. (2017). *Electric Motor Control: DC, AC, and BLDC Motors*, pp. 223-225. Elsevier Science Publishing Co Inc.

[50] B. Schweber. (2019). *Motor field-oriented control, Part 1: Principles* `https://www.powerelectronictips.com/motor-field-oriented-control-part-1-principles-faq/` (27.05.19).

[51] (2016). *FIELD WEAKENING CONTROL OF INDUCTION MOTOR* `https://www.semanticscholar.org/paper/FIELD-WEAKENING-CONTROL-OF-INDUCTION-MOTOR/347e772398c8b3fa1e8d9f17d1972b49701acf04` (28.05.19).

[52] S. D. Borge (2018). *Development, modelling and simulation of control system for isolated induction machine feeding local loads based on filtered back-to-back 2L-3ph VSC topology with S-PWM voltage control.* (Specialization project). Department of Electric Power Engineering: NTNU.

A   Induction machine parameters

Parameter/rating	Unit	#M1	#M2	#M3	#M4
Power (mechanical, no friction), P_N^{Gm}	[kW]	-4.3728	-7.4657	-11.262	-16.684
Power (electrical), P_N^G	[kW]	-3.9725	-7.1147	-10.133	-15.469
Voltage (line-line, rms), $V_N^G \cdot \sqrt{3}$	[V]	400	460	220	220
Current (rms), I_N^G	[A]	7.6132	10.6686	30.094	49.691
Power factor	[-]	-0.7531	-0.837	-0.8836	-0.817
Frequency, f_N^G	[Hz]	50	60	60	60
Mechanical speed, ω_m^G	[rpm]	1555	1829	1240	1847.4
Slip	[-]	-0.037	-0.016	-0.0333	-0.02633
Pole pairs, n_{pp}	[-]	2	2	3	2
Inertia	[kgm^2]	0.0131	0.05	0.4	2.5
Friction factor, μ_f	[Nm s]	0.002985	0.008141	0.0009868	N/A
Stator resistance, r_s	[Ω]	1.405	0.6837	0.282	0.1062
Stator leakage inductance, L_{ls}	[mH]	5.839	4.152	1.3581	0.5690
Rotor resistance, r_r	[Ω]	1.395	0.451	0.151	0.0764
Rotor leakage inductance, L_{lr}	[mH]	5.839	4.152	0.7109	0.5690
Magnetising inductance, L_m	[mH]	172.2	148.6	39.4306	15.4752

Table A.1: Short-circuited rotor induction machine parameters (in generator operation). Rotor quantities referred to stator-side.
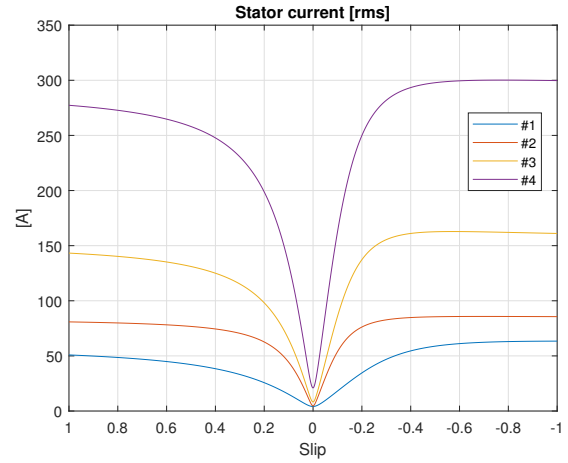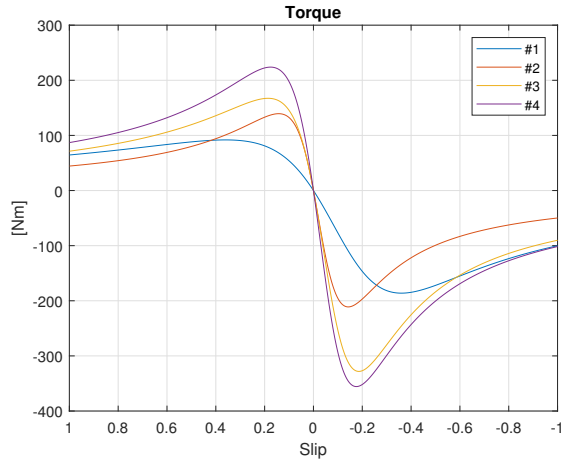

Figure A.1: Torque characteristics at rated voltage

Figure A.2: Current characteristics at rated voltage

Sources:

- **#M1**: MATLAB/Simulink. Preset squirrel-cage machine found in the Simscape-library block "Asynchronous Machine SI Units".

- **#M2**: MATLAB/Simulink. Preset squirrel-cage machine found in the Simscape-library block "Asynchronous Machine SI Units".

- **#M3**: T. F. Chan and K. Shi. (2011). *Applied Intelligent Control of Induction Motor Drives, First Edition*: Appendix B: Parameters of Induction Motors. John Wiley & Sons (Asia) Pte Ltd.

- **#M4**: [1][8]

B LCL-filter design script (MATLAB)

```matlab
%% Based on:
% A. Reznik, M. G. Simoes, A. Al-Durra and S. M. Muyeen. (2012).
% LCL filter design and performance analysis for small wind turbine systems
% 2012 IEEE Power Electronics and Machines in Wind Applications, pp.1-7.

%% Fixed parameters
x=0.05; %power-factor variation seen from load
k_a=0.2; %attenuation factor
delta_i=0.1; %current-ripple-max of rated load

%% Input parameters
f_sw=10^(4); %swithcing frequency, [Hz]

V=230*sqrt(3); %load-voltage, [line-line, rms][V]
f=50; %load-frequency [Hz]
S=sqrt(2)*10^(3)*3.58; %max apparent power, three phase [VA]

mu_s=0.1; % increasment scale of v_n_L
v_m=0.4606; % RMS/DC-model maximum normalized reference

%% Derived parameters

V_DC=V/sqrt(3)*(1+mu_s)/(v_m);

w_n=f*2*pi;
w_sw=f_sw*2*pi;

i_peak=S/(sqrt(3)*V)*sqrt(2);
Z_b=V^2/(S);
C_b=1/(w_n*Z_b);

%% Step 1
L1=V_DC/(6*f_sw*i_peak*delta_i);

%% Step 2
C_f=x*C_b;

%% Step 3
r=0;
k_it=100;
count=0;
delta_r=0.00001;

while (k_it>k_a)
    count=count+1;
    r=r+delta_r;
    k_it=1/abs(1+r*(1-L1*C_f*w_sw^2));
end

L2=L1*r;

%% Step 4
w_res=sqrt((L1+L2)/(L1*L2*C_f));
f_res=w_res/(2*pi);

if(10*f<f_res && f_res<f_sw*0.5)
    fprintf('Resonance: OK\n');
else
    fprintf('Resonance: NOT OK\n');
end
```

```matlab
62  %% Step 5
63  R_f=1/(3*w_res*C_f);
64
65  %% Assign output
66  load_filt_C=C_f;
67  load_filt_L1=L1;
68  load_filt_R=R_f;
69  load_filt_L2=L2;
70
71  %% Display output
72  fprintf('C [mF]:\n')
73  disp(C_f*10^(3))
74  fprintf('L1 [mH]:\n')
75  disp(L1*10^(3))
76  fprintf('L2 [mH]:\n')
77  disp(L2*10^(3))
78  fprintf('R [ohm]:\n')
79  disp(R_f)
80  fprintf('V_DC [V]:\n')
81  disp(V_DC)
82
83  %% Calculate voltage-drop margin
84  fprintf('Voltage drop margin [V]: \n')
85  disp(V/sqrt(3)*mu_s-(L1+L2)*w_n*i_peak/sqrt(2))
```

C   Simulink interconnection of models

NTNU

Norwegian University of
Science and Technology